ABSTRACT

XIAO, ZIYU. Development of Resolution-Enhanced Magnified Neutron Imaging at the PULSTAR Reactor. (Under the direction of Dr. Ayman I. Hawari).

Design and implementation of a Resolution-Enhanced Magnified Neutron Imaging (REMANI) system has been investigated at the PULSTAR reactor at North Caroline State University. In conventional neutron imaging, the system resolution is limited by geometric unsharpness and the intrinsic resolution of the detection system. In this work, these limitations are overcome and improvement in resolution is achieved by using a pinhole aperture and placing the object away from the detection system so that a magnified image is recorded allowing finer details in the object to be resolved. To maintain good signal-to-noise ratio, a mask containing a large number of pinholes is used. The pinholes are arranged in a coded fashion to simplify image reconstruction, which is obligatory in any multi-pinhole imaging system.

Monte Carlo neutron transport simulations using the MCNP code were performed to support system design. Models reflecting the beam characteristics at the PULSTAR Reactor were developed. Based on the conclusion of the simulations, a demonstration of the REMANI system with a coded source was performed using a detection system composed of a ^{6}LiF/ZnS scintillator and an Andor CCD camera. A mask coded with a 178×178 mosaicked modified uniform redundant array was fabricated on a piece of 450 μm-thick gadolinium foil. The mask contains 15,840 pinholes scattered on a grid with a size (pitch) of 200 μm. The diameter of each pinhole is 100 μm. By analyzing the spread of the reconstructed image of a sharp gadolinium edge, the system resolution was shown to be improved from 245 ± 6 μm under the conventional imaging setup to 117 ± 11 μm with a magnification factor of 3.4. As predicted

by theory and simulations, the attained resolution is better than the one set by the detection system, and is limited by the diameter of the pinholes in the mask.

The present work successfully demonstrates the feasibility of variable magnification coded source neutron imaging. It illustrated new ways in enhancing the spatial resolution of a neutron imaging system with currently used detection systems. In fact, using intense neutron sources and longer wavelength neutrons, it can be envisioned that the principles demonstrated in this work could lead to neutron imaging systems with resolution in the micrometer range.

Development of Resolution-Enhanced Magnified Neutron Imaging at the PULSTAR Reactor

by
Ziyu Xiao

A dissertation submitted to the Graduate Faculty of
North Carolina State University
in partial fulfillment of the
requirements for the degree of
Doctor of Philosophy

Nuclear Engineering

Raleigh, North Carolina

2016

APPROVED BY:

Dr. Ayman I. Hawari Committee Chair	Dr. Bernard W. Wehring
Dr. Mohamed A. Bourham	Dr. H. Joel Trussell

DEDICATION

I dedicate this dissertation to my beloved maternal grandmother and my parents.

BIOGRAPHY

Ziyu Xiao was born on February 18, 1986 in Beijing, China. She grew up in Zhuozhou, a small town in HeBei province and moved to Beijing with her family at the age of 13. She attended Tsinghua University from 2003 to 2007, and graduated with a Bachelor of Science degree in Engineering Physics.

In the summer of 2007, Ziyu came to the United States and enrolled as a graduate student in Nuclear Engineering Department at North Carolina State University. Under the guidance of Dr. Ayman I. Hawari, she conducted research on neutron imaging and obtained her Master of Nuclear Engineering in December 2010. Ziyu then continued to pursue her Ph.D degree. She worked on development of a Resolution-Enhanced Magnified Neutron Imaging system with Monte Carlo simulation tools, as well as experimental implementation of the designing system in the Neutron Imaging Facility at the PULSTAR reactor located on NSCU campus.

ACKNOWLEDGMENTS

I would like to express my deepest gratitude to my advisor, Dr. Ayman Hawari, for his guidance and support on my research and graduate studies. I really appreciated this great opportunity he provided to explore this intriguing field. I am grateful for his trust, encouragement and patience with me throughout this project.

I would like to extend my sincere gratitude to Dr. Mohamed Bourham, Dr. Bernard Wehring, and Dr. Joel Trussell, who kindly agree to serve on my dissertation committee members, for their advice and comments on this work.

My thanks go out to Mr. Andrew Cook, Mr. Scott Lassell, Mr. Kerry Kincaid, Mr. Gerald Wicks, and Mr. Greg Gibson for their assistance in developing the system and setting up the experiments. I would also like to thank all the reactor staffs and student operators at the PULSTAR reactor for operating the reactor during the data collection period, sometimes even on the weekends.

I would like to thank my fellow colleagues and friends. Special thanks are given to Dr. Kaushal Mishra, for the discussions and the assistance when I started my graduate studies; to Arka Datta and Abdullah Alomari, for their indispensable aid during the experiments

Finally, I would like to express my thanks to my parents, my grandma, and Bohao Cao for their love, understanding, and unconditional support. Without you, I would not be able to finish this work. I would also like to thank Fan Wang, Siyu Liu, Shiqin Xu and all my friends for their encouragement, entertainment and caring that helped me get through difficult times.

TABLE OF CONTENTS

LIST OF TABLES

LIST OF FIGURES

LIST OF SYMBOLS

Parameters

D: the diameter (or side length) of the aperture
L: the aperture-to-object distance
b: the object-to-image distance
m: magnification factor
A: mask array
G: decoding array
N_1: the number of ones in the mask array
N_T: the number of total elements in the mask array
ρ: the open fraction of the mask
α: the number of pixels of the projection of a mask grid element
κ: parameters for scaling the decoding array
S_A: the physical side length of mask array
S_R: the side length of mask projection onto the image plane
S_O: the side length of the field of view (FOV)
S_M: the side length of the mask
S_P: the side length of the image used in reconstruction
M: Modulation
res: minimum resolvable distance, also known as the resolution of the system

Functions

Note: functions are defined for the conventional and single-pinhole imaging system, if they are not specified.

$A(\eta,\xi)$: distribution of emitted neutrons in the aperture plane
$\Phi_T(u,v)$: distribution of transmitted neutrons in the object plane
$O(u,v)$: distribution of neutron attenuation characteristics in the object plane
$T(x,y)$: distribution of projected neutrons in the image plane
$I(x,y)$: continuous image function
$P(i,j)$: discrete image function
δ: Dirac delta function
$N_\delta(x,y)$: $N(x,y)$ for a point object
$I_\delta(x,y)$: $I(x,y)$for a point object
$A_1(\eta,\xi)$: distribution of neutron emitted from one hole in the multi-pinhole system
$A_\delta(\eta,\xi)$: a collection of Dirac δ functions indicating pinhole location in the multi-pinhole system
$I_{multi}(x,y)$: continuous image function in multi-pinhole system

$P_{multi}(i,j)$: discrete image function in multi-pinhole system
$P_{single}(i,j)$: discrete image function from one hole in multi-pinhole system
$\hat{P}_{\text{single}}(i,j)$: reconstructed image function
$h(u,v)$: impulse response function
$h_d(x,y)$: impulse response function due to detector unsharpness.
λ: intrinsic resolution of the detection system
$h_g(x,y)$: impulse response functions due to geometry unsharpness
U_g: the size of geometric unsharpness
$h_s(x,y)$: impulse response due to sampling
Δs: the size of pixel
$h_r(x,y)$: impulse response due to reconstruction

Abbreviations

REMANI: Resolution-Enhanced Magnified Neutron Imaging
NIF: neutron imaging facility
IP-ND: imaging plate neutron detectors
CCD: charge-coupled device
MCP: microchannel plate
FWHM: full width at the half maximum
LSF: line spread function
PSF: point spread function
MTF: modulation transfer function
ESF: edge spread function
FOV: the field of view
SNR: the signal-to-noise ratio
NEQ: noise equivalent quanta
DQE: detective quantum efficiency
NPS: noise power spectrum
ASTM: American Society for Testing and Materials
SI: Sensitivity Indicator
BPI: Beam Purity Indicator
FZP: Fresnel zone plate
NRA: non-redundant arrays
URA: uniformly redundant array
MURA: modified uniformly redundant array
MLE: maximum likelihood estimator
LSE: least square estimator

Chapter 1

Introduction and Background

Neutron imaging is a powerful tool in non-destructive testing. In this process, an image that reflects the internal structure of the object is formed by neutrons. A typical neutron radiography system consists of three components: a neutron source/beam, an object and an image recording system. A neutron beam generated from the source is collimated and directed onto the object. Neutrons interact with nuclei of the object by scattering or absorption, when they pass through. An image recording device is placed after the object to detect the position and intensity information of the transmitted neutrons and then forms a corresponding image. The contrast of the image represents the two-dimensional material characteristics of the object.

Similar to other types of imaging techniques, the image quality of neutron imaging can be evaluated in three principal components: spatial resolution, contrast, and noise. The definitions are given in many imaging textbooks, such as Hasegawa (1990). The spatial resolution is the smallest distance that two objects can be separated and still appear distinct. It can also be defined in terms of the point spread function (PSF), which is the image of an "ideal" point object. Contrast is the signal difference between an object and its background. Noise is defined as the uncertainty with which the signal is recorded. All the concepts are interrelated and one cannot use a single term to describe the performance of an imaging system. The tradeoff among these properties should be optimized in the system design.

1.1 Introduction to Neutron Imaging

Neutrons, especially thermal neutrons, have unique properties in interacting with matter, which make them useful in imaging applications. Neutrons usually interact with the nuclei of the material by scattering and absorption. The probabilities of the interactions are largely dependent on the energy of the neutrons and the nuclear structure of the material. In contrast to X rays and gamma rays, neutron-nuclei interactions are not related to the atomic numbers of the material and can be different for each isotope.

1.1.1 History of Neutron Imaging

History of neutron imaging can be traced back to 1930s. This section gives a brief review of the development of neutron imaging in a chronological order, focused on facility and detector advancements, as well as, the applications that evolved with these advancements.

In 1935, Kallmann and Kuhn made the first radiographic image with neutrons from a small neutron generator (Kallmann, 1948). Their imaging device was multiple layer plates including a photo-emulsion film and a lithium foil enclosed in an exhausted receptacle (Kallmann & Kuhn, 1940).

In 1950s, the image quality was enhanced with the availability of higher intensity neutron beams and the improvement of the film system. Thewlis successfully conducted the imaging experiment with neutrons from a high flux reactor (Thewlis, 1956). Neutron imaging started to have practical applications as a non-destructive testing tool.

In the 1960s, more work was done at neutron beams from reactors. Barton proposed a divergent beam collimator, which is still widely used in today's facilities (Barton, 1967). Some organizations started to offer neutron radiography as a commercial service (Berger, 1976). At the meanwhile, fast, epithermal, and cold neutron imaging had also been studied.

With growing interest in applications on radioactive fuel imaging, transfer techniques and track-etch methods that were less of sensitivity to gamma radiation were developed. More neutron converting materials were explored as the converter in these methods (Berger, 1971).

Real-time neutron imaging was also explored to observe dynamic events. In mid-1960s, testing results of a neutron television system were published. The system was a neutron sensitive image intensifier tube, coupled to a vidicon television camera (Berger 1966). There were other systems that used image intensifiers to amplify images created from phosphor screens doped with neutron capture elements. For example, a sophisticated system, usually referred as a Thompson tube, used a gadolinium oxy-sulfide screen as a neutron convertor (Thompson-CSF). Later, amorphous silicon sensors were developed for their temporal performance (Estermann, 2005).

In the past two decades, with the advancement in computer science and imaging sensor, significant advancements were made in digital neutron imaging. Inspired by the X-ray imaging plate (IP) using a photo stimulated luminescent (PSL) phosphor, an imaging plate neutron detectors (IP-ND) was developed for neutron digital radiography. The optimized design with admixture of Gd_2O_3 was made commercially available by Fuji Photo Film Co., Ltd. Though the spatial resolution was not as high as the film system, IP-NDs had many advantages, such as the capability of direct data acquisition on a computer, a wide range of linearity, high sensitivity and repeated usage (Karasawa, 1995, Takahashi, 1996, & Kobayashi, 1999).

Neutron sensitive scintillator screens coupled with a camera using a charge-coupled device (CCD) sensor became popular after 1990s. Due to the low output from the scintillator, the requirement for the camera was stringent, high quantum efficiency and low dark current noise. Some systems replaced scintillator screens with neutron sensitive microchannel plates (MCP) (Fraser, 1990) to increase the light intensity available for the camera. Such digital imaging systems made neutron tomography possible for routine examination.

The advancements in digital imaging systems extended the range of applications and techniques that can be performed with neutrons. New ways of achieving image contrast have been introduced in order to obtain additional structural information (Strobl, 2009). For example, phase contrast imaging shows contrast enhancement on the edges of the sample, which depends upon the neutron coherent scattering lengths of the materials and the degree of spatial coherence of the neutron beam (Mishra, 2011). Energy selective imaging uses monochromatic neutrons instead of a white spectrum; thus a material can show the energy dependence response, such as grain structures in crystalline materials by Bragg scattering (Lehmann, 2009). Polarized neutron imaging visualizes the magnetic field inside and around the sample by detection of the polarization changes in the transmitted beam (Kardjilov, 2008).

1.1.2 State-of-the-Art High Resolution Neutron Imaging Facilities

Due to the limited accessibility of intense neutron sources, neutron imaging is not as popular as X-ray or gamma-ray imaging. However, based on the survey by International Society for Neutron Radiology (“Neutron Imaging Facilities Survey”, 2014), there are more than 40 facilities with capabilities to conduct neutron imaging applications globally. Some facilities focusing on research development are not included in this report, such as the neutron imaging facility (NIF) at North Carolina State University PULSTAR Reactor.

Neutron imaging has a wide range of applications in the fields of industry and scientific research. The subjects cover physics, material science (Luo, 2007), biology (Schwarz, 2005 & Moghaddam, 2008), archaeology (Kockelmann, 2006), aerospace (Chalovich, 2004), and more. High spatial resolution is always preferable in examining the details of objects. Currently, the state-of-the-art imaging techniques are carried out in Europe and the United States, both in terms of the beam conditions and the detection system. Researches on improving the spatial resolution to the order of micrometers have been conducted. This section summarizes the developments on different components that limit the resolution and the state-of-the-art performances achieved in current facilities.

The first key component in determining the resolution of an imaging system is the scintillator screen, which converts the incident neutrons into visible light for detection. Usually, neutrons are converted to secondary radiation by absorption. Optical photons are then created by these products which deposit energy in the scintillating material.

Scintillator screens can be classified into two categories: powder screens and crystal screens. In powder screens, the emitted photons leave the screen by scattering in all directions. The resolution in terms of full-width at half maximum (FWHM) of the line spread function (LSF) is approximately equal to their thickness (Swank, 1973). Thinner scintillating layers are preferred to improve the resolution, but limitations on thickness exist to maintain sufficient light output. In neutron imaging, two prominent scintillation materials used in the powder screens are ^{6}LiF/ZnS and Gd_2O_2S:Tb (referred as P43 or Gadox). Gadox has better performance in terms of resolution for two reasons. First, it can be made much thinner due to higher absorption cross-section of gadolinium. Secondly, the mean free path of secondary radiation created by Gadox are much smaller than the ones by ^{6}LiF/ZnS. Lehmann et al. performed experiments with ^{6}LiF/ZnS screens with a thickness range of 25 μm - 300 μm, and 10 μm Gadox screen (Lehmann, 2007). Kardjilov et al. studied the performance of 5 μm Gadox with different substrate materials and different coating (Kardjilov, 2011). In crystal scintillators, only photons within the crystal angle are allowed to leaving the screen, thus producing much better spatial resolution. Matsubayashi et al. used a 3 mm-thick LiF crystals and a fluorescent microscope as the imaging device and achieved a spatial resolution of 5.4 μm (Matsubayashi, 2010). Williams et al. have performed high resolution imaging with 1 mm-thick GGG single crystal scintillator (Williams, 2012). Research has also been done in other perspectives on the development of neutron scintillator, such as new types of scintillator materials (Van Eijk, 2004) and structured scintillators (Nagarkar, 2001 & Shestakova, 2007).

Scintillator are usually coupled with high-end digital cameras with CCD sensors. The leading CCD sensors used in neutron imaging have a pixel size of 13.5 μm×13.5 μm, 16-bit output depth, and more than 95% quantum efficiency for the wavelength of the scintillator emission peak. Deep cooling is required during operation to minimize dark current noise.

Optical lenses are used to provide focusing of the scintillating image onto the CCD sensor. The reproduction ratio, defined as the image size on the sensor compared to the real-life size of the object, is one of the most important parameters of a lens system influencing the spatial resolution. The effective pixel size is calculated as the pixel size on the CCD divided by the reproduction ratio, representing the sampling distance on the scintillator plane. Higher reproduction ratio indicates finer sampling on the scintillating image; thus higher resolution can be achieved under the same condition. Photographic lens with a maximum reproduction ratio of 1:1 are usually used in neutron imaging. Spatialized micro-focusing optical lenses have been developed (Lehmann 2007), and infinity corrected optical design ("macroscope" design) was employed (Williams, 2012) to minimize the aberration of the optical system. To increase the scintillator-to-sensor magnification, the detector can be tilted so that the image can be stretched in one direction (Frei, 2009).

Other devices with high resolution potential have been developed, such as micro-channel plates (MCP). An MCP is an event-counting imaging detector, which has a boron-doped or gadolinium-doped glass structure with straight-through open channels. Charged particles are created by neutron absorptions in the wall and get amplified through the channels by the high voltage applied across the plate. Their intensity and position information can be recorded by a cross delay-line readout, cross strip readout, and a Medipix 2 readout system (Siegmund, 2009). Therefore, the resolution of the resulting image is determined by the diameter and center-to-center separation of the channels (Hussey, 2007).

A neutron microscope has gained attention recently which involves the concept of magnification. Trtik used on a very thin gadolinium oxysulfide (Gd2O2S:Tb+) scintillator screen and magnifying optics (2015). A neutron microscope using a reflective neutron magnifying lens based on Wolter optics (Liu, 2013) is being developed at NIST (Hussey, 2014). It can be seen that though the forms are different, magnification must be introduced in the system in order to overcome the limitation on the resolution set by the detection system.

1.1.3 Standards for Image Quality in Neutron Imaging

Standardization is necessary in the field of neutron imaging. Currently, there are two active groups producing standards in neutron radiography: the American Society of Testing and Materials (ASTM) in the US and the International Organization for Standardization (ISO) internationally.

Listed are ASTM standards that are related to neutron imaging and neutron imaging beams:

1) ASTM E748-02 (Subcommittee E07.05, 2008) describes neutron radiography as a general method and provides a guidance for the application.
2) ASTM E545-14 (Subcommittee E07.05, 2014) describes the methods for determining image quality in thermal neutron radiographs, with the use of Beam Purity Indicators (BPI) and Sensitivity Indicators (SI). The fabrication of the BPI and SI is given in ASTM E2861-11 and E291-14.
3) ASTM E803-91 (Subcommittee E07.05, 2013) describes the method for determining the L/D ratio of neutron radiographic beams.
4) ASTM E1496-05 (Subcommittee E07.05, 2010) describes methods for measuring of the dimensions of the objects in neutron radiography.
5) ASTM E261-15 and E262-13 (Subcommittee E10.05) describes methods for determining the neutron flux and thermal neutron flux by radio-activation techniques, which is also useful in determine the strength and cadmium ratio of the neutron radiographic beam.

These standards provide a basis to monitor and compare the performance of neutron imaging facilities. They have been widely used for commercial neutron radiographic non-destructive testing. However, they are neither comprehensive to cover all the imaging quality factors, or accurate for advanced imaging systems. Methods beyond these standardizations are adopted to evaluate the quality of the neutron imaging system in this work. Details are given in Section 2.4.

1.1.4 Coded Mask Techniques in Imaging

The coded source technique applied in the REMANI system was inspired by coded apertures used in X-ray and gamma-ray imaging. High energy photons cannot be easily focused by refraction, reflection or diffraction. Thus pinhole cameras are usually used to image such incoherent radiation. To increase collection efficiency of the camera, the pinhole aperture was replaced by a coded aperture.

The coded aperture technique was first proposed by Mertz and Young in 1961 and was applied to X-ray star photography (Mertz, 1961). The aperture used was a Fresnel zone plate (FZP) consisting of several radially symmetric rings called zones. The image that was formed on the camera was an ensemble of FZP by geometric shadowing of the stars and resembled Gabor holograms (Gabor, 1949). The desired star image can be reconstructed by an optical system, where the collected hologram was used as a lens to form an image of a monochromatic point source. The FZP was then applied in nuclear medicine by Barret (1972) to image small objects such as a thyroid gland, and in gamma-ray imaging by Rogers (1972). Digital recording and reconstruction of the holograms have been exploited by Singleton (1976). A tomographic imaging was successfully demonstrated by Ceglio (1977) of X-rays emitted from a laser-compressed target.

In 1968, Dicke and Ables proposed a random array of pinholes to image incoherent radiation (Dicke, 1968; Ables, 1968). The aperture is covered with a large number of randomly distributed pinholes on an opaque material. The overlapping images can be unscrambled to a single image by matched filtering decoding. However, the inherent noise structure is not avoided in the reconstruction.

In 1971, Golay presented a new family of mask pattern - non-redundant arrays (NRAs). The autocorrelation of these arrays is a single peak, with no sidelobe up to a small lag. The reconstructed image for a small object would be perfect with, at most, a d.c. term. But the limited field of view prohibits the application in imaging large objects (Golay, 1971). Golomb and Kopilovich suggested algorithm in constructing larger NRAs (Golomb, 1984; Kopilovich, 1988). It has been applied in infrared stellar imaging (Aitken, 1981) and nuclear medicine (Fleming, 1984).

Another important family in coded aperture is referred to as uniformly redundant array (URA), generated from cyclic difference set (Baumert, 1971). If circular correlation is used, the correlation function has a central peak with a flat side-lobe. Gunson and Polychronopulos proposed constructing a one-dimensional mask for X-ray telescope (Gunson, 1976). The idea was generalized to constructing a two-dimensional mask, which was obtained by folding a 1D cyclic difference set sequence along the extended diagonal (Proctor, 1979). Fenimore proposed a different algorithm for a two-dimensional URA with size of $r \times s$ (1978), which required both r and s be prime numbers and $r - s = 2$. It was a subset of URA, but was the most popular reference in URA due to convenience in application. In 1989, a square aperture - Modified URA (MURA) - was introduced based on the same algorithm. It has equally superior imaging performance as URA, but with a wider selection of apertures to match particular needs (Gottesman, 1989).

1.2 Objective

The objective of this work is to design and implement a Resolution-Enhanced Magnified Neutron Imaging (REMANI) system at the PULSTAR Reactor at North Carolina State University. Resolution of a neutron imaging system is limited by many factors in the process of image formation. Two main components are geometric unsharpness and detector unsharpness. Geometric unsharpness refers to the loss of sharpness due to divergence of the neutron beam and the geometric arrangement of the system. Detector unsharpness refers to the intrinsic resolution that a detection system can achieve.

Conventionally, a neutron imaging system is set up in such a way that the geometric unsharpness is as small as practically possible. The resolution enhancement is achieved by technical improvements in the hardware of the detection systems.

In a REMANI system, the resolution enhancement is achieved from a new perspective. The detection system is placed away from the object so that a magnified image is obtained. With magnification, it is possible to resolve two points in the object that are closer than the detector intrinsic resolution. Therefore, system resolution can overcome the limitation set by the detection system. The size of the aperture is required to be small because it limits the system resolution. Multiple pinholes are used to compensate for the signal loss due to the small opening of each pinhole and reconstruction is obligatory. To simplify image reconstruction and to reduce artifacts introduced by this process, the pinholes are arranged in a coded fashion and the aperture is replaced by a coded mask.

Chapter 2

Conventional Neutron Imaging at the PULSTAR Reactor

A neutron imaging facility (NIF) at the PULSTAR Reactor has been set up and used for research development and industrial applications for many years. It will be modified for the implementation of a REMANI system. Therefore, characteristics of the beam and the image quality of the currently available imaging systems are the baseline for the design of a new system.

Based on the descriptions of the NIF, this chapter explains the conventional neutron imaging system and methods for image quality evaluation. The beamline has been optimized and characterized for thermal neutron imaging application. The performance of the scintillator system has been thoroughly evaluated in spatial domain and in frequency domain. Some concepts and methods that were widely used in X-ray imaging have been adapted for neutron imaging.

2.1 Neutron Imaging Facility at the PULSTAR Reactor

The PULSTAR Reactor is located at North Carolina State University. It has been operational and used for teaching, research and service to the public since 1972.

The core of the reactor has dimensions of 15” × 13” × 24” (L × W × H). It is loaded with a five by five array of fuel assemblies, each of which contains 25 fuel pins. The fuel pins consist of a stack of uranium dioxide pellets with 4% enrichment, and covered by Zircaloy-2 cladding. A 15,000-gallon open tank of water surrounded by concrete shielding is used as the coolant and the moderator. The response characteristics are very similar to commercial light water power reactor. The reactor is operational at the currently licensed maximum power of one megawatt. An upgrade of the reactor system has been initiated to increase the power to two megawatts.

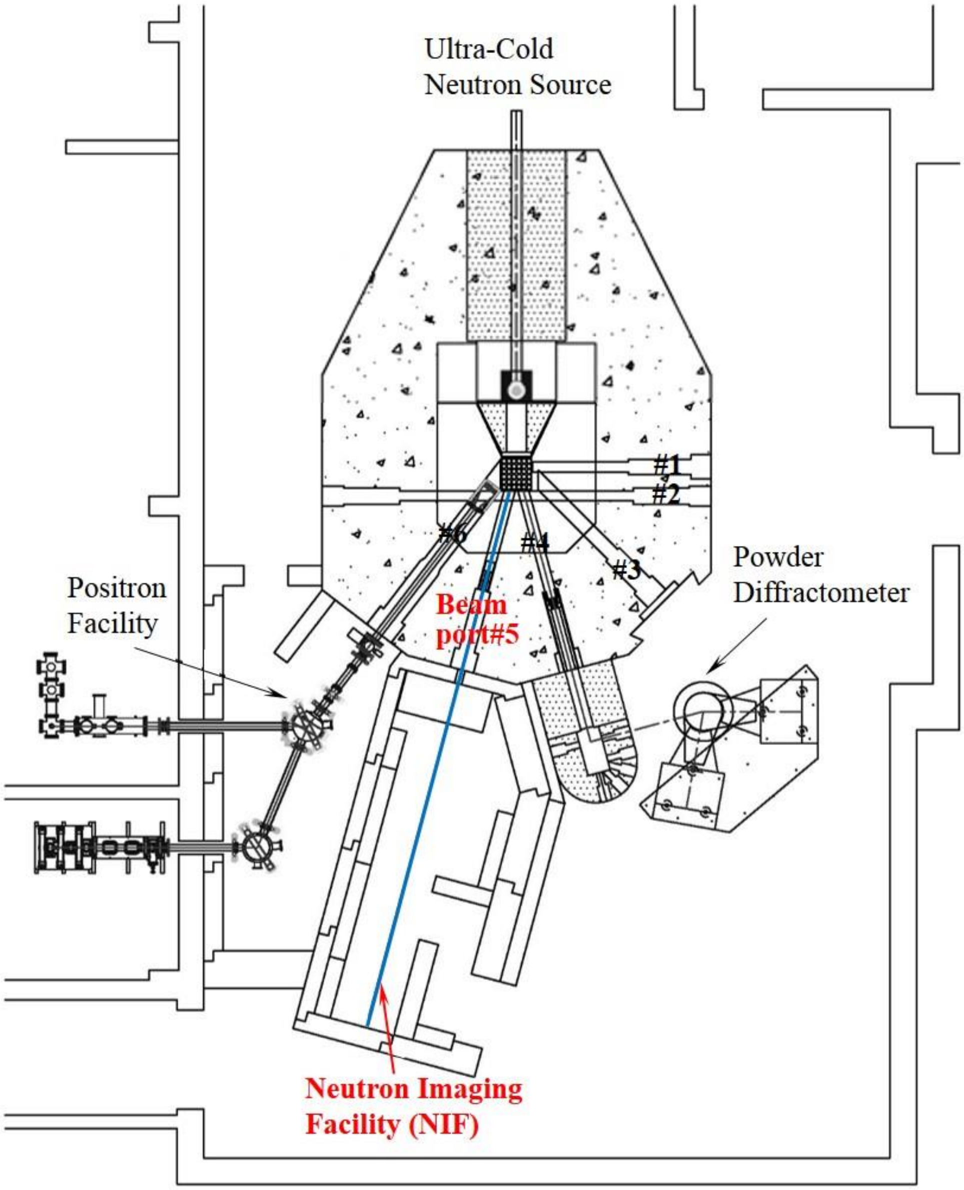

Figure 2.1 The layout of PULSTAR Reactor

There are six beam ports in the PULSTAR Reactor, which are marked as #1 to #6 in the reactor layout shown in Figure 2.1. Beam ports are air-filled aluminum tubes that extend from the edge of the core through the biological shielding of the reactor, and provide neutron beams for various applications. Except Beam port #2, which is a through beam and is parallel to the surface of the core, all the beam ports directly face towards the core. It means that the neutron beams obtained have large thermal fluxes as well as relatively high gamma contaminations. The neutron imaging facility (NIF) is located at beam port #5, because the available distance is the longest in this direction.

Figure 2.2 shows a side view of the NIF facility. It can be considered as three parts: the collimator, which is used to contain the neutrons emerging from the source and to guide them to the object being imaged (Domanus, 1992); the shutter system, which provides a safe

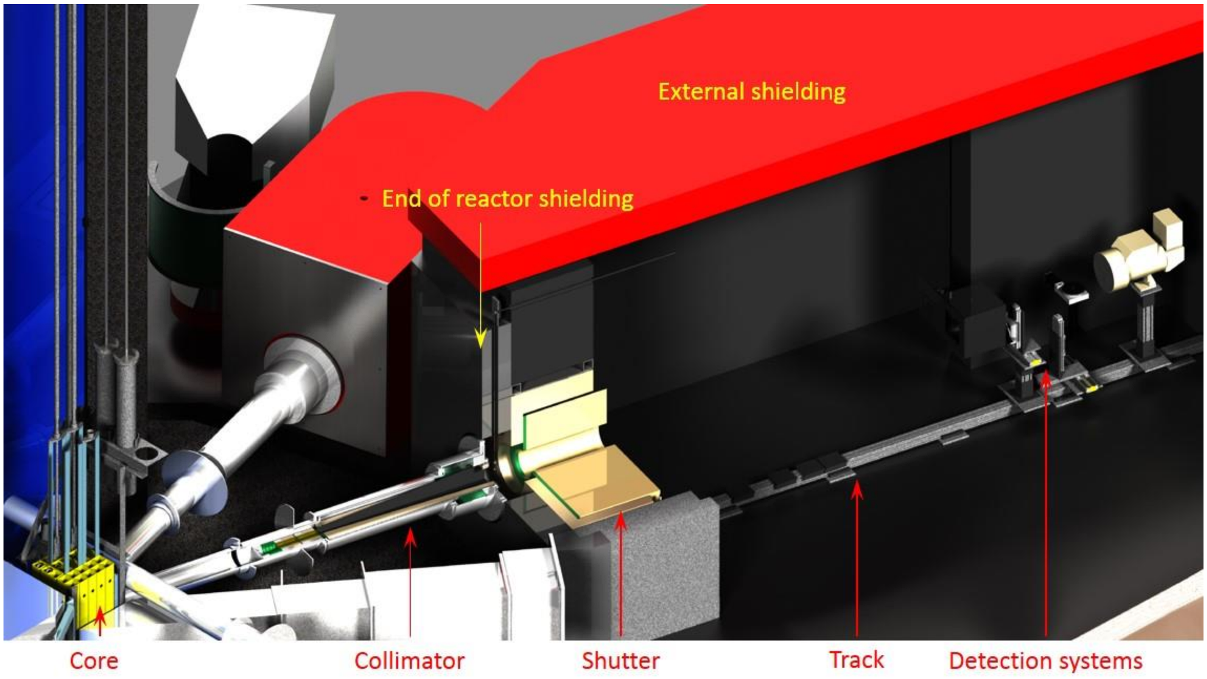

Figure 2.2 Beamline of NIF and imaging cave

access radiation level for the experimenters; and the detection system that record and output the images.

2.2 Neutron Imaging Beam

In order to perform neutron imaging, the beamline is required to have high-intensity uniformly-distributed thermal neutrons as well as low fast neutrons and low gamma component.

2.2.1 NIF Collimator

The collimator of NIF is installed completely inside of the beam port #5. From Figure 2.1 and Figure 2.2, it can be seen that this beam port is a cylinder tube with an angle of 15 degrees to the normal to the core surface. The tube consists of three sections with increasing diameters. From the beam entrance (at the surface near the reactor core) to the beam exit (at the biological shielding of the reactor), the diameters are 6 inches, 9 inches and 15 inches; and the lengths are 65 inches, 40 inches and 10 inches, respectively.

Figure 2.3 shows a section view of the collimator. It is constructed in segments and then assembled together in an aluminum outer tube with the front side sealed. In order to match the shape of the beam port, the outer tube has two steps: the first step is 18 inches long and 6 inches in diameter; the second step is 50 inches long and 9 inches in diameter, extending up to the beam exit. The outer space in the third section of the beam port is filled with vestibule shielding composed of 7-inch long borated polyethylene and 3-inch long lead.

Major components of the collimator include a precollimator, beam filters, and a main collimator. The precollimator is 6-inch long and has a convergent shape, leading the neutrons

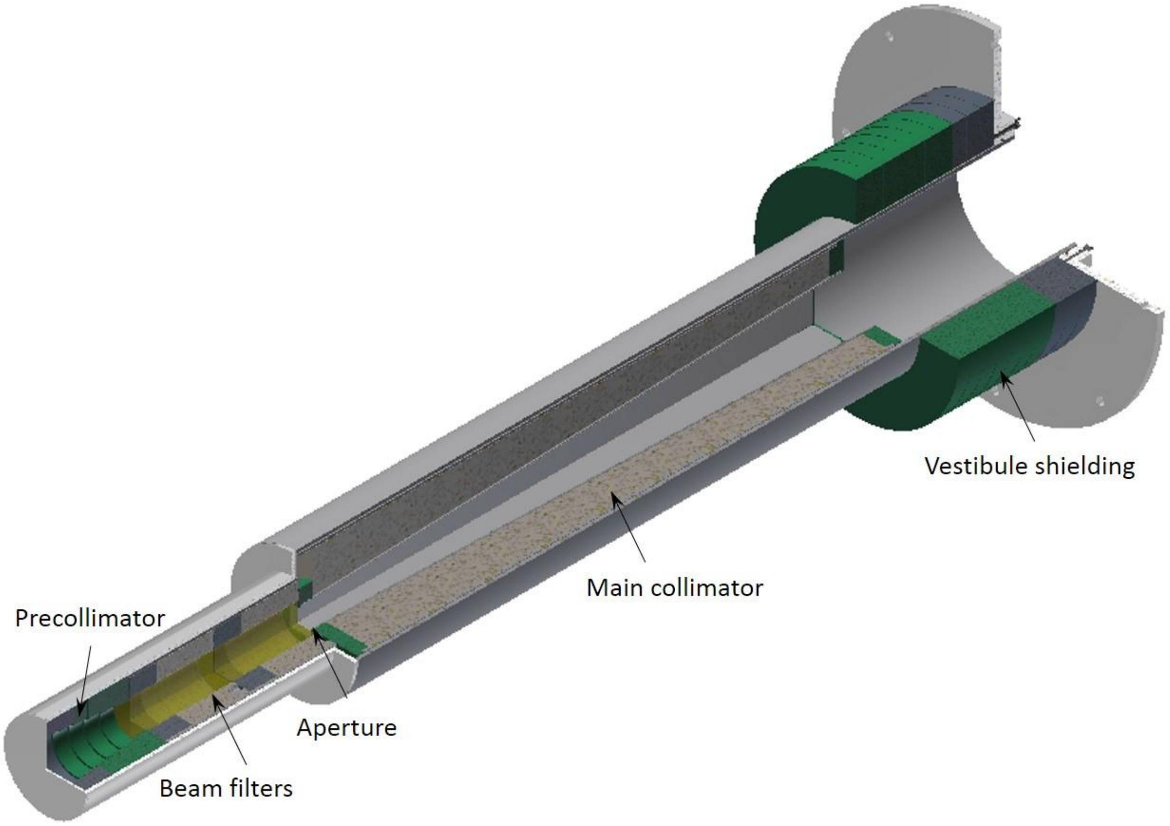

Figure 2.3 NIF collimator inside of beam port # 5

to the following beam filters and the aperture. The beam filter is used to reduce the fast neutron and gamma contents of the beam, while pass through thermal neutrons. There are different filters combinations available at the facility, the optimization will be discussed in detail in the next section. The inlet of the main collimator is a 4 cm × 4 cm square, which is the defining aperture of the beam. The collimator is divergent with a form of truncated pyramid. The length of this part is 100 cm and the outlet is an 11 cm × 11 cm square. Thus the divergence of the beam is about 2 degrees. The inner wall is lined with 0.1-inch thick Boral, which consists of a core of mixed aluminum and boron carbide particles and aluminum cladding. The ^{10}B loading of 33 mg/cm^2 makes it a strong neutron absorbing material, thus reduces the neutron scattered from the wall into the beam. The collimator is filled with a heat resistant neutron shielding material called SWX-277, which provides more than twice the hydrogen as ordinary concrete and a boron content of 1.56%.

The collimator is followed by a transition plate with a thickness of 9.5 inches and a rotating drum type of beam shutter with a thickness of 25.5 inches. A 12-inch diameter hole on the shutter is aligned with the collimator at the open position. Other details of the facility design and construction can be found in Mishra's thesis (2010).

An imaging cave has been built to enclose the beam shutter. Figure 2.4 (a) and (b) show the inside view and the outside view of the cave. The opening and closing of the beam shutter is controlled by a computer system outside of the cave and safety switches at the entrance door. The wall made out of precast concrete blocks keeps the radiation level in the working area below 0.2 mR/hour when the imaging facility is operated at the 1-MW full power.

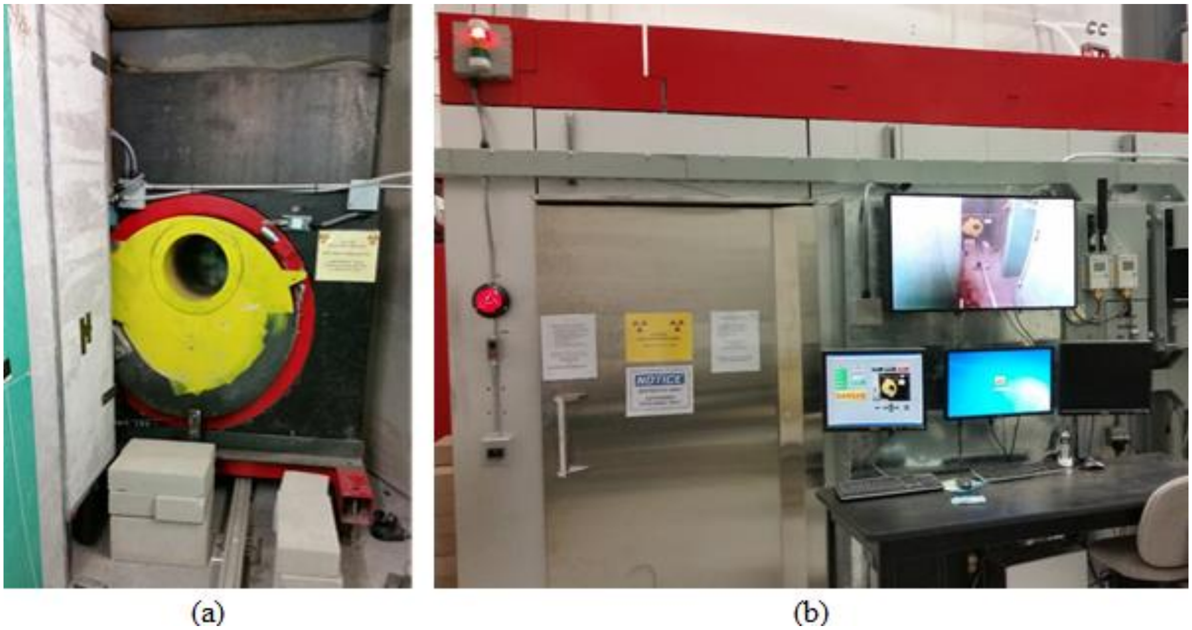

Figure 2.4 (a) The inside view and (b) the outside view of the imaging cave

In the imaging cave, a sliding track is available for setting up the samples to be imaged and the detection systems during the exposure. The distance to the aperture can be adjusted from 230 cm to 650 cm. An aluminum shelf is also installed at the end of the cave for film system or imaging plate system, where the longest aperture-to-image distance is obtained, 680 cm.

2.2.2 Filter Optimization

Currently, three filters are available to use at NIF. One filter is a piece of bismuth 4 inches long and 2.5 inches in diameter, composed of large single crystals oriented randomly. Two additional filters are pieces of sapphire, both Hemlux-grade single crystals, 6 inches in length and 2.5 inches in diameter. In general, all filters are effective fast neutron and gamma filters; thus, they can be used alone or together. Five combinations have been considered: (1) no filters presented, (2) 4-inch bismuth filter only, (3) 6-inch sapphire filter only, (4) 4-inch bismuth with 6-inch sapphire filters, and (5) 12-inch sapphire filters.

The performance of each filter combination has been studied with simulations using MCNP code (X-5 Monte Carlo Team, 2003). Figure 2.5 (a) shows the MCNP model of NIF in 3D view. It includes the beam port #5, the collimation system, the shutter system and the external shielding of the facility. Figure 2.5 (b) is the cross section of this model. A gadolinium object is placed at 4 meters away from the aperture, and tallies are set on the image plane directly behind the object. Inside of the dash lines is a zoom selection area on the collimation system. Figure 2.5 (c) shows an enlarged view of this area with a list of materials indicated by different colors.

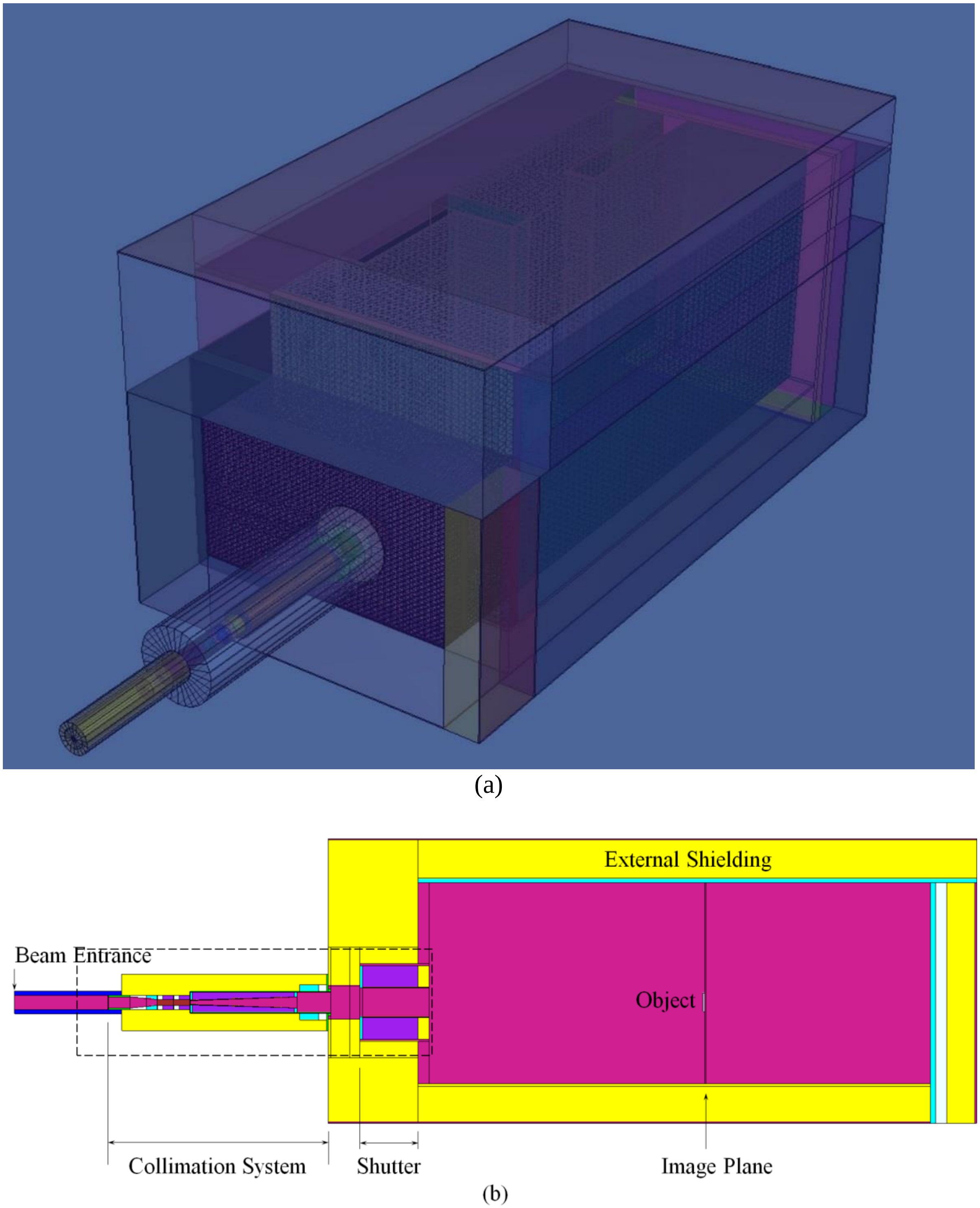
(a)
External Shielding
Beam Entrance
Object
Collimation System
Shutter
Image Plane
(b)

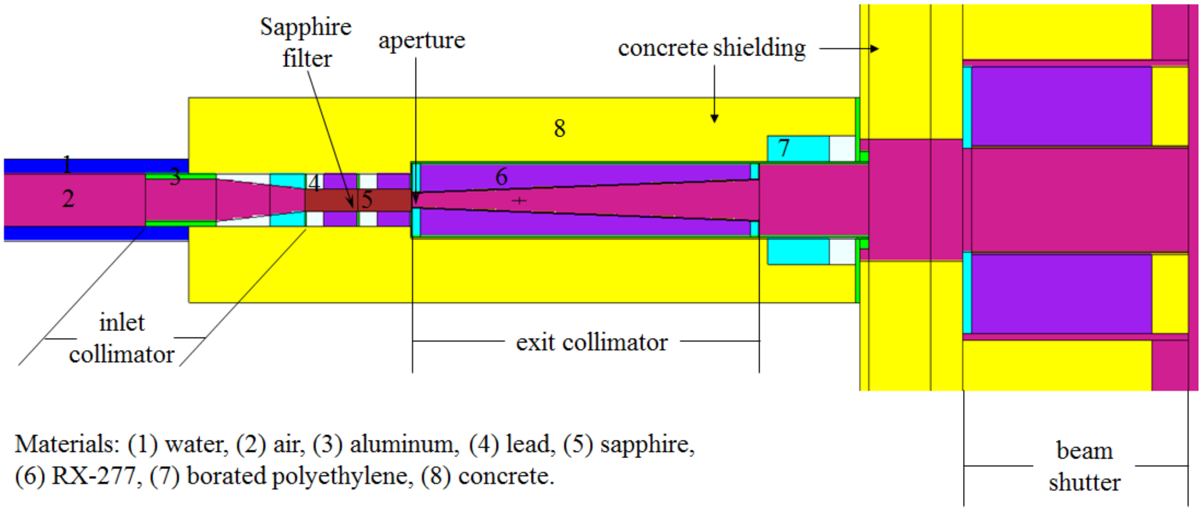

(c)

Figure 2.5 (a) The 3D visualization of an MCNP model of NIF. (b) The cross section of the model, with a zoom selection area on the collimation system inside of the dashed lines. (c) An enlarged view of the selected area

Neutron and gamma sources are emitted from the entrance of the beam port, with a uniform forward mono-directional distribution. The sources have energy distributions as shown in Figure 2.6, which were generated from the MCNP simulations of PULSTAR reactor core model (Mishra, 2010). The strength of the source is set based on the flux at this location. For neutrons, the flux is 4.51×10^{12} $n\cdot cm^{-2}sec^{-1}$, measured by a fission chamber; for gamma, the flux is 5.78×10^{13} $\gamma\cdot cm^{-2}sec^{-1}$, estimated from the gamma dose measured along the beamline (listed in Section 3.2).

Figure 2.7 shows the total neutron flux (for the entire spectrum from thermal to fast) at imaging locations along the beamline calculated with the MCNP neutron model, when different combinations of filters were used. To be noted, for the filter materials of sapphire and bismuth, special cross-section data treatments are necessary in thermal neutron simulations, but no accurate data are available in the MCNP libraries. The bounded neutron cross sections were generated using quantum mechanical ab initio methods (Hawari, 2004), assuming mono-crystal structure for both materials.

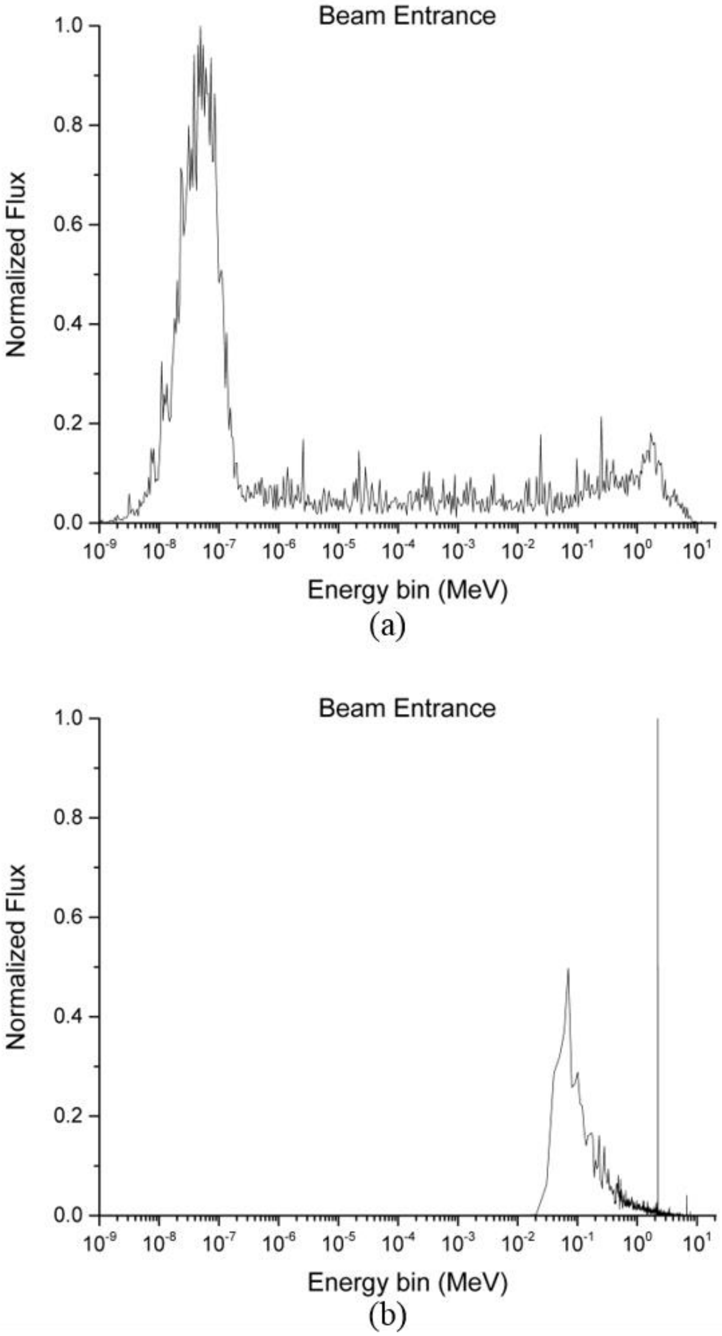

(a)

(b)

Figure 2.6 Energy distributions at the entrance of beam port #5 for (a) neutron and (b) gamma

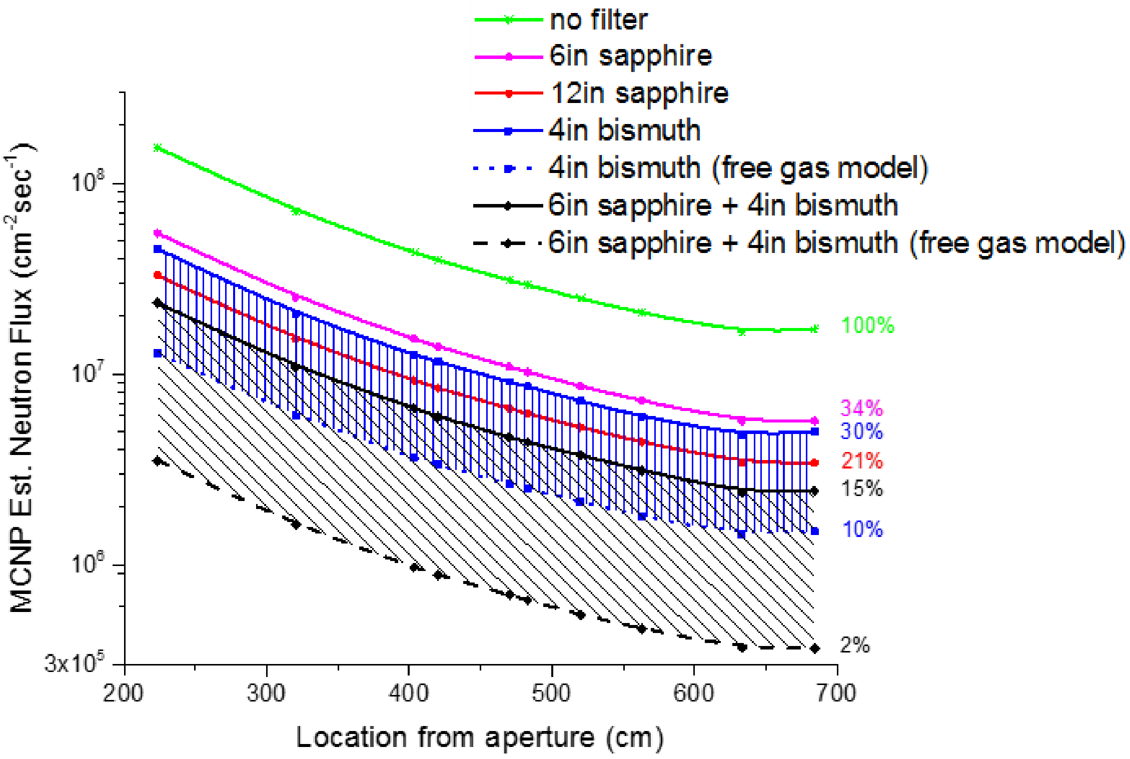

Figure 2.7 The neutron flux along the beamline calculated by the MCNP simulations, with different combinations of the filters.

The simulation results (see Figure 2.7) with 12-inch sapphire filters agree well with the neutron flux measurements with Indium foils. However, for the cases where the bismuth filter was used, the simulation results obtained using ab-initio model cross sections were much higher than the actual flux. This is because that bismuth is assumed to be single crystal in the model, while the available bismuth filter is composed of many single crystals oriented randomly. Due to the lack of knowledge on the size and orientation of each single crystal, a more accurate cross section for this particular bismuth filter was hard to obtain. The actual neutron flux should fall into a range between calculations using ab-initio model (solid lines) and free gas model (dashed lines), which are the areas filled with line patterns on the graph.

Figure 2.8 (a)-(e) are neutron energy spectra evaluated at an imaging location 4 meters away from the aperture, with different filter combinations. All the spectra were normalized to

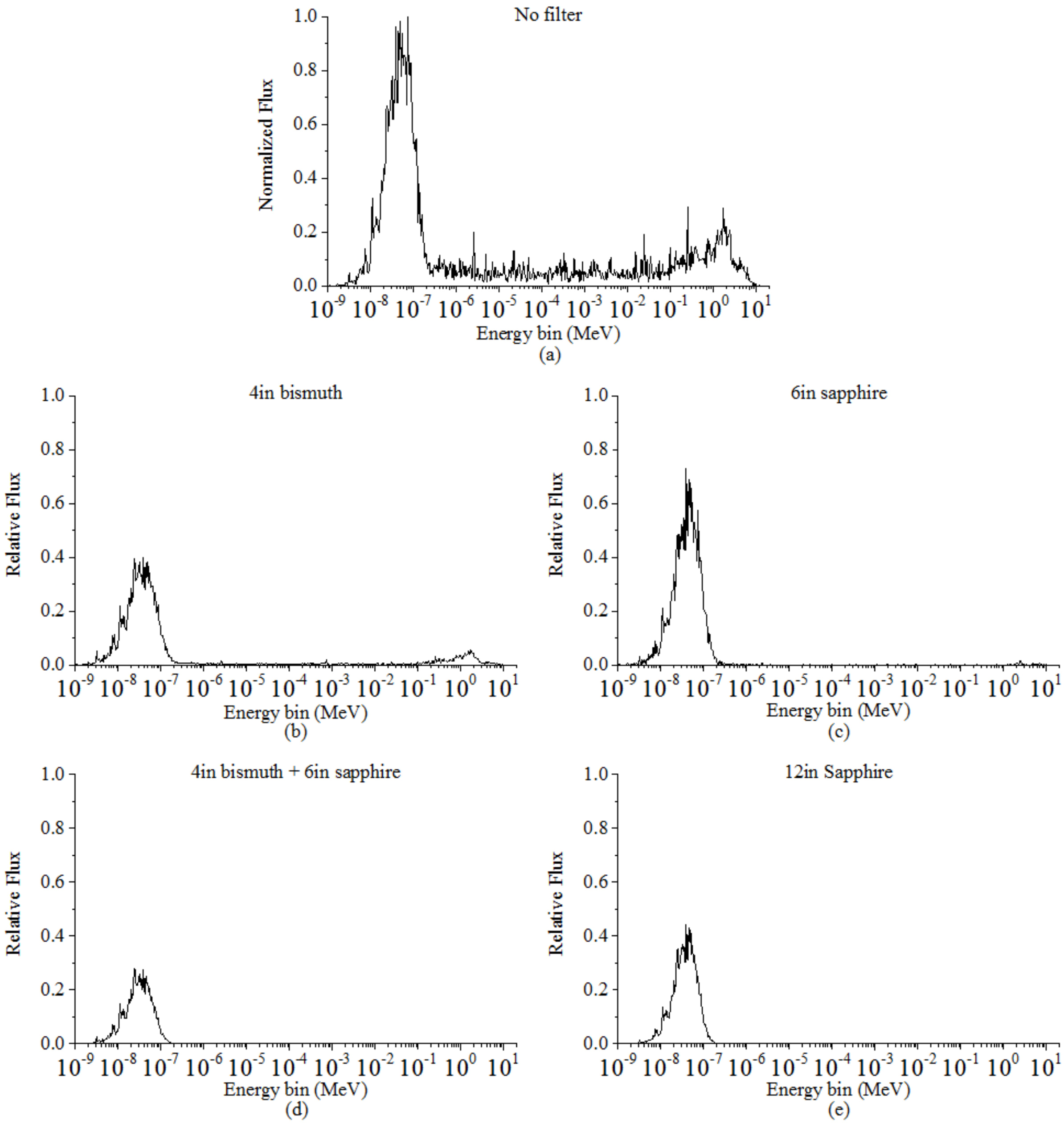

Figure 2.8 The neutron spectra at the imaging location 4m away from the aperture, with (a) no filters presented, (b) 4-inch bismuth filter only, (c) 6-inch sapphire filter only, (d) 4-inch bismuth with 6-inch sapphire filters, and (e) 12-inch sapphire filters. All the spectra were normalized to the maximum value in (a).

the maximum value in case of no filters as shown in Figure 2.8 (a). It can be seen that 6-inch sapphire is more effective in filtering out fast neutrons and allows higher thermal neutron flux, compared to 4-inch bismuth. Among all filter combinations, thermal neutron content, which is the ratio of thermal neutron flux to total neutron flux, reaches the highest value when 12-inch sapphire filters are used. Total neutron flux with 12-inch sapphire filters is about 21% of the one with no filter presented.

Figure 2.9 shows the gamma flux at imaging locations along the beamline with different filter combinations, calculated with the MCNP gamma model. Figure 2.10 (a)-(e) are gamma energy spectra evaluated at the imaging location 4 meters away from the aperture with different filter combinations. It can be seen that bismuth is more effective than sapphire in

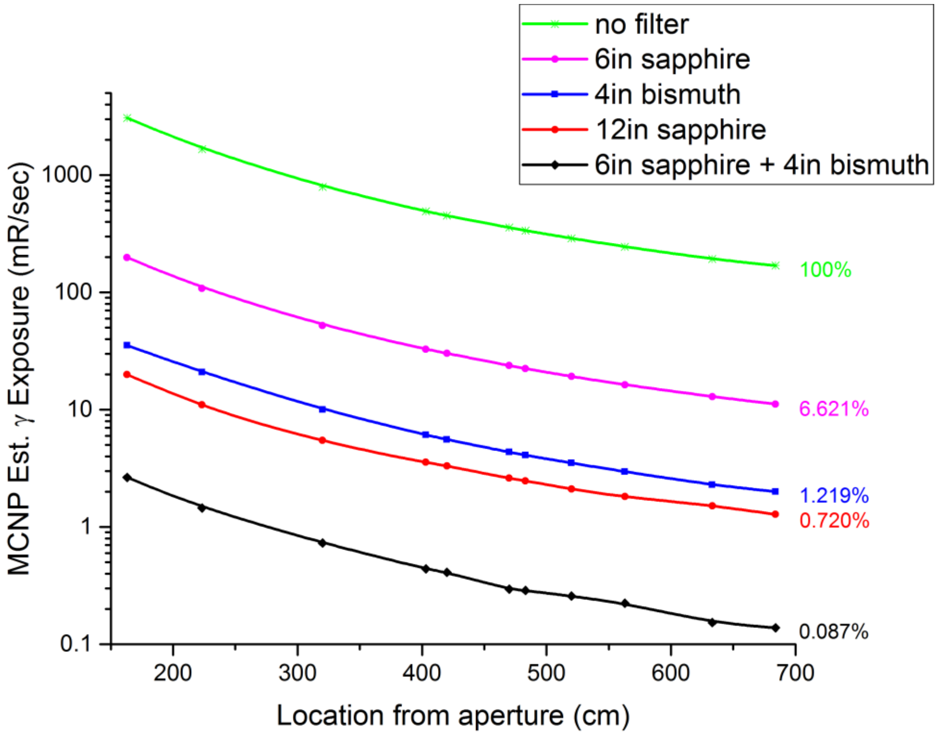

Figure 2.9 The gamma flux along the beamline calculated by the MCNP simulations, with different combinations of the filters.

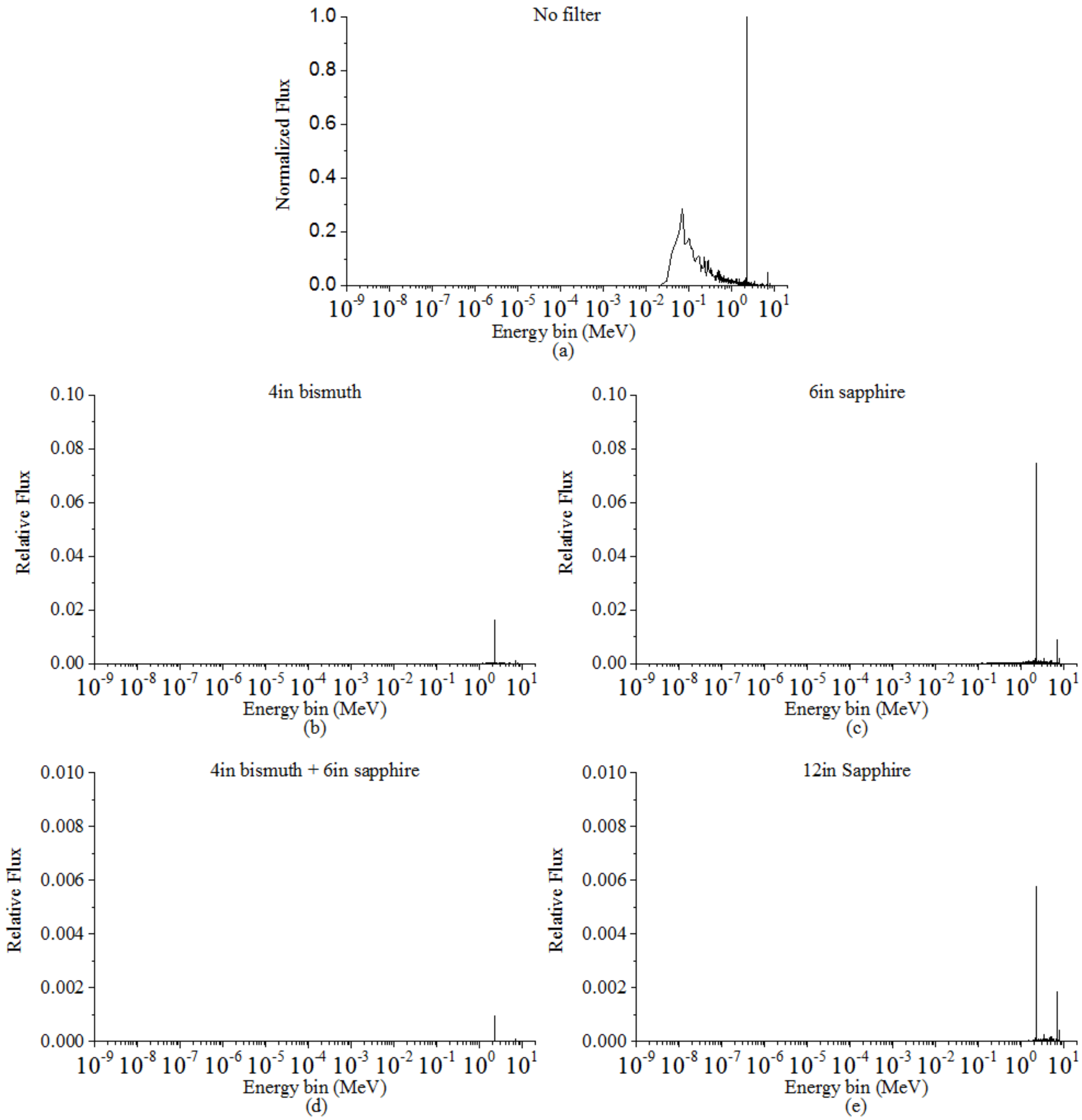

Figure 2.10 The gamma spectra at the imaging location 4m away from the aperture, with (a) no filters presented, (b) 4-inch bismuth filter only, (c) 6-inch sapphire filter only, (d) 4-inch bismuth with 6-inch sapphire filters, and (e) 12-inch sapphire filters. All the spectra were normalized to the maximum value in (a) and the scales of y-axes are different.

removing the gamma content. A 4-inch bismuth is equivalent to nearly 12-inch sapphire. Both of the materials has better filtering performance on gamma radiations with lower energies.

If only consider the filtering performance, 4-inch bismuth along with 6-inch sapphire can provide the cleanest thermal neutron beam out of all the combinations. However, neutron flux has equal if not higher importance in the design of a REMANI system. On balance, the 12-inch sapphire filters were used in the final design of the system.

2.2.3 Characteristics of the Neutron Imaging Beam

The characteristics of the neutron imaging beam have been examined thoroughly along the beamline. This section summarizes some important conclusions.

First of all, standard indicators prescribed by American Society for Testing and Materials (ASTM) are adopted. Based on ASTM E545-14 (Subcommittee E07.05, 2014), Sensitivity Indicator (SI) and Beam Purity Indicator (BPI) were used with gadolinium conversion screen and single-emulsion silver-halide films. The ASTM designation of quality level is given in a form of NC-H-G, where NC is thermal neutron content and values of H and G are indications of sensitivity level. The measurements showed that the value at NIF is 74-8-7 and the facility belongs to Category I (the highest grade).

Secondly, as discussed previously, images can be taken along the imaging track, thus the L/D ratio can be adjusted from 56 to 170. The size of the beam increases with the L/D ratio. Since the aperture and the cross section of the collimator are both square, the neutron beam has a square-like shape as well. At the furthest imaging plane, the side of beam is about 17 inches. The beam uniformity was evaluated at this location by taking a radiographic film of an open beam. The densities were measured by a photo optical densitometer on a 1 cm × 1 cm grid on the film and were plotted as a density map as shown in Figure 2.11. The dispersion

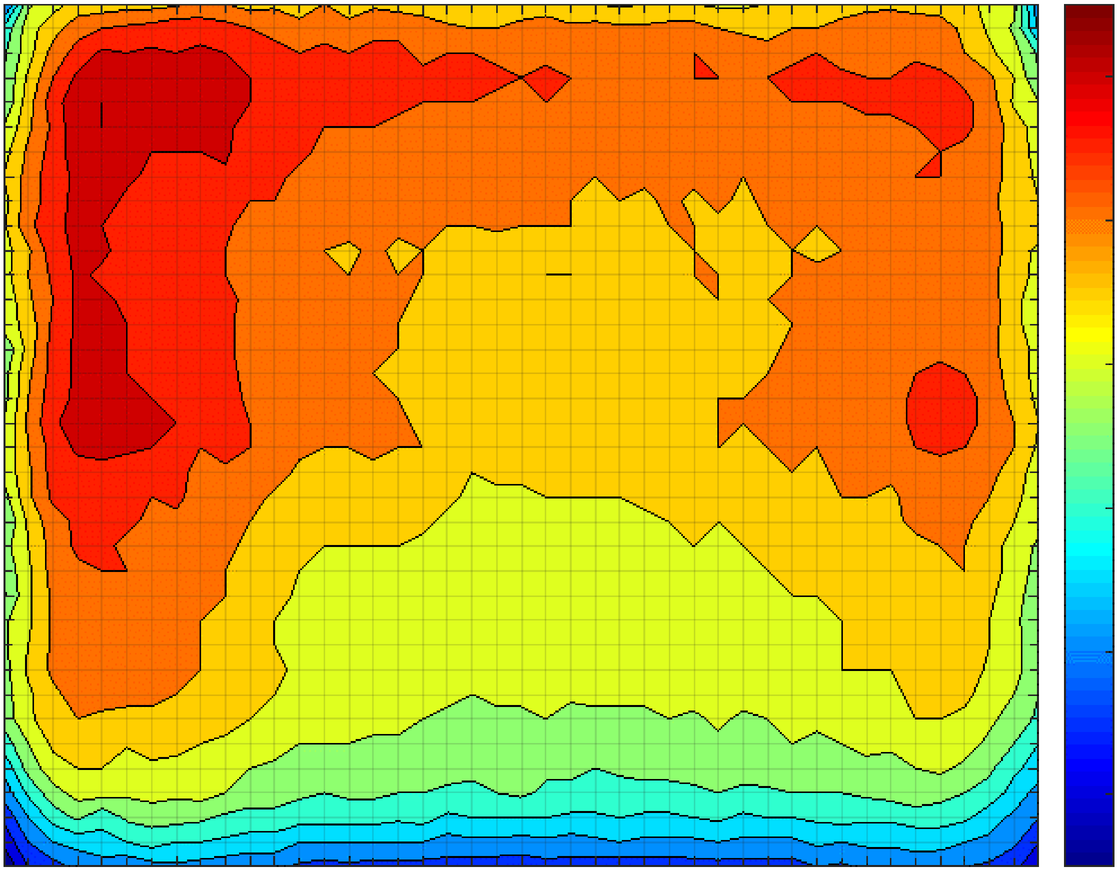

Figure 2.11 Film density map on the 680 cm imaging plane.

of the density from the average value is within ±6%. Many reasons may contribute to the non-uniformity, for example, scattering from the collimator wall, the flux variation of the core, and the angle between the beam port and the surface of the core.

Intensities of neutron and gamma fields were measured at different locations along the beamline. The results are shown in Figure 2.12 (a) and (b), compared to the MCNP results as in the solid black lines. The neutron flux was measured with Indium foil activation method. The Gamma exposure was measured by gamma dose rate detector FHZ 612-10. The horizontal axis represents the distances from the aperture to the measurements. The neutron-to-gamma ratio is 2.6×10^6 $cm^{-2}mR^{-1}$ on the average. At the meanwhile, the Cadmium ratio was measured to be 450 (Mishra, 2010).

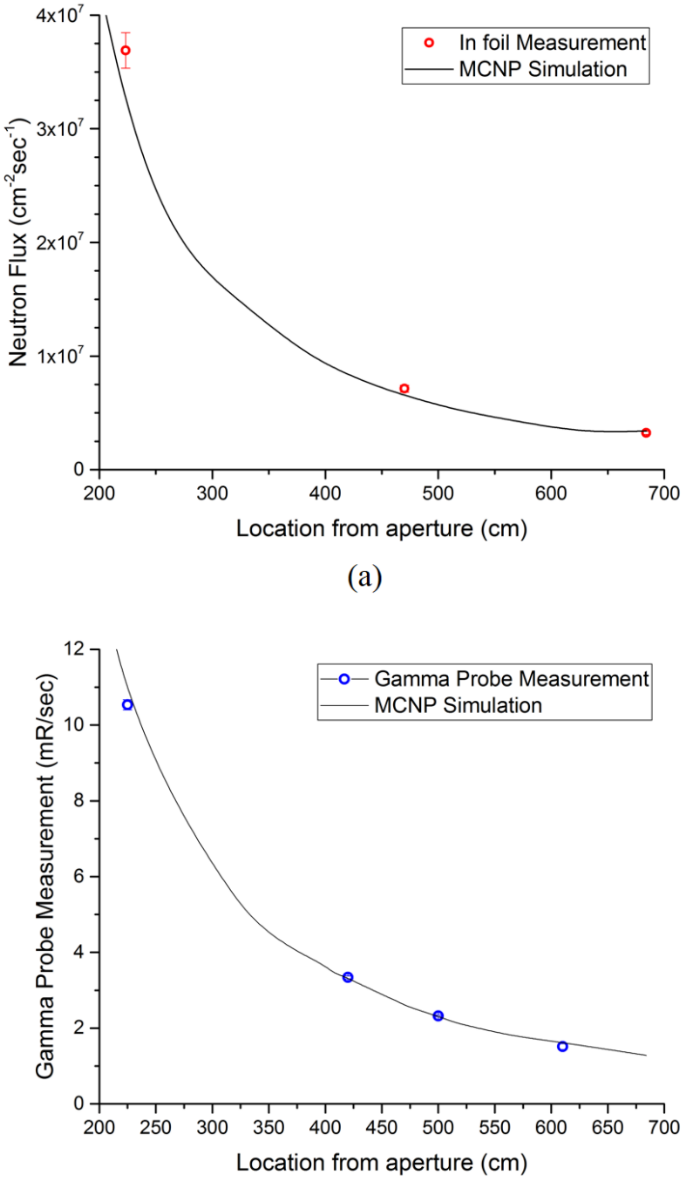

(b)

Figure 2.12 Measurements of (a) neutron flux and (b) gamma exposure along the beamline

2.3 Detection Systems

There are several detection systems available at the NIF for neutron radiography, including:

1) Film with gadolinium conversion screen, and film scanner;
2) Digital neutron imaging plate;
3) Thompson tube;
4) Scintillator screen with CCD camera system;
5) Microchannel plate (MCP) with CCD camera system.

Thompson tube and MCP system are excluded from being used in the REMANI system due to low dynamic range and small detection area respectively. Film system, imaging plate system and scintillator system are suitable for this application. The properties of the former two systems have been discussed in details in Mishra's thesis (2010).

The scintillator system has two main components: a powder scintillator screen and a CCD camera, which are mounted on two adjacent faces of a light-tight anodized aluminum box. Figure 2.13 shows an isometric projection of this arrangement. The smaller drawing in the bottom right shows the complete view and the larger drawing is a breakout view that removes the box's top surface and part of the front and left surfaces and shows the internal details. A standard evaporated front surface mirror is placed at 45° to the scintillator surface, and reflects photons emitted from this surface to the CCD camera. The reflectivity of the mirror is more than 94% for visible light. Such an arrangement removes the camera from the

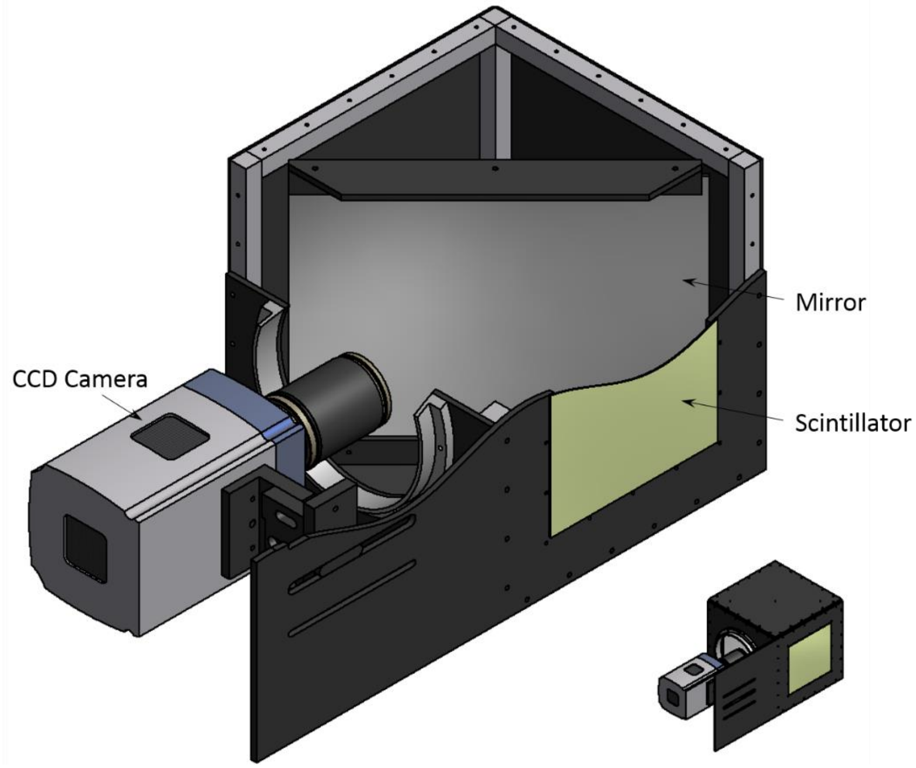

Figure 2.13 A breakout view of the scintillator and CCD camera arrangement (a complete view is shown at the bottom right).

direct path of the neutron beam, thus reducing radiation damage and easing additional shielding for the camera.

The scintillator screen is formed from a blend of ^{6}LiF and ZnS:Cu,Al,Au phosphor powder, provided by Applied Scintillation Technologies (now Scintacor). The grain sizes ranges from 1.5 µm to 7 µm. A common mass ratio of ^{6}LiF:ZnS are 1:2 and 1:3. While the former one ratio has a better capturing efficiency, the latter one provides higher light yield and higher light attenuation (Yehuda-Zada, 2014). The manufacturer does not provide the mixing ratio of our screen, but guarantees to optimize for thermal neutron imaging applications. (Applied Scintillation Technologies, 2000) The activators in the phosphor produce very low gamma sensitivity. The screen has a size of 8 inches by 8 inches, flush mounted to a 0.5 mm-thick aluminum substrate, which allows large area imaging if necessary. Two screens are available, with density of 2.4 g/cm^3. The thicknesses are 250 μm and 420 μm respectively, and the coating weights are 61 mg/cm^2 and 102 mg/cm^2.

Neutron detection is according to the following nuclear reaction:

^{6}Li + n → He + ^{3}H + 4.78 MeV

Thermal neutrons get absorbed with a cross section of 940 barns (Knoll, 2010). The secondary products are short-range particles, alpha (α) and triton (t), with kinetic energies T_α = 2.05 MeV and T_t = 2.73 MeV (Peresedov, 2006). Their mean ranges in the scintillator estimated by SRIM software (Ziegler, 2008) are listed in Table 2.1. ZnS:Cu,Al,Au phosphor is excited by these secondary products and emits luminescence photons with wavelength peaking at 540nm along their travelling path. The photons propagating through the screen will expand and degrade the spatial resolution. The degradation is proportional to the thickness of the screen.

Table 2.1 Range* of secondary products in the scintillator materials, calculated by SRIM (Ziegler, 2008)

Material	^{6}LiF	ZnS	^{6}LiF:ZnS mixture with mass ratio of	
			1:3	1:2
range of α particle T_α = 2.05MeV	6.05 μm	5.95 μm	8.94 μm	8.60 μm
range of t particle	33.57 μm	31.85 μm	48.51 μm	46.86 μm

Note: *SRIM outputs the mean projected range.

The scintillation photons, after reflected by the mirror, are collected and measured by a CCD image sensor. It is composed of a two-dimensional array of capacitors, or known as pixels. In each pixel, the detected photons are converted into electron charges. The probability of a detected photon creating an electron charge is referred as the quantum efficiency, which varies with the wavelength of the photon. The generated charge packets are then read one pixel at a time and digitized into a gray value by an analog-to-digital converter.

The camera used in the current system is an Andor's iKon-L 936 back-illuminated CCD camera. The quantum efficiency is more than 90% for photons of wavelengths within the scintillator spectral range. It can exceed 95% at the emission peak. The image sensor has a 2048×2048 pixel array and a pixel size of 13.5 µm. A thermoelectric (TE) cooler is used to reduce dark current and associated shot noise. By air cooling, the CCD temperature can reach -70°C and dark current can be as low as 0.0004 electrons/pixel·sec. The A/D convertor is 16-bit, corresponding to 65535 grey levels. As specified by the manufacturer, the camera linearity is excellent, better than 99%.

The lens coupled with the camera is Micro-Nikkor 55 mm f/2.8, through which the scintillator photon image is projected onto the CCD image sensor. The lens aperture size ranges from f/2.8 to f/32. This lens can focus continuously from infinity to a reproduction ratio of 1:2 (at 25 cm focus distance). When mounted to the camera box, the position of the camera can be adjusted through a custom-made sliding bracket and the focus distance can be changed from 14.5 inches to 25.5 inches. Thus the range of the reproduction ratio is from 1:4.4 to 1:9.4, and the range of the effective pixel size is from 60 µm to 127 µm.

2.4 Image Quality Evaluation of the Scintillator System

The concepts of spatial resolution, contrast, and noise are principal components in determining the image quality and are closely interrelated. In this section, we introduce the methods to evaluate these components and quantify them with the scintillator system as an example.

2.4.1 Mathematical Model for Conventional Neutron Imaging

To start with, a conceptual model as shown in Figure 2.14 is established for a mathematical description of the process of neutron image formation. Neutrons emanating from the source are shaped and directed towards the object through a collimation system. One of the most popular design is a divergent collimator with a small aperture. In this arrangement, the collimated neutron beam incident onto the object can be approximated to be uniformly distributed and the flux Φ_0 is proportional to D^2/L^2, where D is the diameter of the aperture (or one side, depending on aperture shape), and L is the distance from the aperture to the object. The angular spread of the beam casts geometric unsharpness on the image, which is linear to the object-to-detector distance and the inverse of the L/D ratio.

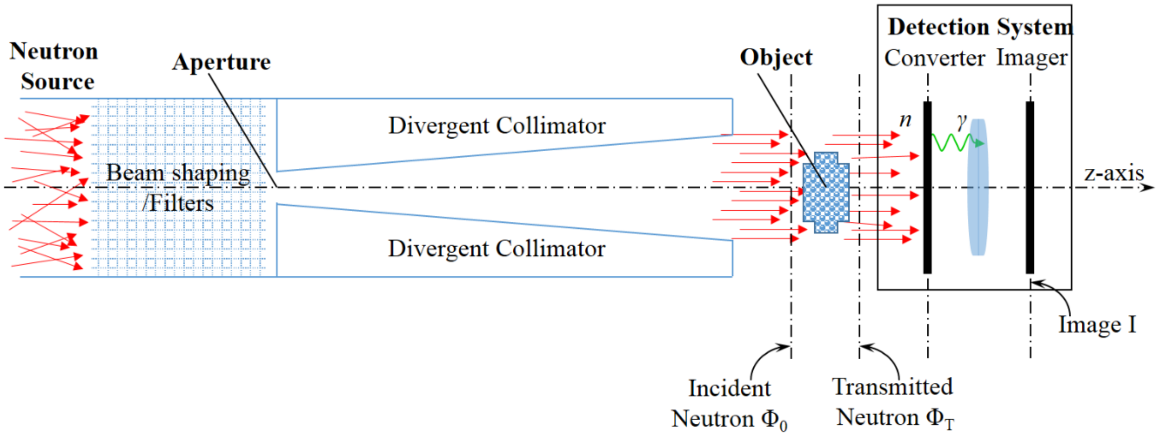

Figure 2.14 A conceptual model of a conventional neutron imaging system

Let function $\Phi_T(u,v)$ represent the spatial distribution of the neutron beam after its passage through the object (Harms, 1986), where (u,v) are coordinates on the object plane. The relationship is determined by Lambert attenuation law:

$$\Phi_T\left(u,v\right)=\Phi_0\cdot B\cdot\exp\left[-\int_{obj}\Sigma_T\left(u,v,z\right)dz\right] \tag{2.1}$$

where Σ_T is the total neutron macroscopic interaction cross-section, and z-axis is perpendicular to the object plane indicating the beam direction. The transmitted neutron flux Φ_T includes the uncollided flux and the scattered flux; thus, a correction factor B is used for highly scattering objects and is defined as the ratio of the total flux over the scattered flux. The exponential part in Equation (2.1) is the characteristics of the object that a neutron image represents. For simplicity, it is denoted as the object function $O(u,v)$.

In the detection system, the transmitted neutrons are first converted to a secondary radiation in the converter. Then the distribution of the secondary radiation is either stored and digitized as in the indirect methods such as film or imaging plate system, or focused and detected as in the direct methods such as scintillator system.

The image produced is the neutron field modulated by the object, with further impacted by the responses of a series of components during the neutron image formation. It can be represented by an image function $I(x,y)$, where (x,y) are coordinates on the image plane. It is a convolution of the object function with an impulse response function $h(u,v)$.

$$I(x,y)=O(u,v)*h(u,v) \tag{2.2}$$

2.4.2 Evaluation of Spatial Resolution

Spatial resolution is the minimum distance that two points in the object can be separated and still be visibly resolved. There are many ways to define resolvability and to measure the distance. Resolution evaluations both in spatial domain and in frequency domain will be discussed in the following.

2.4.2.1 Indicators of Resolution

In spatial domain, resolution can be described by how the system responds to an impulse input. It includes the point spread function (PSF) and the line spread function (LSF), which are the image of an infinitesimal point object and the image of a line object. The PSF is the impulse response function $h(u,v)$ in Equation (2.2). It has two dimensional variables, thus gives a thorough description of the system in terms of resolution. The LSF equals to the integration of the PSF over the direction of the line. Through the process of image formation, an input will be blurred by different components in the system. For example, in the scintillator system, they include the degradations due to the geometric unsharpness, light diffusion in the scintillator and the lens system, and the sampling effect in the CCD sensor. An individual response function can be assigned to describe the degradation from each component. The system spread function is the convolution of all the individual response functions. The widths of the system spread functions can serve as scalar metrics quantifying the system resolution. Usually, the full width at the half maximum (FWHM) of the PSF or the LSF is used.

In spatial-frequency domain, resolution can be specified by the modulation transfer function (MTF), the definition of which is illustrated in Figure 2.15. By means of Fourier transform, the object distributions (system inputs) and the image distributions (system outputs) can be viewed as a combination of sine waves with various spatial frequencies. The black lines and blue lines shown in Figure 2.15 give examples of the Fourier transform components of the input signal and output signal at three frequencies. In thermal neutron imaging as discussed in this work, the input signal is the spatial distribution of the total neutron attenuation characteristics in the object, and the output signal is the corresponding neutron image.

Modulation *M*, as a measure of contrast, is calculated as the amplitude of the irradiance divided by the bias level:

$$M = \frac{L_{\max} - L_{\min}}{L_{\max} + L_{\min}} \qquad (2.3)$$

where L_{max} and L_{min} are the maximum irradiance and the minimum irradiance of the sine-wave signals, respectively. Typically, if the modulation in the object is constant, the modulation in

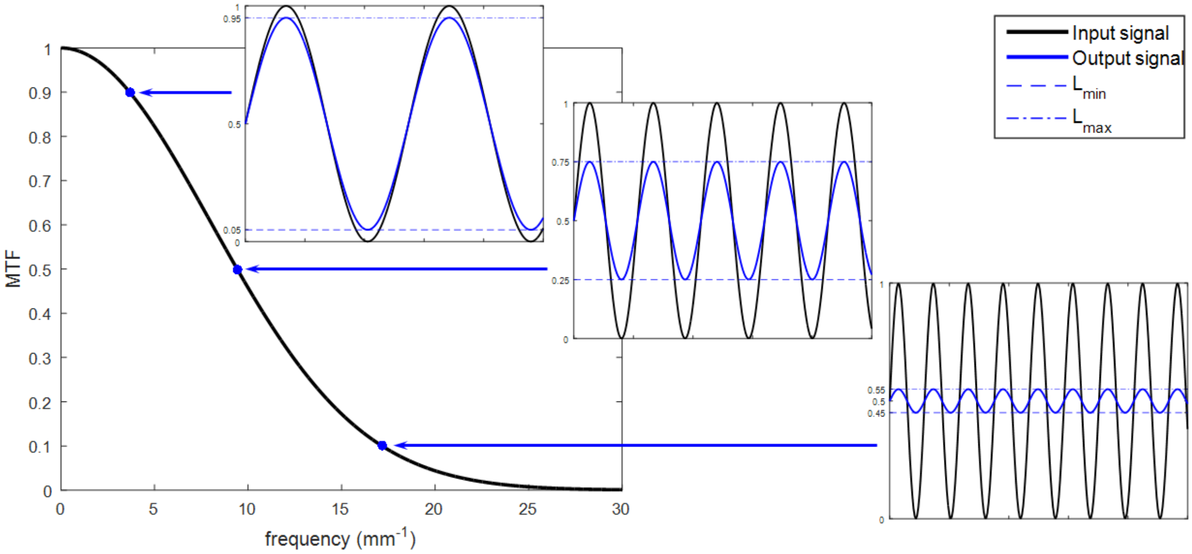

Figure 2.15 Illustration of the concept of modulation transfer function. In thermal neutron imaging, the input signal is the spatial distribution of the total neutron attenuation characteristics in the object, and the output signal is the corresponding neutron image.

the image decreases when the spatial frequency increases. The MTF is the ratio of the output modulation to the input modulation as a function of spatial frequency.

Mathematically, MTF is the magnitude of Fourier transform of impulse response function. Thus, convolution operation in the spatial domain is the same as multiplication in the frequency domain. The total MTF is equal to the product of the MTFs of the constituent components, which the Fourier transforms of individual impulse response functions. The resolution can be defined as the limiting frequency at which the MTF falls below a certain threshold. Usually, 10% of the maximum value is chosen which correlates well with average visual impression by eye (Scanco Medical).

2.4.2.2 Methods of Evaluating Resolution

In practice, PSF and LSF can be obtained by imaging a point or a line that is much smaller or narrower than the system resolution. But this is difficult to achieve due to the low flux of such images.

One of the practical approaches in determining the resolution is to image a phantom as shown in Figure 2.16 (a). It is widely used in deciding the resolving power of an imaging system, conforming to MIL-STD-150A standard. The pattern is composed of several elements with different sizes. As shown in Figure 2.16 (b), each element consists of two sets of parallel lines at right angle to each other. There are three lines separated by spaces of equal width in each orientation. The width of a line pair (one line and one space) is denoted by *x* microns. Each line is 2.5x microns long and 0.5x microns wide, with space 0.5x microns wide between the lines. (MIL-STD-150A). The size of the smallest pattern that can be discerned on the

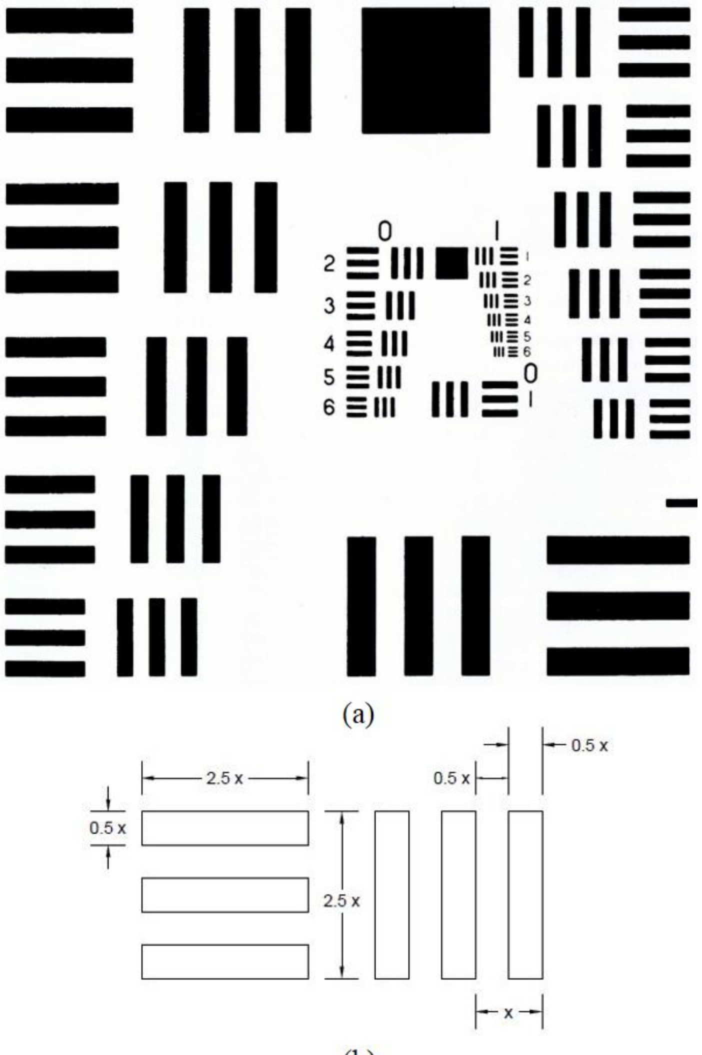

(a)

(b)

Figure 2.16 (a) A resolution test pattern conforming to MIL-STD-150A standard, consists of multiple tri-bar elements with different sizes. (b) The dimension of each tri-bar element.

image gives an estimation of the resolution. This approach can give a direct reading of resolution without any analysis. However, perception and judgement are involved and measurements could be inconsistent.

Another commonly used method is to measure and evaluate the edge spread function (ESF), by imaging a knife-edge object. The ESF is the profile of such an image and the LSF is obtained by differentiating the ESF. Resolution can be determined by the FWHM of the LSF or from the MTF analysis based on Fourier transform of the LSF. Such measurements can provide much more flux than directly measuring LSF. But it will accentuate noise in the data due to the use of spatial-derivative operation.

2.4.2.3 Experimental Results on Resolution of the Scintillator System

The system resolutions of film system and imaging plate system have been measured by Mishra (2010). The results are 33±3 µm and 110±15 µm, reported from the FWHM of the LSF. The resolution of the scintillator system was thoroughly investigated in the following measurements.

As shown in Figure 2.17 (a), a resolution phantom was directly attached to the scintillator screen by aluminum tape, in order to minimize the geometric unsharpness. In this case, the object-to-image distance was 0.5 mm and the aperture-to-object distance was 400 cm. The geometric unsharpness was estimated to be around 5 µm, which was negligible. Figure 2.17 (b) is a photographic picture of the phantom. It was custom-made out of a 4 cm×4 cm square gadolinium foil, with a thickness of 100 µm. Straight lines grouped into tri-bar sets were fabricated in the center. Seven sizes were selected and the dimensions are shown in Figure 2.17 (c). In this figure, '*x*' denotes the width of the line pairs, which is twice of the fabricated line width. This is a direct indicator of the system resolution and ranges from 100 µm to 700 µm, with an increment of 100 µm. The edges of the foil can be used to obtain the ESF of the system. Then the resolution can be measured from the following LSF and MTF analysis.

(a) (b) (c)

Figure 2.17 (a) A picture of the phantom to be used in resolution analysis; (b) the dimension of the tri-bar elements fabricated in the center of the phantom.

Imaging exercises have been conducted with two scintillators and two sampling sizes. The thickness of two scintillators were 250 µm and 420 µm respectively. The lens was carefully adjusted to focus on the scintillator screen and two focusing settings were selected. The effective pixel sizes were measured to be 60.1±0.5 µm and 100.0±1.0 µm.

Figure 2.18 lists the measured neutron images of the resolution phantom under different combinations of scintillator thickness and pixel size. The images were zoomed into the tri-bar elements. To determine the smallest resolvable pattern, the profiles were specifically evaluated along the red lines corresponding to 200 µm, 300 µm and 400 µm per line pair, and were plotted on the smaller figures at the sides. It can be seen that though with slight differences, the resolutions for all the cases are around 300 µm.

The resolution can be evaluated more precisely from the image of an edge. Again, four combinations of scintillator thickness and pixel size were evaluated. The details are shown in Figure 2.19. For each condition, four figures are presented. The top-left one shows the region

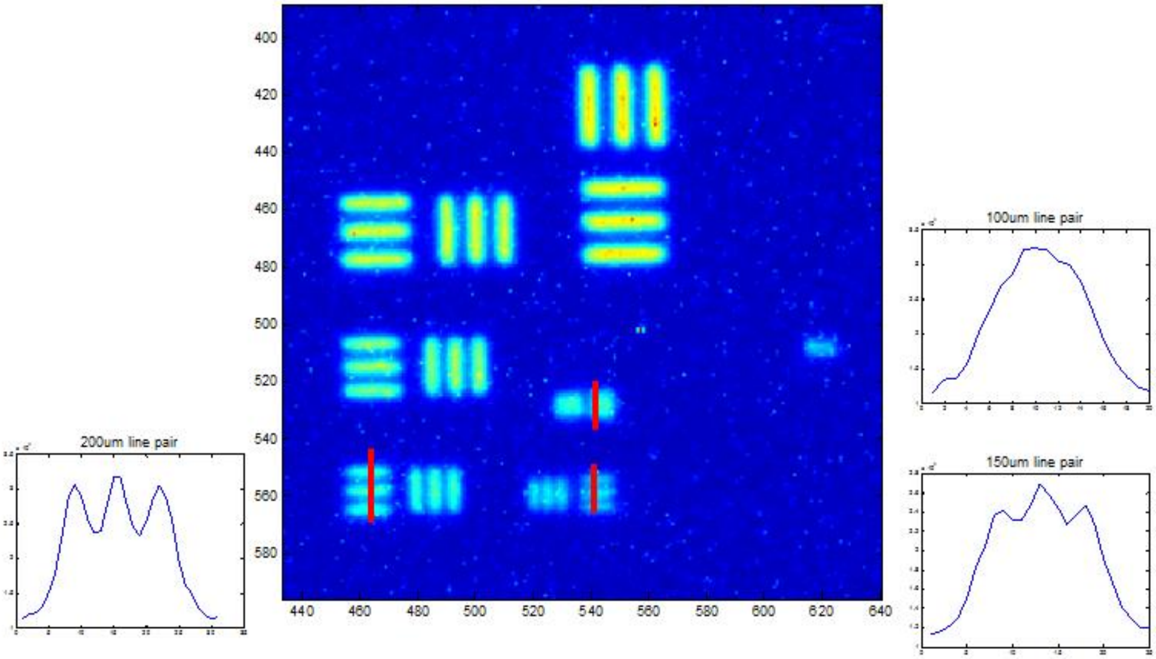

(a) with 250 µm-thick scintillator, at 60 um pixel size

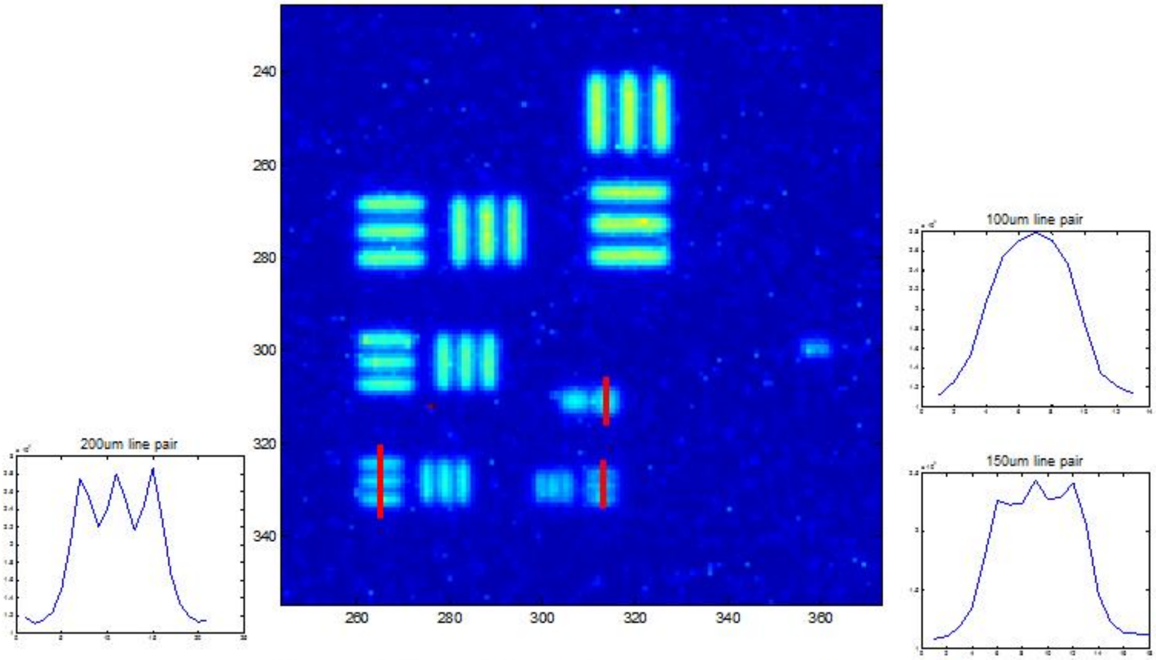

(b) with 250 µm-thick scintillator, at 100 um pixel size

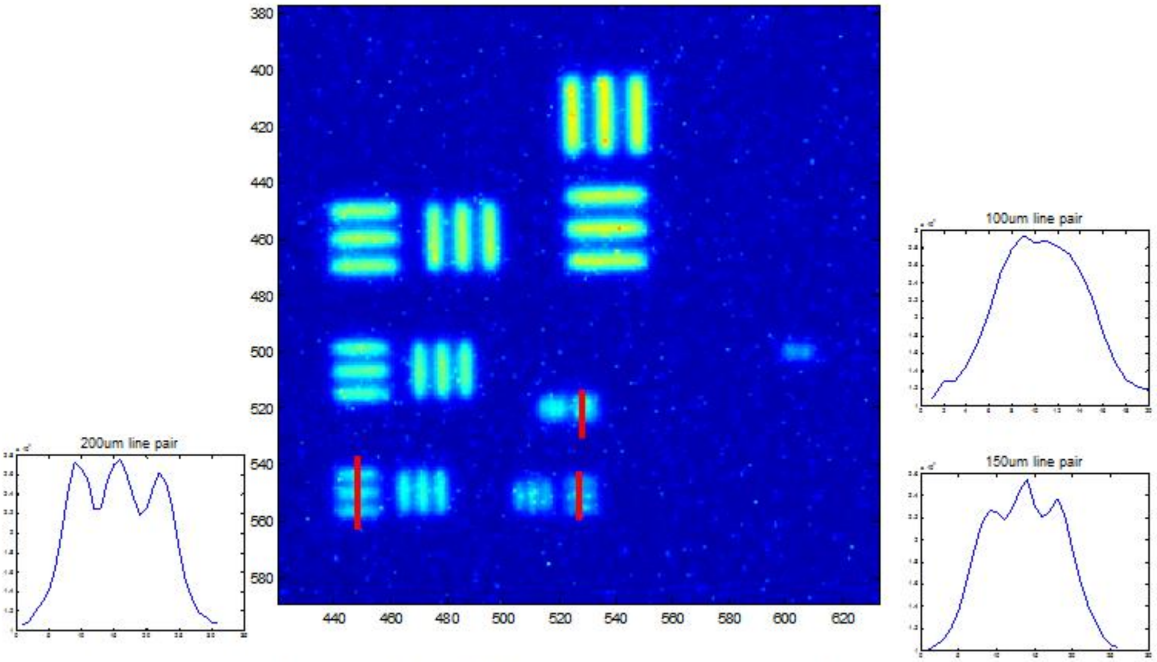

(c) with 450 µm-thick scintillator, at 60 um pixel size

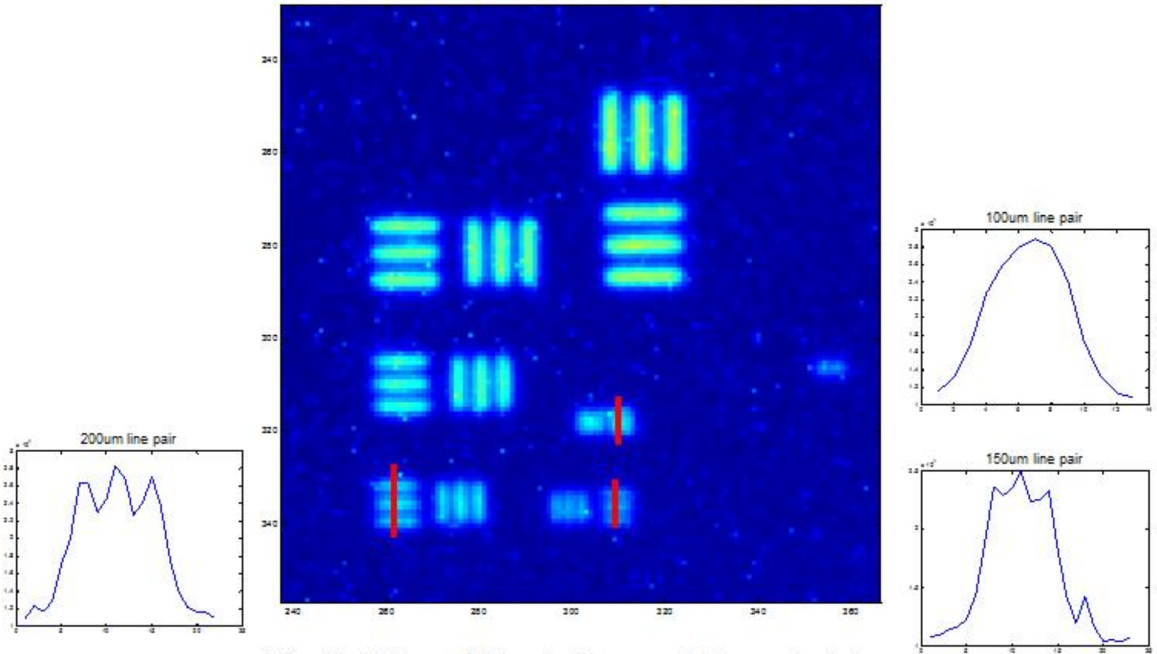

(d) with 450 µm-thick scintillator, at 100 um pixel size

Figure 2.18 Neutron images of the tri-bar elements under different conditions: (a) using a 250 µm-thick scintillator at 60 µm pixel size; (b) using a 250 µm-thick scintillator at 100 µm pixel size; (c) using a 420 µm-thick scintillator at 60 µm pixel size; (d) using a 420 µm-thick scintillator at 100 µm pixel size.

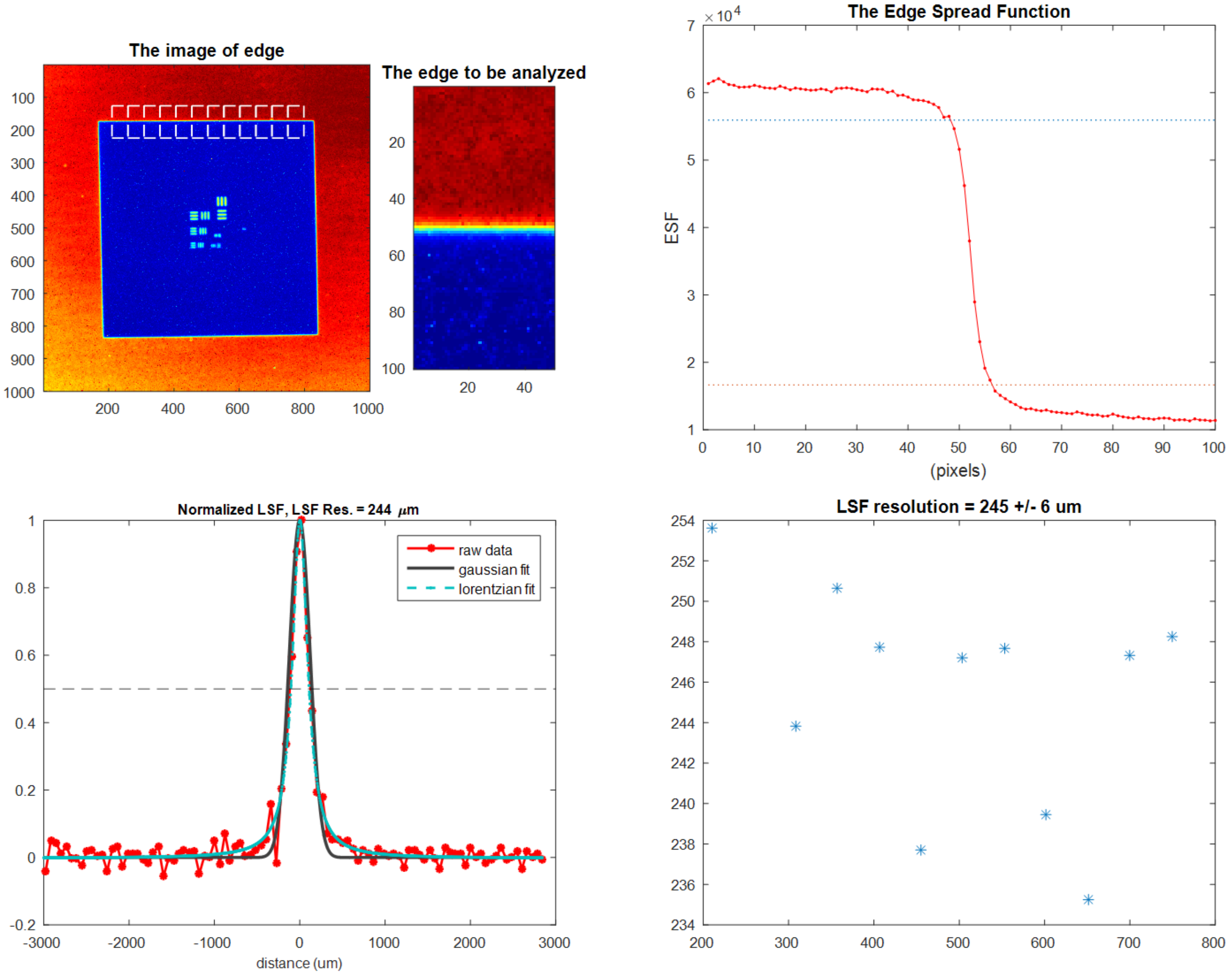

(a) with 250 µm-thick scintillator, at 60 µm pixel size

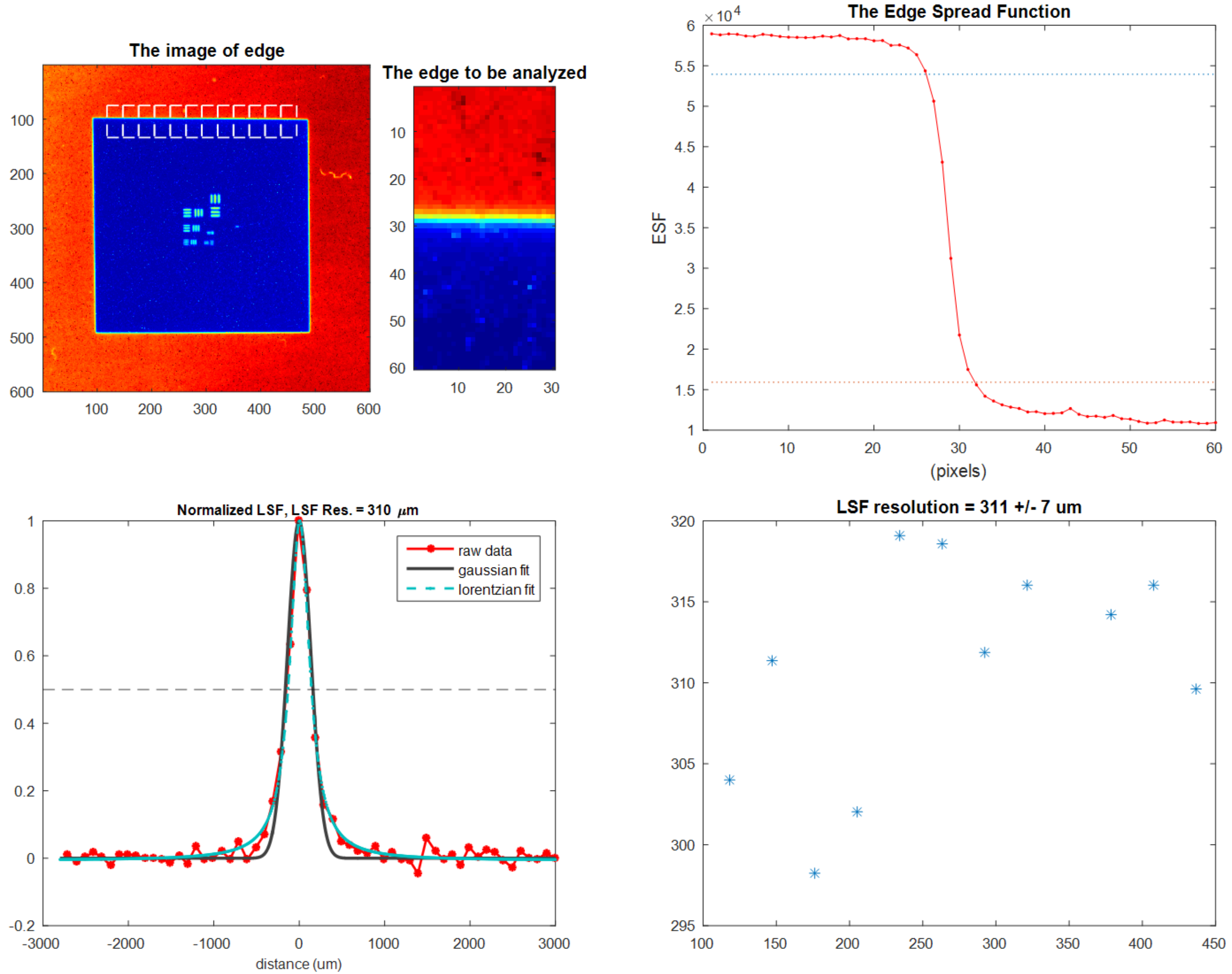

(b) with 250 µm-thick scintillator, at 100 µm pixel size

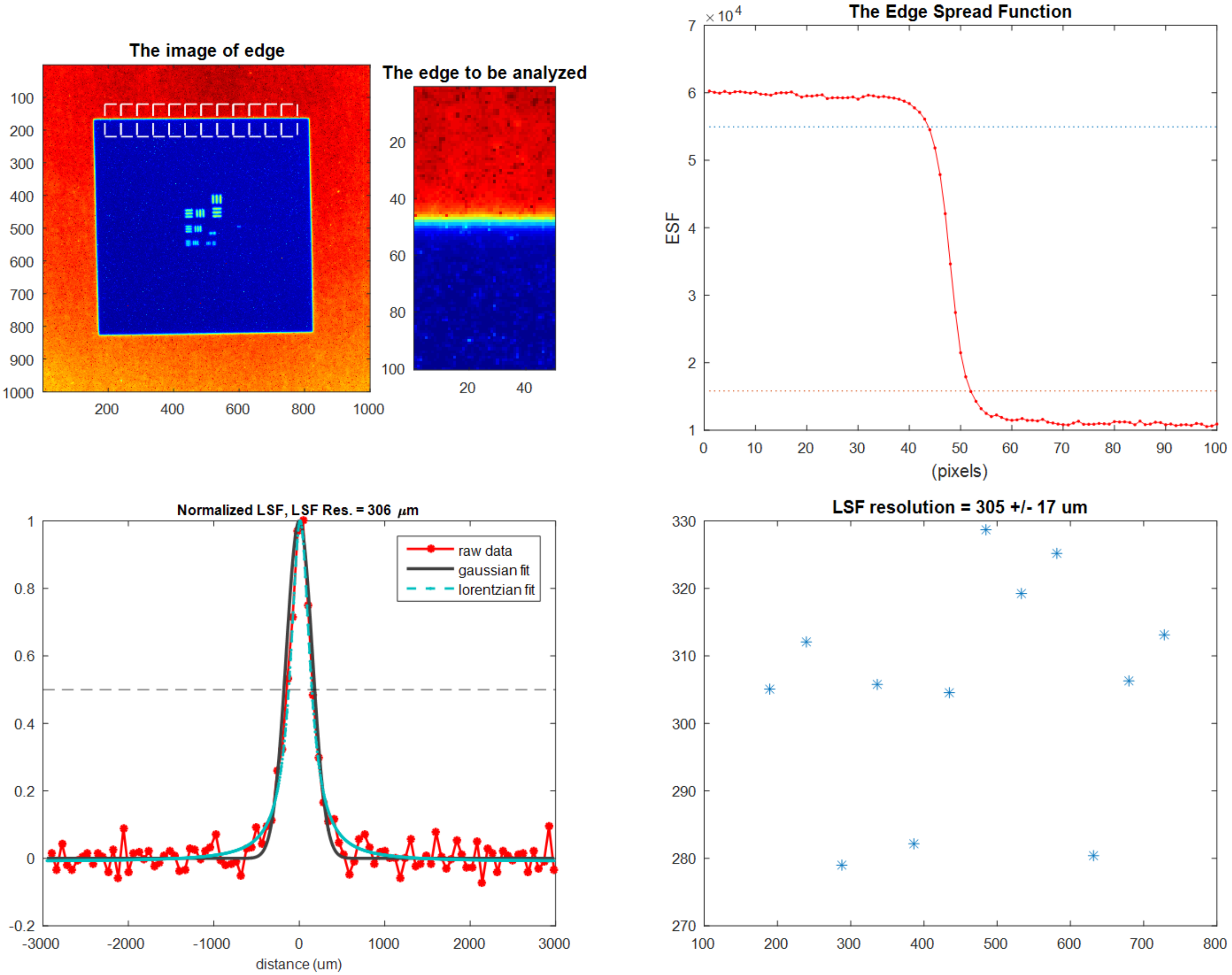

(c) with 420 µm-thick scintillator, at 60 µm pixel size

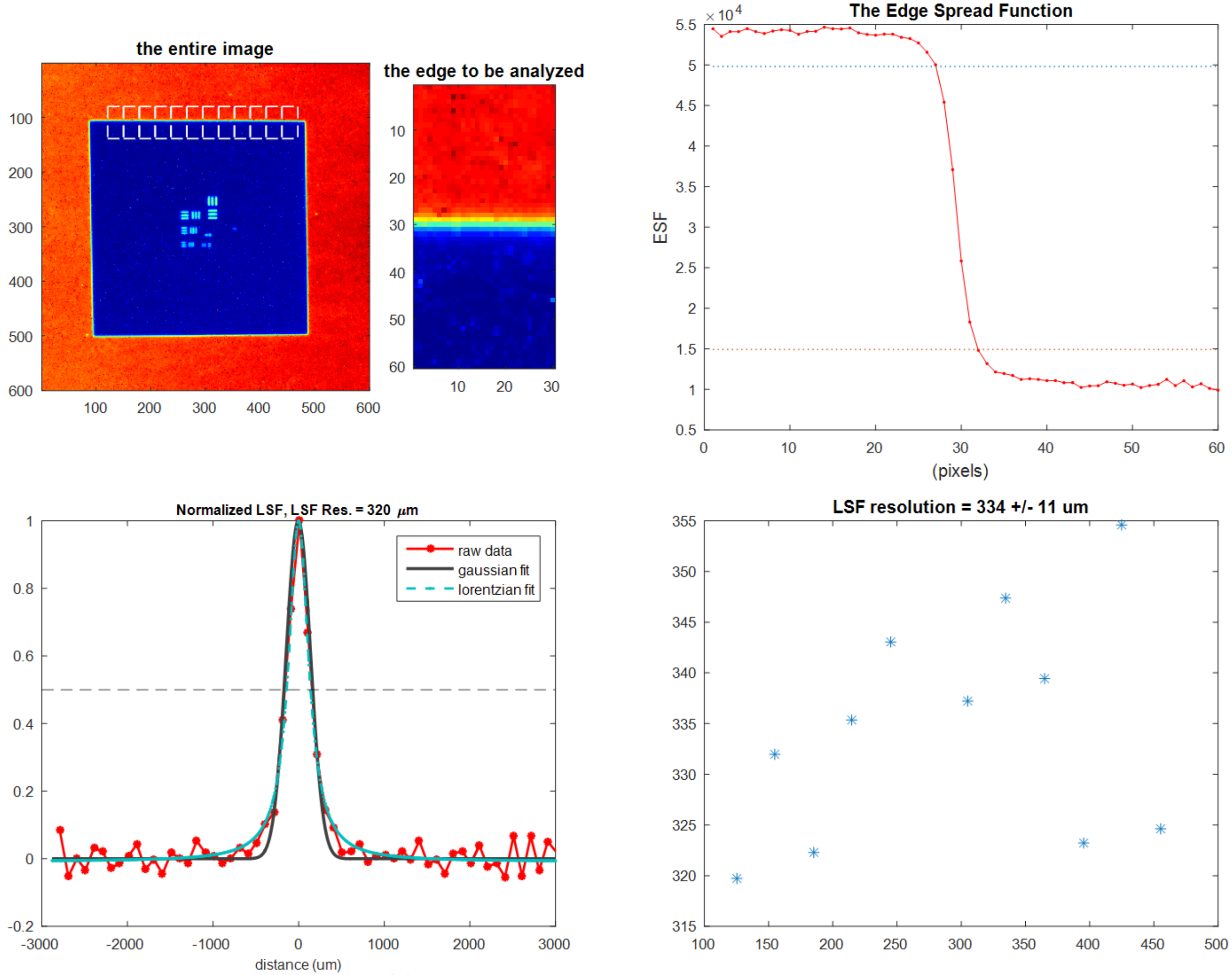

(d) with 420 µm-thick scintillator, at 100 µm pixel size

Figure 2.19 The ESF and LSF analysis of the edge image under different conditions (see the caption of Figure 2.18) of interest to be analyzed. The portion inside of each white frames that represented a 3 mm-long edge was selected. The top-right ones are the ESF obtained by taking the average along the edge. The edge was aligned parallel with respect to the pixel array thus averaging only reduced the statistical fluctuations but not increased the spread. The bottom-left one is the LSF and the corresponding Gaussian fit and Lorentzian fit. The FWHM of the LSF was measured as the LSF resolution. The analysis was repeated on 12 sequential regions along one edge of the phantom. The bottom-right figure plots the LSF resolution vs. the location of the regions. The mean value and the standard deviation of multiple measurements are reported as the final results of the system resolution and are summarized in Table 2.2.

Table 2.2. The system resolution with different scintillator and pixel sizes, obtained from the FWHM of the LSF.

	60 µm pixel size	100 µm pixel size
250 µm-thick scintillator	245 ± 6 µm	311 ± 7 µm
420 µm-thick scintillator	305 ± 17 µm	334 ± 11 µm

The MTF analysis has also been done. In order to investigate the effects of different components, the edge was imaged with neutrons and ambient light respectively. Figure 2.20 (a) shows the MTF of the images taken with pixel size of 60 µm and the 250 µm-thick scintillator. Figure 2.20 (b) shows the MTF of the images taken with pixel size of 100 µm and the 420 µm-thick scintillator. In both cases, the black curves were measured from the neutron images, and the red curves measured from the light images.

In order to obtain a smooth function, a presampled MTF was investigated, which is generated by imaging an edge tilted by a small angle with respect to the pixel array. The

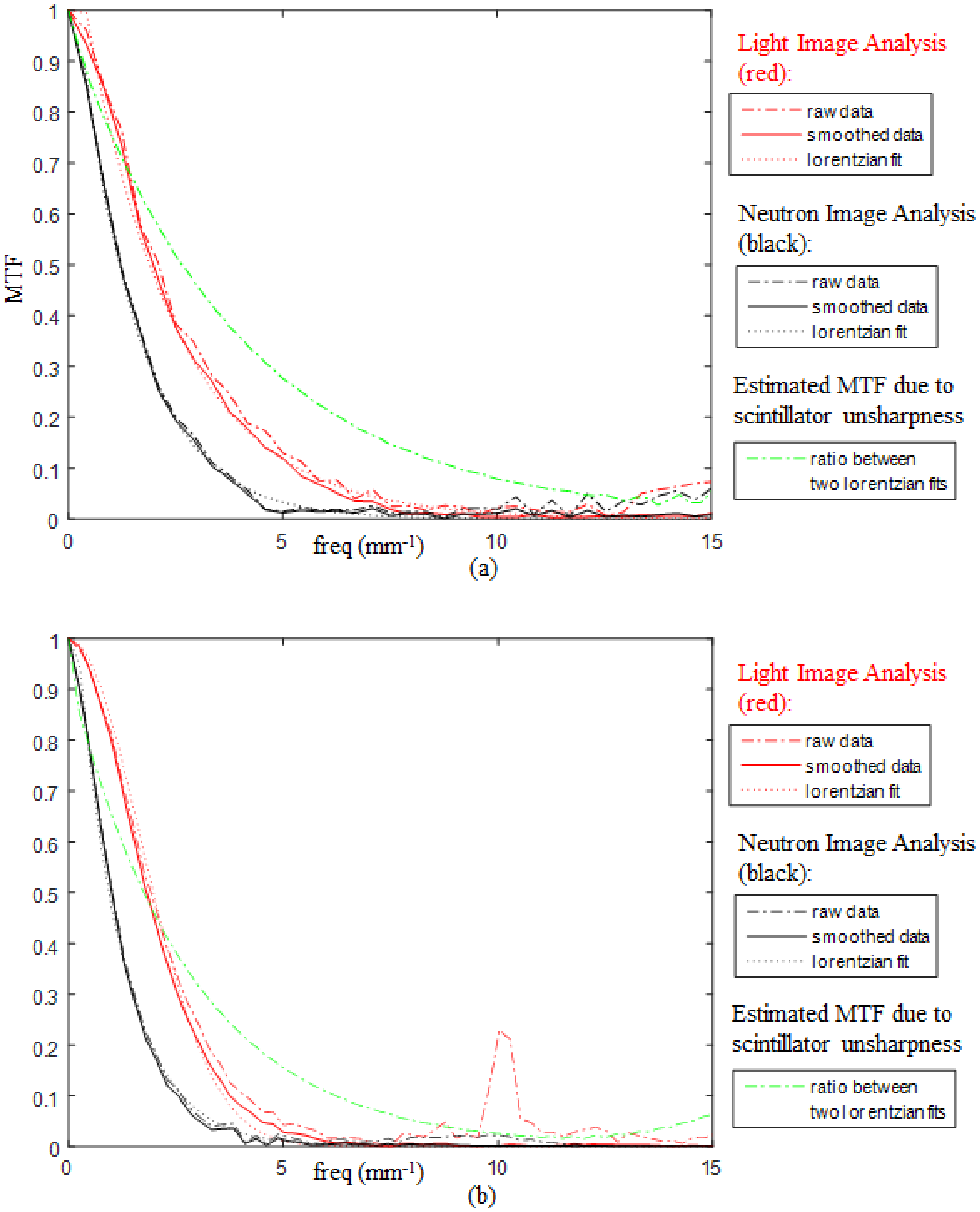

Figure 2.20 The MTF analysis from a light image (red) and a neutron image (black) taken with the scintillator system. Under conditions: (a) using 250 μm-thick scintillator at 60 μm pixel size; (b) using 420 μm-thick scintillator at 100 μm pixel size

applied methods followed the procedure proposed by Samei (1998) for X-ray imaging devices. Simply speaking, a presampled edge function was obtained in the following manner: the peak of the LSF was calculated for each row and was fitted to a straight line as an indication of the location of the edge. Then the image values were rearranged with the respect to the distance to this location, with tenth of the pixel size bins. The edge function was then smoothed by a median filter with the width of a pixel size, and was fitted to a Lorentzian function. The regular MTF analysis was applied to the raw, the smoothed and the fitted data. The results were plotted in different line styles.

The light image measures the degradation only due to the imager, including abberations in the optics system and sampling effect by CCD sensor. The neutron image measures measures the overall image degradation. Besides the unsharpness from the imager, it is also impacted by geometric unsharpness and degradation in the scintillator. Since geometric unsharpness is small and can be negligible, the ratio between to two measured MTF's can provide an estimation of the scintillator unsharpness. The green lines in the plots is equal to the Lorentzian fitted MTF of neutron image to the one of light image.

The FWHM of the LSF was measured from the light images. With a pixel size of 60 µm, this value was 186 ± 5 µm. With a pixel size of 100 µm, this value was 236 ± 4 µm. Quadrature subtracting these values from the ones measured from the corresponding neutron images, the results are 160 ± 11 µm and 236 ± 16 µm. They agree well with the half of the scintillator thickness and the estimated MTF mentioned above.

2.4.3 Evaluation of Image Noise

Generally speaking, for neutron imaging, signal is referred to as the differences between the values that correspond to the object of interest and the background in the produced image. Noise is the fluctuations of the output values. It is unavoidable in any practical system. Signal-to-noise ratio (SNR) is a performance parameter of importance for an imaging system.

There are various sources of the noise in neutron imaging. The most dominating factor is quantum noise, due to the statistical variations in neutron quanta incident on the detector. It follows Poisson distribution. To be noted, the process of converting the absorbed neutrons to the visible light in the scintillator should not be considered as random, but spatial filtering. This is because the scintillator gives a large light output. For example, the LiF/ZnS:Ag emits about 160,000 photons per absorbed neutron. (Yen, 2006) Secondly, the structure of the scintillator screen, digital receptor or other components in the formation path can introduce structural noise into the images. Thirdly, electronic noise arises in various detection devices, e.g., the dark current in a CCD camera. Usually it occurs in a random fashion and is referred as Gaussian white noise. Lastly, gamma and fast neutron in the beam come along with neutron sources. They have different behaviors in forming the image and introduce additional variations as background noise.

As a primary component in image degradation, noise is one of the basic concepts in determining the imaging quality. In X-ray imaging, noise power spectrum (NPS) and detective quantum efficiency (DQE) are used along with MTF in describing the output image quality. Here we introduced the concepts and calculate these parameters of the scintillator system.

2.4.3.1 Indicators of Noise

Noise can be quantified by various means. Intuitively speaking, noise can be calculated as the root-mean-square deviation of many noisy images. A more practical way is to analyze a single image of a stationary process, where the neutron beam shines uniformly on the area of the image and the object content is unchanging. The pixel values in such an image have a mean value $\bar{P}$ and a standard deviation σ_P, which can be used as an indicator of signal and noise. The value of $\bar{P} / \sigma_P$ is the output SNR of the system SNR_{output}.

Consider an ideal system where the quantum noise is the only source of the noise, the minimum number of neutrons required to produce a SNR_{output} is defined as noise equivalent quanta (NEQ).

$$NEQ \equiv SNR_{output}^{2} = \left(\frac{\bar{P}}{\sigma_P} \right)^{2} \tag{2.4}$$

It is related to the number of neutrons that are used to produce the resultant image (Oakley, 2003).

Let N denote the number of neutrons incident on the system, which can be calculated as $N = \Phi \cdot s_{pixel}$, i.e., the neutron fluence times the size of a pixel, which represents the input of an imaging system. Thus, the input SNR of the system is $SNR_{input} = N / \sigma_N = \sqrt{N}$. A figure of merit called the detective quantum efficiency (DQE) is used to quantify the relationship between the output SNR and the input SNR.

$$DQE = \frac{SNR_{output}^2}{SNR_{input}^2} = \frac{NEQ}{N} \tag{2.5}$$

It can be used to compares the performance of different systems at the same level of input SNR, thus is a more exclusive parameter in describing the system performance than SNR_{output}.

The noise performance of an imaging system can be evaluated in the spatial frequency domain, just the same as the system resolution. A noise power spectrum (NPS) or Wiener spectrum is a more inclusive way to describe the characteristics of the system noise, indicating not only the magnitude, but also the texture of the noise. NEQ and DQE can also be evaluated as functions of spatial frequency.

For a continuous image *I(x,y)* corresponding to a stationary process, Dainty and Shaw (1974) defined the mean value $\overline{I}$ and the fluctuation function $\Delta I\left(x,y\right)$ as

$$\begin{aligned} \overline{I} &= \lim_{\mathrm{X,Y}\to\infty} \frac{1}{2X}\frac{1}{2Y}\int_{-X}^{X}\int_{-Y}^{Y} I\left(x,y\right)dxdy \\ \Delta I\left(x,y\right) &= I\left(x,y\right) - \overline{I} \end{aligned} \tag{2.6}$$

The autocorrelation function and the NPS of the fluctuations are

$$\begin{aligned} C(s,t) &= \lim_{\mathrm{X,Y}\to\infty} \frac{1}{2X}\frac{1}{2Y}\int_{-X}^{X}\int_{-Y}^{Y} \Delta I\left(x,y\right)\Delta I\left(x+s,y+t\right)dxdy \\ W(f_x,f_y) &= \lim_{\mathrm{X,Y}\to\infty} \left\langle \frac{1}{2X}\frac{1}{2Y}\left|\int_{-X}^{X}\int_{-Y}^{Y} \Delta I\left(x,y\right)e^{-2\pi i\left(f_x x+f_y y\right)}dxdy\right|^2 \right\rangle \end{aligned} \tag{2.7}$$

where $\langle\cdot\rangle$ denotes the ensemble average.

Based on the Wiener-Khintchin theorem, the NPS is the Fourier Transform of the autocorrelation function. The autocorrelation function and NPS are essentially equivalent measures of image noise in much the same way as the PSF and the MTF are equivalent ways of describing resolution (Dainty, 1974).

For a discrete image *P(i,j)*, the NPS can be considered as the variance of a particular spatial-frequency component per frequency bin. If an image consists of $N_x \times N_y$ pixels with pixel size of *Δs*, the frequency bins f_i and f_j are defined as $f_i = \frac{i}{N_x \Delta s}$, $f_j = \frac{j}{N_y \Delta s}$.

The NPS is calculated as

$$NPS\left(f_i, f_j\right) = \lim_{N_x, N_y \to \infty} \left\langle \frac{\Delta s^2}{N_x N_y} \left| \sum_{i=1}^{N_x} \sum_{j=1}^{N_y} \Delta P\left(i, j\right) e^{-2\pi \mathbf{i}\left(f_i i \Delta s + f_j j \Delta s\right)} \right|^2 \right\rangle \qquad (2.8)$$

where $\Delta P\left(i, j\right) = P\left(i, j\right) - \bar{P}$ is the fluctuations of pixel values around the global mean $\bar{P}$. To be distinguished from the pixel index *i* of an image function, the imaginary unit used in Fourier transform is denoted by boldface letter **i**.

Figure 2.21 illustrates the basic idea of NPS. If the inputs are sine waves with different frequencies, the variation in the amplitudes of the output sine waves will drop when the frequency increases. NPS measures the change in the variation as a function of spatial frequency.

The concepts of noise equivalent quanta (NEQ) and detective quantum efficiency (DQE) are also defined in the spatial frequency domain. The noise equivalent quanta (NEQ) is equal to the square of the output SNR. Since the MTF describes how well an imaging system

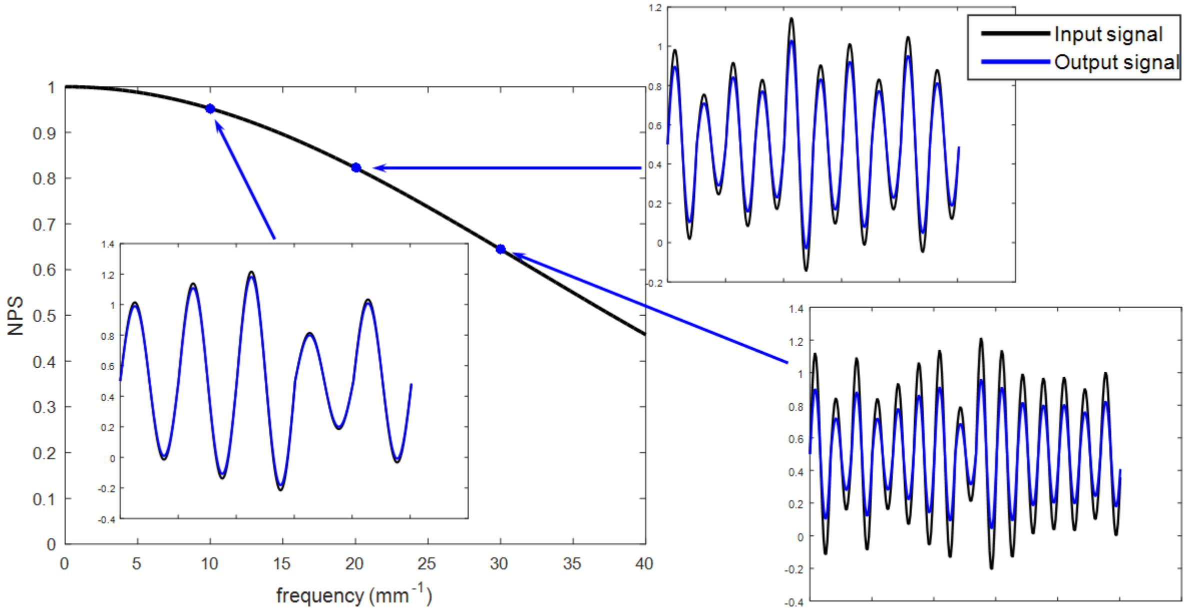

Figure 2.21 Illustration of the concept of noise power spectrum.

processes the signal and the NPS describes how well an imaging system processes the noise, NEQ is given by

$$NEQ \equiv SNR_{output}^{2} = \frac{MTF^{2}(f)}{NPS(f)/\bar{P}} \tag{2.9}$$

where $\bar{P}$ is the average pixel value in the image to be analyzed. The detective quantum efficiency (DQE) is the ratio of NEQ to the square of input SNR, which is the number of incident neutrons *N*.

$$DQE = \frac{NEQ}{N} = \frac{\bar{P}}{N}\frac{MTF^{2}(f)}{NPS(f)} \tag{2.10}$$

2.4.3.2 Methods of Evaluating Noise Performance

As opposed to Equation (2.7) and (2.8) where the NPS is defined by an ensemble average of analysis on infinite extend of imaging data, in practice, the NPS is measured on a single discrete image with limited amount of samples. Usually, evaluations are performed on the selected regions of interest (ROIs) of a flat-field image, which is obtained in an open beam without any object. The ensemble average can be approximated by dividing ROI into M sub-ROIs and calculating the mean of the analysis of each sub-ROI. Therefore, a two-dimensional NPS is obtained through the following computation,

$$NPS\left(f_i, f_j\right) = \frac{1}{M}\frac{\Delta s^2}{N_x N_y}\sum_{m=1}^{M}\left|\sum_{i=1}^{N_x}\sum_{j=1}^{N_y}\left[P_m\left(i, j\right) - S_m\left(i, j\right)\right]e^{-2\pi \mathbf{i}\left(f_i i \Delta s + f_j j \Delta s\right)}\right|^2 \qquad (2.11)$$

where $P_m(i,j)$ is the recorded data in the mth sub-ROI. To be distinguished from the pixel index i of an image function, the imaginary unit used in Fourier transform is denoted by boldface letter i. The function $S_m(i,j)$ reflects the fixed pattern that the noise is superimposed on, such as non-uniformity in the beam. It is usually obtained by least-square regression fitting the data in sub-ROI to a first-order or second-order polynomial model.

2.4.3.3 Experimental Results on Noise of the Scintillator System

NPS was determined from a flat-field image as shown in Figure 2.22. It was taken using the 250 µm-thick scintillator and the CCD camera with a pixel size of 60 µm. This was the same condition when the image of the resolution phantom in Figure 2.19 (a) was obtained.

The computational methods applied followed the procedure in the international standard IEC 62220-1 (2005) for X-ray imaging devices. A centered portion of the image was

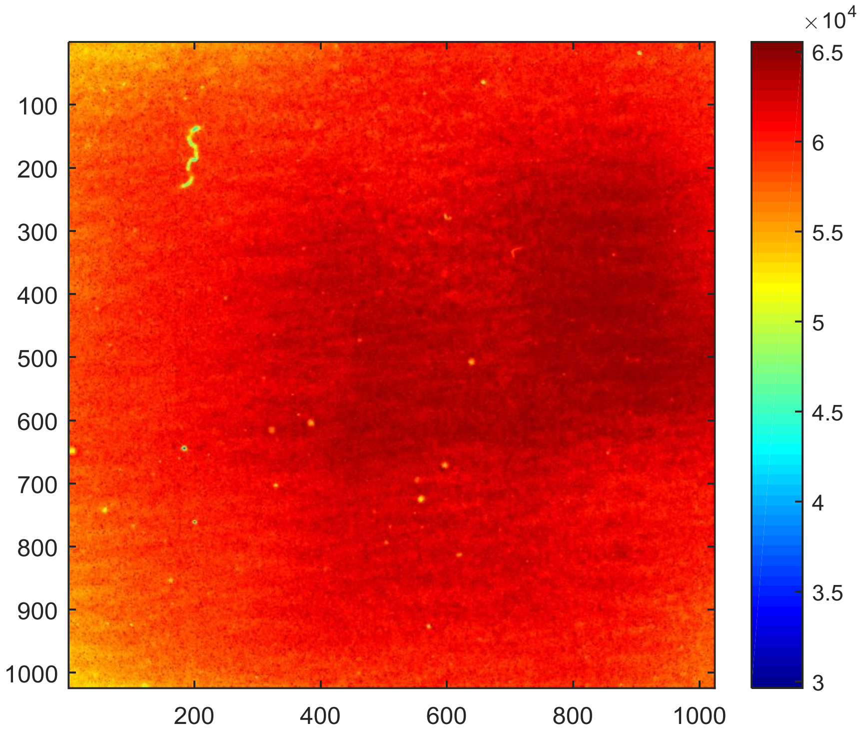

Figure 2.22 The center portion of a flat-field image taken with the 250 µm-thick scintillator at 60 µm pixel size, used in noise evaluation of the system

divided into ROIs with dimensions of 64×64 pixels. A two-dimensional second-order polynomial fitted functions was subtracted from each ROI to remove the effects from the non-uniformity of the beam. The two-dimensional Fourier transform of each images was calculated. Then the square of the magnitude was taken and the results was averaged over all the ROIs. To further reduce statistical error, as well as to present a simple, one-dimensional NPS representation, radial rebinning of the data points comprising the two-dimensional NPS into 32 integer frequency bins was performed, followed by an averaging of values within each bin (Boedeker, 2007). Figure 2.23 (a) and (b) show the calculated two-dimensional NPS and one-dimensional NPS.

With the use of Equation (2.10) and the MTF shown in Figure 2.20 (a), DQE was calculated and was shown in Figure 2.24 (a). Furthermore, the normalized NPS, MTF and DQE were plotted together in Figure 2.24 (b). It appears that the shape of MTF is more influential on the shape of DQE, which means the detectability of the scintillator system is determined by the MTF.

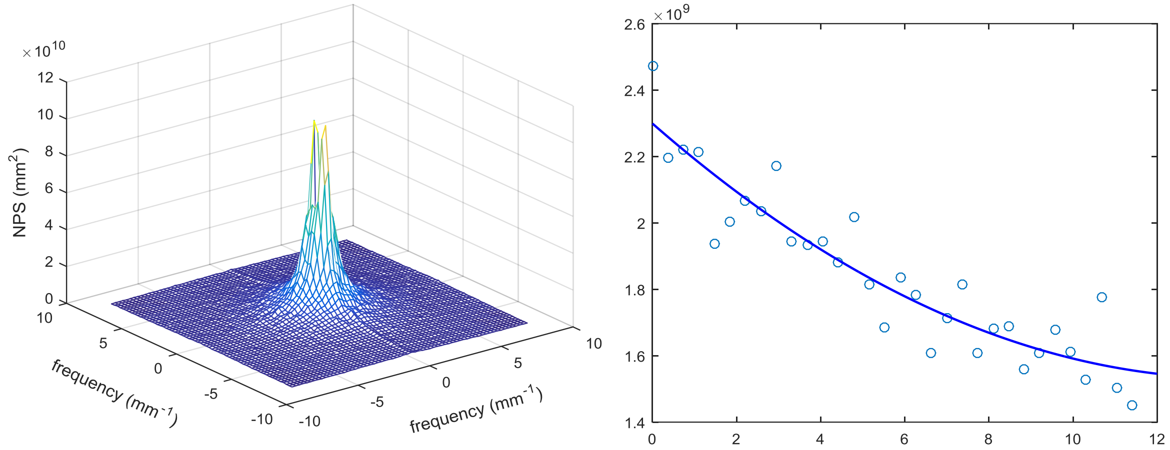

(a) (b)

Figure 2.23 (a) The two-dimensional NPS, and (b) the one-dimensional NPS of the scintillator system.

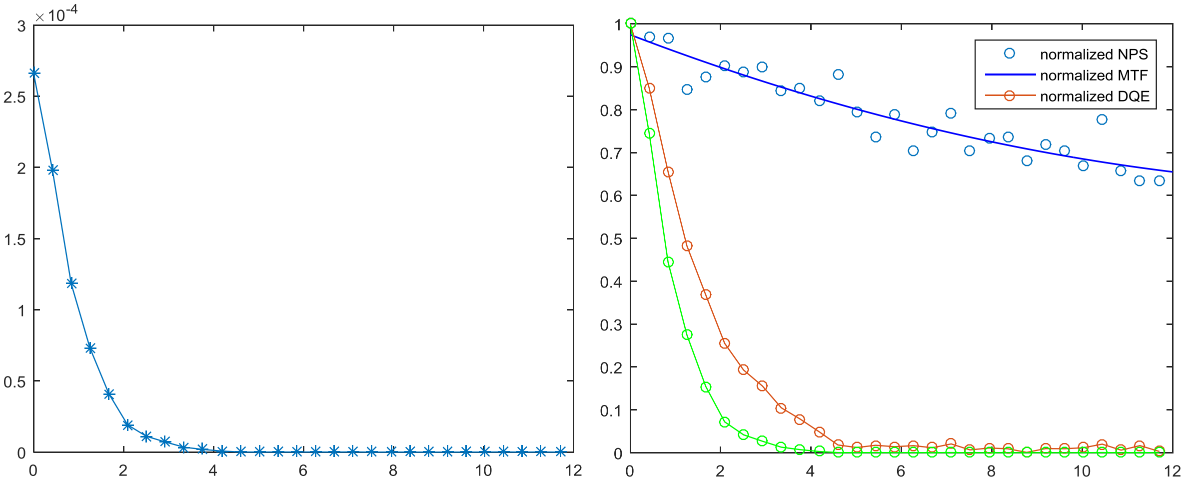

(a) (b)

Figure 2.24 (a) DQE of the scintillator system; and (b) normalized NPS, MTF and DQE of the scintillator system.

Chapter 3

Resolution Enhanced Magnified Neutron Imaging

The principles and development of a Resolution Enhanced Magnified Neutron Imaging (REMANI) system are explored in this chapter. Firstly, to enhance the resolution, magnification is introduced to neutron imaging over the conventional arrangement. Following that, multiple-pinhole imaging techniques and coded imaging techniques are used to improve the system in terms of signal-to-noise performance and reconstruction performance. Details on coded patterns and system parameters complete this chapter.

3.1 Magnified Neutron Imaging System

As stated in Section 2.4, conventionally, a neutron image reflects the neutron field modulated by the object, which is further impacted by the responses of a series of components during the neutron image formation. One of the degradation components, the geometric unsharpness, is linearly related to the object-to-detector distance and the inverse of the *L/D* ratio. Thus to achieve high resolution, a large *L/D* ratio is required and the detection system is always placed as close as possible to the object. However, here we propose a different arrangement with magnification to enhance the resolution of the system.

3.1.1 Mathematical Model of Magnified Neutron Imaging

Figure 3.1 shows an illustration of a magnified neutron image system. A magnified image is obtained on the detection system that is moved away from the object. The magnification factor *m* is defined as the ratio of the size of the projected image to the size of

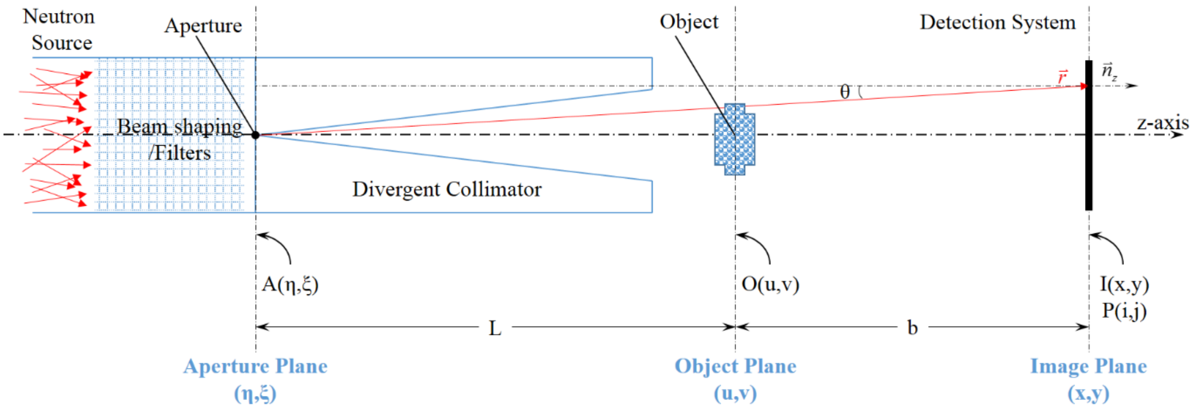

Figure 3.1 A conceptual model of a magnified neutron imaging system

the object. It can be determined by the aperture-to-object distance *L* and the object-to-image distance *b*.

$$m = \frac{L+b}{L} \tag{3.1}$$

The same as conventional imaging, the *L/D* ratio still defines the inverse divergence of the beam. The geometric unsharpness quantifies the broadening due to this divergence. The size of the broadening can be calculated as

$$U_g = \frac{b}{L/D} = (m-1)D \tag{3.2}$$

For a value of *m* much larger than one, the size of the aperture *D* must be very small to restrain the image degradation. It can be treated as an isotropic point source. Let function *A(η,ξ)* represent the number of neutrons emitted from the point *(η,ξ)* in the aperture plane. The object function $O(u,v) = \exp\left[-\int_{obj} \Sigma_T(u,v,z)\,dz\right]$ represents the object characteristics at point *(u,v)* on the object plane. The number of neutrons projected at point *(x,y)* on the image plane within an infinitesimally small area *dS* can be given as

$$T\left(x,y\right)dS=\frac{A\left(\eta,\xi\right)}{4\pi r^{2}}O\left(u,v\right)\left(\frac{\vec{r}}{r}\cdot\vec{n}_{z}\right)dS \tag{3.3}$$

where $\vec{n}_z$ is the unit vector of the image plane and $\vec{r}$ is the vector of the neutron trajectory on which points *(η,ξ)*, *(u,v)* and *(x,y)* are all located. By ray tracing, the relationship among the coordinates of the points are $x=mu-\left(m-1\right)\eta, y=mv-\left(m-1\right)\xi$. Let θ denote the angle between $\vec{r}$ and $\vec{n}_z$, thus their dot product is $\vec{r}\cdot\vec{n}_z=r\cos\theta$. Since $r\cos\theta=L+b$ and the neutron source have a small diameter of *D* in practice, the distribution of function *T(x,y)* is obtained by integrating Equation (3.3) over the area of the pinhole aperture.

$$T(x,y)=\iint_{Aperture}A(\eta,\xi)\frac{\cos^{3}\theta}{4\pi\left(L+b\right)^{2}}O(u,v)d\eta d\xi \tag{3.4}$$

If the image plane is far enough from the aperture plane, θ is very small and the value of $\cos^3\theta$ is approximately equal to one at any point on the image plane. This holds true in the NIF at the PULSTAR due to the dimension of the beamline. With the constant term neglected and coordinate transfer applied, *T(x,y)* can be re-written as in Equation (3.5), which is in the form of convolution. The derivation is in Appendix A.1.

$$\begin{aligned}T(x,y)&=\left(\frac{1}{m-1}\right)^{2}\iint A'\left(x-x',y-y'\right)O'\left(x',y'\right)dx'dy'\\&=\left(\frac{1}{m-1}\right)^{2}A'\left(x',y'\right)*O'\left(x',y'\right)\end{aligned} \tag{3.5}$$

where $x' = mu,\ y' = mv$, $A'\left(x', y'\right) = A\left(\frac{-x'}{m-1}, \frac{-y'}{m-1}\right)$ and $O'\left(x', y'\right) = O\left(\frac{x'}{m}, \frac{y'}{m}\right)$. Function *O'*(·)is obtained by magnifying the object function *O*(·) along the spatial coordinates by *m* times. Function *A'*(·) is obtained by reversing the aperture function *A*(·) around the origin then magnifying along the spatial coordinates by (*m-1*) times.

The function *I*(*x*,*y*) represents the output produced by the detection system. It is equal to the transmitted neutron distribution *T*(*x*,*y*) impacted by the response of the converter and the optical components, which can be denoted by another impulse function $h_d(x,y)$ and referred as the detector unsharpness.

$$I\left(x, y\right) = \left(T * h_d\right)\left(x, y\right) \tag{3.6}$$

If a digital system is used, the output image has a discrete form, and can be represented by a two-dimensional matrix *P(i,j)*. The sampling acts as integration of this intensity over the area of a pixel and digitization is linear to the integral in the imager.

$$P\left(i, j\right) = \int_{(i-0.5)\Delta s}^{(i+0.5)\Delta s} \int_{(j-0.5)\Delta s}^{(j+0.5)\Delta s} I\left(x, y\right) dxdy \tag{3.7}$$

where Δs is the size of a pixel.

3.1.2 Resolution of Magnified Neutron Imaging System

The definition of resolution is the minimum distance between two points on an object that can be resolved. In conventional neutron imaging, the image function is the convolution of the object function and the PSF. Therefore, the FWHM of the PSF can be used as an indicators of the system resolution. However, in a magnified neutron imaging system, it is unfair to measure the resolution with the spread of a point directly.

We start with evaluating an image of a point located at (u_δ, v_δ) on the object plane. It can be obtained by setting the object function $O(u,v)$ as a Dirac delta function $O(u,v) = \delta(u - u_\delta, v - v_\delta)$.

Denote the transmitted neutron distribution through this point object as $T_\delta(x,y)$. With the derivation shown in Appendix A.2, the distribution of $T_\delta(x,y)$ is

$$T_\delta(x,y) = \left(\frac{m}{m-1}\right)^2 A\left(-\frac{x - mu_\delta}{m-1}, -\frac{y - mv_\delta}{m-1}\right) \tag{3.8}$$

It can be written as the correlation of a delta function.

$$\begin{aligned} T_\delta(x,y) &= \left(\frac{m}{m-1}\right)^2 A\left(-\frac{x}{m-1}, -\frac{y}{m-1}\right) * \delta(x - mu_\delta, y - mv_\delta) \\ &= h_g(x,y) * \delta(x - mu_\delta, y - mv_\delta) \end{aligned} \tag{3.9}$$

And the function $h_g(x,y)$ represents the geometric unsharpness and is defined as

$$h_g(x,y) = \left(\frac{m}{m-1}\right)^2 A\left(-\frac{x}{m-1}, -\frac{y}{m-1}\right) \tag{3.10}$$

It has the same distribution as the aperture function but magnified $(m-1)$ times. The function $T_\delta(x,y)$ is the function $h_g(x,y)$ with the center shifted to (mu_δ, mv_δ). If the pinhole aperture has a square shape with a side of D and the center at the origin. Functions $A(\eta,\xi)$, $h_g(x,y)$ and $T_\delta(x,y)$ have distributions,

$$A(\eta,\xi) = rect\left(\frac{\eta}{D},\frac{\xi}{D}\right)$$

$$h_g(x,y) = \left(\frac{m}{m-1}\right)^2 rect\left(-\frac{x}{(m-1)D},-\frac{y}{(m-1)D}\right) \tag{3.11}$$

$$T_\delta(x,y) = \left(\frac{m}{m-1}\right)^2 rect\left(-\frac{x-mu_\delta}{(m-1)D},-\frac{y-mv_\delta}{(m-1)D}\right)$$

The detector unsharpness is due to the dispersion of the secondary radiation converted from neutrons and the light aberration in the mirror/lens system. The degree of detector unsharpness is a property of the detection system. In most cases, especially the phosphor plates and the powder scintillators, the emission of the secondary radiation can be treated as isotropic, and the size of dispersion is largely dependent on the thickness of the neutron conversion layer. Depends on the type of the detectors in use and the range of the position variable chosen, its distribution can be approximated by Gaussian, Lorentzian or exponential functions (Harms, 1977). The function of $h_d(x,y)$ includes the response of both the convertor and the optical system. The width of the function is equivalent to the intrinsic resolution of the detection system, denoted by a parameter λ. If a Gaussian function (Gaskill, 1978) is used as an approximation, the function $h_g(x,y)$ can be written as

$$h_d(x,y) = Gauss\left(\frac{x}{\lambda},\frac{y}{\lambda}\right) = \exp\left(-\pi\frac{x^2}{\lambda^2}\right)\exp\left(-\pi\frac{y^2}{\lambda^2}\right) \tag{3.12}$$

The process of sampling has two main effects on image quality: the loss of resolution and aliasing. First, the sampling operation is not shift invariant, since the resulted images will be affected by the relative position between the transmitted neutron distribution and the imaging pixels. If the distribution to be images is assumed to be randomly located with respect to a grid of pixels, sampling $I(x,y)$ can be equivalent to taking the convolution with a sampling impulse response $h_s(x,y)$, which is defined as a two-dimensional function representing the area of one pixel. Usually, the pixel is a square with a side of Δs, and the function $h_s(x,y)$ is a rectangular function.

$$h_s(x,y) = rect\left(\frac{x}{\Delta s}, \frac{y}{\Delta s}\right) \tag{3.13}$$

It is easier to be understood in the frequency domain. Fourier transform of the rectangular function is equivalent to the average of the MTFs that would be realized for an ensemble of source locations, uniformly distributed with respect to the sampling pixels (Boreman, 2001). Thus function $h_s(x,y)$ can represent the process of sampling impacted on the degradation of resolution.

Aliasing is an image artifact that occurs when the sampling interval is not sufficiently fine, so that high frequency signals are perceived as low frequency in the digital image. Shannon's theorem states the condition to avoid aliasing artifact: the sampling frequency must be higher than twice the highest frequency component of the signals, which is also called Nyquist rate. Failure to satisfy this condition, signals higher than Nyquist rate will be lost and false low frequency signals will be generated. For an imaging system where the Nyquist criterion has been satisfied, the image of the point object can be recovered. The distribution can be expressed as

$$\begin{aligned} I_\delta(x,y) &= (T_\delta * h_d * h_s)(x,y) \\ &= (h_g * h_d * h_s)(x,y) * \delta(x - mu_\delta, y - mv_\delta) \end{aligned} \tag{3.14}$$

where functions h_g, h_d and h_s are the impulse response functions describing geometry effects, detection system effects, and sampling effects, respectively. Their convolution is the PSF of the system.

$$PSF(x,y) = (h_g * h_d * h_s)(x,y) \tag{3.15}$$

With the distributions of functions h_g, h_d and h_s defined as in Equation (3.11), (3.12), and (3.13), the FWHM of the PSF can be calculated by the parameters *m, D, λ, and Δs*. Figure 3.2 shows an example of these distributions when D = 100 µm, λ = 245 µm, and Δs = 60 µm at magnification factor of 4. It can be seen that the PSF (red line), as the convolution of three functions, is close to a Gaussian function and the FWHM is 341 µm. Figure 3.3 shows how the FWHM of PSF changes with the magnification factor, when other parameters are the same.

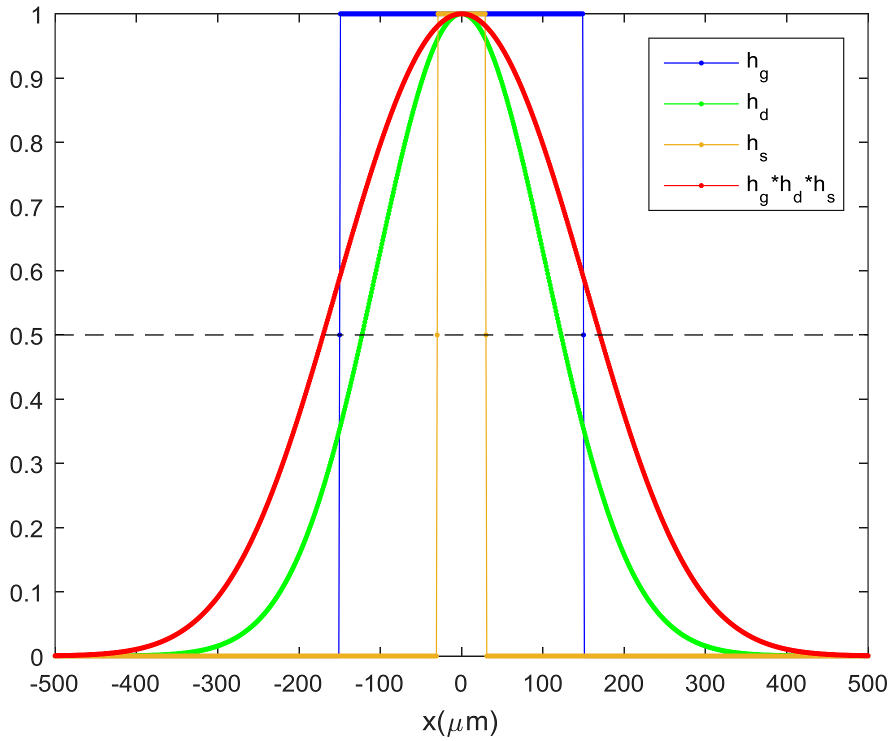

Figure 3.2 The distributions of functions h_g, h_d, h_s, and their convolution as PSF when D = 100 µm, λ = 245 µm, and Δs = 60 µm at magnification factor of 4.

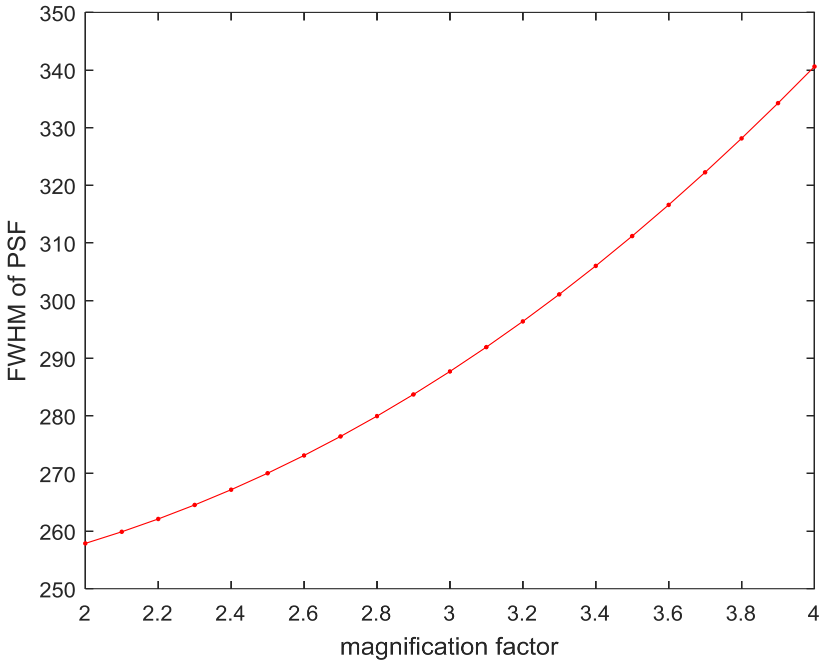

Figure 3.3 The FWHM of the PSF variation with the magnification factor, when *D* = 100 µm, *λ* = 245 µm, and *Δs* = 60 µm.

To obtain a formula that can quickly estimate the FWHM of the PSF and can be easily used in designing the system, all the impulse functions are approximated by Gaussian distributions with the FWHM kept the same as in Equation (3.11), (3.12), and (3.13). The FWHM of the PSF is the root-sum-square of the FWHM of all the impulse functions.

$$\begin{aligned} FWHM_{PSF} &\approx \sqrt{FWHM_g^2 + FWHM_d^2 + FWHM_s^2} \\ &= \sqrt{(m-1)^2 D^2 + \lambda^2 + \Delta s^2} \end{aligned} \tag{3.16}$$

The image of $O(u,v) = \delta(u - u_\delta, v - v_\delta)$, which is a point located at (u_δ, v_δ) on the object plane, can be rewritten as

$$I_\delta(x,y) = \delta(x - mu_\delta, y - mv_\delta) * PSF(x,y) \tag{3.17}$$

In order to resolve the images of two points, the distance between the centers of two point images must be larger than the FWHM of the PSF. Therefore, the minimum resolvable distance, also known as the resolution of the system, can be calculated as

$$res = \frac{1}{m} FWHM_{PSF} \approx \frac{1}{m}\sqrt{(m-1)^2 D^2 + \lambda^2 + \Delta s^2} \tag{3.18}$$

Figure 3.4 compares the system resolutions calculated with two assumptions at different magnification factors, when D = 100 μm, λ = 245 μm, and Δs = 60 μm. In the original assumption, the impulse response functions h_g, h_d and h_s follow distributions defined as in Equation (3.11), (3.12), and (3.13). In the Gaussian approximation, these impulse response functions all have Gaussian distributions.

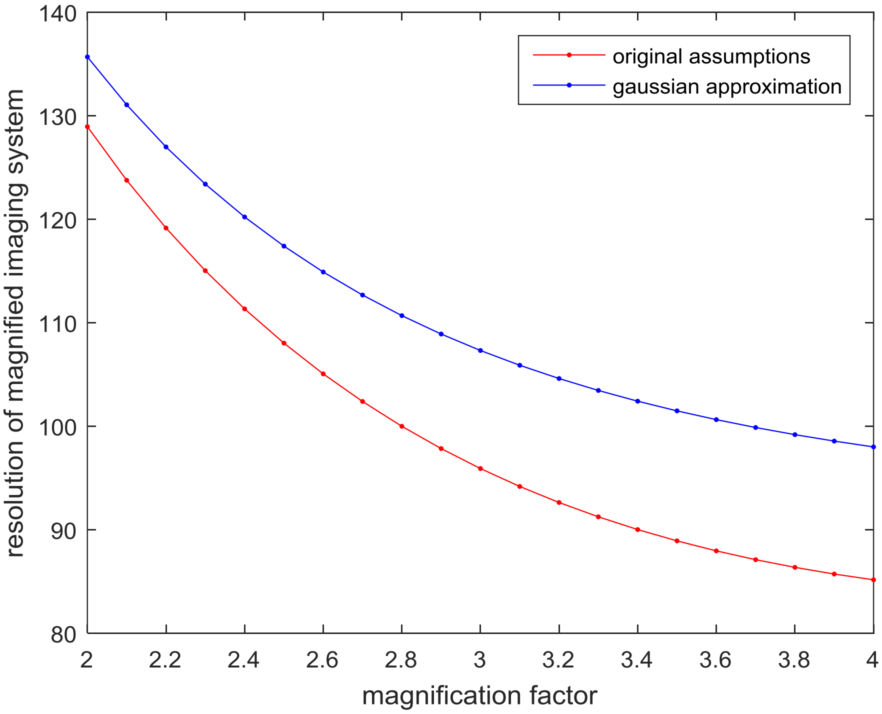

Figure 3.4 The resolution of the system calculated with two assumptions at different magnification factors, when *D* = 100 μm, *λ* = 245 μm, and *Δs* = 60 μm.

When *m* is close to one, Equation (3.18) also applies to conventional neutron imaging. The resolution of the system is mainly limited by the intrinsic resolution of the detection system λ and the pixel size for sampling. In a magnified neutron imaging system where *m* is much larger than one, the system resolution can be smaller than the intrinsic resolution of the detector that is determined by λ and Δs. The system resolution improves with the value of magnification factor *m*. Eventually, it approaches to the size of the pinhole aperture as *m* approaches infinity (Xiao, 2011).

3.2 Multi-pinhole Neutron Imaging System

The size of the pinhole aperture in a magnified neutron imaging system must be very small, because it limits the resolution that the magnified system can achieve. In order to achieve enhanced resolution, it is required that the size of the pinhole is on the order of hundred microns or even smaller. Obviously, with the current neutron source, the neutron flux at the image plane will be too low to produce reasonable input SNR during a practical exposure time.

To realize an arrangement with magnification, multiple pinholes are proposed to be used in forming the aperture instead of a single pinhole. The signals arriving at the image plane are proportional to the opening area in the aperture plane and the SNR can be improved as well. The recorded image is composed of multiple images overlapped with each other. Each image is casted by one of the multiple pinholes in the aperture. Thus reconstruction is required to retrieve the object distribution from the recorded image. Unfortunately, the reconstruction process may introduce additional degradation to the system resolution.

3.2.1 Mathematical Model of Multiple-pinhole Neutron Imaging

An illustration of a multiple-pinhole neutron imaging system is shown in Figure 3.5. The function $A(\eta,\xi)$ still represents the strength of the neutron sources emitted from the aperture plane. For a multiple-pinhole system within the scope of this thesis, the pinholes composing the aperture have the same shape and size. Function A can be written as

$$A(\eta,\xi) = A_\delta(\eta,\xi) * A_1(\eta,\xi) \tag{3.19}$$

where $A_1(\eta,\xi)$ describe one hole in the mask, and $A_\delta(\eta,\xi)$ is a collection of Dirac δ functions each indicating the position of a pinhole in the mask.

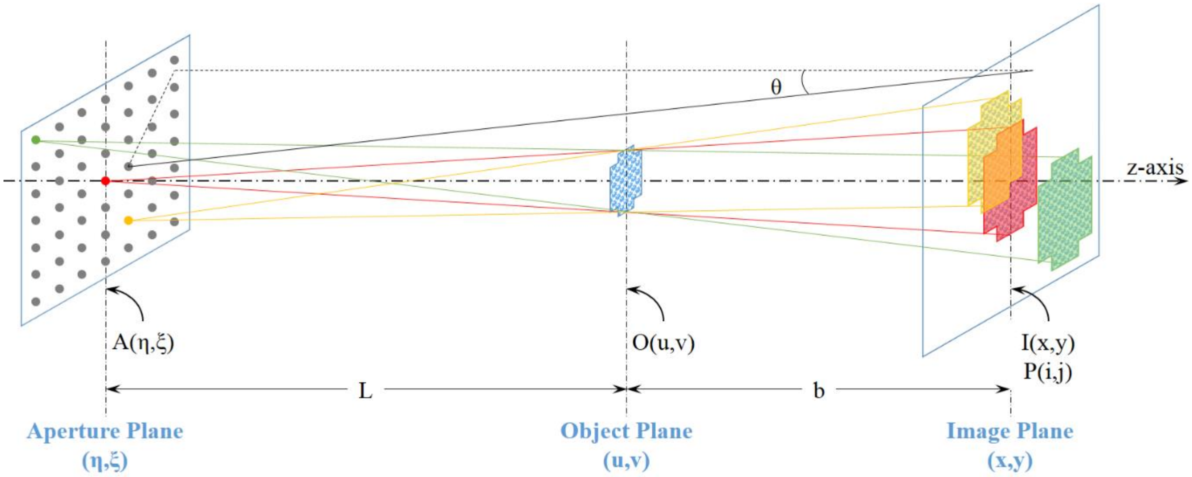

Figure 3.5 The illustration of a multiple-pinhole neutron imaging system.

With the same definition and similar derivation shown in last section, the recorded image is given in the following equation.

$$
\begin{aligned}
I_{\text{multi}}(x,y) &= \left(\frac{1}{m-1}\right)^2 \left(A_\delta{}'*A_1{}'*O'*h_d\right)(x,y) \\
P_{\text{multi}}(i,j) &= \int_{(i-0.5)\Delta s}^{(i+0.5)\Delta s}\int_{(j-0.5)\Delta s}^{(j+0.5)\Delta s} I_{\text{multi}}(x,y)\,dxdy
\end{aligned}
\tag{3.20}
$$

where $A_{\delta(\text{or }1)}{}'(x',y') = A_{\delta(\text{or }1)}\left(\frac{-x'}{m-1},\frac{-y'}{m-1}\right)$, $O'(x',y') = O\left(\frac{x'}{m},\frac{y'}{m}\right)$ and $h_d(x,y)$ is the impulse response function corresponding to the intrinsic resolution of the detection system. To be noted, function $A_\delta{}'$ is equal to function A_δ scaling by a factor of $-(m-1)$ and is also a collection of Dirac δ functions.

Let function $\tilde{O}'(x,y)$ and $\tilde{O}_s{}'(i,j)$ be the continuous and the discrete representation of the single pinhole image of the object *O*. The single pinhole has the same shape and size as the ones in the multi-pinhole aperture. Based on Equation (3.6) and (3.7),

$$
\begin{aligned}
I_{\text{single}}(x,y) &= \left(\frac{1}{m-1}\right)^2 \left(O'*A_1{}'*h_d\right)(x,y) \\
P_{\text{single}}(i,j) &= \int_{(i-0.5)\Delta s}^{(i+0.5)\Delta s}\int_{(j-0.5)\Delta s}^{(j+0.5)\Delta s} I_{\text{single}}(x,y)\,dxdy
\end{aligned}
\tag{3.21}
$$

Equation (3.20) can be written as $I_{\text{multi}}(x,y) = \left(A_\delta{}'*I_{\text{multi}}\right)(x,y)$. It represents that the multi-pinhole image is a collection of single-pinhole images shifted with respect to the locations of the holes in the aperture plane indicated by function $A_\delta{}'$. With the derivation in Appendix A.3, the digital image $P_{multi}(i,j)$ can be written in the form of discrete convolution.

$$
P_{\text{multi}}(i,j) = \left(A_s{}'*P_{\text{single}}\right)(i,j) \tag{3.22}
$$

where $A_s{}'(i,j)$ is obtained by sampling continuous functions $A_\delta{}'(x,y)$ with an interval of Δs.

Since $A_\delta'(x,y)$ is a collection of Diract delta functions, $A_s'(i,j)$ is a collection of Kronecker δ functions. It is given by Equation (3.23).

$$A_s'(i,j) = \sum_p \delta\left(i - i_p', j - j_p'\right), \text{ where } i_p' = \frac{x_p'}{\Delta s}, j_p' = \frac{x_p'}{\Delta s} \tag{3.23}$$

To be noted, in order to make i_p' and j_p' to be integer numbers, it is required the rectilinear distance between the mask holes to be an integral multiple of the pixel size.

Reconstruction is obligatory to retrieve the distribution of the object from the recorded multiplexed image. In the ideal case, a perfect reconstruction would result in a summation of all the single pinhole images without location shifting.

$$\hat{P}_{\text{ideal}}\left(i,j\right) = NP_{\text{single}}\left(i,j\right) \tag{3.24}$$

where $N = \sum A_s'(i,j)$ is the number of pinholes in the aperture plane.

Compare to the magnified imaging system with a single pinhole, the number of neutrons incident on the image plane increase by a factor of N. Thus the input SNR of the imaging system will gain a factor of $\sqrt{N}$. At the meanwhile, the reconstructed image would carry the enhanced resolution that is shown in Equation (3.18) as the magnified imaging system does.

3.2.2 Image Reconstruction for Multiple-pinhole System

A perfect reconstruction shown in Equation (3.24) is hardly possible to achieve for a large value of N, let alone the consideration of noise in practice. In this section, we introduce two reconstruction methods for multi-pinhole imaging system.

3.2.2.1 Inverse Problem

Reconstruction for multi-pinhole imaging system is an ill-posed inverse problem in the sense of Hadamard.

A forward problem is to predict the output image of the multi-pinhole system with a known object. Reconstruction is to recover the object function from the multiplexed, noisy images that are registered by the detection system. We solve for P_{single} with the forward problem set by Equation (3.22).

In image processing, a two-dimensional problem is usually expressed in terms of linear equations with matrix-vector notation. Equation (3.22) can be re-written as

$$p = Ws + e \tag{3.25}$$

The vectors p and s are obtained by lexicographic ordering of the matrices P_{multi} and P_{single}, respectively. The matrix W is generated by packing the array A_s' to be block Toeplitz (Caroli, 1987). The vector e is a lexicographic ordering vector from a matrix that is corresponding to the noise in the recorded image.

A problem is called well-posed in the sense of Hadamard if there exists a unique solution that continuously depends on its data (Wang, 2012). Otherwise it is called an ill-posed problem. For a system with a large number of pinholes in the aperture, as is often the case, the function A_s' is ill-conditioned, thus the problem in (3.25) is an ill-posed problem. Therefore, the matrix inverse solution $W^{-1}p$ or the singular value decomposition cannot provide a stable solution to the problem.

In the following sections, we provide two reconstruction methods to derive estimator $\hat{s}$ given the image data p and the matrix W corresponding to the distribution of the multi-pinhole aperture.

3.2.2.2 Maximum Likelihood Estimation with Richard-Lucy Algorithm

To put it simply, the maximum likelihood estimation is to find an estimator of the single-pinhole image $\hat{s}$ that is most likely to produce the measured multi-pinhole image p, based on statistical models assumed for the measured data.

In this case, we assume that elements of the measured image are independent Poisson random variable. The probability of obtaining the measured data p_i at the i^{th} element of p is $f\left(p_i \mid k\right)=\dfrac{k^{p_i}e^{-k}}{p_i!}$, where k is the expected value, and is equal to the i^{th} element of the vector Ws, denoted by $\left[Ws\right]_i=\sum_j w_{ij}s_j$.

A likelihood function can be defined as a function of s in the following Equation

$$L(s)\triangleq \ln\prod_i f\left(p_i \mid n\right)=\sum_i\left\{p_i\ln\left[Ws\right]_i-\left[Ws\right]_i-\ln\left(p_i!\right)\right\} \tag{3.26}$$

The maximum likelihood estimator (MLE) maximizes this argument $L(s)$, so that,

$$\hat{s}_{MLE} = \arg\max_{s} L(s) \tag{3.27}$$

An iterative solution was proposed by Richardson (1972) and Lucy (1974) independently, known as Richardson-Lucy deconvolution algorithm.

$$s_j^{(n+1)} = \frac{s_j^{(n)}}{\sum_i w_{ij}} \sum_i \frac{w_{ij} p_i}{\left[W s^{(n)} \right]_i} \tag{3.28}$$

3.2.2.3 Least Squares Estimation with Tikhonov Regularization

From Equation (3.25), the error between the measured image *p* and the image produced by *Ws* is $e = p - Ws$. The least square estimator (LSE) minimizes the squares of the error $\| p - Ws \|^2$ among all the possible *s*, where $\|\cdot\|$ the Euclidean norm. However, for an ill-posed problem, there are many *s* can fit the data appropriately. Therefore, we need to select the one with desirable properties by introducing a penalty term *R(s)* to the squares of the error to be minimized. This is a regularization method and the regularized LSE is

$$\begin{gathered} \hat{s}_{LSE} = \arg\min_{s} \Psi(s) \\ \Psi(s) = \| p - Ws \|^2 + \beta R(s) \end{gathered} \tag{3.29}$$

where *R(s)* penalizes *s* according to its deviation from the desirable image properties, and the regularization parameter β controls the weight of regularization. In particular, Tikhonov regularization introduce a L_2 penalty, so that

$$\begin{gathered} \Psi(s) = \| Ws - p \|^2 + \beta \| \Gamma s \|^2 \\ \hat{s}_{LSE} = \left(W^T W + \beta \Gamma^T \Gamma \right)^{-1} W^T p \end{gathered} \tag{3.30}$$

where Γ is called Tikhonov matrix and can choose the solutions with desirable properties. For example, an Identity matrix I will choose the solutions with a small norm.

Both reconstruction methods can be applied with the prior knowledge of the multi-pinhole aperture. However, both methods unavoidably introduce resolution degradation and noise amplification to the reconstructed results.

3.3 Coded Source Neutron Imaging

For a multi-pinhole neutron imaging system, the only requirement on the pinholes is that the centers of their projections on the image plane can be sampled properly with a pixel size of Δs. If the arrangement of the pinholes is carefully designed, the reconstruction can be simplified and the degradation and artifacts on the reconstructed image can be reduced. We refer the aperture with multiple pinholes arranged in a coded fashion as coded aperture. Since the coded aperture is used to code the neutron source in a neutron imaging system, we refer such system as coded source neutron imaging system.

3.3.1 Image Formation and Reconstruction in Coded Source Imaging

A coded aperture falls into a class of multi-pinhole apertures. Therefore, the model proposed in Section 3.2 still holds for coded source neutron imaging. The recorded image is given by Equation (3.20) and (3.22), which is $P_{\text{multi}}(i,j)=\left(A_s{}'*P_{\text{single}}\right)(i,j)$.

Reconstructed image can be obtained by correlating the recorded image P_{multi} with a decoding array G. The reconstructed result $\hat{O}$ can be calculated as,

$$\hat{P}_{\text{single}}(k,l)=P_{\text{multi}}(i,j)\times G(i,j)=P_{\text{single}}*\left(A_s{}'\times G\right)+N\times G \tag{3.31}$$

where × denotes the discrete correlation operation. If the correlation term $(A_s' \times G)$ is a δ function, the reconstructed image $\hat{P}_{\text{single}}$ is equal to the single-pinhole image with additional noise term.

In signal processing, this technique is called matched filtering, because the reconstructed results are deduced by scanning through the recorded data to match a particular distribution. It has been demonstrated as the optimal linear filter for maximizing the signal-to-noise ratio (SNR) in the presence of additive stochastic noise (Heusdens 2012).

It can also be expressed in the form of a linear system of equations. The matrix $\bar{W}$ is constructed by reordering the decoding array G in the same way as generating W from the A_s'. The result is given by

$$\hat{s} = \bar{W}p = \bar{W}Ws + \bar{W}e \tag{3.32}$$

The vector $\hat{s}$ can be fold into the two-dimensional matrix $\hat{P}_{\text{single}}$.

Depending on the distribution of the coded aperture, the correlation operation for reconstruction can be auto-correlation, balanced correlation or circular correlation.

3.3.2 Families of Coded Array

As discussed above, $A_s'(i,j)$ is a collection of Kronecker δ functions. Thus it can be represented by a binary array with values of one and zero. It is obtained by scaling the function A_δ describing the locations of the pinholes on the mask by a factor of $-(m-1)$ and then sampling the scaled function by interval Δs. Therefore, the discrete representation of the aperture function is also a binary array with values of one and zero. The array is referred as mask array, denoted by A.

In the mask array, the ones indicate the open elements on the mask, where the holes are located; the zeros indicate the opaque elements on the mask. The open fraction is defined as the percentage of the opening area on the mask over the size of the entire aperture, denoted by ρ.

$$\rho = \frac{N_1}{N_T} \tag{3.33}$$

where N_1 and N_T are the number of ones and the number of total elements in the mask array.

A perfect reconstruction requires the correlation between the mask array A and the decoding array G to be a δ function. Otherwise, the non-zero values off the peak in the correlation function will introduce artifacts in the reconstructed results. These artifacts are not related to stochastic noise or background noise in the system. Thus they are called inherent noise.

There are various patterns that satisfy this requirement and can be used to perform coded source imaging. This section summarizes some patterns that have been practically used for coded aperture imaging. The content is focused on the generation rules of mask array A and the corresponding decoding array G. To compare the performances of coded patterns, two aspects are considered: the correlation properties that determines the artifacts on reconstruction, and the open fraction that determines the strength of the neutron sources to form the image.

3.3.2.1 Random Array

A random array aperture consists of a large number of randomly spaced pinholes. The decoding array is the same as the mask array. Figure 3.6(a) shows an example of a 13 × 13 random array. The dash lines mark the grid of the array, while the areas filled with black are the opening pinholes. Figure 3.6(b) is it circular autocorrelation function.

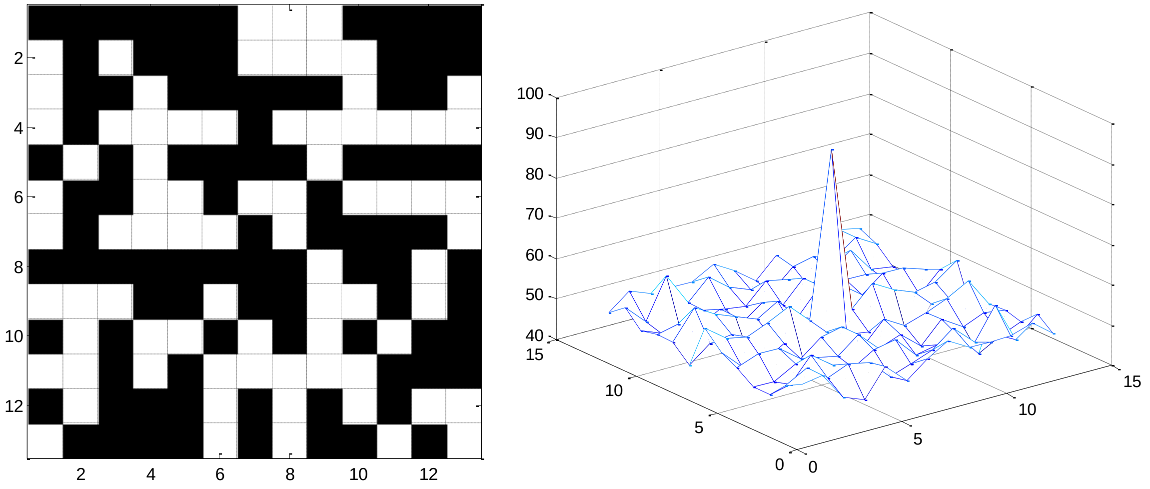

(a) (b)

Figure 3.6 (a) A 13 × 13 random array and (b) its circular autocorrelation function.

There is no specific limit on the open fraction of the mask, as long as N_1 elements are randomly selected out of N_T elements for the locations of ones in the mask array. However, the value of ρ largely affects the correlation function.

If the mask array A and the decoding array G are aligned, the summation of their Hadamard product is equal to N_1 and contributes to the peak in the correlation function. The rest of the elements in the correlation function are the summations of the Hadamard products of A and cyclic shifted G. Due to the randomness of pinhole locations, the probability of each element in A being one is equal to ρ. After cyclic shift, the probability of a one in A still matching a one in G is also equal to ρ. On average, the off-peak values in the correlation function is ρN. The standard deviation is $\left(1-\rho\right)\sqrt{\rho N_1}$. Thus a random aperture has inherent noise. The ratio of the contrast (difference between the peak value and the average off-peak value) and the standard deviation in the inherent noise is maximized when ρ is 50%.

3.3.2.2 Non-Redundant Array

In non-redundant array (NRA), all the rectilinear distances between two holes must be unique. This is the meaning of 'non-redundant' in the name. The decoding array is the mask array itself. The correlation function is obtained by autocorrelation operation. Figure 3.7(a) shows an example of a 9 × 9 non-redundant array with 10 holes (black) and Figure 3.7(b) is its autocorrelation function.

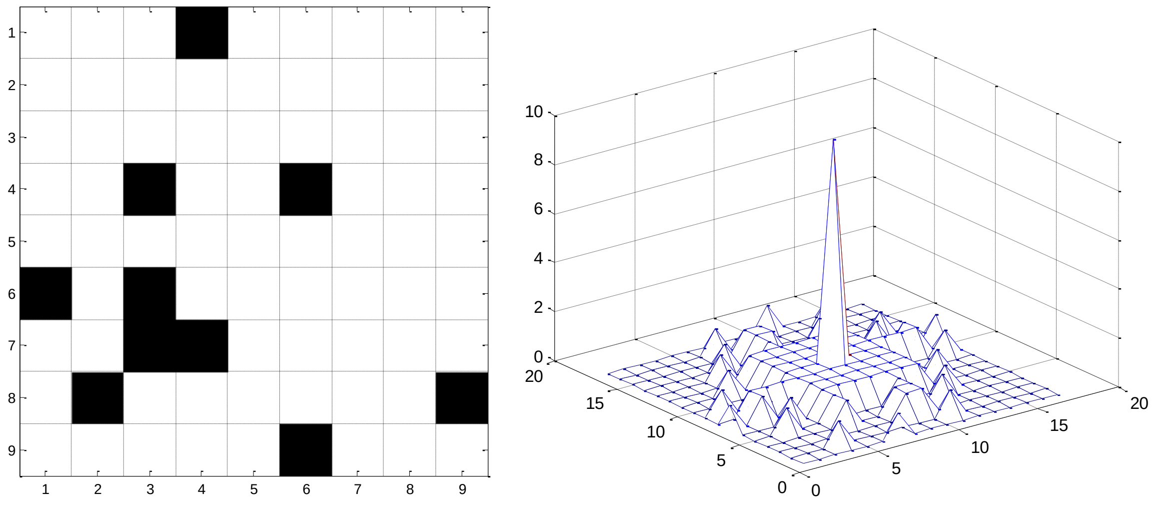

(a) (b)

Figure 3.7 (a) A 9 × 9 non-redundant array and (b) its autocorrelation function

Several algebraic methods can be used to generate NRA arrays. The search algorithm allows constructing an N_1-element NRA for $N_1 \leq 10$. It simply starts with a pair of neighboring points in the field and adds successively to each n-point array, the point nearest to its center of gravity that would form with it an (N_1+l)-point array having a non-redundant autocorrelative array (Golay, 1971). With use of the logarithm table, one can generate an N_1-element NRA on an $N_1 \times N_1$ grid, with exactly one hole in each row and column, for N_1 up to 360 with a few exceptions (Golomb, 1984). Based on relative difference set and cyclic difference set, one can generate NRA for $N_1 \leq 1000$ (Kopilovich, 1988). Therefore, the open fraction of NRA is very low, not greater than the reciprocal of the number of holes on the mask.

The peak in the correlation function has a value of N_1. The maximum distance between two holes in the array is also N_1. For a shifting step less than N_1, there must be one and only one hole in A overlapping with a hole in the shifted G. Therefore, the off-peak value in the correlation function is equal to one within the range of $\sqrt{N_1}$ around the peak. Outside of the range, the values oscillate between zero and one. As can be seen from Figure 3.7(b), the correlation function of NRA is a perfect δ function but the flat sidelobe without fluctuation is very small.

3.3.2.3 Uniformly Redundant Array

In a uniformly redundant array (URA), all the rectilinear distances between the ones occur a constant number of times (λ). Non-redundant array is a special case in uniformly redundant array, when λ is one. The decoding array G is obtained by replacing zero in A by g, where $g = -\frac{\rho}{1-\rho}$. The correlation operation is circular autocorrelation. The correlation function is a perfect δ function. Figure 3.8(a) shows an example of a 13 × 11 uniformly redundant array (ones as black) and Figure 3.8(b) is its circular correlation function with the decoding array *G*.

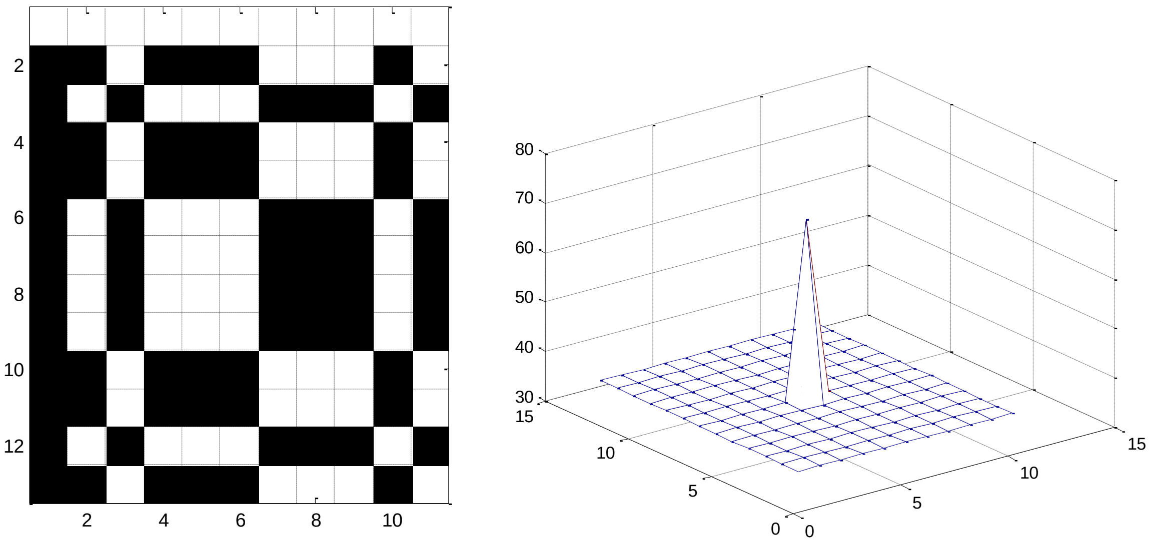

(a) (b)

Figure 3.8 (a) A 13 × 11 uniform redundant array and (b) its circular autocorrelation function

Mathematically speaking, URA is generated based on cyclic difference sets (Baumert, 1969). A cyclic difference set *D* has a set of parameters (v, k, λ). It is defined as a collection of k distinct residues d_l, …, d_k modulo v, for which the non-zero congruence $d_i - d_j = b$ (mod v) has exactly λ distinct solution pairs. Based on the value of v, the difference sets can be divided into sub families. For example, quadratic residues and twin prime sets are two of the sub families. Their parameters (v, k, λ) satisfy the relationship ($4t - 1$, $2t - 1$, $t - 1$), where t is an integer. If v is a prime number, it is a quadratic residue. If $v = r(r+2)$ where r is a prime number, it is a twin prime set. A binary sequence $\{a_i\}$ with length v is associated with each difference set. If i is belongs to D, then $a_i = 1$; otherwise, $a_i = 0$. URA can be obtained by folding such a binary sequence into two-dimensional array along an extended diagonal. Thus it is required that the length of the sequence v can be factorized into two mutually prime numbers (Proctor, 1979).

Fenimore (1978) proposed an algorithm to construct a URA without generating the cyclic difference sequence. It is equivalent of ordering a twin prime sequence along the extended diagonal. The size of the mask array is $r \times s$, where r and s must be prime numbers and $r - s = 2$. The values of the elements are determined by

$$A(I,J) = \begin{cases} 0, \, if \;\; I = 0 \\ 1, \, if \;\; J = 0, \; I \neq 0 \\ 1, \;\; if \;\; C_r(I)C_s(J) = 1 \\ 0, \;\; otherwise \end{cases} \tag{3.34}$$

where C_r and C_s are two quadratic residues sequences with length of r and s.

$$C_r(I) = \begin{cases} 1, \text{if } \exists \text{ an integer } x, 1 \leq x < r, \text{and } I = \text{mod}_r \, x^2 \\ 0, \text{otherwise} \end{cases}$$

$$C_s(I) = \begin{cases} 1, \text{if } \exists \text{ an integer } x, 1 \leq x < s, \text{and } I = \text{mod}_s \, x^2 \\ 0, \text{otherwise} \end{cases}$$

Based on the property of cyclic difference set, the number of ones and the number of total elements must satisfy $N_T = 2N_1 + 1$. The open fraction approximates 50% if a large number of holes are used to form the mask.

$$\rho = \frac{N_1}{2N_1 + 1} \approx 50\%$$

The correlation function is obtained by circular correlation. The peak has a value of N_1, when no shifting between A and G occurs. If G is cyclic shifted with any steps, there are λ ones in A overlapped with ones in G and the rest of ones overlapped with g in G. The summation of all will be zero, indicating zero sidelobe in the correlation function. Therefore, the correlation function of URA is a perfect δ function, with the same size of the mask array and the decoding array.

3.3.2.4 Modified Uniformly Redundant Array

Using the same algorithm given in Equation (3.34), one can construct a square array by making r and s to be the same prime number, which is called modified uniformly redundant array (MURA). The decoding array G is obtained by replacing zero in A by $-\rho/(1-\rho)$, then setting the first element to be one. The circular correlation between A and G is still a δ function. Now the quadratic residues sequences C_r and C_s used in the generating algorithm are the same, the aperture has a symmetric distribution after cyclic shift. Figure 3.9(a) shows an example of a symmetric 13 × 13 modified uniformly redundant array (ones as black) and Figure 3.9(b) is its circular correlation function. Same as the URA, the open fraction of MURA is about 50%, and the correlation function is a perfect δ function with the same size of the mask array.

A more comprehensive list of coded aperture family can be found in Accorsi's dissertation (Accorsi, 2001). Here are only listed some popular algorithms in generating a coded aperture. Among them, (M)URAs give perfect correlation functions and the largest

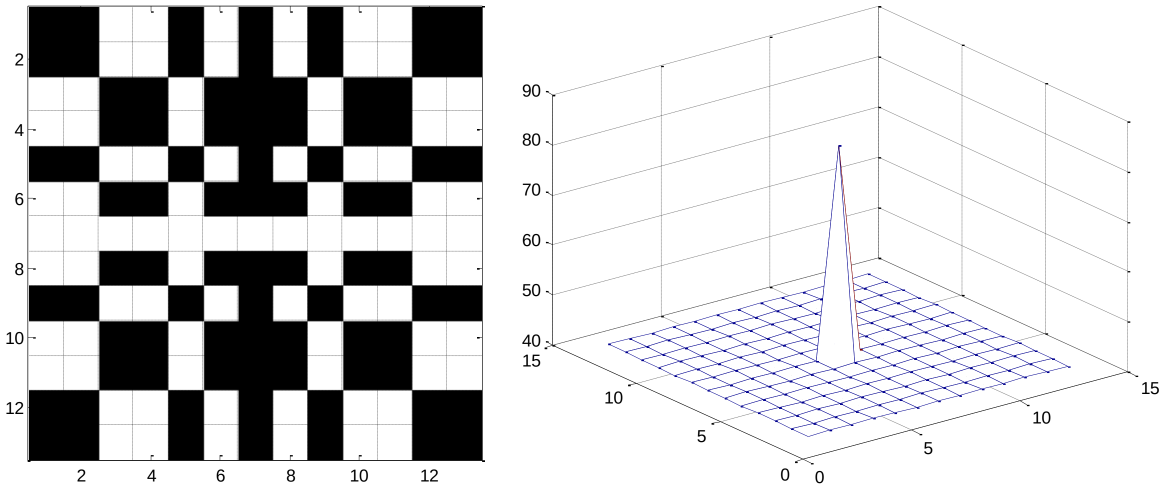

(a) (b)

Figure 3.9 (a) A 13 × 13 modified uniform redundant array and (b) its circular correlation function

open fraction (near 50%). Since MURAs allow a wider choice on the size of the aperture than URAs, the author has chosen MURAs and circular correlation to be used in the design of the coded aperture.

3.3.3 Resolution of Coded Source System

Even though the correlation function of MURA is a perfect δ function, the reconstructed image is not perfect as in Equation (3.24). As shown in Equation (3.31), it has a reconstruction term $\left(A_s' \times G\right)$ in the convolution operation and a noise term $N \times G$ in addition operation. The resolution can be evaluated from the FWHM of the PSF.

From Equation (3.15) and (3.31), the reconstructed PSF of a coded source system is

$$PSF_{\text{coded}} = \left[h_g * h_d * h_s\right] * \left[h_r\right] \tag{3.35}$$

where the bracket symbol [·] represents discrete functions, sampled by interval of Δs. The distributions of functions h_g, h_d and h_s are defined as in Equation (3.11), (3.12), and (3.13). The function h_r refers to the reconstruction term $\left(A_s' \times G\right)$. The additional noise term provides a pedestal level. The effects on resolution can be neglected if its mean value is subtracted from the result, thus it is omitted here. As shown in Figure 3.9 (b), the correlation function of MURA is a δ function with a central peak and zero sidelobe, so is reconstruction term $\left(A_s' \times G\right)$. The size of h_r is determined by scaling of the decoding array G.

The pinholes on the mask are distributed on a square grid, which has a one-to-one correspondence with the elements in mask array A. Let 'a' denote the physical grid size of elements. Scaled by a factor of $-\left(m-1\right)$, the projection of each grid element on the image plane has a size of $\left(m-1\right)a$. Define α as $\alpha = \frac{\left(m-1\right)a}{\Delta s}$. It is required that α is an integer.

Each element in the decoding array G must also cover $\alpha \times \alpha$ pixels. As shown in the previous section, G is a binary array with two non-zero values. There is more than one way to fill the corresponding $\alpha \times \alpha$ pixels for each value. To keep the symmetry of the system, the non-zero fillings must always be square with α possible sizes. Figure 3.10 shows an example when α = 4. One can set κ×κ pixels in the center to be the values in G, where κ can be any integer number between 1 to α, while keep the rest pixels as zeros. Since A_s' is a collection of δ functions, the central peak of $\left(A_s' \times G\right)$ is the same as the fillings for the non-zero elements

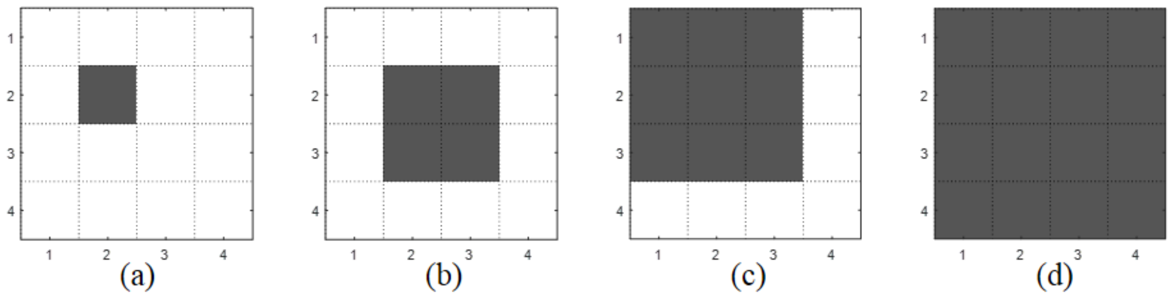

Figure 3.10 An example of α possible ways of filling a non-zero element in the decoding array to $\alpha\times\alpha$ pixels, in this case, $\alpha = 4$. Set (a) 1×1, (b) 2×2, (c) 3×3 and (d) 4×4 pixels as the non-zero values (gray), while the rest as zero (white).

in G. The size of h_r is equal to the size of κ pixels. Since the correlation operation in Equation (3.35) is between discrete functions, the effects on resolution due to h_r should be $(\kappa\text{-}1)\Delta s$.

Use similar Gaussian approximations as in Equation (3.16), the FWHM of the PSF and the resolution of the system is

$$\begin{aligned} FWHM_{PSF} &\approx \sqrt{FWHM_g^2 + FWHM_d^2 + FWHM_s^2 + FWHM_r^2} \\ &= \sqrt{(m-1)^2 D^2 + \lambda^2 + \Delta s^2 + (\kappa-1)^2 \Delta s^2} \\ res_{\text{coded}} &\approx \frac{1}{m}\sqrt{(m-1)^2 D^2 + \lambda^2 + \Delta s^2 + (\kappa-1)^2 \Delta s^2} \end{aligned} \tag{3.36}$$

If the case shown in Figure 3.10(a) is used in scaling the decoding array G, only one pixel is set to be non-zero and κ=1. The resolution of the reconstruction image is the same as the single pinhole image with the magnification factore m, which is the optimal case in terms of resolution. This is called δ decoding. If κ is chosen to be other values, the resolution in reconstructed image will be larger, but the SNR might be improved.

3.4 Geometry of a REMANI System

A practically achievable Resolution Enhanced Magnified Neutron Imaging (REMANI) system is a magnified imaging system with the use of a multi-pinhole aperture coded as a MURA array. There are many constraints on the geometric setup of a REMANI system. In this section, the details of considerations on the geometry of the system are presented.

3.4.1 Realization of Mask

First of all, the realization of a coded mask based on the mask array *A* is considered. As discussed in the previous section, the pinholes on the mask are distributed on a square grid with a grid size *a*. Each grid element corresponds to an element in the mask array. When the element in *A* is equal to one, a pinhole is placed in the center of the corresponding grid.

The shape of the pinholes is determined by the function $A_1(\eta,\xi)$. Ideally it is a two-dimensional square function. This is because the sampling elements of the system – the pixels are square. However, square holes are very hard to machine, and the opening may have other shapes. For example, if the mask were fabricated by drilling method, the holes are usually round. Sampling round projections with square pixels may introduce artifacts in reconstructed results, if the size of the holes and the size of the pixels are close.

For any shape, the size of the hole is an important parameter. It is worth noting that in a MURA array, some zeros are surrounded by ones on all four sides. So if the size of the opening equals to the grid size, not all of the opaque elements are not connected thus the array is not self-supported. In order to obtain a self-supported structure, the size of the openings *D* must be smaller than the grid size *a*. Figure 3.11 (a) is a 38 × 34 mosaicked URA array. The

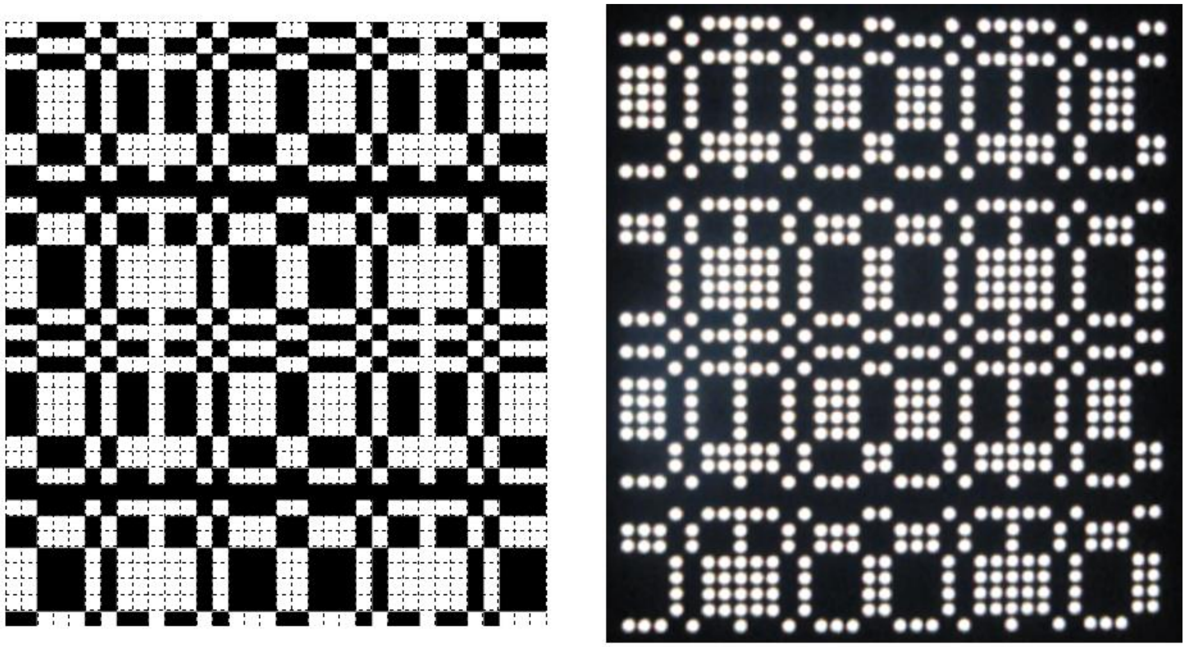

(a) (b)

Figure 3.11 (a) A mosaicked URA array and (b) a picture of the corresponding coded mask

concept of mosaic will be explained in Section 3.4.2. The white areas are ones, corresponding to the open elements; the black areas are zeros, corresponding to the opaque elements. Figure 3.11 (b) is a picture of a real mask based on this array. The openings are circles with a diameter of 700um. The size of each elements *a* is 1000um. In this case, the open fraction of the real mask is smaller than the open fraction in *A*, as calculated in Equation (3.33).

3.4.2 Field of View

For a MURA mask, since the reconstruction is realized by circular correlation operation, the size of the object is strictly limited. The maximum size of the object that can be perfectly reconstructed is called the field of view (FOV).

Figure 3.12 shows an illustration to estimate the field of view. The reconstructed result is a circular correlation between the recorded image and the decoding array *G*. Assume the mask array has a square shape and the physical length of one side is s_A. (For rectangular masks, the following calculations still hold but two directions need to be treated separately.) The projection that the mask deposits through one point on the object plane onto the image plane is also a square and the length of one side is s_R, where $s_R = (m-1)s_A$. Apparently, the decoding array and the reconstructed object have the same size as this projection. Since the reconstructed image is the object scaled by a factor of *m*, the field of view (FOV) is within the area with a physical dimension of $s_O \times s_O$, where

$$s_O = \frac{1}{m}s_R = \left(1-\frac{1}{m}\right)s_A \tag{3.37}$$

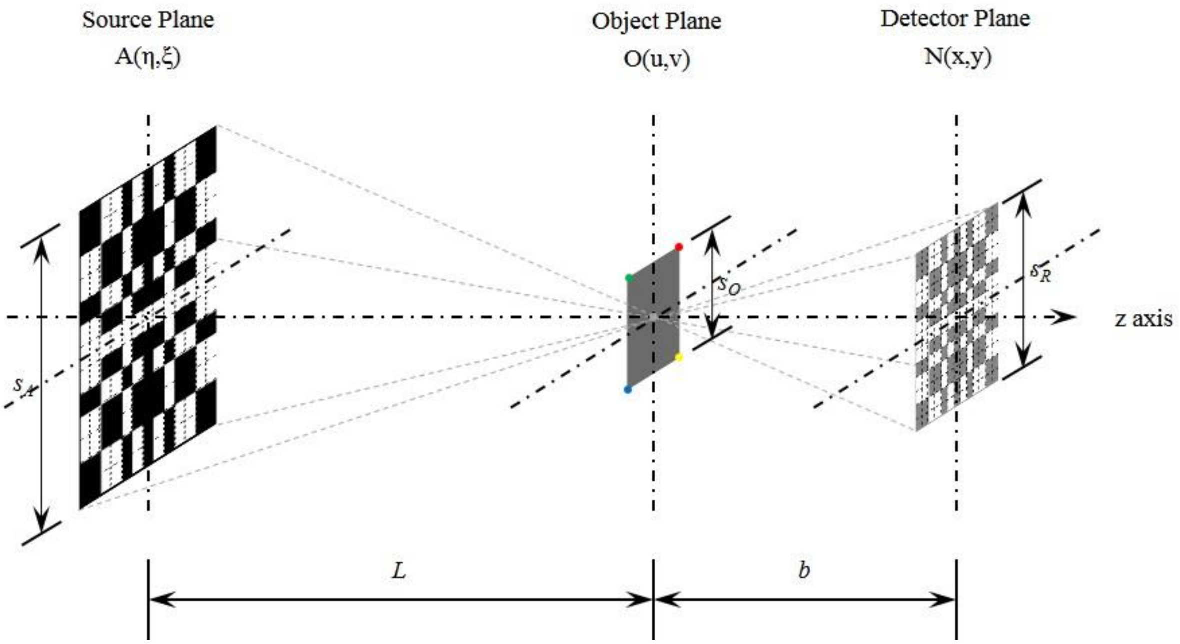

Figure 3.12 The field of view of coded source system

Anything outside of the FOV will introduce artifacts in the reconstructed results through circular correlation. Therefore, in a coded source experiment, neutron shielding with an opening less than FOV has to be placed on the object plane.

3.4.3 System Geometric Arrangement

With an MURA mask, in order to correctly reconstruct the object distribution, circular correlation must be applied to the area of the image that contains the projections of the complete mask array through the entire FOV. In this section, we show two geometric arrangements for a REMANI system.

The first one can be referred as non-cyclic arrangement, which is shown in Figure 3.13. The mask pattern is based on to the mask array and the size of the mask is $s_M = s_A$. The corners of the FOV, marked by four different colors in the figure, are the furthest points on the object

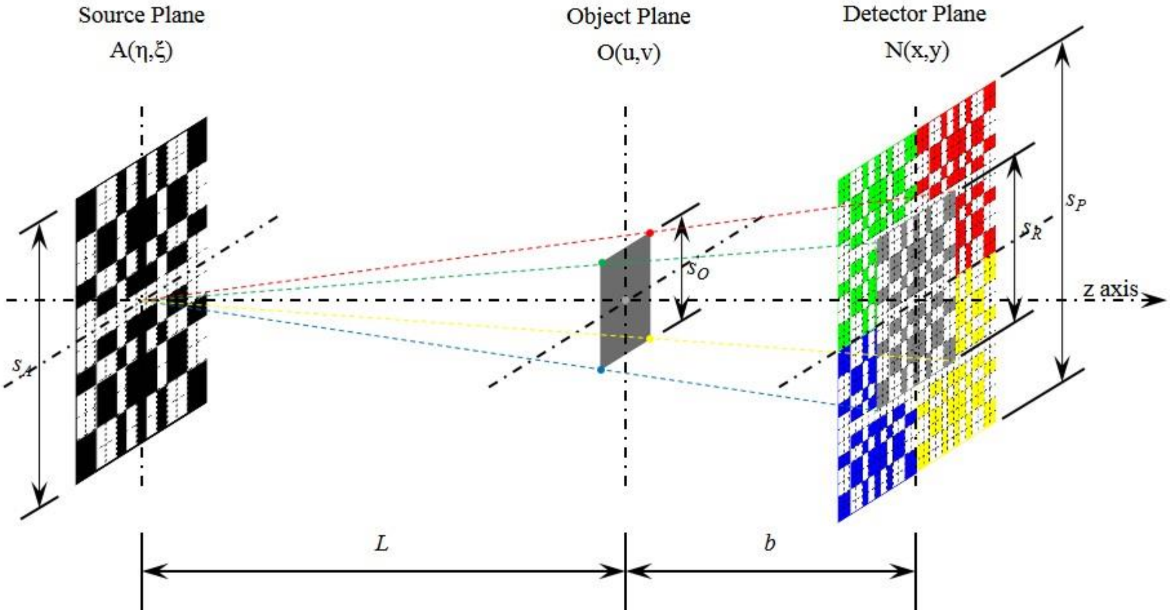

Figure 3.13 The non-cyclic arrangement for a coded source imaging system

plane to be images. Their coordinates are $\left(\pm\frac{s_O}{2},\pm\frac{s_O}{2}\right)$, where s_O can be calculated using Equation (3.37). The projections of the mask through these points, also marked by the corresponding colors, determine the size of the image. These projections all have a size of $s_R \times s_R$, and their centers are located at points $\left(\pm\frac{s_O \cdot m}{2},\pm\frac{s_O \cdot m}{2}\right)$ respectively. Therefore, the image used in reconstruction has an area of $s_P \times s_P$, where $s_P = s_O \cdot m + s_R$. When the size of the object is the FOV, the image size reaches the maximum, which is $s_P = 2\left(m-1\right)s_A = 2\left(m-1\right)s_M$.

The second one can be referred as cyclic arrangement, which is shown in Figure 3.14.

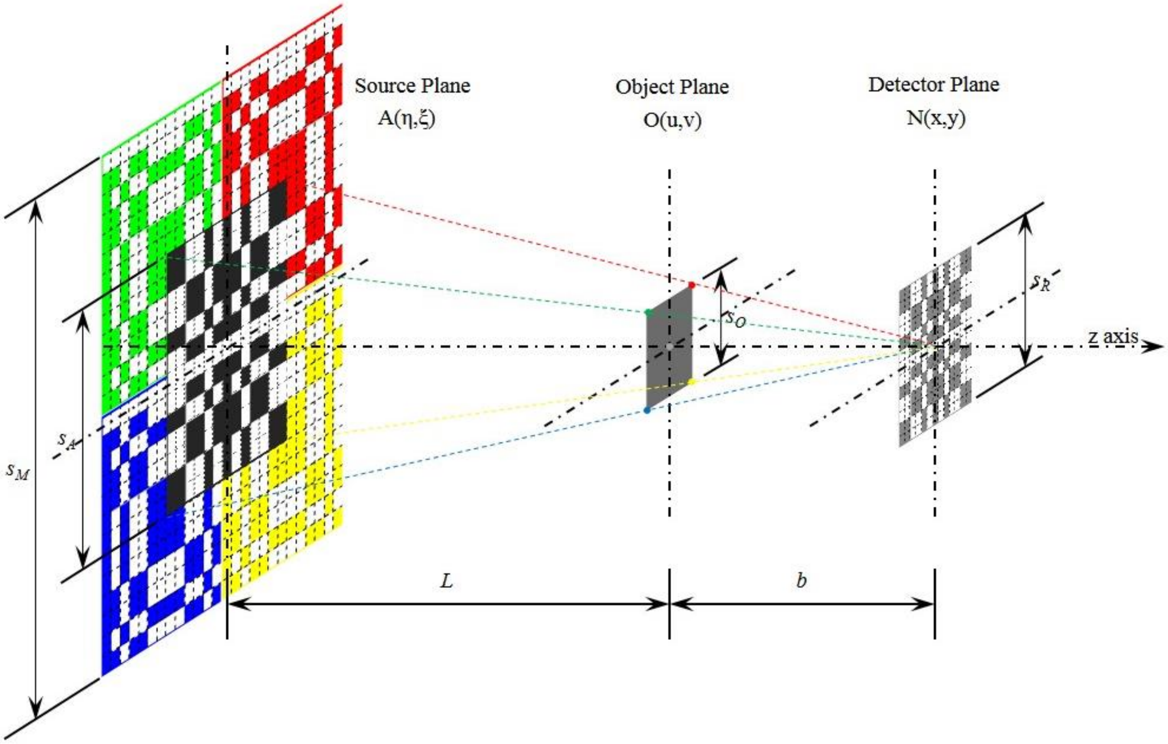

Figure 3.14 The cyclic arrangement for a coded source imaging system

The mask is a cyclic repetition of the mask array. The mask array is called basic array in this arrangement. Through any object point within the FOV, there will be a part of the mask with a size of $s_A \times s_A$ that deposit its projection onto the center portion of the image with a size of $s_R \times s_R$. The $s_A \times s_A$ mask contains a complete basic array, although the pattern will be cyclic shifted. Thus, the $s_R \times s_R$ image is sufficient to be used alone in reconstruction. Since the size of the object is limited, the size of the mask is also limited. As shown in Figure 3.14, the four colored portions of the mask, each with the size of $s_A \times s_A$, project onto the center area $s_R \times s_R$ of the image, through four corners of the FOV. These four portions confine the size of the mask to an exact 2 × 2 replication of the basic array. If the mask is beyond 2 × 2 replication, it will cast partial projection onto the image and introduce artifacts.

The 2 × 2 replication of the basic array, which is called mosaic, is illustrated in Figure 3.15. The entire mask consists of the basic array in the center part (black) and the surrounding mosaicked part (gray). The size of the mask is $s_M = 2s_A$. Considering the size of the object is

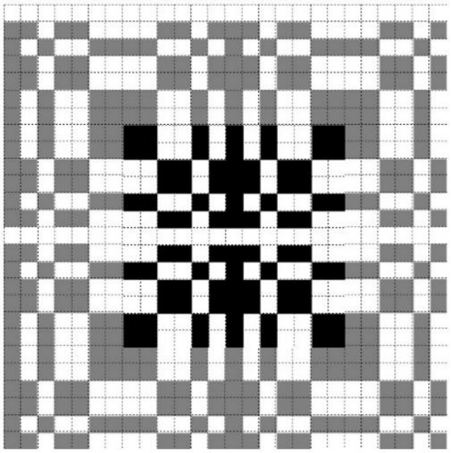

Figure 3.15 The mosaicked mask used in the cyclic arrangement

$s_O \times s_O$, the size of the image $s_P \times s_P$ is determined as

$$s_P = s_O \cdot m + s_M \cdot (m-1) \tag{3.38}$$

When the size of the object is the FOV, the image size reaches the maximum, which is $s_P = 3(m-1)s_A = 1.5(m-1)s_M$.

There are two options to choose the image to be used in reconstruction with correlation method. One can use the complete image, with a size of $s_P \times s_P$, where $s_P = 3(m-1)s_A$. One can use the center portion of the image, with a size of $s_R \times s_R$, where $s_R = (m-1)s_A$. The former one is referred as the complete correlation and the latter one as the basic correlation in this work.

3.4.4 The Magnification Factor

Based on Equation (3.36), the resolution of a coded source neutron system is enhanced with increasing the magnification factor and it approaches the size of the pinhole on the mask. However, there are some requirements on the selection of magnification factor so that the recorded image can be successfully reconstructed.

In an imaging facility, the total length of the beamline, denoted as L_T, is restricted. The magnification factor *m* is smaller than L_T/L., where *L* is the aperture-to-object distance. In order to take images with a high magnification factor in a short time, it is intuitive to place the object as close to the aperture as practically possible. However, the value of *L* is restricted by the divergence of the beam. The neutron sources can be treated as neutrons uniformly emitted from points over the source plane with an angle following a cosine distribution. Denote the maximum divergence angle as φ, which is determined by the collimator used in the beamline. As illustrated in Figure 3.16, the blue and the yellow areas are the extreme cases that can be covered by the neutron sources. The object must fall in their overlapping area – the green shaded portion in the figure. From ray-tracing, a lower level for the aperture-to-object distance L can be set as,

$$L > \frac{s_M + s_O}{2\tan\varphi} = \left(\frac{3}{4} - \frac{1}{4m}\right)\frac{s_M}{\tan\varphi} \tag{3.39}$$

In the design process, since the values of φ and s_M are usually set, this limitation increases with the magnification factor m. Substitute L in the inequality $m < \frac{L_T}{L}$ with this limitation, it can be derived that,

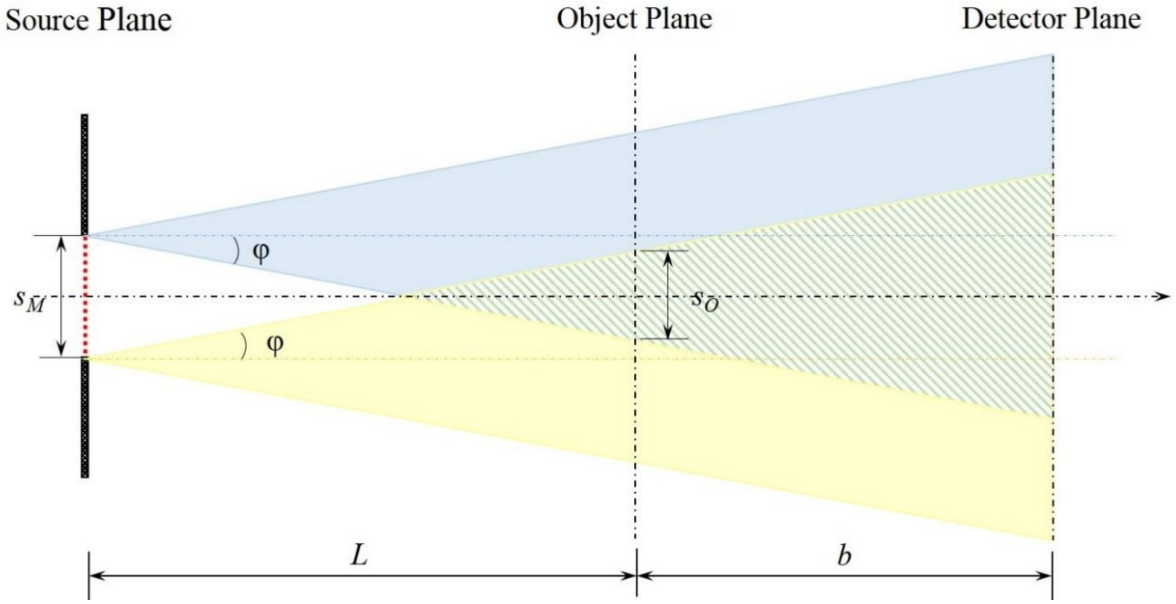

Figure 3.16 The divergence of beam

$$m < \frac{1}{3} + \frac{4L_T}{3s_M} \tan\varphi \tag{3.40}$$

The value of magnification factor is also limited by the size of the detector s_D. Consider the case that the mask size is set to be $s_M \times s_M$. If the non-cyclic arrangement is used, the size of the image for reconstruction is $s_P = 2(m-1)s_M$. If the cyclic arrangement is used, the size of the recorded image for reconstruction is $s_P = \frac{1}{2}(m-1)s_M$. It is required that the size of the detector is larger than s_P. Therefore,

$$\begin{gathered} m < \frac{s_D}{2s_M} + 1 \ (\text{non-cyclic arrangement}) \\ \text{or} \\ m < \frac{2s_D}{s_M} + 1 \ (\text{cyclic arrangement}) \end{gathered} \tag{3.41}$$

Finally, not all the values satisfying Equation (3.40) and (3.41) can be used in the REMANI system. In fact, only a few values within the range can be used as a magnification factor. In Section 3.3, a parameter α is defined as the ratio of the size of the projection of a grid element on the mask $(m-1)a$ to the size of a pixel in the detector Δs. To be able to obtain the perfect correlation reconstruction and avoid aliasing, the value of α is required to be an integer larger than two. The magnification factor must satisfy

$$m = \frac{\alpha \Delta s}{a} + 1 \tag{3.42}$$

In summary, the magnification factor m in a coded source system must satisfy Equation (3.40) to (3.42) at the same time.

Chapter 4

REMANI System Design and Monte Carlo Simulations

A REMANI imaging system has been designed for the neutron imaging facility at NC State PULSTAR Reactor, based on the characteristics of the beamline. The design objective is to obtain a REMANI system whose resolution excels the intrinsic resolution of the detector. Monte Carlo neutron transport calculations were performed using MCNP code to evaluate the image quality of the system.

4.1 Mask Thickness and neutron transmission

In order to form a multiple-pinhole coded source, the material of the mask is required to have high neutron absorption cross-section and good machinability. As a result, it was decided to use commercially available gadolinium foils with a purity > 99.9%.

To start with, the thickness of the mask material should be optimized. On the one hand, the mask has to be thick enough to prevent neutrons passing through the opaque elements. On the other hand, the thickness should be as small as possible with consideration of manufacturing challenges.

The relationship between neutron transmission and the thickness of gadolinium was investigated with MCNP simulations. The model was based on the one illustrated in Figure 3.4 and 12-inch sapphire filters were used. The 4 cm × 4 cm aperture was fully covered by a piece of gadolinium foil. Multiple cases were run, in which gadolinium thickness varied from zero to 500 μm. In each case, neutron fluxes were tallied at the different locations along the beamline. Neutron transmission was obtained as the ratio between the tallied fluxes with and without a gadolinium foil presented at the aperture. Figure 4.1 plots the mean values of neutron transmission at different locations against the thickness of the gadolinium foils. From the standard deviations included as the error bars in the vertical axis, it can be seen that neutron transmission is not sensitive to locations of the measurements. But it drops remarkably with increasing thickness. Only 0.11% neutrons can pass through a 200μm-thick gadolinium foil and contribute as transmission noise. Further increasing the thickness will have little effect on reducing the noise (Xiao, 2009). Therefore, the material of the mask was chosen to be a gadolinium foil, with a size of 5 cm × 5 cm and a thickness not less than 0.008 inches (203.2 μm).

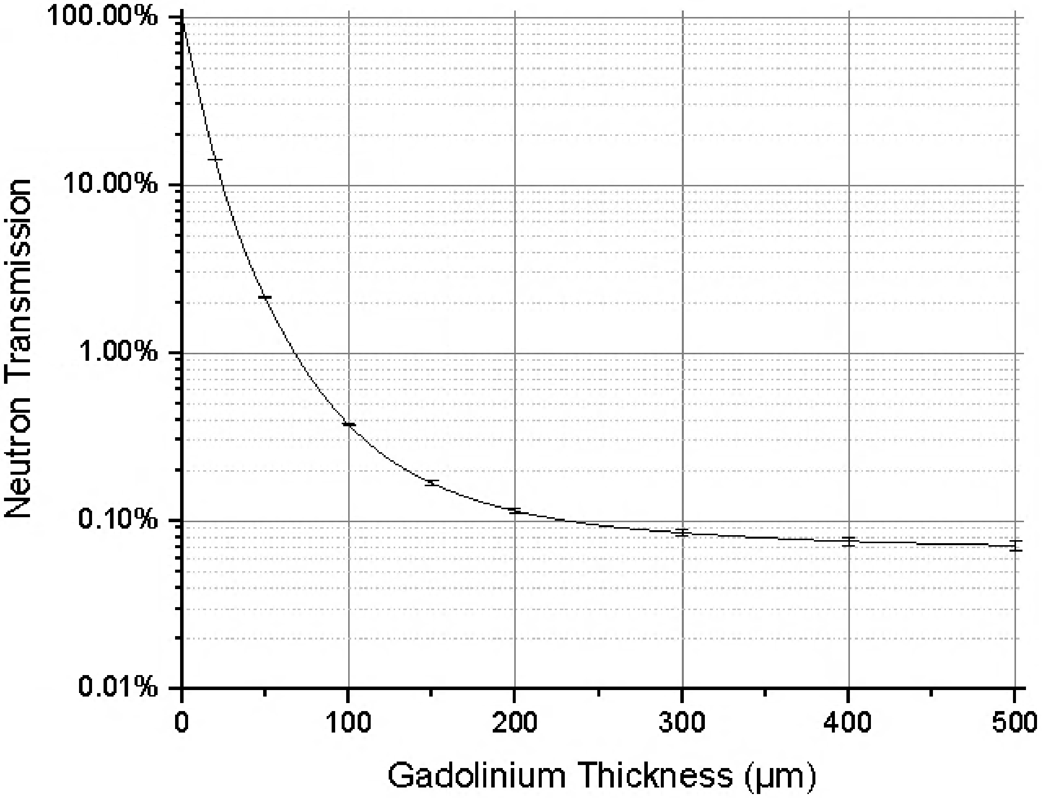

Figure 4.1 Percentage of neutrons transmitted through gadolinium foils of various thickness

4.2 MCNP Models of REMANI System

Three MCNP models have been constructed to evaluate the design of a REMANI system. To be noted, the 12-inch sapphire crystals were used as the beam filters in all the simulations.

Figure 4.2 shows the cross-section of a model to simulate the conventional neutron imaging facility, referred as *Model A*. The geometry specifications are the same as the model previously. All the essential components are included and labelled in the figure. The neutron sources were defined at the entrance of the beam port, uniformly emitted from a planar surface that is normal to the beamline. As stated in Section 3.1, the energy spectrum was shown in Figure 2.6 (a), which was obtained by the PULSTAR reactor core simulations.

The detection system was simulated by setting a Flux Image Radiograph (FIR) tally at the maximum length of the imaging beam, 6.5m away from the aperture. FIR tally is an array

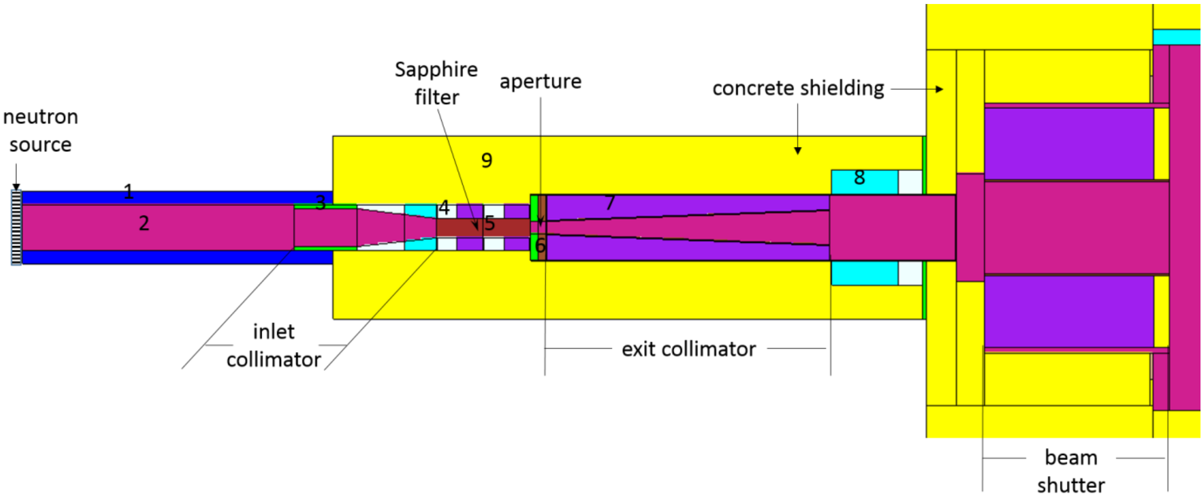

Figure 4.2 MCNP *Model A* for conventional neutron imaging beam. The various materials are: (1) water, (2) air, (3) aluminum, (4) lead, (5) sapphire, (6) Boral, (7) RX-277, (8) borated polyethylene, (9) concrete.

of point detectors. Each detector point represents one pixel of a flux image. The grid of the FIR tally was set to be the same as the pixel size of a detection system (X-5 Monte Carlo Team, 2003). A gaussian low pass filter was then applied to the flux images to represent the degrading effects from the detector unsharpness. Three detectors in the facility were suitable to be used in REMANI, including film system, imaging plate system and scintillator system. The properties are listed in Table 4.1. The pixel sizes were the smallest settings for the current systems. The resolutions were the best achievable ones that were measured from the experiments with the use of these pixel sizes. Detector unsharpness was estimated by subtracting in quadrature the sampling effects from the system resolutions. This values represent the limitation of the current detector system in conventional imaging. For simplicity's sake, the detector unsharpness was rounded into an integer multiple of the pixel size, which the FWHM of the low-pass filter was set to be. All the systems can be simulated in this model.

Table 4.1 The properties of the imaging detection systems.

Detection system	Size of detector	System Resoltuion	Pixel size	Detector unsharpness
Film	35 cm × 43 cm	33±3 µm	12.5 µm	~ 25 µm
Imaging Plate	20 cm × 25 cm	110±15 µm	25 µm	~ 100 µm
Scintillator	12.3 cm × 12.3 cm	245 ± 6 µm	60 µm	~ 240 µm

Two objects, a Siemens star and a sharp edge, were used in the model to investigate the resolution. Figure 4.3 shows the pattern of a Siemens star. It consists of 16 spokes that only meet at the center and beam outwards. But in the image, the spokes of the star appear to touch at certain distance from the center. The spacing between resolvable spokes indicates the

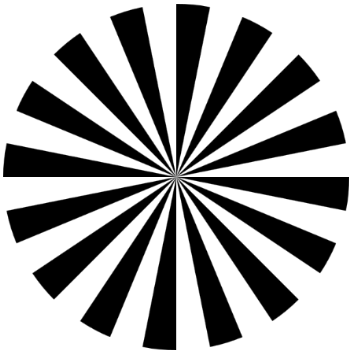

Figure 4.3 The Siemens star used as an object in the MCNP model

resolution of the system. The sharp edge was one side of a rectangular opening on a piece of foil. It was used to measure the edge spread function. Both objects were made out of 500 µm-thick gadolinium, and were placed 0.1 cm away from the detector, which is the thickness of the aluminum substrate in the scintillator screen.

The second MCNP model, referred as *Model B*, was built to examine the resolution for REMANI system. As shown in Figure 4.4, it is simplified compare to previous ones, in order to enhance calculation speed. First of all, the neutron sources were moved from the beam entrance to the aperture location. The energy and direction distributions used for the source were the ones shown in Figure 4.5 (a) and Figure 4.5 (b), which were calculated with *model A*. The neutron sources were composed of multiple circular surface sources, each of which simulated one pinhole on the mask. The pattern of the mask was generated based on 47×47 URA. In *model B*, only the components after the aperture (current neutron sources) were retained. The same Siemens star and the rectangular opening on gadolinium foil were used as the objects. Since the beam divergence at the aperture plane θ is about 2.35°, the mask-to-object distance was set to be 120 cm to obtain the maximal field of view. The detection systems

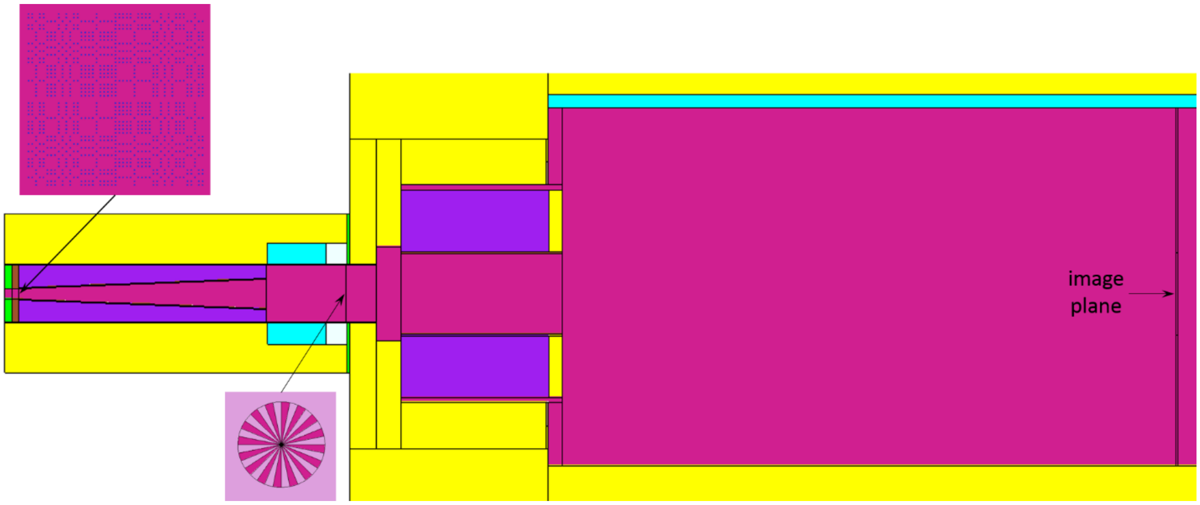

Figure 4.4 MCNP *model B* to evaluate resolution for the REMANI system

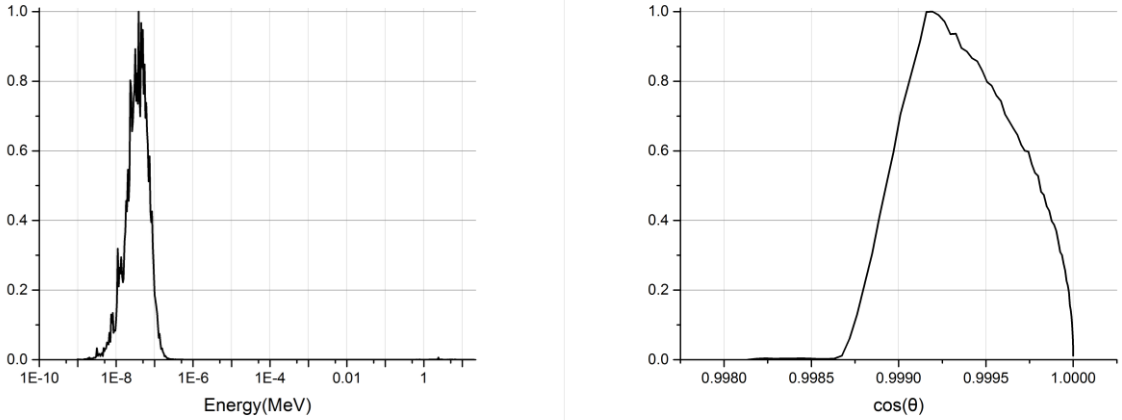

(a) (b)

Figure 4.5 (a) The energy distribution and (b) the direction distribution of the neutron sources at the aperture location

were the same as in *Model A*, which was a low-pass gaussian filter applied to the output of an FIR tally.

Another MCNP model is shown in Figure 4.6, referred as *Model C*. It was used to study the effects of noise transmitted through the opaque area of the mask. The geometry and

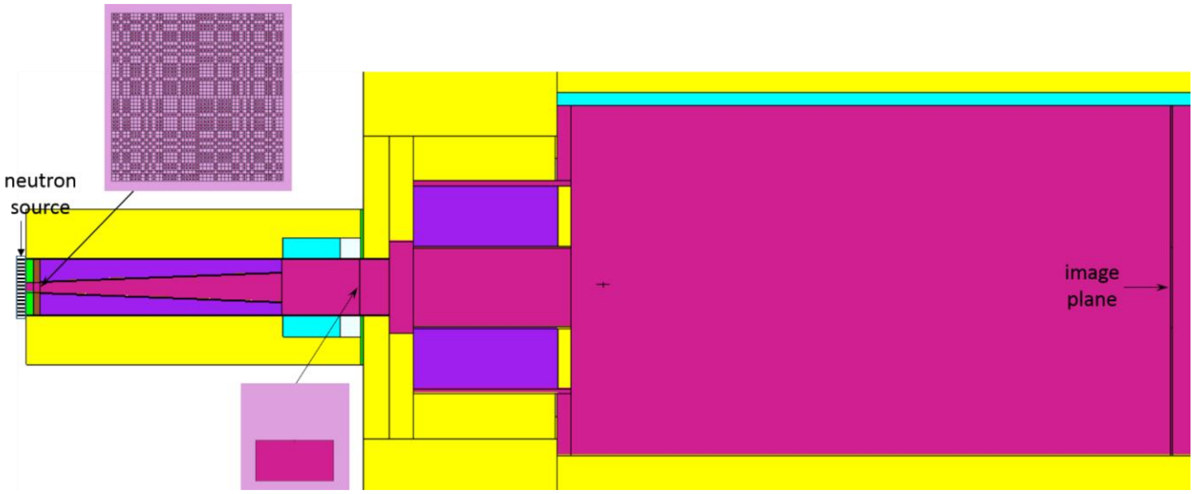

Figure 4.6 MCNP *model C* to study noise effects for REMANI system

the tallies were set up in the same way as in *Model B*, with the only exception that the aperture was covered by a 200 µm-thick gadolinium coded mask. The mask pattern was still 47×47 URA. The neutron sources were emitted uniformly from a planar surface in front of the mask. The object was a rectangular opening on gadolinium foil.

4.3 Results of Simulations

The results of all the simulations are presented in this section. First, the simulation results on conventional imaging were compared to the experimental data. Then, the relationship between resolution and several design parameters were thoroughly studied for the REMANI system. Finally, the effects of transmission noise on the system performances were evaluated.

4.3.1 Results of Conventional Neutron Imaging

Model A simulated conventional neutron imaging systems. By comparing the resolutions obtained from the simulated images to the experimental measurements, one can verify the validity and accuracy of the simulation models.

Figure 4.7 (a) – (c) show the simulation results of imaging a Siemens star using film system, imaging plate system and scintillator system, respectively. These images give a sense of system resolution directly. The ones on the left are the simulated images and the red dashed line outlines the smallest radius where all the 16 spokes can be discernable. The ones on the right shows pixel values at the red lines in 3D. The corresponding resolutions measured from these images are 35 µm, 105 µm and 265 µm. To be noted, in Figure 4.7 (a) and (b), the diameter of the star was 1000 µm, while in Figure 4.7 (c), a Siemens star with a diameter of 2000 µm was used. This is because a diameter of 1000 µm is corresponding to a line pair of 200 µm, which is smaller than the scintillator system resolution. This is confirmed in Figure 4.7 (d), where the 1000 µm-diameter Siemens star was imaged by the scintillator system. The images of adjacent spokes blended together thus contained no detailed information.

The simulation results of imaging a gadolinium edge and the corresponding analysis are shown in Figure 4.8. The FWHM's of the LSF's shown on the left are 25 µm, 100 µm and 241 µm for the film. The resolutions corresponding to the 10% cut-off frequencies of MTF's are 30.6 µm, 125 µm and 298 µm.

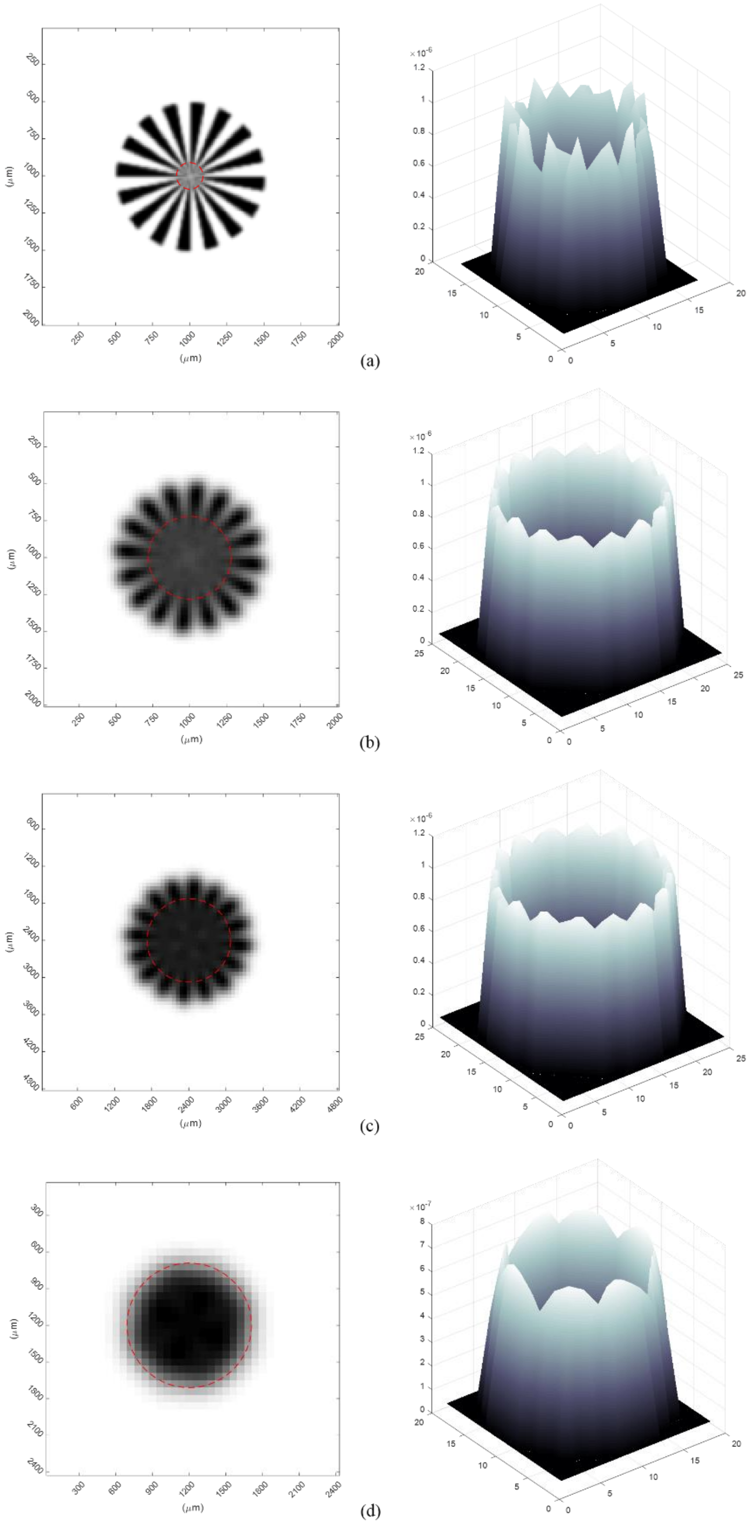

Figure 4.7 Simulated results of imaging a Siemens star (a) with a diameter of 1000 µm using film system; (b) with a diameter of 1000 µm using imaging plate system; (c) with a diameter of 2000 µm using scintillator system; (d) with a diameter of 1000 µm using scintillator system.

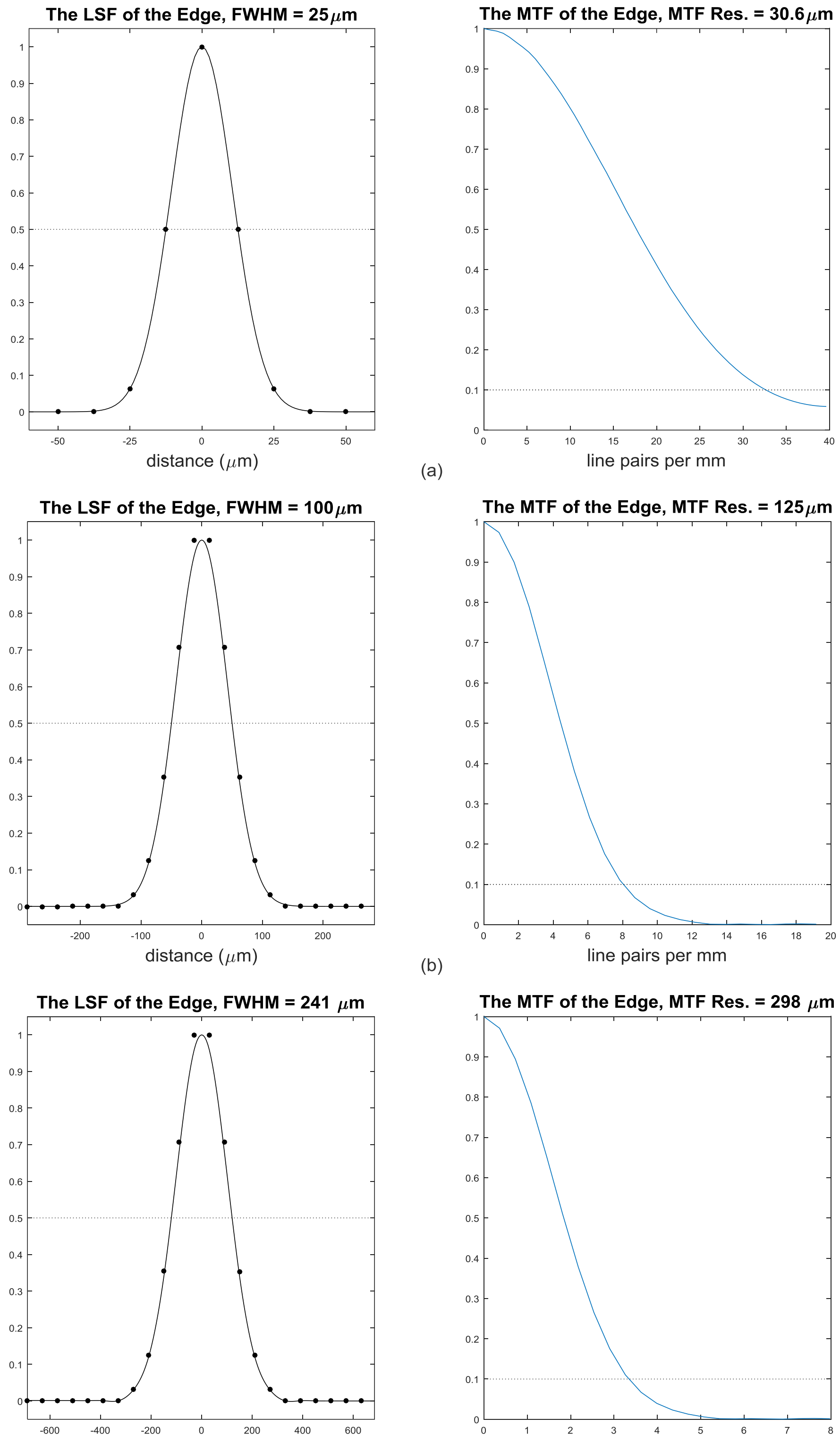

(a)

(b)

(c)

Figure 4.8 The simulated results of imaging a gadolinium edge for (a) film system, (b) imaging plate system and (c) scintillator system.

In summary, the system resolutions obtained from simulations with *Model A* are listed in Table 4.2. Also are listed the experiment results, which were obtained from the FWHM of the LSF as shown in Section 2.4.2.3. They are in good agreement with the simulations. The LSF results tends to be smaller, because in simulations the detection system first sampled the neutron flux map then introduced a blurriness by convolution; while in practice it is the opposite way. The blurriness was assumed to have a gaussian distribution, thus the 10% cut-off frequency of the MTF is slightly larger than the FWHM of the LSF. From the measurements, the LSF's of the imaging plate system and the scintillator system are closer to Lorentizan distribution, while the one of the film system has a gaussian shape.

Table 4.2 The system resolutions obtained by simulating different imaging detection systems with MCNP *Model A*

Detection System	System resolution			
	Estimated from star image	FWHM of LSF	MTF analysis	Experimental Result
Film	35 μm	25 μm	31 μm	33 μm
Imaging Plate	110 μm	100 μm	125 μm	110 μm
Scintillator	265 μm	241 μm	298 μm	245 μm

4.3.2 Results on Resolution of a REMANI System

Model B was constructed to study the resolution of the coded system. The mask pattern used in the model was a 47×47 URA. Not all the zero elements have at least one horizontal or vertical neighbor, thus it is not a self-supported array (Accorsi, 2001b). To realize the design, the opaque areas have to be connected. The mask pattern can be viewed as a square grid and every element (zero or one) is distributed at the center of one grid. At the locations of pinholes that correspond to ones, as long as the hole has a size smaller than the size of the grid, it can be any shape. For the sake of easy machining, round holes were selected. Simulations has been done to explore the dependence of the system resolution upon the size of the pinhole, the size of the grid and the magnification factor.

4.3.2.1 Effects of the Size of the Grid on Resolution

The effect of the size of the grid on system resolution was investigated with a model of film system. An FIR tally was calculated with a pixel size of 12.5 µm. A gaussian filter with FWHM of 25 µm was applied to the tally output to obtain simulated images. The objects were the Siemens star with a diameter of 150 µm and a 150 µm × 300 µm rectangular opening on the gadolinium foil. The object-to-image distance was set to be 300 cm, thus the magnification factor *m* was equal to 3.5. The diameter of the pinhole on the mask was 12 µm. Four cases have been tested. In each case, the grid size of the mask was 15 µm, 20 µm, 30 µm and 40 µm, respectively. Figure 4.9 (a) – (d) plot the distributions of neutron source of four cases in the same scale. The signal strength was the same in all the cases due to the same pinhole sizes. The larger the grid size, the more sparsely the pinholes distributed, thus the larger the entire mask was.

The reconstructed results are shown in Figure 4.10 (a) – (d). The resolution is very close in all the cases, 9.4 µm to 9.5 µm measured from LSF and 11.6 µm to 11.8 µm measured from MTF. Therefore, the system resolution is independent to the spacing between the pinholes in the mask.

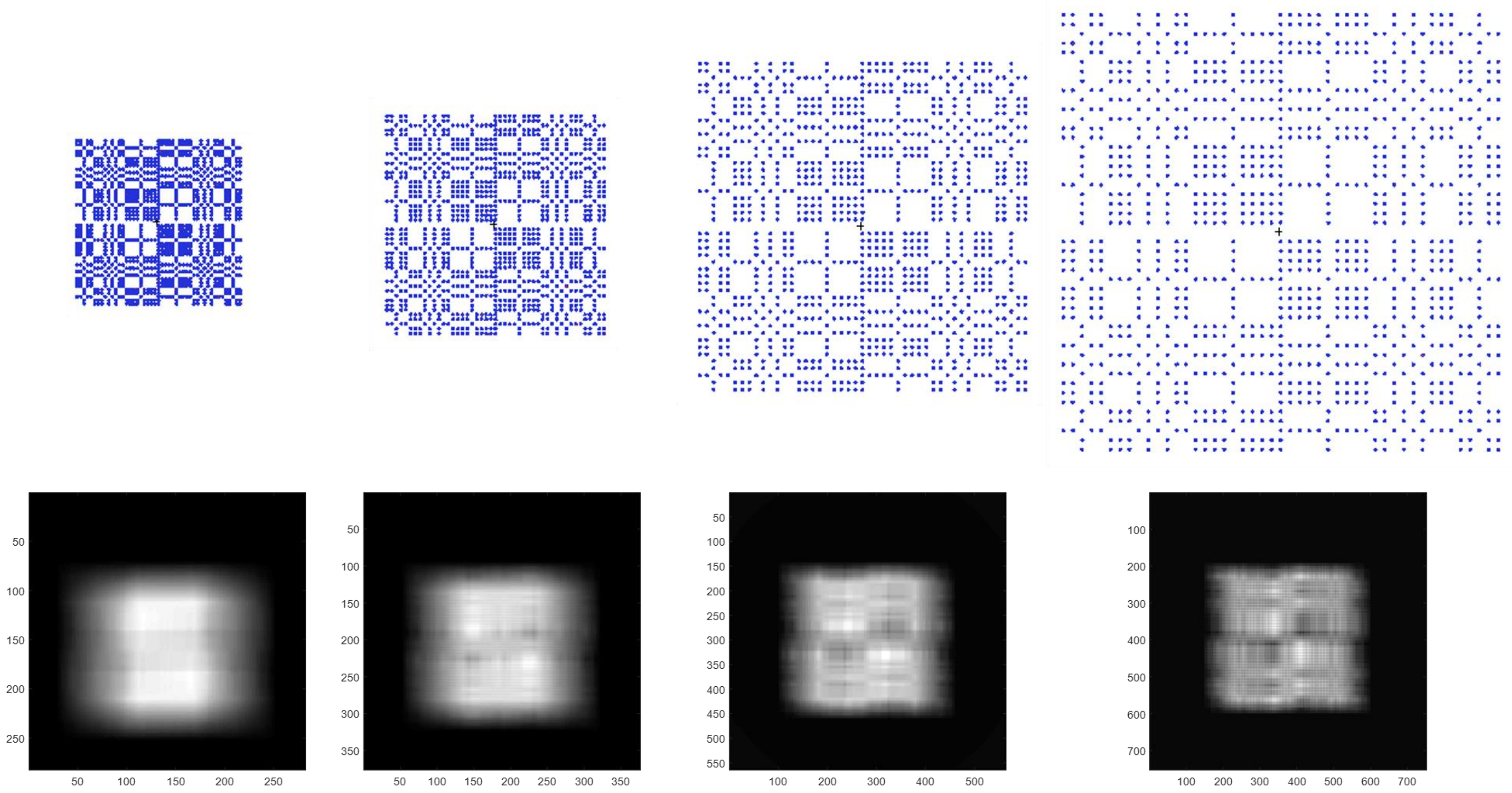

(a) (b) (c) (d)

Figure 4.9 The distributions of the neutron sources with the pinhole diameter of 12 μm and the grid size of (a) 15 μm, (b) 20 μm, (c) 30 μm and (d) 40 μm.

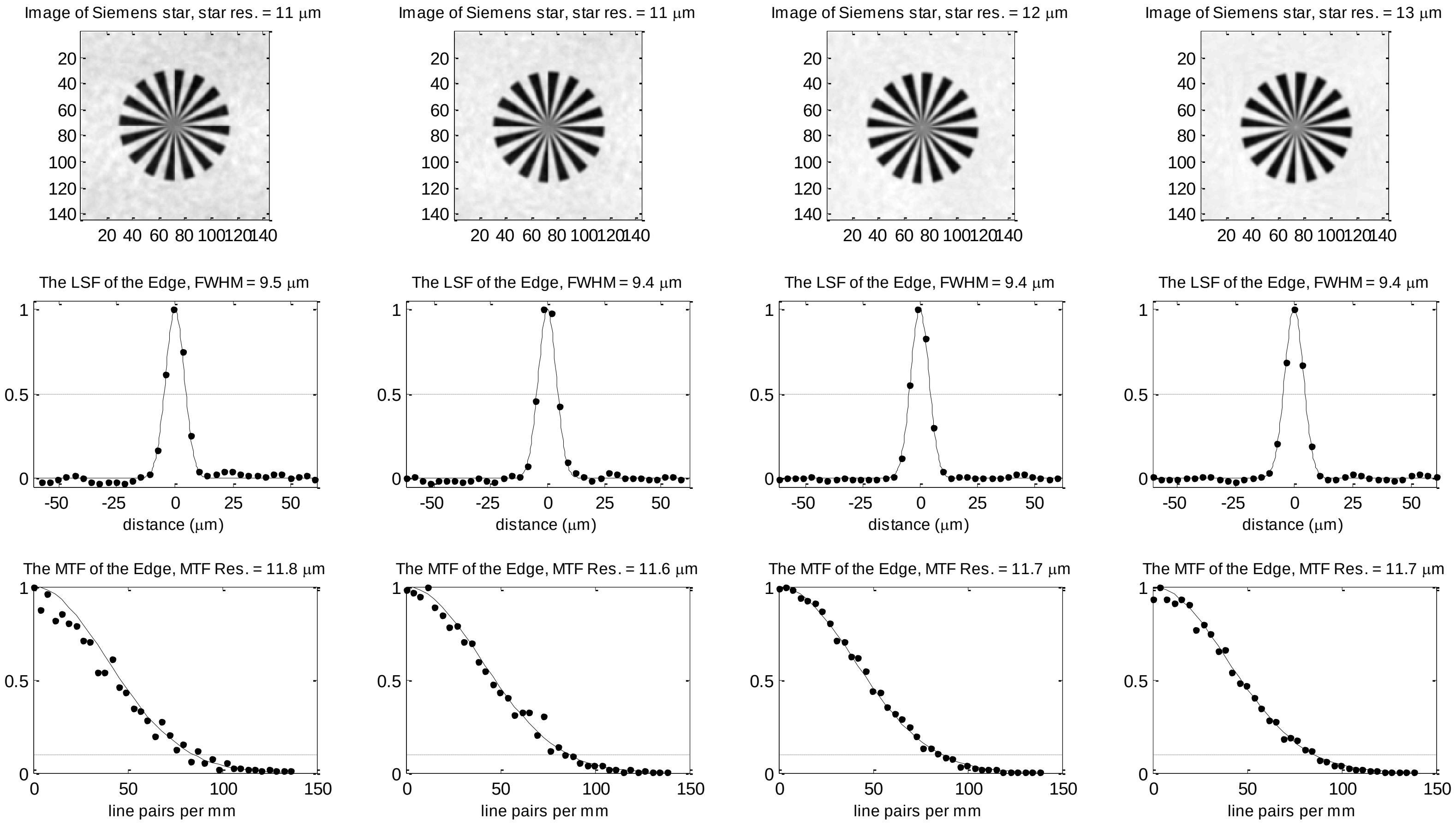

(a) (b) (c) (d)

Figure 4.10 The reconstruction results with a mask hole size of 12 μm and different grid size: (a) 15 μm, (b) 20 μm, (c) 30 μm, (d) 40 μm.

4.3.2.2 Effects of the Size of the Pinhole on Resolution

The next observation was the effect of mask hole sizes on resolution. The parameters of the tally, the objects and the geometric arrangement remained the same. Images were taken by FIR tallies with pixel size of 12.5 µm, and additional Gaussian blurriness with FWHM of 25 µm. The objects were the Siemens star with a diameter of 150 µm and a 150 µm × 300 µm rectangular opening on the gadolinium foil. The magnification factor *m* was 3.5.

The diameters of the holes on the mask were set to be 8 µm, 12 µm, 16 µm, and 20 µm respectively. The corresponding grid sizes were set to be 12 µm, 15 µm, 20 µm, and 25 µm, which are 1.25 times as large as the pinhole diameters. In Figure 4.11, the top row shows the distribution of the neutron sources in each case and the bottom row is the simulated images. Figure 4.12 shows all the reconstructed results obtained from the correlation method. The resolutions measured from the LSF are 10.4 µm, 11.8 µm, 13.8 µm and 15.4 µm. This agrees well with the expectation. The resolution calculated based on Equation (3.36) are 9.2 µm, 11.2 µm, 13.5 µm, 15.9 µm. It can be seen that the accuracy of this model increases with the size of the hole. This is because for the smaller holes, the noise introduced by reconstruction distorts the details.

4.3.2.3 Resolution at Different Magnification Factors

As opposed to conventional neutron imaging system where the object-to-image distance is set to be as small as possible to reduce the geometric unsharpness, the image plane is moved away from the object in order to acquire a magnified image in a REMANI system. The relationship between the resolution and the magnification factor is essential in the design of a coded system.

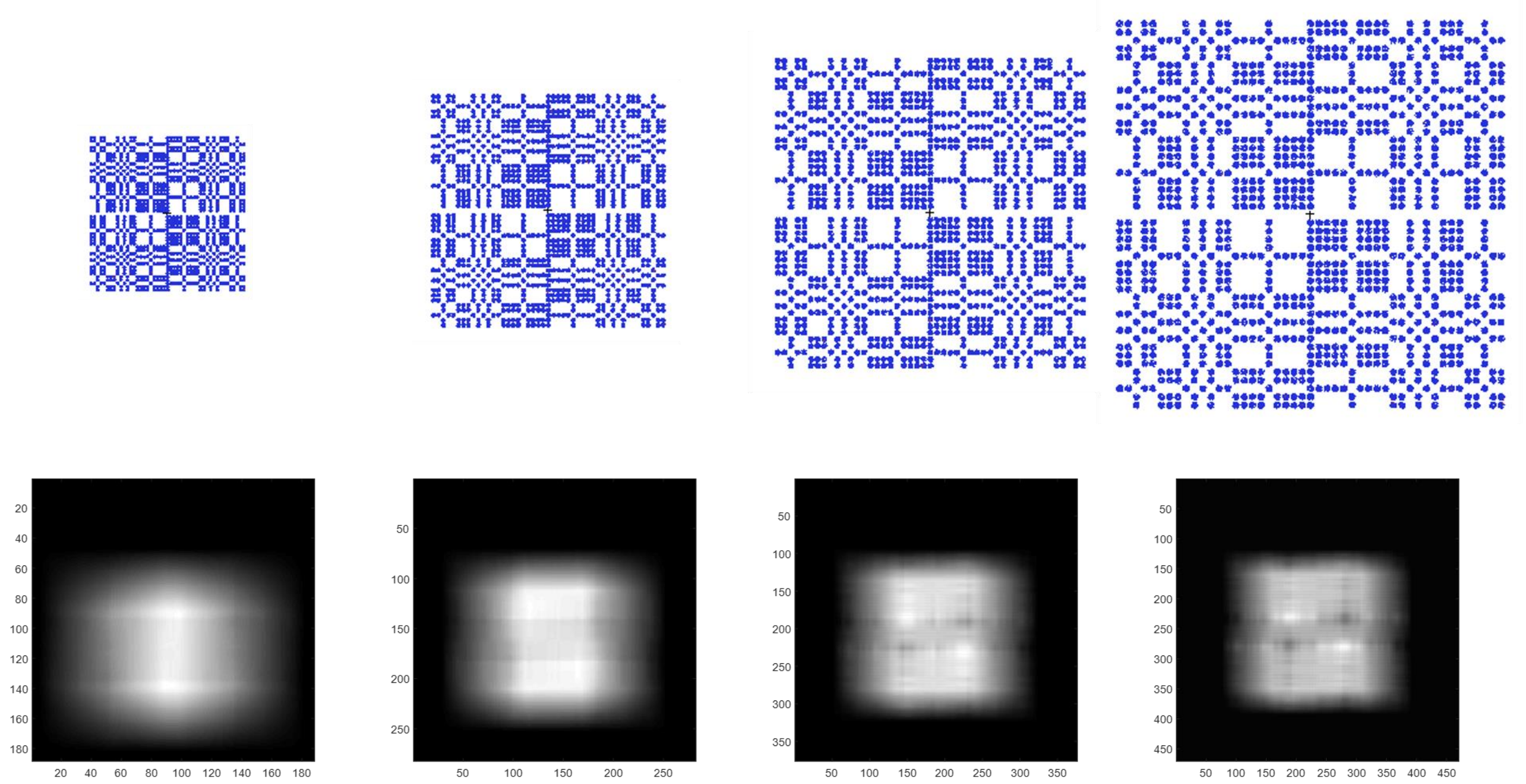

(a) (b) (c) (d)

Figure 4.11 The neutron source distribution in the MCNP simulations (top); and the simulated images (bottom).

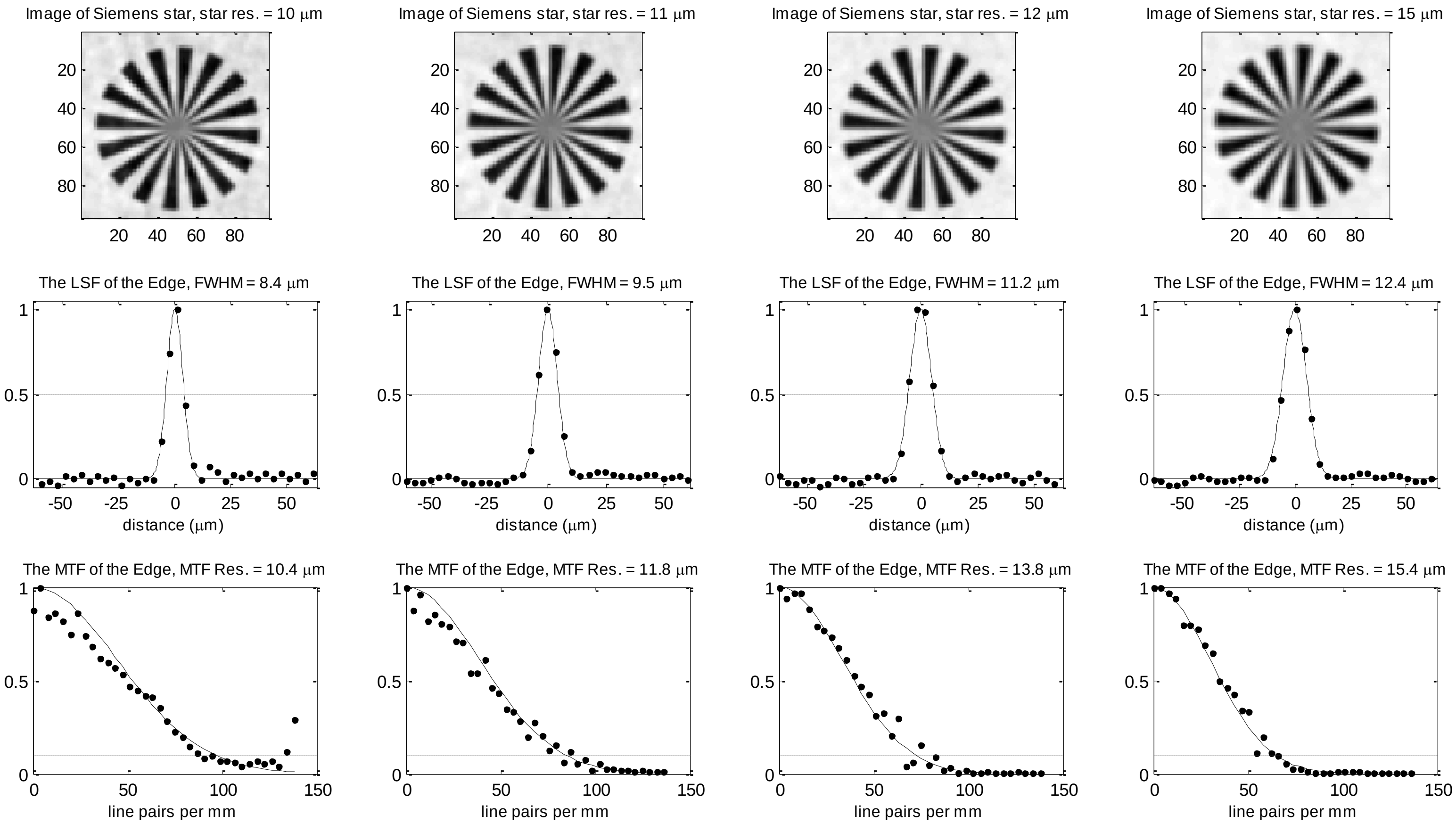

(a) (b) (c) (d)

Figure 4.12 The reconstructed results with different sizes of holes on the mask: (a) 8 µm, (b) 12 µm, (c) 16 µm, (d) 20 µm.

In the following model, the diameter of the holes in the mask was 12 µm and the size of the grid was 15 µm. The Siemens star and the rectangular opening was placed 120 cm away from the mask as objects. The object-to-image distances were set to be 200 cm, 300 cm, and 400 cm. Thus the magnification factors were 2.67, 3.50, and 4.33, accordingly. The correlation reconstructed results are shown in Figure 4.13 (b) – (d). As a comparison, Figure 4.13 (a) shows the images of the same Siemens star and the same edge taken with a conventional set up where $m \approx 1$. In order to facilitate comparison, the images of the star are plotted in different scales so that the star appears in the same size. The resolutions measured from the MTF analysis were 14.1 µm, 11.8 µm and 10.7 µm, corresponding to the expected values of 12.0 µm, 11.1 µm and 10.8 µm. It can be seen that magnification of 3.5 gives an evident improvement over magnification of 2.67. However, the system resolution is very stable for larger m, which means that the size of mask pinhole becomes the dominant factor.

The imaging plate system is also investigated by the simulations. The tally pixel size was 25 µm and the FWHM of the additional Gaussian filter was 100 µm. The object was a rectangular opening with a size of 750 µm × 1500 µm on the gadolinium foil. The diameter of the holes and the spacing between the holes were 50 µm and 60 µm. Figure 4.14 shows the simulated imaging at magnification of 1 and reconstructed results at magnification of 2.67, 3.50, and 4.33. It can be seen clearly the image of the edge gets sharper with larger magnification. The resolutions were measured to be 53.2 µm, 45.9 µm and 42.2 µm from MTF analysis, while the expectation values were 48.8 µm, 45.7 µm and 44.8 µm.

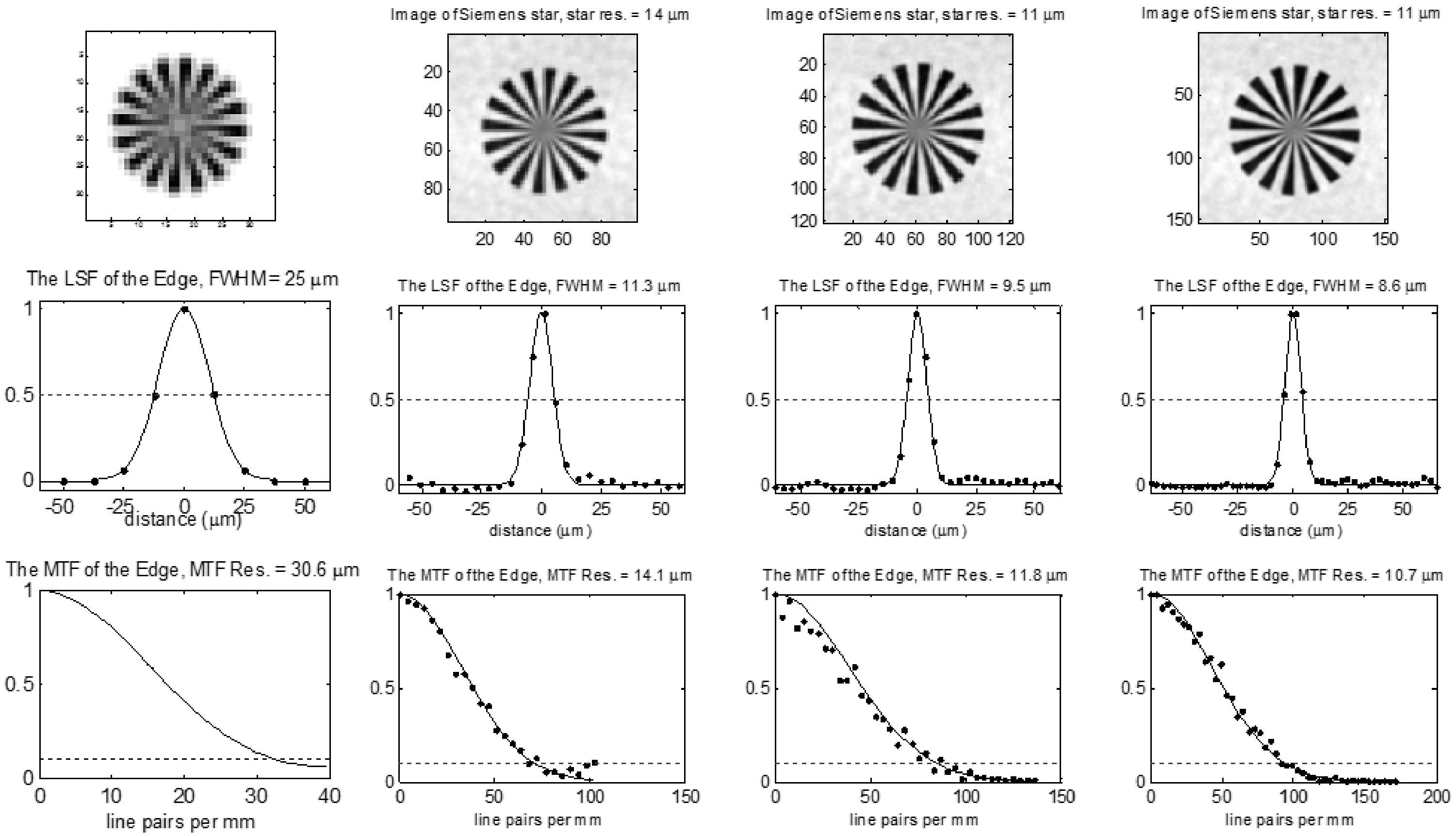

(a) (b) (c) (d)

Figure 4.13 The reconstructed results with different magnification factor: (a) 1, (b) 2.67, (c) 3.50, (d) 4.33.

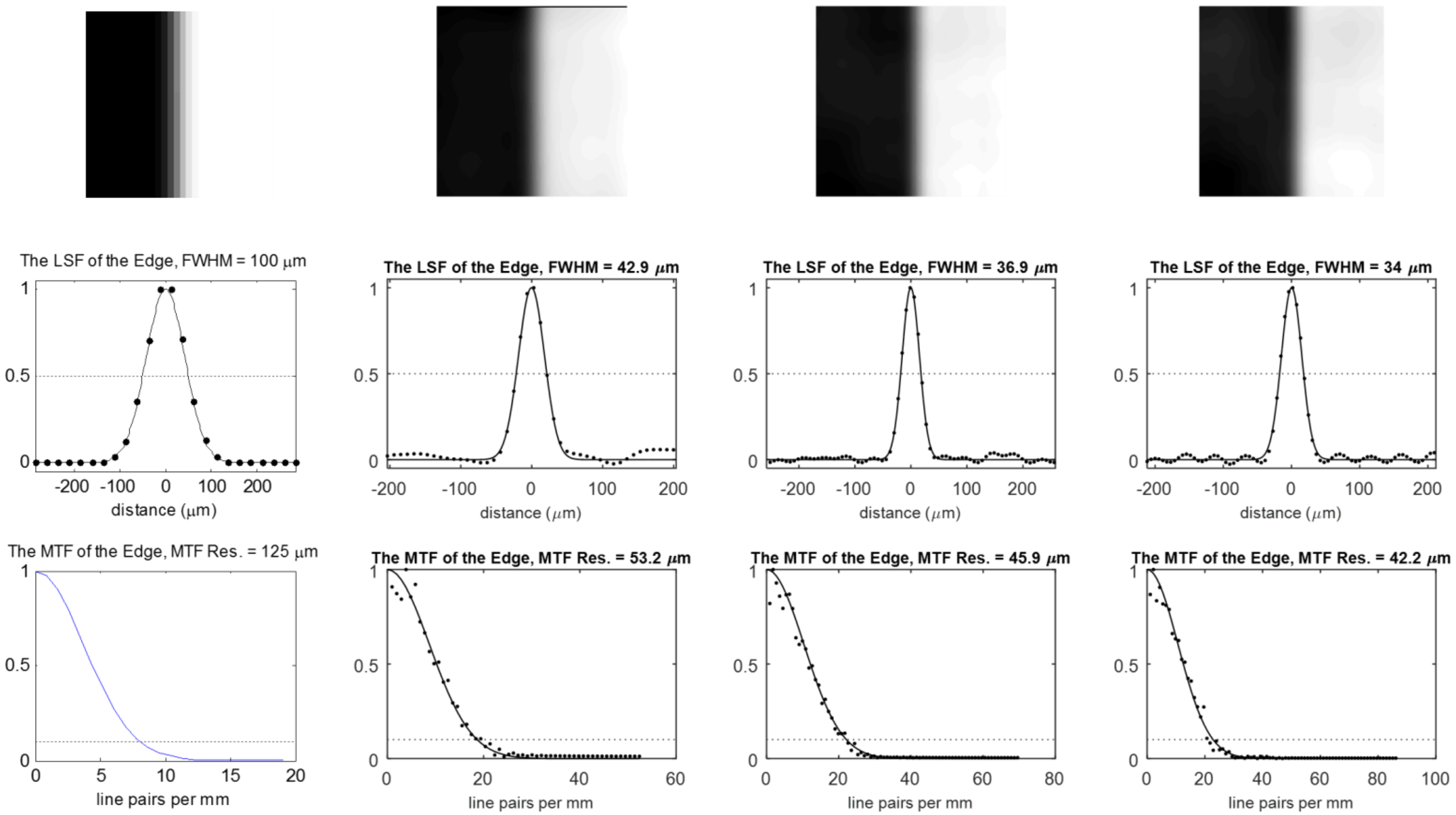

(a) (b) (c) (d)

Figure 4.14 The reconstructed result for imaging plate with different magnification factor: (a) 1, (b) 2.67, (c) 3.50, and (d) 4.33

4.3.3 Results on Noise of a REMANI System

Noise is one of the essential components in evaluating image quality, especially for a REMANI system, since it is very sensitive to noise. One of the most important parameters in system design influencing the noise performance is the ratio between the hole size and the grid size. If the diameter of the pinhole is fixed, larger the grid size is, more sparsely are the pinholes distributed on the mask, and smaller is the open fraction of the mask. As a result, the intensity of the signal containing information of the object is reduced. Moreover, larger the opaque area on the mask tends to introduce higher transmission noise on the image. The film system, the imaging plate system and the scintillator system were all simulated with Model C.

For the film system, a FIR tally was set at the magnification factor of 3.5, with a pixel size of 12.5 µm, and then blurred with a Gaussian filter with FWHM of 25 µm. In the mask, the holes with diameter of 12 µm were distributed on the grids with sizes of 15 µm, 30 µm and 40 µm respectively. The Siemens star and the rectangular opening were both used as objects. Figure 4.15 shows the reconstructed star images, the LSF's and MTF's measured from the reconstructed edge images. The system resolution was expected to be 11.2 µm in such set-ups. It was measured from the simulated images as 11.6 µm, 11.4 µm and 11.7 µm. The signal-noise-ratio are different in these cases and the results are listed in Table 4.3.

Table 4.3. The simulated results for film system with different open fractions on the mask

Grid size	Open fraction	MTF resolution	Noise level in recorded image	SNR in reconstructed image
15 µm	25.1%	11.6 µm	12.3%	33
30 µm	6.3%	11.4 µm	62.7%	26
40 µm	3.5%	11.7 µm	81.0%	24

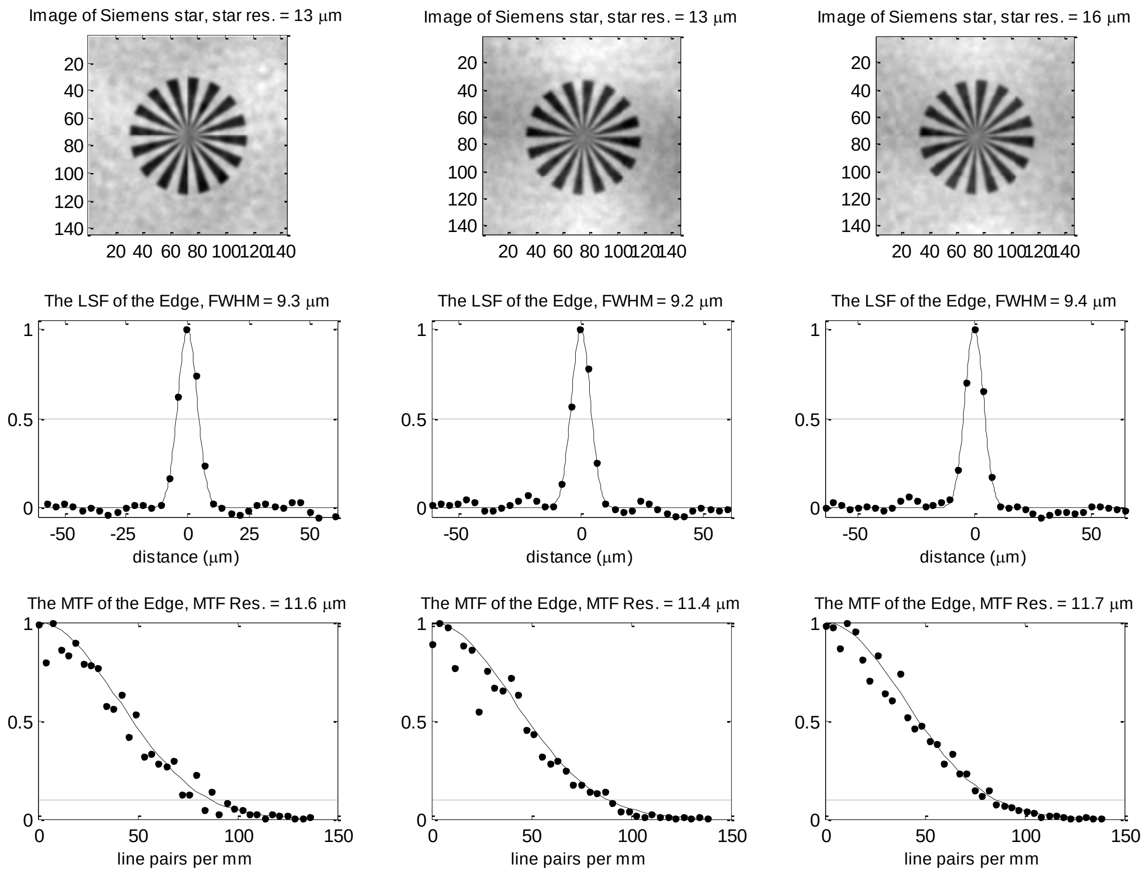

(a) (b) (c)

Figure 4.15 The reconstructed result at the magnification factor of 3.5, with 12 µm- diameter mask pinholes distributed on the grid sizes of (a) 15 µm, (b) 30 µm and (c) 40 µm respectively

The noise level in the recorded image was obtained as the ratio of the maximum value and the minimum value of the tally output. The signal-to-noise ratio is calculated as the mean over the standard deviation of the reconstructed image of the rectangular opening.

For the imaging plate system, a FIR tally was set at the magnification factor of 3.5, with a pixel size of 25 µm, and then blurred with a Gaussian filter with FWHM of 100 µm. In the mask, the holes with diameter of 50 µm were distributed on the grids with sizes of 60 µm, 80 µm and 100 µm respectively. The rectangular opening on a gadolinium foil was used as an object. The reconstructed images and the corresponding LSF's and MTF's are shown in Figure 4.16. Table 4.4 lists the measured resolutions and SNR's with different open fractions. The SNR in reconstructed image decrease with the open fraction of the mask. The lowest SNR is 35.6, obtained with the smallest open fraction of 9.8%. However, this is still greater than the highest one in film simulation (33.2 with open fraction of 25.1%). This is because the size of the pixel used to simulate imaging plate is twice as large as the one used for film simulation. More neutrons have been registered in the tally thus improving the SNR performance.

Table 4.4. The simulated result for the imaging plate system with different open fractions on the mask

Grid size	Open fraction	MTF resolution	Noise level in recorded image	SNR in reconstructed image
60 μm	27.2%	46.1 μm	6.9%	49
80 μm	15.3%	46.8 μm	17.1%	42
100 μm	9.8%	46.6 μm	31.9%	36

4.4 Conclusion and Mask Design

The system resolution and noise performance of a REMANI imaging system has been estimated with MCNP simulations. The results agree well with the expectations derived from the mathematical models in Chapter 2. It was found that the system resolution can be significantly improved over the limit set by the inherent resolution of the detector. The resolution is insensitive to the grid size of the mask, but is largely dependent on the size of the hole of the mask and magnification factor.

Four masks have been proposed with the use of the imaging systems that are currently available and suitable for this performance, including the film system, the imaging plate system

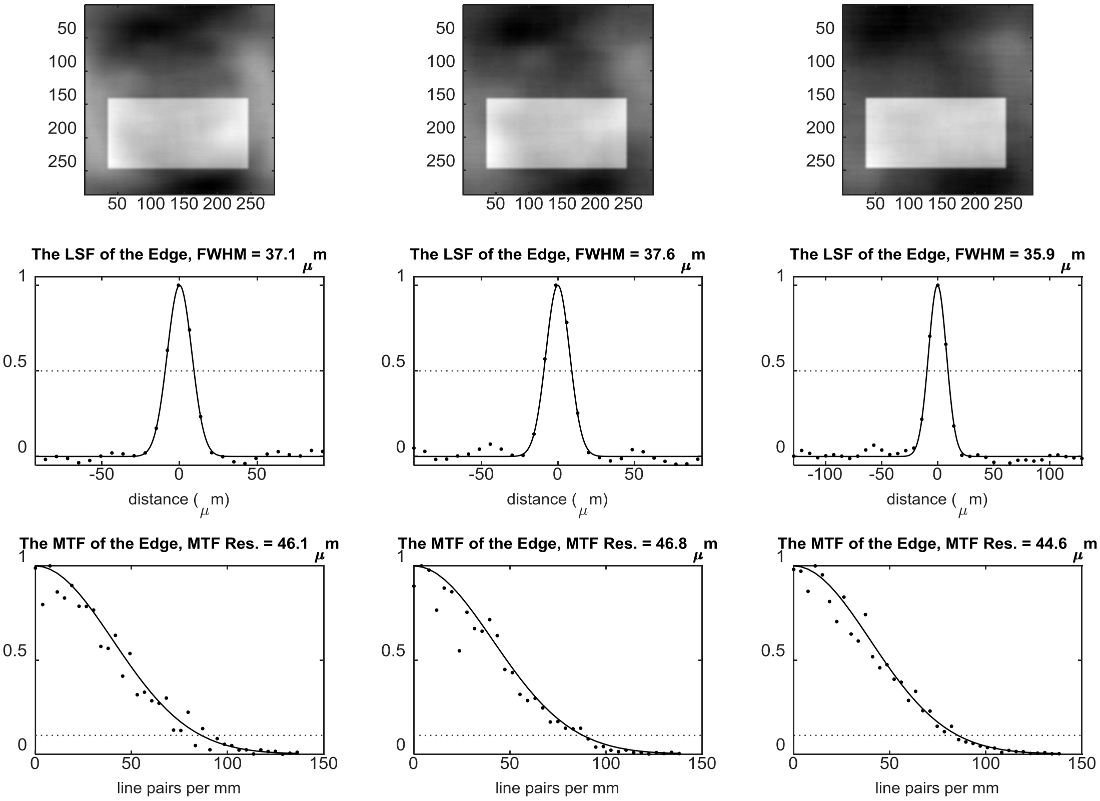

Figure 4.16 The reconstructed result with different open fractions

and the scintillator system. The configurations of the proposed masks are summarized in Table 4.5.

Based on the experimental results, the optimized resolutions of the film system and the imaging plate system were found to be in the order of 30 µm, 110 µm. For the real time system using scintillator screen, the resolutions were measured to be 250 µm and 300 µm when the pixel sizes were 60 µm and 100 µm respectively. The diameters of the pinholes in the proposed masks were chosen to be smaller than these values. If the mask can be successfully fabricated and implemented, the expected system resolutions can be improved to around 10 µm, 50 µm 100 µm and 200 µm with the same settings on the detection systems.

Table 4.5 The mask design for different imaging detection systems

Imaging System	Film	Imaging Plate	Scintillator	
Measured resolution in conventional setup	33±3 µm	110±15 µm	245 ± 6 µm	304 ± 13 µm
Pixel size of the detector	16 µm	25 µm	60 µm	100 µm
The thickness of the mask	200 µm	200 µm	450 µm	450 µm
The diameter of the mask hole	12 µm	50 µm	100 µm	200 µm
The grid size	40 µm	100 µm	200 µm	400 µm
The size of MURA pattern	887×887	362×362	178×178	94×94
The size of the mask	3.55 cm	3.62 cm	3.56 cm	3.76 cm
Number of holes	393,384	65,520	15,840	4416
Open fraction over 4 cm aperture	2.85%	8.04%	7.80%	8.67%
Expected Resolution (mag = 4)	12 µm	46 µm	107 µm	185 µm
Field of View	2.8 cm	2.3 cm	2.7 cm	2.82 cm

Chapter 5

Experimental Demonstration of REMANI System

The design of REMANI system has been implemented at the Neuron Imaging Facility (NIF) at the PULSTAR reactor (the initial work can be found in Xiao, 2010). This chapter recorded a series of exercises that aim to demonstrate the principles of REMANI system and the experimental results. Three masks and several objects have been fabricated and have been used with different detection systems. The characteristics of the reconstructed images have been analyzed.

5.1 Collimator Modification

The collimation system of a REMANI system is different from the one of the conventional system. Fortunately, the modular design of the NIF beamline allows modifications to be made on the collimator.

Figure 5.1 (a) is the design drawing of the conventional collimator that is currently used in the NIF beamline. Figure 5.1 (b) and (c) show the pictures of the front side (the reactor side) and the back side (the shutter side).

A coded mask was installed on the front side of the collimator. An aluminum plate as shown in Figure 5.2 (a) was fabricated and fitted to the outer tube of the collimator. In the center of the plate, there was a 5 cm × 5 cm shallow recess that was carefully aligned with the side plates of the collimator. A coded mask can be placed in the recess and fixed into place by bolting a cover plate as shown in Figure 5.2 (b). Figure 5.2 (c) is a picture of a coded mask mounted on top of the collimator.

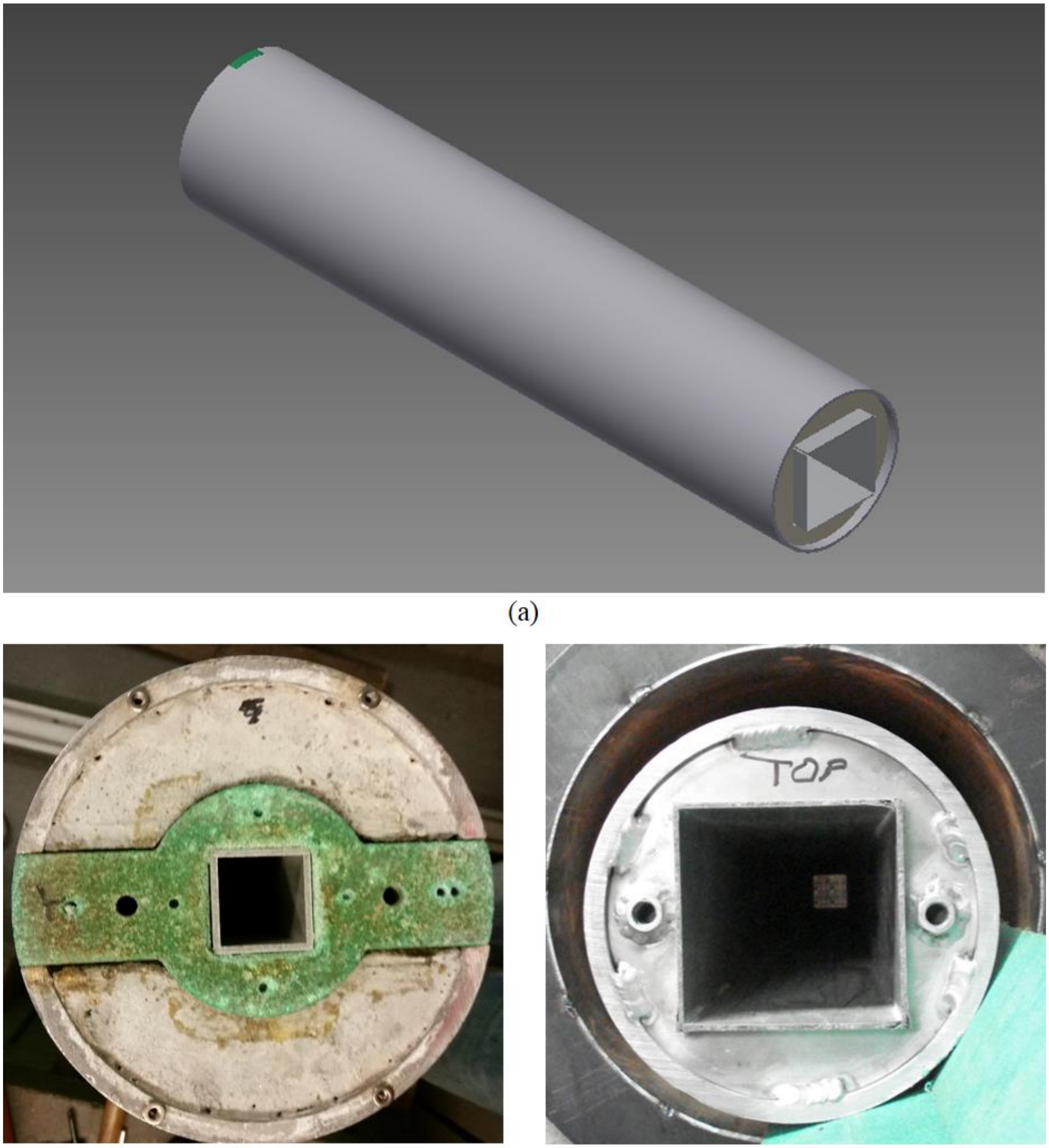

(a)

(b)

(c)

Figure 5.1 (a) The design drawing, (b) a picture of the front side and (c) a picture of the back side of the conventional collimator in the NIF beamline.

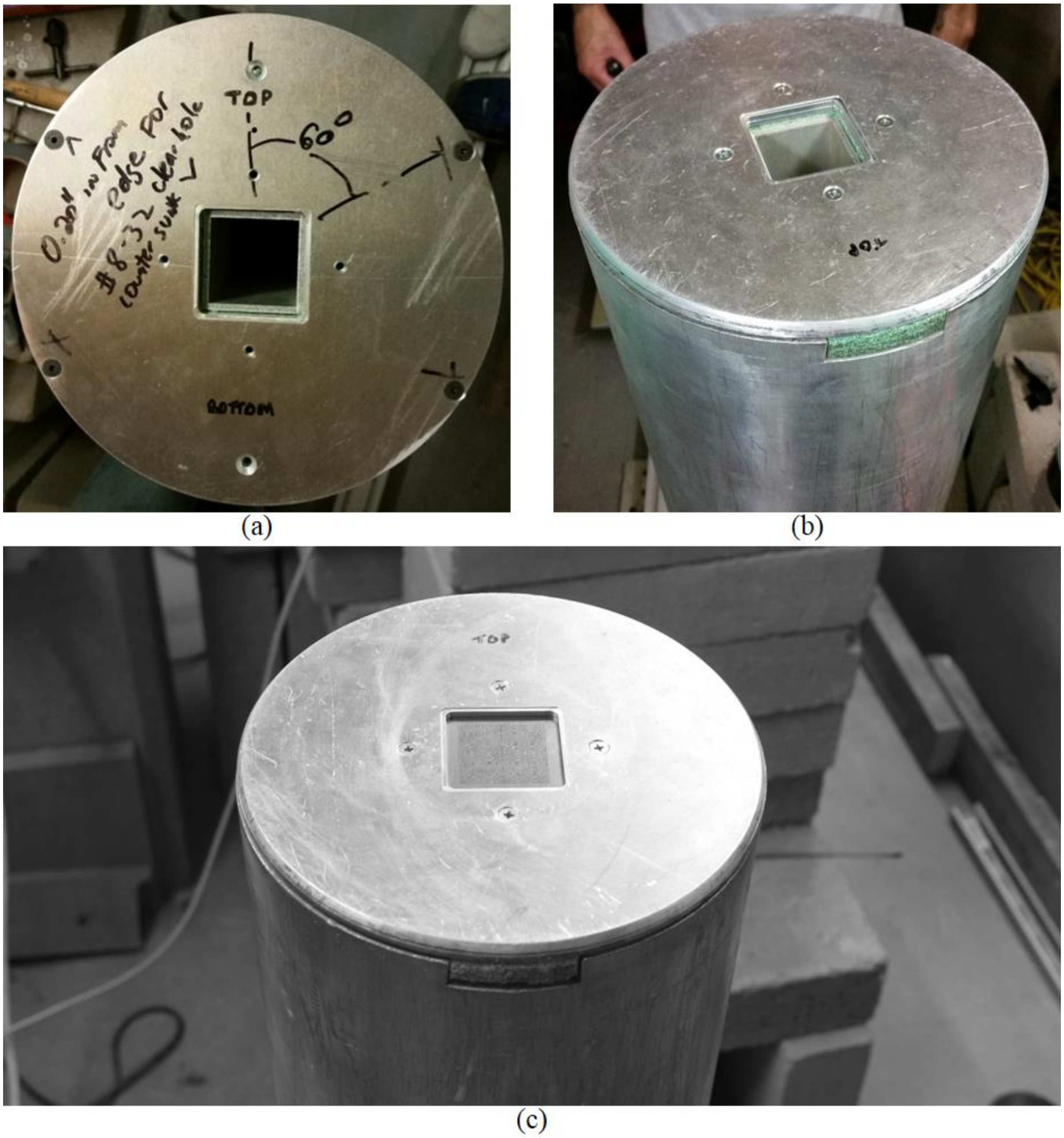

Figure 5.2 (a) An aluminum plate and (b) its cover to install the coded mask on the front side of the collimator. (c) A picture of a mounted coded mask with the use of this plate.

To demonstrate resolution enhancement effects with the use of REMANI system, gadolinium foils with different patterns was chosen to be used as the objects. In order to take magnified images at as many locations as possible, the distance between the mask and the object was set to be 120 cm. It was required that the object was placed before the beam shutter. Therefore, an extension tube was attached to the end of the collimator in order to hold the object at the exact location.

The extension tube consisted of two parts as shown in Figure 5.3. The left part was mounted on the collimator at the beginning of the experiment and cannot be changed during the measurements. The right part was used to hold the objects which can be removed and changeable between each shot.

Figure 5.4 shows the assembly of the fixed part of the extension tube in detail. It was made out of borated polyethylene plates, each with thickness of 1 inch. The first piece had an

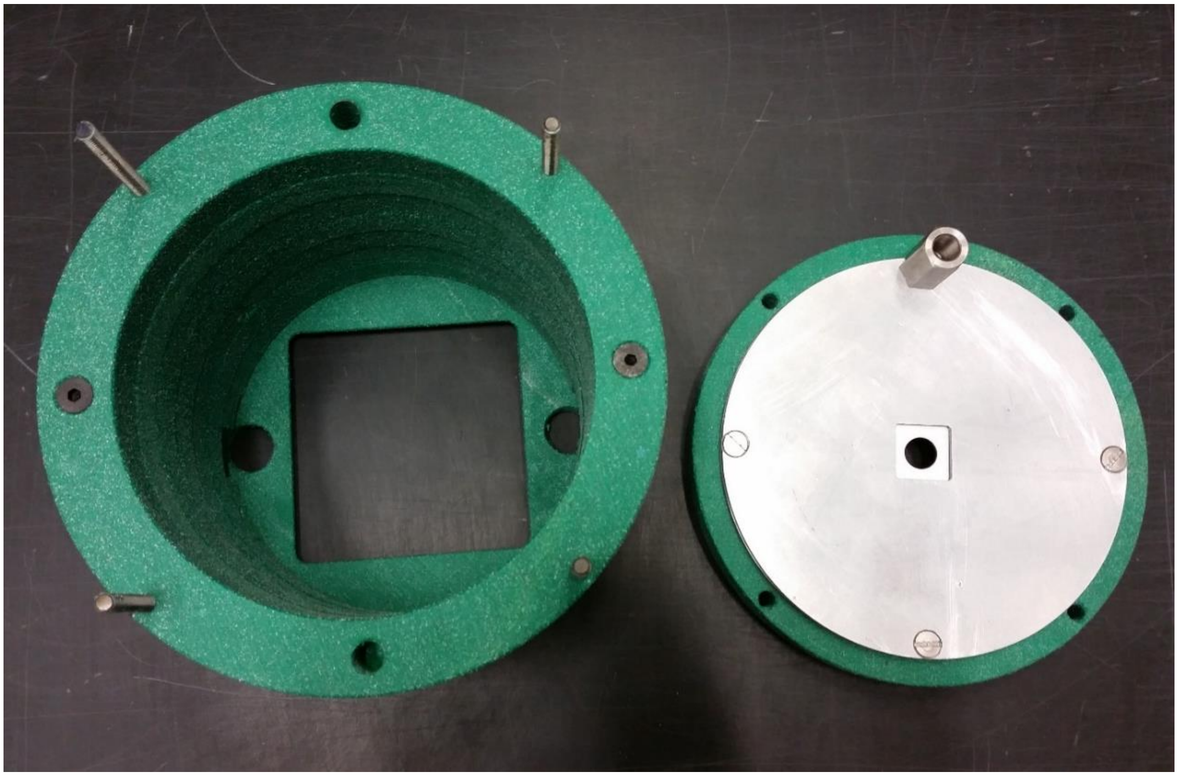

Figure 5.3 The extension tube to hold the object to be imaged

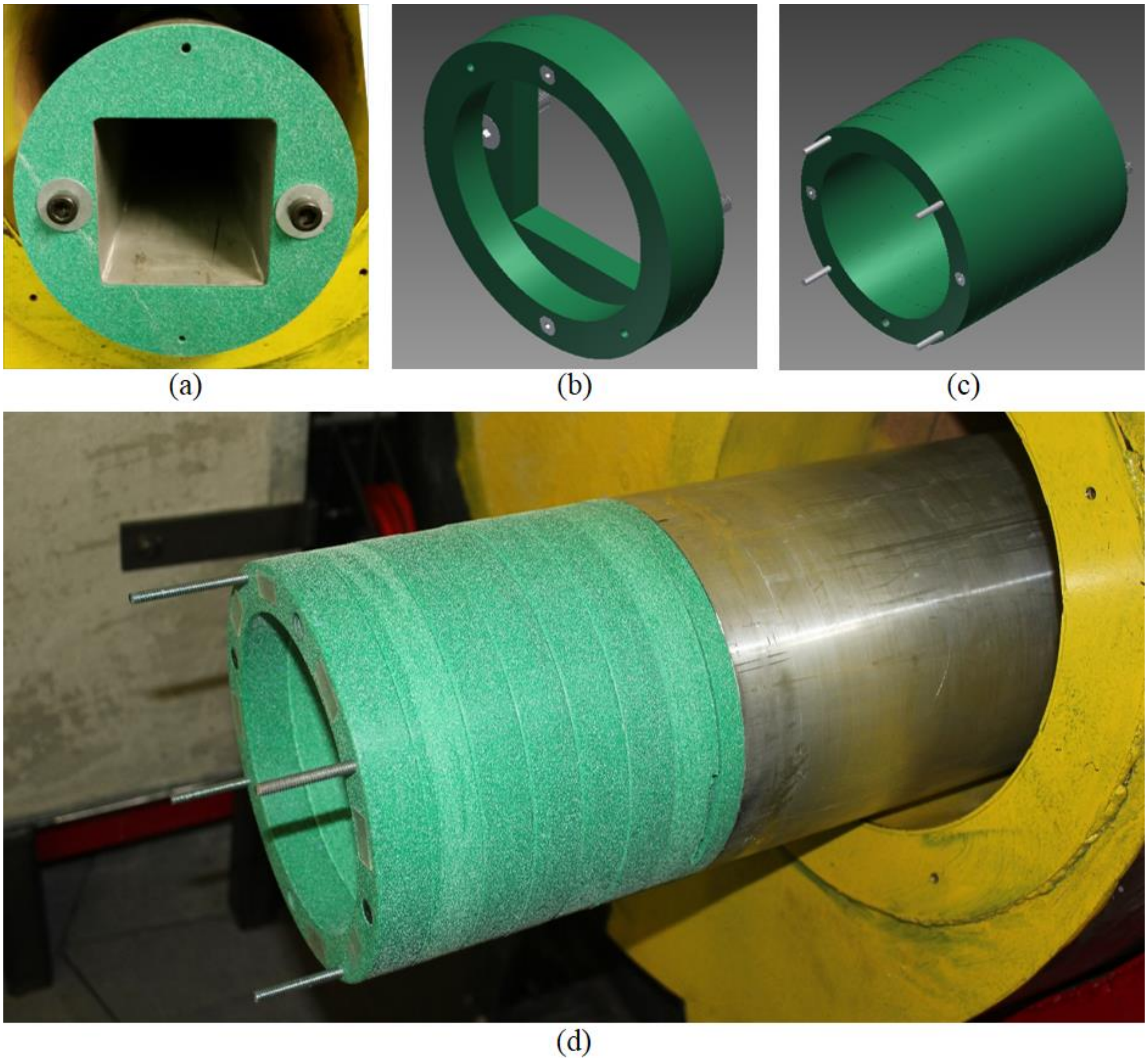

Figure 5.4 The fixed part of the extension tube: (a) the first piece (picture), (b) the second piece (drawing), (c) the following seven pieces (drawing) and (d) the whole assembly attached to the collimator (picture).

11 cm × 11 cm square cut in the center and can be fit on the end of the collimator as shown in Figure 5.4 (a). Followed were seven pieces of plates with circular cut as shown in Figure 5.4 (b) and (c), which were bolted to each other sequentially. Four one-end-threaded studs were screwed to the last piece where the removable piece can be placed on. Figure 5.4 (d) is a picture of this assembly attached to the collimator.

Figure 5.5 shows the removable part of the extension tube. As shown in Figure 5.5 (a), it consisted of a borated polyethylene plate, a cadmium sheet and Aluminum cover. In a REMANI system, any signal outside of the field of view (FOV) will introduce artifacts in the reconstructed results. Thus a 2 mm-thick cadmium sheet was used to shield neutrons and a circular opening with diameter of 1.6 cm was cut out in the center to define the field of view. The objects to be imaged, which were gadolinium foils, can be placed in the recess of the cadmium sheet. Figure 5.5 (b) and (c) shows the front view and the back view of this removable part with an object foil mounted inside.

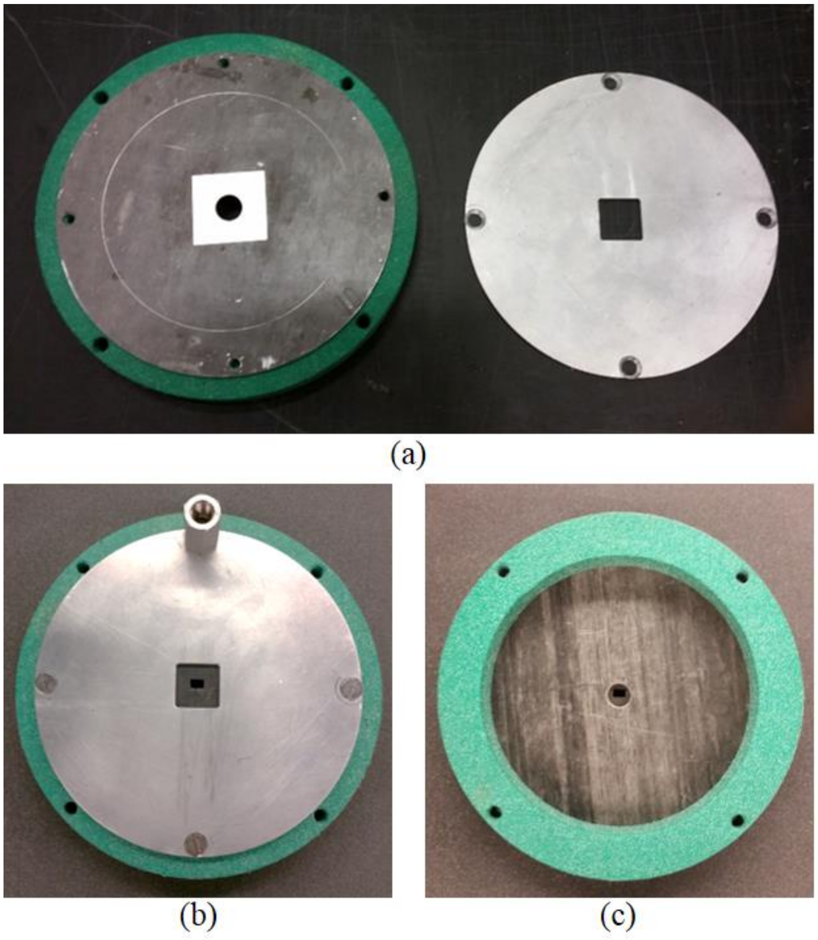

Figure 5.5 The removable part of the sample holder: (a) the components; the picture of (b) the front view and (c) the back view of this part with an object foil mounted inside.

Figure 5.6 (a) shows how the removable part was placed on the rest of the extension tube. To be noted, one of the four screws fastening the cover plate of the removable part was replaced by a binding post extension. A threaded rod can screw into the binding post and took the removable part out from a distance, when both parts were installed in the beam tube as shown in Figure 5.6 (b). After installation, the exact distance from the aperture to the object foil was measured to be 122 ± 1 cm.

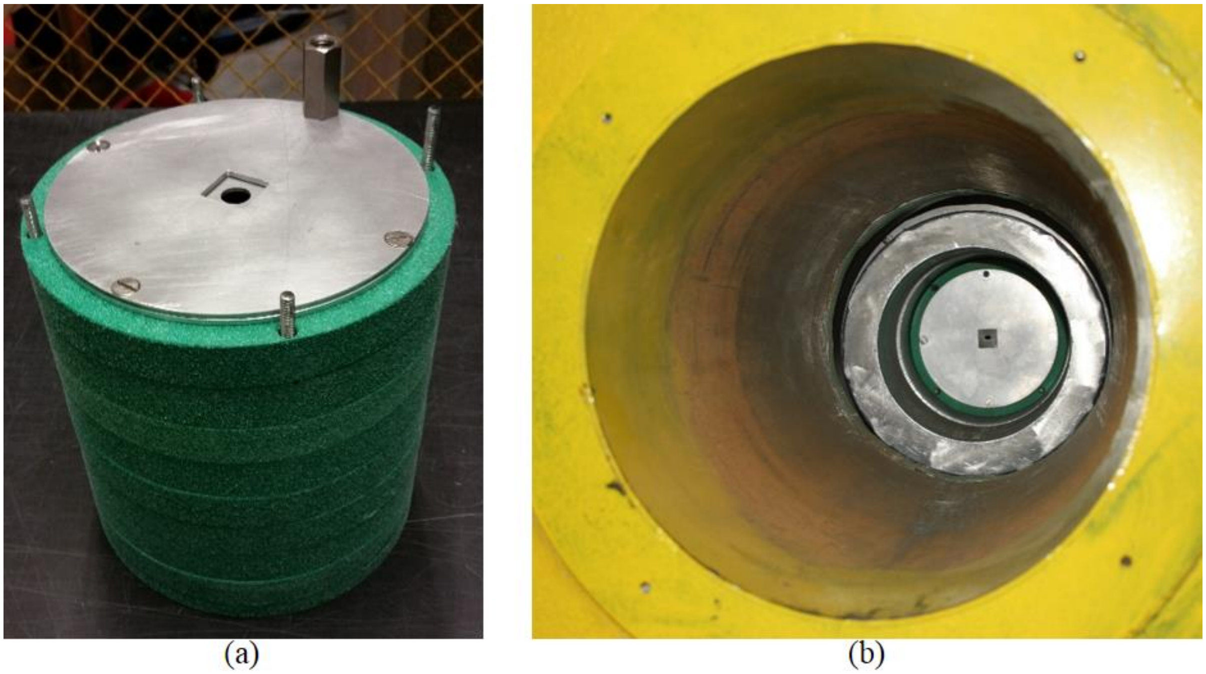
(a) (b)

Figure 5.6 (a) The removable part was placed on the fixed part of the extension tube and (b) both parts were installed in the beam tube.

5.2 Beamline Alignment and Experimental Setup

A REMANI system requires high accuracy on the alignment between the aperture, the object and the detection system. Therefore, the sliding track where the detection systems were placed on has been aligned with the beamline using the reflecting laser method as shown in

Figure 5.7 (a). To begin with, a laser line mirror, as shown in Figure 5.7 (b), was placed in front of the divergent collimator inside of the beam tube. A laser pointer, as shown in Figure 5.7 (c), was placed at the end of the track, and provided a self-leveled laser beam towards the mirror. When the light of the laser beam was completely aligned with beam tube, the reflected laser point would coincide with the emission point.

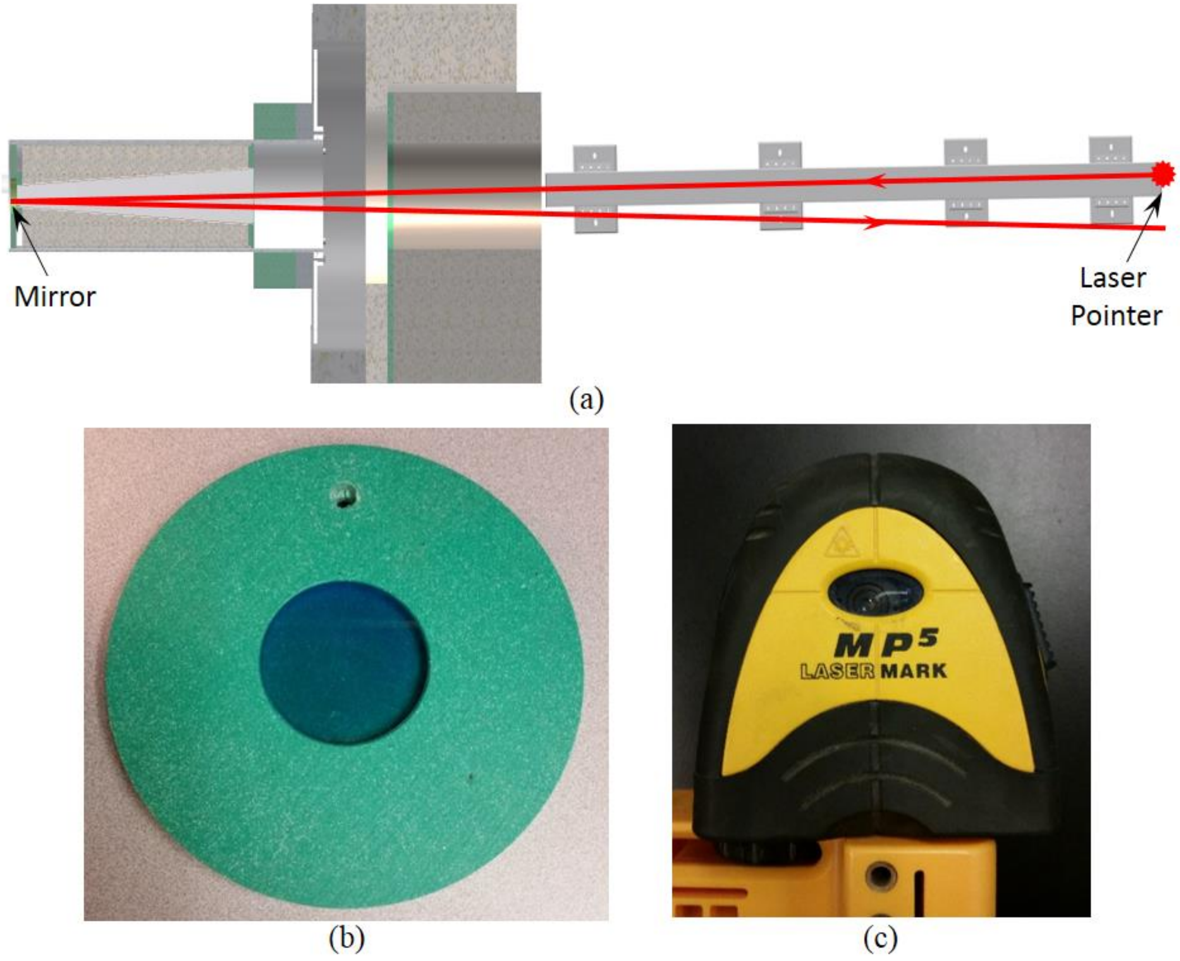

(a)

(b)

(c)

Figure 5.7 (a) The reflecting laser method to align the sliding track with the beamline; (b) the laser mirror and (c) the laser pointer used in the alignment.

Figure 5.8 (a) shows the picture of the emission point and the reflection point of the laser beam when the alignment was optimized. The accuracy was determined by the distance between the two points. They were measured to be 0.5 cm horizontally and 7.5 cm vertically. The distance from the laser pointer to the mirror is 650 cm, thus the angle between the direction of the laser beam and the direction of the beamline was 0.04° horizontally and 0.66° vertically. The track was then carefully adjusted. As shown in Figure 5.8 (b) and (c), when the emission point and the reflection point appeared at the same time on an upright post sliding along the track, it means that the track was set to be parallel to the laser beam.

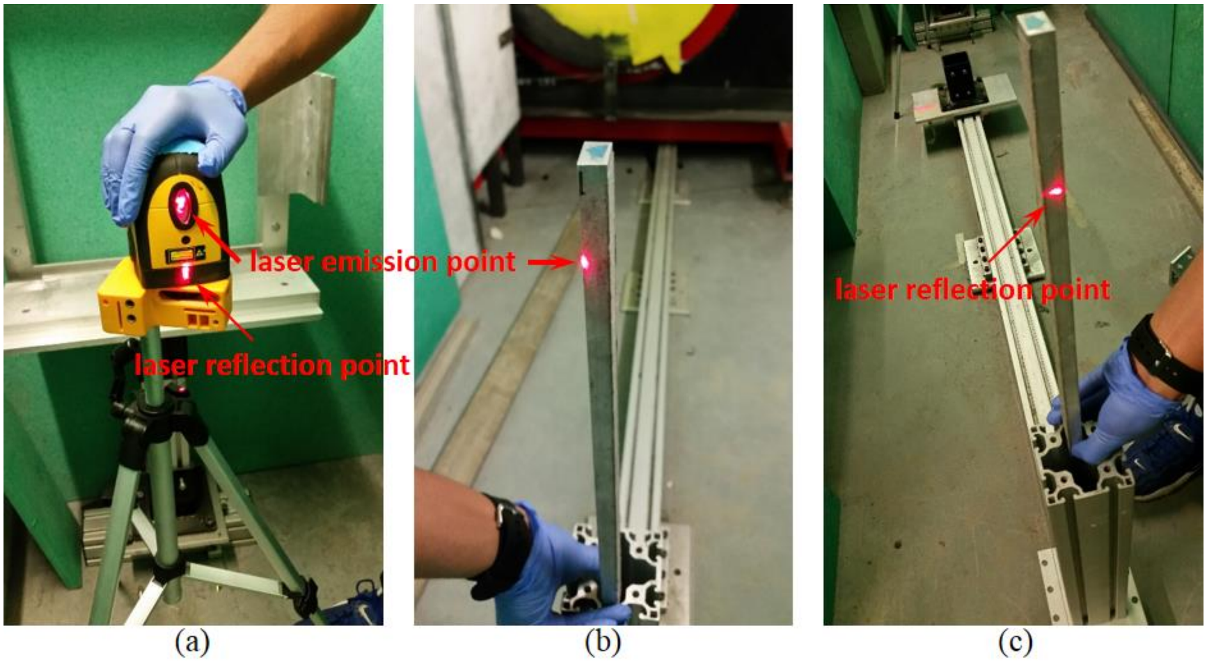

Figure 5.8 (a) The picture of the emission point and the reflection point of the laser beam when the alignment was optimized; (b) Align the track to the laser beam using (b) the emission point and (c) the reflection point.

Another spatial alignment was the rotation of the coded mask about the axis of the beamline. It was achieved with the used of laser system as shown in Figure 5.9. Since the coded mask was mounted parallel to the side plates of the collimator on the front side, the rotational alignment was achieved by lining up the side plates the self-leveled cross-line lasers on the exit side. Figure 5.9 (b) shows the picture with the final alignment.

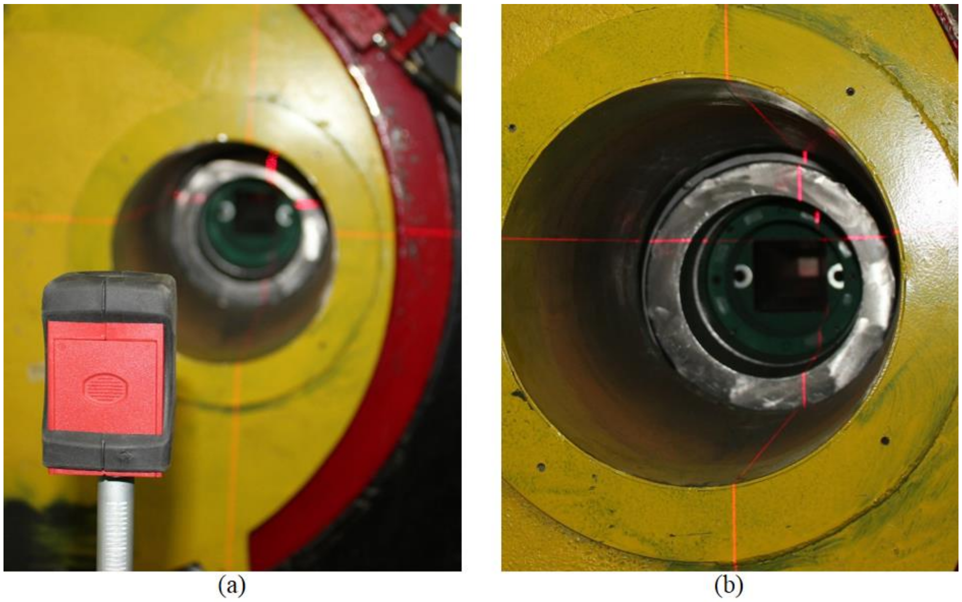
(a) (b)

Figure 5.9 The rotational alignment of the coded mask and the collimator

The film, imaging plate and scintillator system have been used as the detection system. Figure 5.10 shows the setup for the film system and the imaging plate system. It was relatively easy to use these two detection systems, because no additional shielding was required. The setup of the scintillator system was shown in Figure 5.11. The camera box was assembled as described in Section 2.3 and the opening was sealed by a black rubber that guaranteed the light-tight condition. The box was then mounted in the upright position on a stand that can move along the slide track. The rotational angle and the horizontal and vertical location of the box can be precisely adjusted by the handles on the stand. Figure 5.11 (a) and (b) are the front and back views of this system mounted in the beamline.

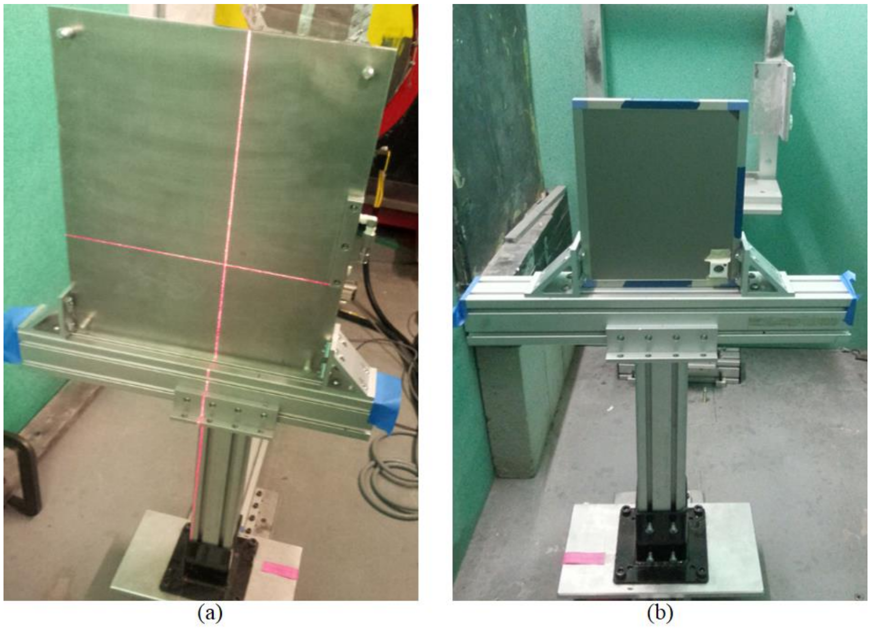
(a) (b)

Figure 5.10 The setup of (a) film and (b) imaging plate as detection systems

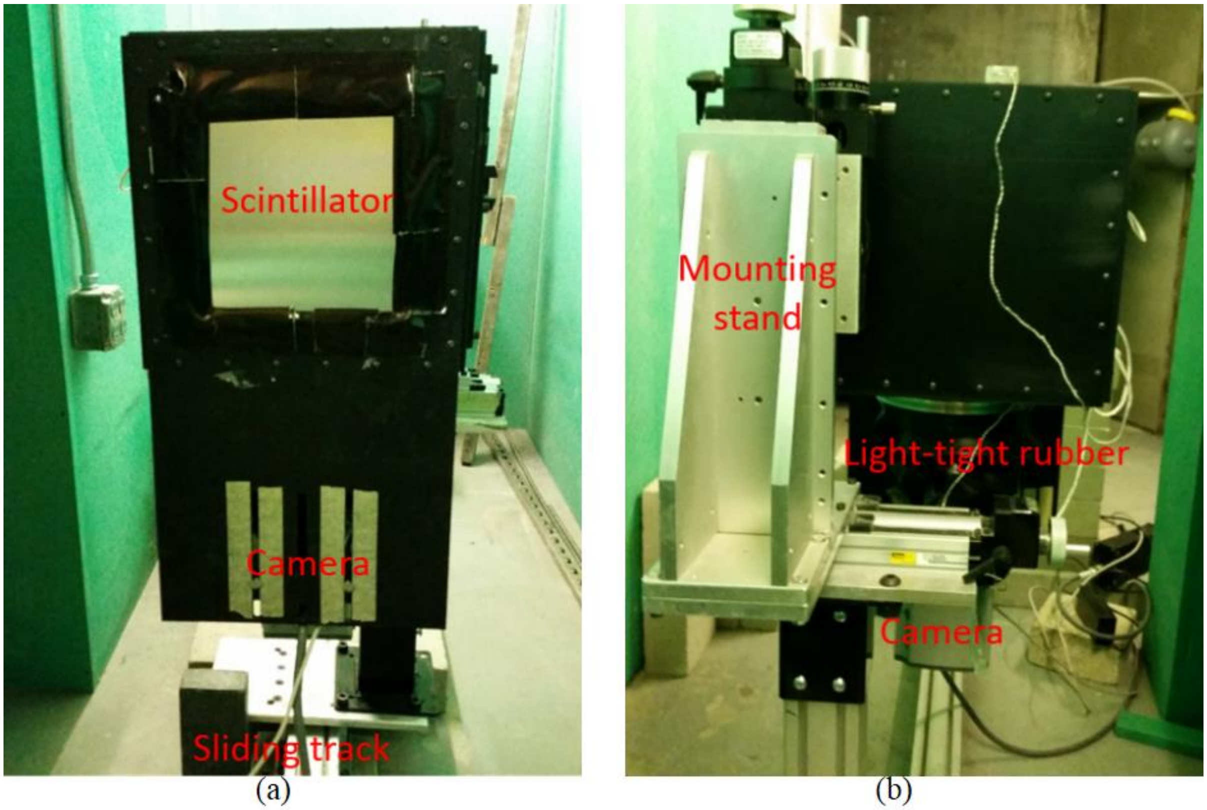
(a) (b)

Figure 5.11 The scintillator system was set up on a mounting stand in the beamline, viewed from (a) the front side and (b) the back side.

To reduce the possibility of radiation damage to the CCD, additional shielding was built surrounding the scintillator system. As shown in Figure 5.12, the shielding was mainly composed of concrete blocks. Lead and borated polyethylene plates were also used.

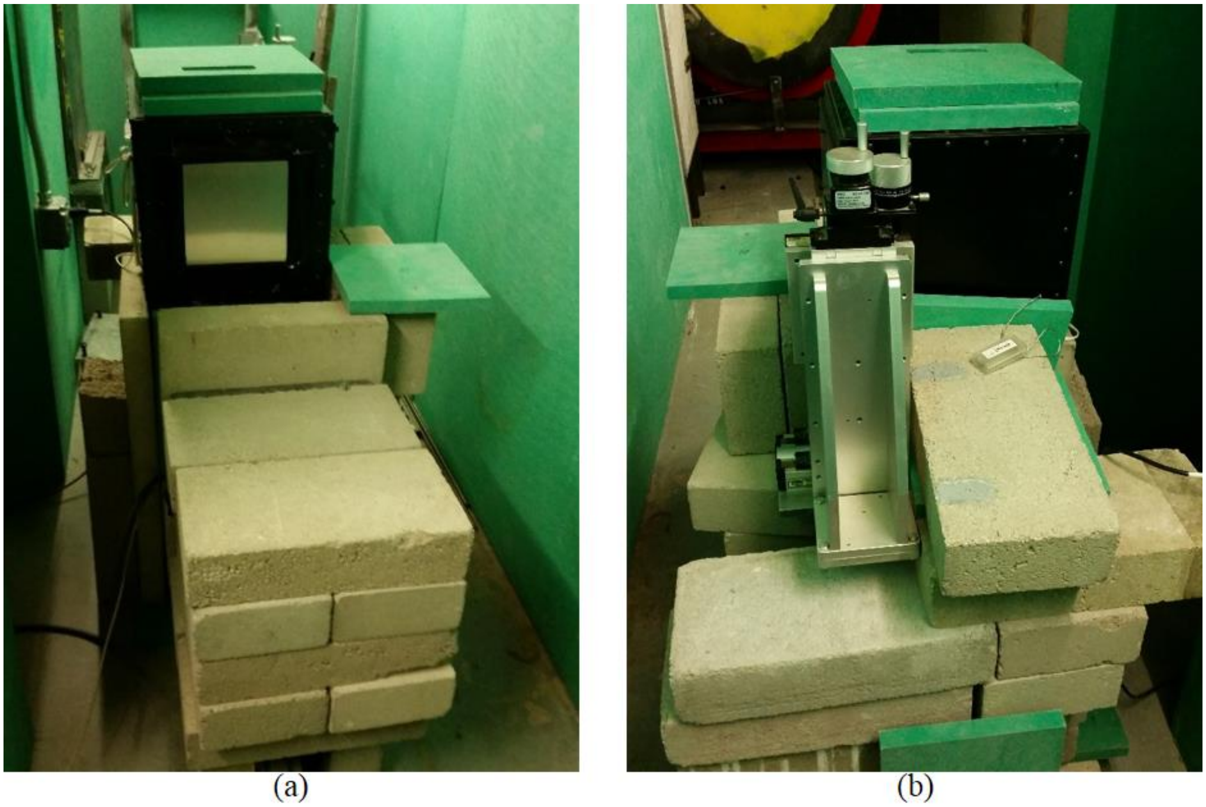

Figure 5.12 The setup of the scintillator system with shielding, viewed from (a) the front side and (b) the back side.

5.3 Mask Fabrication Methods

Three coded masks have been made for the REMANI system and are shown in Figure 5.13. They are arranged in the order that they were fabricated. For convenience, the masks will be referred in this thesis by the diameters of the holes, which are 12 µm, 200 µm and 100 µm from left to right. The grid sizes are 40 µm, 400 µm and 200 µm, respectively. All of the

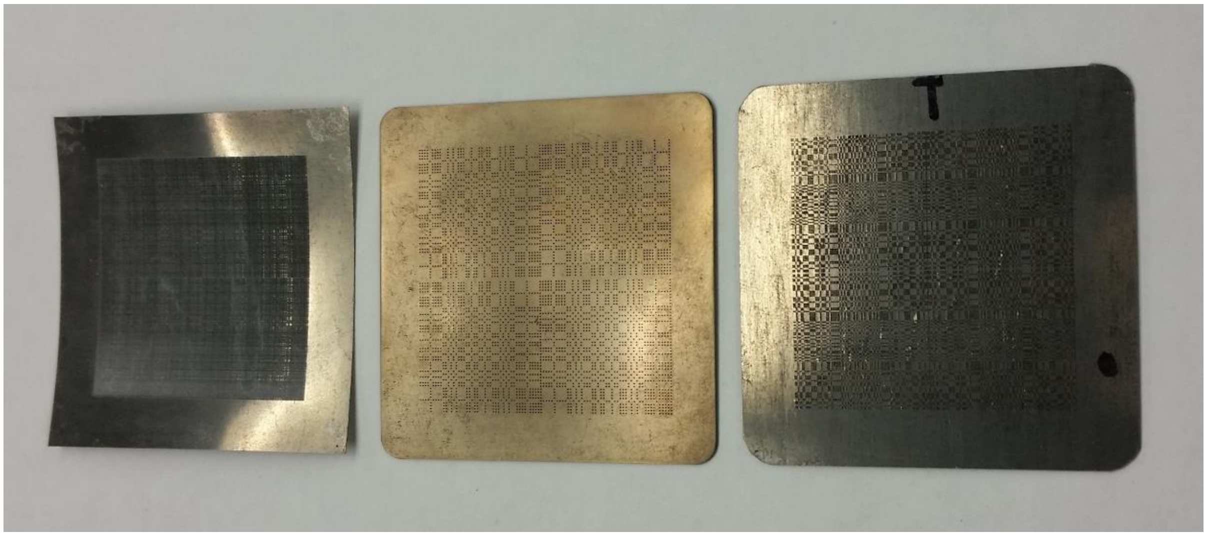

Figure 5.13 Three coded masks have been made for the REMANI system.

three masks have a physical size of 5 cm × 5 cm, with pinholes in the center. Since the original aperture is a 4 cm × 4 cm square, the pinholes are distributed within the area with sides of 3.6 cm to 3.8 cm, leaving 0.1 cm to 0.2 cm spaces on each side to the original borders.

On the first attempt, the mask on the left was made by laser drilling technique at Lenox Laser, Inc. The material used to fabricate the mask was a gadolinium foil with a thickness of 200 µm, allowing a neutron attenuation less than 0.11%. The aspect-ratio of the holes, which is the ratio of the depth to the diameter, is as high as 16.7:1.

During the laser drilling process, the gadolinium material melted and vaporized by absorbing the energy from a focused laser beam thus pinholes were created. It has the advantages in producing holes with high-aspect-ratio. However, it also has some obstacles which can be seen clearly under optical microscope. Figure 5.14 (a) is a zoomed in picture of the fabricated mask. Some of the holes were not drilled through due to the high aspect-ratio.

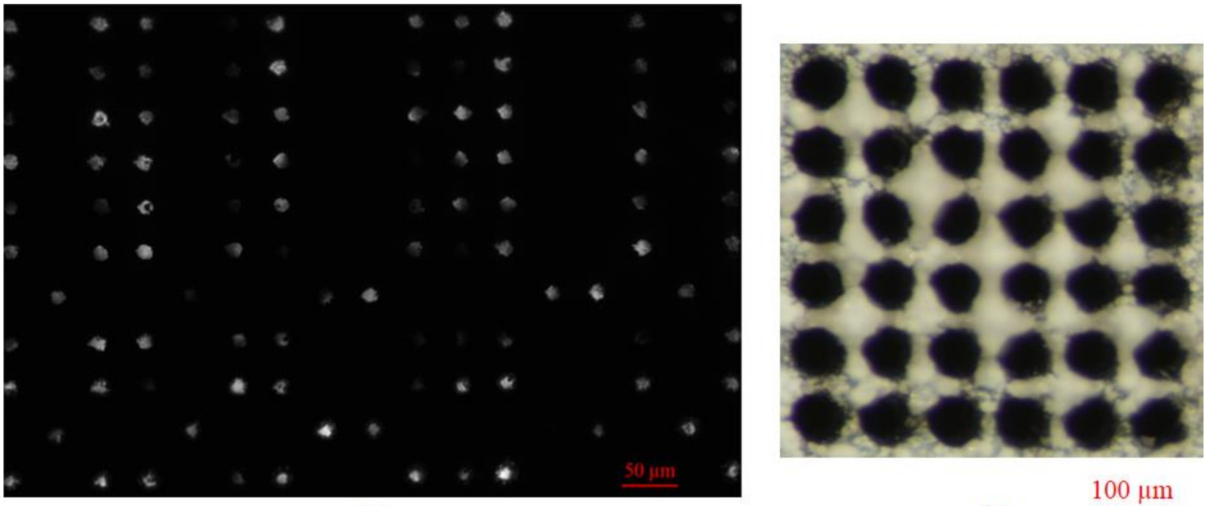

(a) (b)

Figure 5.14 The optical microscope picture of the laser drilling mask

We have also tested this technique on the same material to make larger holes. Figure 5.14 (b) shows a picture of a test piece, on which the diameters of the holes were 70 µm and the grid size was 100 µm. The quality of the holes was better than the ones on the 12 µm mask, however, it can be clearly seen that the molten material got solidified on the fabrication edges, which was the main reason for the warpage of the finished mask.

Mechanical drilling technique was considered as fabrication method for the mask. Two masks have been made by Micro-milling CNC machining center in Precision Instrument Machine Shop at NCSU. The pictures of the 200-µm mask and 100-µm mask are shown in Figure 5.15 and Figure 5.16. To avoid distortion, the gadolinium foils used had thickness of 450 µm. Thus the aspect-ratio of the holes were 2.25:1 and 4.5:1.

To keep swarf from building up in the holes while drilling, the peck drilling process was used. The drill bits were plunged into the material by only 10 µm each time and then retracted back to the surface. The tapping run for the entire pattern and was repeated from the beginning until all the holes were finished. Even though localized heating was generated at the contact of the material and the drill bit, it can be dissipated in time before the next tapping happened at this location. Comparing to the laser drilling technique, the cuts with mechanical drilling were clearer and the distortion was less on the finished piece.

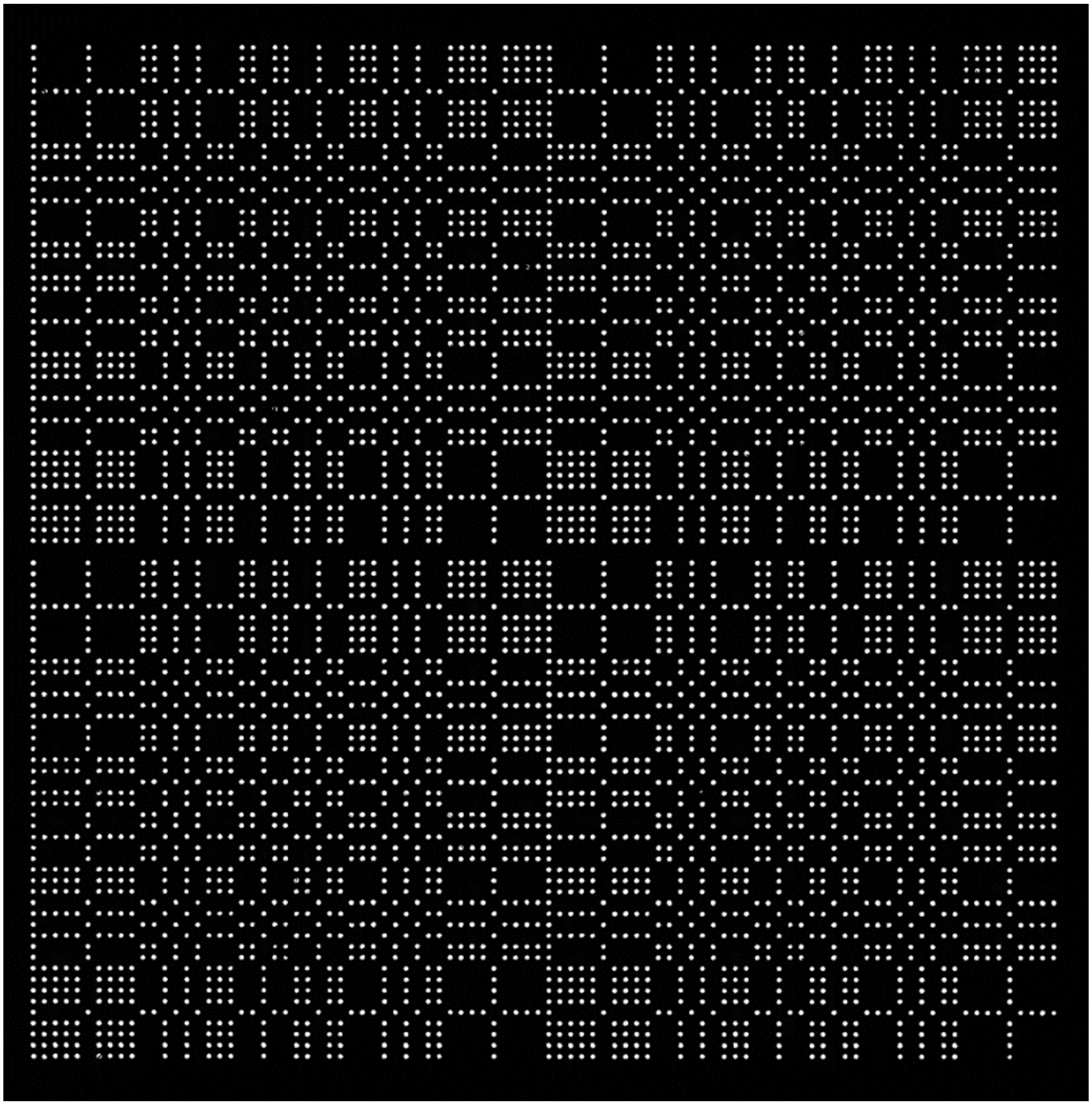

Figure 5.15 The coded mask made by mechanical drilling, with 200 μm-diameter holes

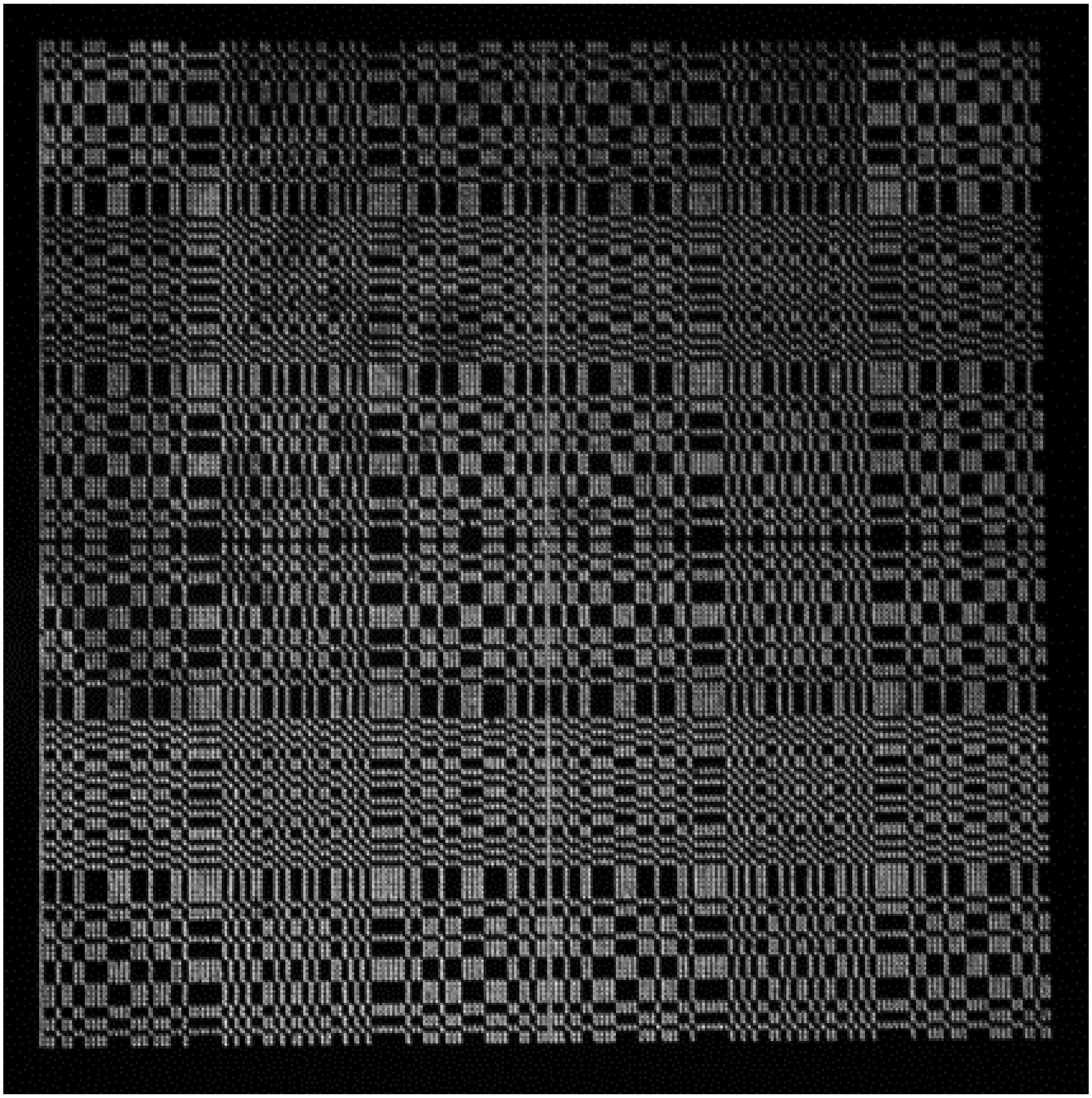

Figure 5.16 The coded mask made by mechanical drilling, with 100 μm-diameter holes

5.4 Measurement of Flat Images

The detection systems that have been used with the three masks include the film system and the scintillator system. Although the outputs of both systems are 16-bit images, the sensitivity and noise performance are quite different.

A film scanner works by passing a focused beam through the film and measuring the intensity of the transmitted light. Thus the logarithm of the values on an output image has a negative linear relationship with the density of the input film, and the same with the local neutron exposure. As plotted in Figure 2.12, the neutron flux is approximately 4.3×10^6 neutron/cm^2·sec at the location that is 600 cm away from the aperture. Films were exposed at this location for different periods of time and then digitized by the film scanner. The average of the density and the pixel values was measured in a 2”×2” area in the center of film. Their relationships with neutron fluence over the exposure time are shown in Figure 5.17. The logarithm conversion has to be applied in a coded measurement before reconstruction.

The maximum density that the film scanner can detect is 3.4. However, from the experience, the digital value is off linearity for density larger than 2.6. Thus the saturation level was defined as neutron fluence of 1.7×10^9 neutron/cm^2. Since the film system generates a negative image, the output SNR cannot be used as an indicator of noise.

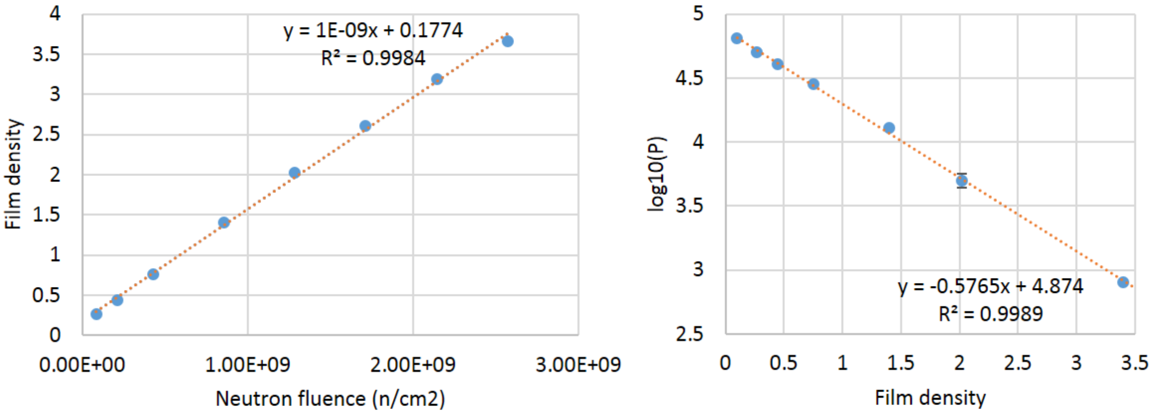

(a) (b)

Figure 5.17 (a) The linear relationship of the film density vs. neutron fluence; (b) the linear relationship of the logarithm of pixel values vs. the film density.

The scintillator system utilizes CCD sensor to digitize the signals. The output pixel value is linear to the number of neutrons accumulated in the scintillator and the saturation occurs when the charge capacity in each pixel element is reached. Flat images were measured at the location 366 cm from the aperture, where the neutron flux was estimated to be 1.2×10^{7} neutron/cm^{2}·sec. Figure 5.18 shows an area of 10.24 cm × 10.24 cm in the center of the flat images and the corresponding histograms with pixel sizes of 100 μm and 60 μm. The exposure times were 16 seconds and 20 seconds, thus the number of neutrons corresponding to one pixel were 19200 and 8640, respectively. The input SNR of the system with 100 μm pixel size are about 1.5 times of the one with 60 μm pixel size.

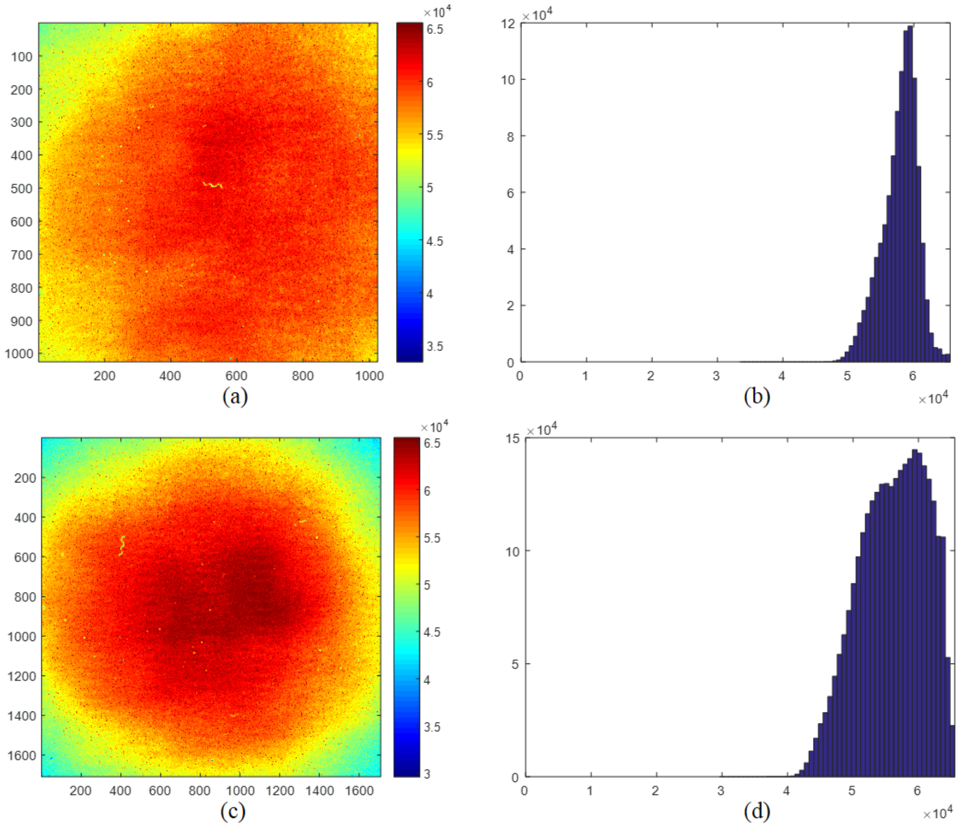

Figure 5.18 (a) The flat image taken by the scintillator system with a pixel size of 100 μm and (b) the corresponding histogram; (c) the flat image taken by the scintillator system with a pixel size of 60 μm and (d) the corresponding histogram.

Some basic analysis with the two settings was summarized in Table 5.1. Based on Equation (2.4), the output SNR for each flat image are calculated as the ratio of the mean value and the standard deviation of the pixel values. It is much lower than the input SNR because of the non-uniformity in the pixel values, which is mainly due to the neutron sources and the response of the lens.

Table 5.1 Evaluation of the flat images taken by the scintillator system with pixel sizes of 60 µm and 100 µm.

Pixel size	Exposure time	Neutrons/pixel	Mean pixel values	SNR_{output}	Contrast
100 µm	16 sec	19200	5.79×10^4	17.2	0.81
60 µm	20 sec	8640	5.61×10^4	8.8	0.80

The contrast of a gadolinium object was also measured with Figure 2.19 (a) (b) and Figure 5.18 (a) (c). Figure 2.19 were images of a 200 µm-thick gadolinium foil taken under the same conditions as Figure 5.18. The difference between the averages of the pixel values with and without the foil were calculated. The contrast was obtained as this difference divided by the average pixel values of the flat image. The contrasts were about 0.80 for both pixel settings, meaning nearly 20% of the measured signals passed through the gadolinium foil. However, based on the MCNP simulation results as shown in Figure 4.1, neutron transmission of a 200 µm-thick gadolinium was estimated only to be 0.11%. Thus these pixel values transmitted through the gadolinium are not thermal neutrons but noise.

5.5 Measurements of REMANI System and Reconstruction using Correlation Method

This section presents the multiplexed images measured with three masks and the reconstructed results using the correlation method. Since correlation method is a linear operation, different values in the decoding array only result in a linear transformation of the reconstructed image and do not affect the resolution and the SNR of the images. For convenience, the values in the decoding array were set to be 1, -1 and 0.

5.5.1 Measurements with 12 μm Mask

The 12 μm mask was used with the film system, the size of which is 43 cm×36 cm. The recorded film image was digitized by a scanner at the 1600dpi, which was equivalent to 15.875 μm. The mask pattern is an 887×887 MURA, with the grid size of 40 μm. The non-cyclic arrangement was used to maximize the field of view. Based on Equation (3.40) to (3.42), the magnification factor has to be selected from 1.8 to 5.4, with an increment of 0.4. The maximum magnification is due to the limited length of the beam line.

The object to be imaged was a 15 mm × 10 mm rectangular opening, formed by four gadolinium foils stacking together. A film was exposed at the magnification factors of 1.8 for 7200 seconds. At this location, the projection of the mask grid has a size of 32 μm×32 μm, covering approximately 2×2 pixels. The resolution of the conventional system was measured to be 33 μm, which was the effect of h_d and h_s. The FWHM of h_g was 9.6 μm at this magnification. Based on Equation (3.16), the FWHM of the PSF in a magnified system can be estimated as be 34 μm. For correlation reconstruction, the value of κ can be 1 or 2, and the resolutions of the reconstructed images were expected to be 21 μm and 26 μm accordingly.

From Figure 5.17, it is known that the neutron exposure is linear to the logarithm of the pixel values of the film system output. Since cross correlation is a linear operation, logarithm of the image is used as the reconstruction input. Figure 5.19 (a) and (b) show the direct output

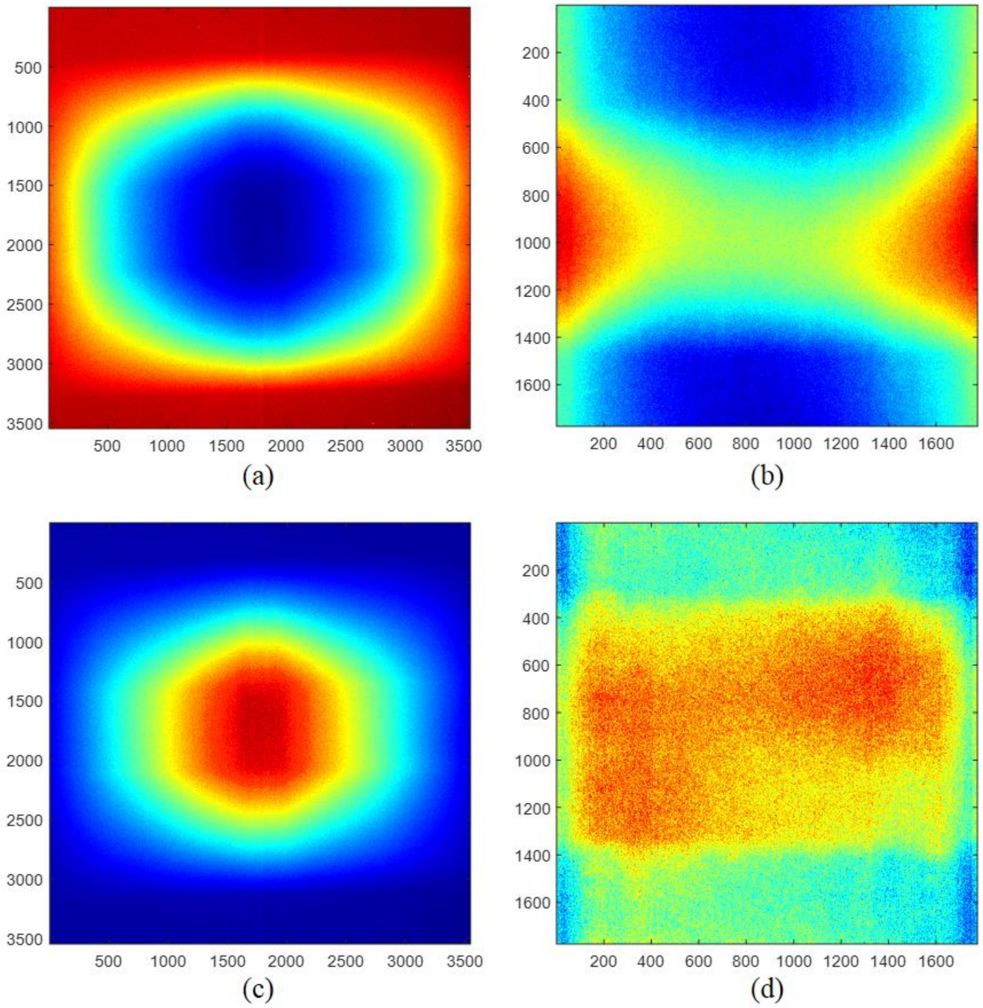

Figure 5.19 (a) The output of the film system, taken with 12 µm mask at magnification of 1.8 and (b) the reconstructed results using correlation method when κ=2. (c) The logarithm of the film image and (b) the corresponding reconstructed results.

of the film system and the reconstructed result when κ was set to be 2. Figure 5.19 (c) and (d) are the image and the reconstructed result after logarithm conversion was applied. The object can be clearly recovered in the reconstructed image in Figure 5.19 (d).

The resolution and SNR were evaluated from the reconstructed image. The SNR was measured to be 2.9. A portion of the edge as shown in Figure 5.20 (a), which was the area

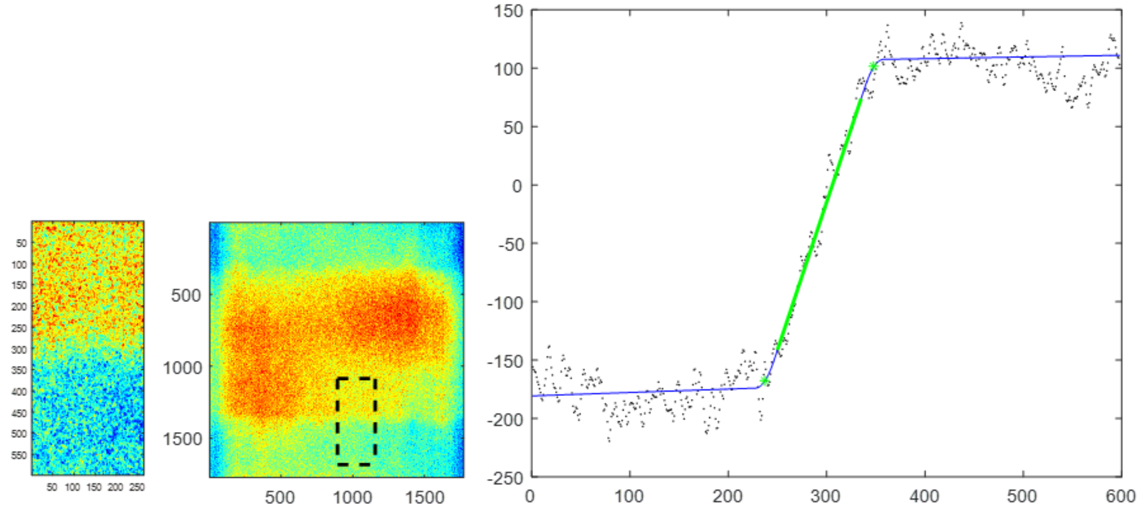

(a) (b) (c)

Figure 5.20 (a) A portion of the edge, which was the area inside of the dash line of (b) the reconstructed image, was selected for resolution analysis. (c) The ESF was obtained by taking the average along the edge.

inside of the dash line in Figure 5.20 (b), was selected from the analysis. Figure 5.20 (c) shows the ESF was obtained by taking the average along the edge. The background, the rising edge and the open area were fitted by three line segments. The width between 10% ESF to 90% ESF was measured to be 680.3 μm, which is much higher than expected. It might be due to two reasons. First, it could be that the SNR was too low that the signal in high frequency domain was submerged in noise and cannot be evaluated. It may be due to the distortion of the mask. The projection from each mask pinhole has been shifted but the correlation operation still reconstructed the image as they were in the designed locations. Thus the edge in the reconstructed results was not as sharp as expected.

5.5.2 Measurements with 200 µm Mask

The 200 µm mask was used to with the scintillator system with a pixel size of 100 µm. The size that is available for imaging is 18.3 cm×18.3 cm, which is the dimension of the scintillator. If a non-cyclic arrangement were used, the system can only be used with magnification factor of 2, limited by the detector size as indicated by Equation (3.41). With a cyclic arrangement, the magnification factor can be set from 2 to 4, an increment of 1, limited by the available beam length. The mask pattern is a 94×94 mosaicked MURA.

With a magnification factor *m*, the mask pinhole projection on the image plane has a diameter of 200(*m*-1) µm, covering 2(*m*-1)×2(*m*-1) pixels. The mask grid projection on the image plane covers 4(*m*-1)×4(*m*-1) pixels. For the correlation reconstruction, the value of κ can be any integer between 1 and 4(*m*-1). The expected system resolution can be calculated based on Equation (3.36). Table 5.2 lists the calculations when the value of κ equals to 1, 4, and 8 for each magnification factor.

Table 5.2 The expected resolution in the reconstructed images with the use of 200-µm mask

Mag (*m*)	κ = 1				κ = 4				κ = 8			
	①	②	③	System res.	①	②	③	System res.	①	②	③	System res.
2	100	156	0	185 µm	100	156	150	238 µm	--	--	--	--
3	133	104	0	169 µm	133	104	100	196 µm	133	104	233	288 µm
4	150	78	0	169 µm	150	78	75	185 µm	150	78	175	243 µm

Note: ① refers to the geometric unsharpness, $FWHM_g / m = (1 - 1/m) D$;

② equals to the resolution of conventional system divided by the magnification factor *m*. The conventional system resolution is due to the detector unsharpess and sampling unsharpness. Based on the results in Section 2.4.2, it was measured to be 311 ± 7 µm;

③ refers to the reconstruction unsharpness, $FWHM_r / m = (\kappa - 1) \Delta s / m$;

All the values are in the unit of µm. The system resolutions are the quadrature sum of these terms.

Two patterns on 200 µm-thick gadolinium foils have been used as the objects in the experiments. As shown in Figure 5.21 (a), one object consists of 16 pinholes in four rows, separating by 3 mm. The diameters of the holes on each row are 800 µm, 600 µm, 400 µm and 200 µm. Since the FOV at magnification of 2 is 9.4 mm × 9.4 mm, only 12 pinholes in three rows were used. The other object is shown in Figure 5.21 (b), which is an 8 mm × 5 mm rectangular opening.

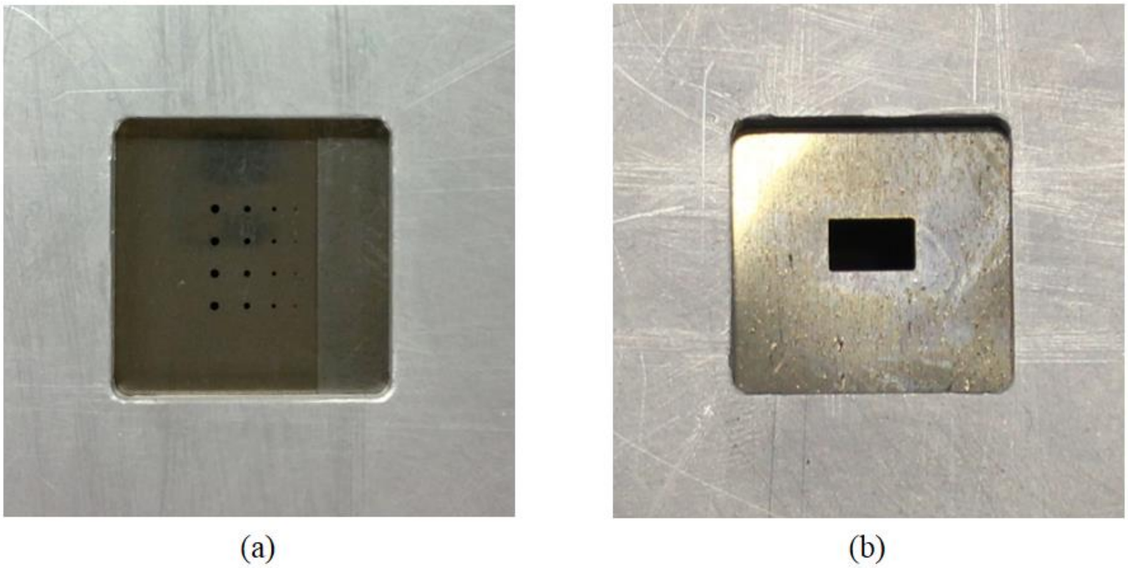
(a) (b)

Figure 5.21 The objects used with 200 µm mask: (a) an 8 mm × 5 mm rectangular opening and (b) 16 pinholes with various sizes on 200 µm-thick gadolinium foils

First of all, the image of the 12 pinholes was taken at the magnification factor of 2. The exposure time was 3600 seconds. The recorded image and the reconstructed images are presented. Figure 5.22 (a) is the complete recorded image. Figure 5.22 (b) to Figure 5.22 (d) are the reconstructed images with complete correlation, when the κ values were set to be 1, 2 and 4, respectively. Figure 5.22 (e) is the center portion of the recorded image. Figure 5.22

(f) to (h) are the reconstructed images with basic correlation, when the κ values were set to be 1, 2 and 4, respectively.

Next, images of a rectangular opening on a gadolinium foil were also taken. For this object, measurements were performed at three magnification factors: 2, 3 and 4. The exposure times were 720 seconds, 2700 seconds and 6300 seconds, respectively.

Figure 5.23 shows the recorded image and the reconstructed images at the magnification factor of 2. Figure 5.23 (a) is the complete image and Figure 5.23 (b) to (d) are the reconstructed images with complete correlation, with κ value of 1, 2 and 4. Figure 5.22 (e) is the center portion of the recorded image and Figure 5.23 (f) to (h) are the reconstructed images with basic correlation, with κ value of 1, 2 and 4.

Similarly, Figure 5.24 and Figure 5.25 shows the recorded image and the reconstructed images at the magnification factor of 3 and 4. Figure (a) is the complete image and Figure (b) to (d) are the reconstructed images with complete correlation. At magnification 3 and 4, the value of κ was set to be 1, 4 and 8. Figure (e) is the center portion of the recorded image and Figure (f) to (h) are the reconstructed images with basic correlation, with κ value of 1, 4 and 8.

Comparing vertically, it can be seen clearly that the complete correlation results have much higher contrast and are less sensitive to the non-uniformity than the basic correlation results. Comparing vertically, the reconstructed images appear to be blurrier and smoother with κ increasing.

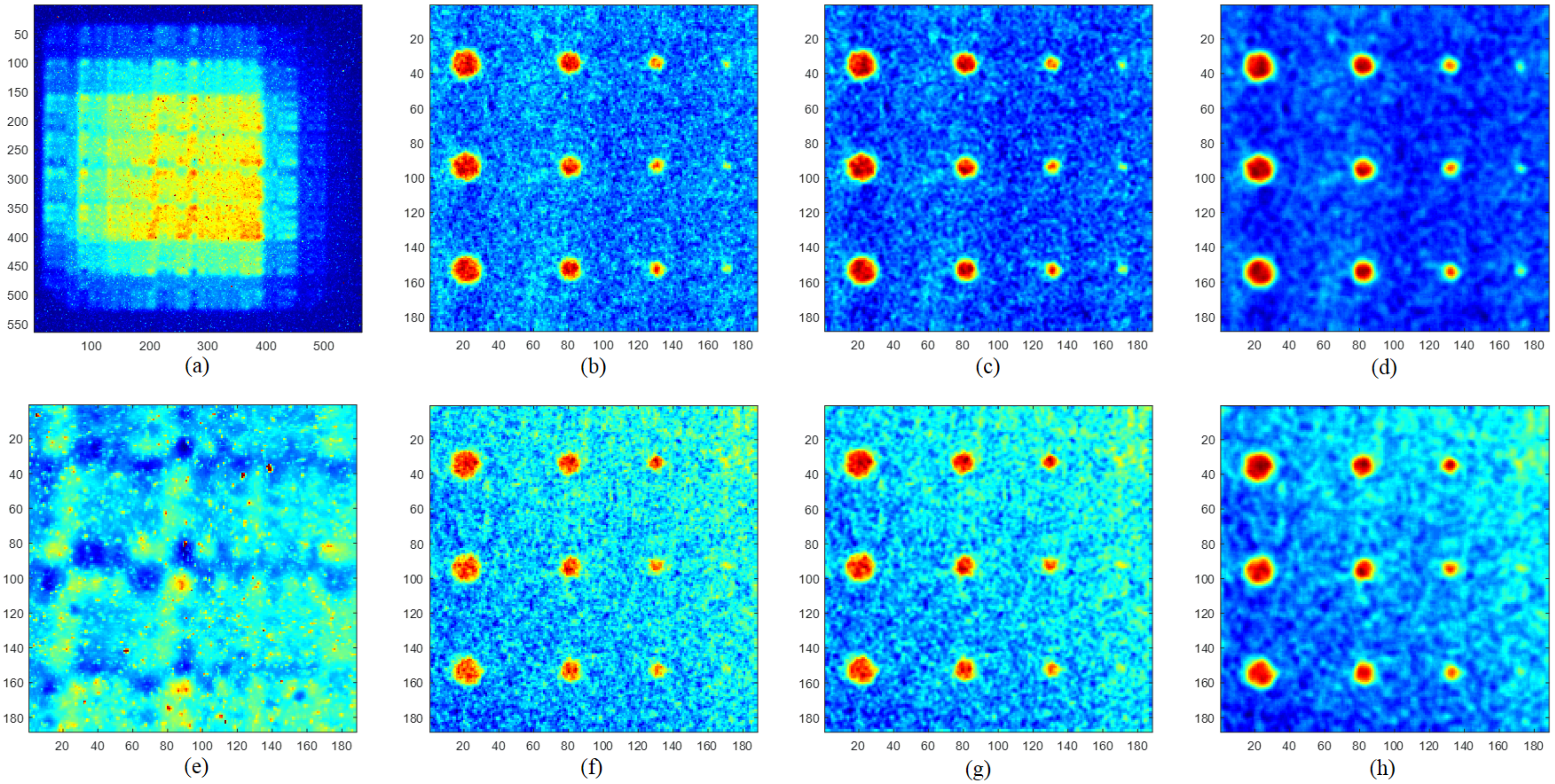

(a) (b) (c) (d)

(e) (f) (g) (h)

Figure 5.22 (a) The complete image of 12 pinholes, taken with the 200 μm mask and scintillator system at magnification of 2, and the reconstructed images with complete correlation method when (b) κ=1, (c) κ=2, and (b) κ=4. (e) The center portion of the image that can be used alone for reconstruction, and the reconstructed images with basic correlation method when (f) κ=1, (g) κ=2, and (h) κ=4.

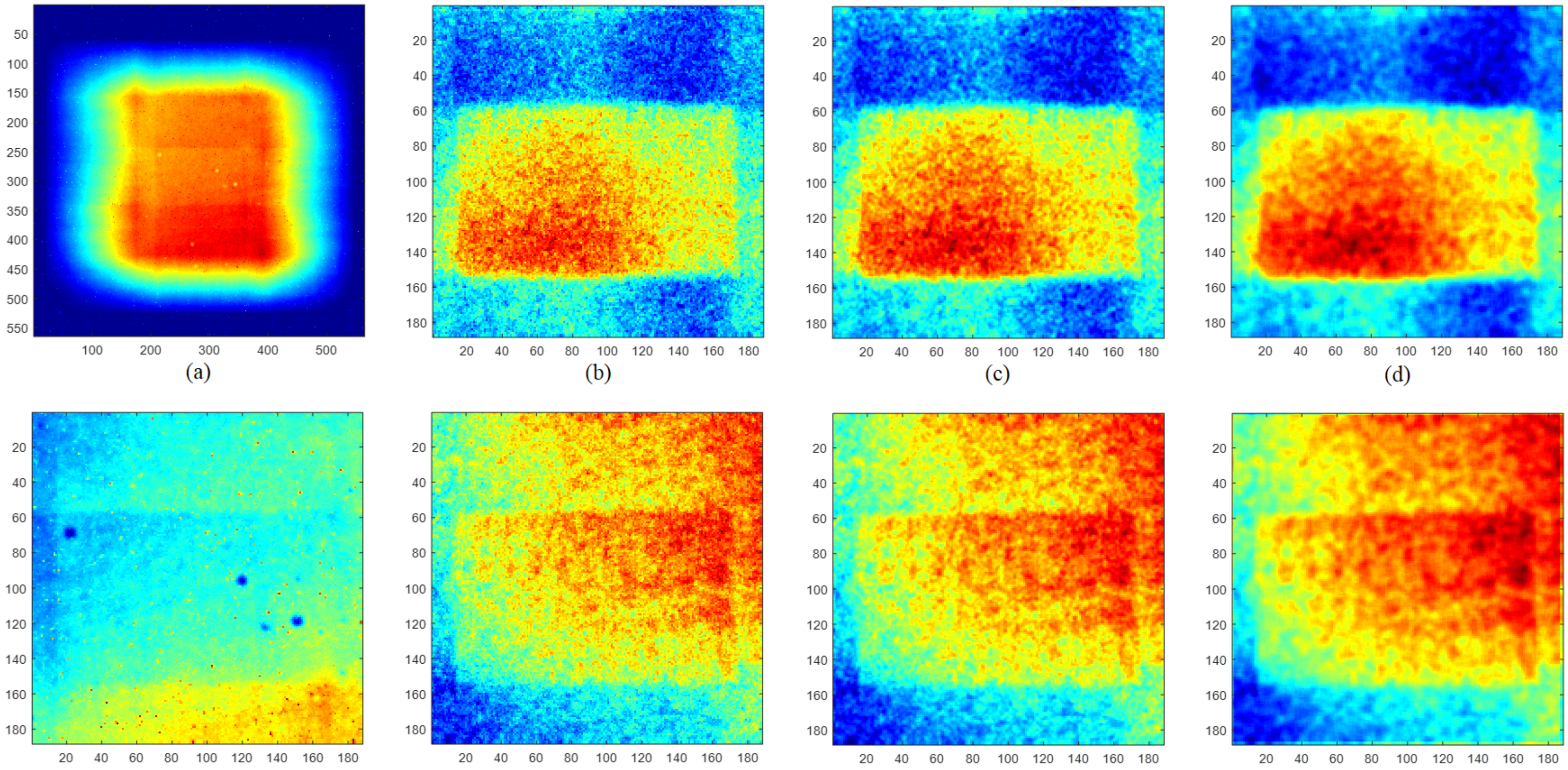

(a) (b) (c) (d)

(e) (f) (g) (h)

Figure 5.23 (a) The complete image of a rectangular opening, taken with the 200 μm mask and scintillator system at magnification of 2, and the reconstructed image with complete correlation method when (b) κ=1, (c) κ=2, and (b) κ=4. (e) The center portion of the image that can be used alone for reconstruction, and the reconstructed image with basic correlation method when (f) κ=1, (g) κ=2, and (h) κ=4.

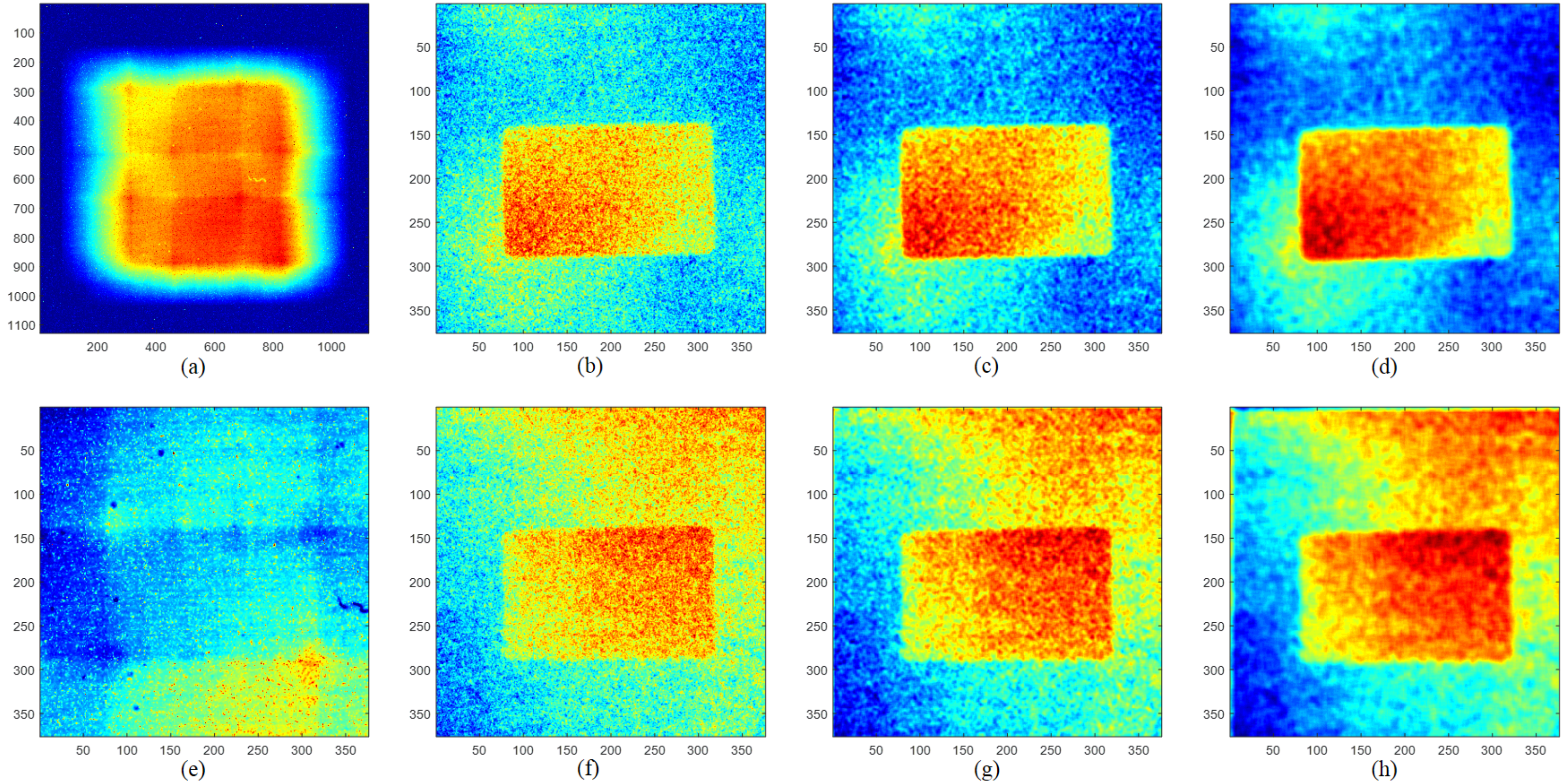

(a) (b) (c) (d)

(e) (f) (g) (h)

Figure 5.24 (a) The complete image of a rectangular opening, taken with the 200 μm mask and scintillator system at magnification of 3, and the reconstructed image with complete correlation method when (b) κ=1, (c) κ=4, and (b) κ=8. (e) The center portion of the image that can be used alone for reconstruction, and the reconstructed image with basic correlation method when (f) κ=1, (g) κ=4, and (h) κ=8.

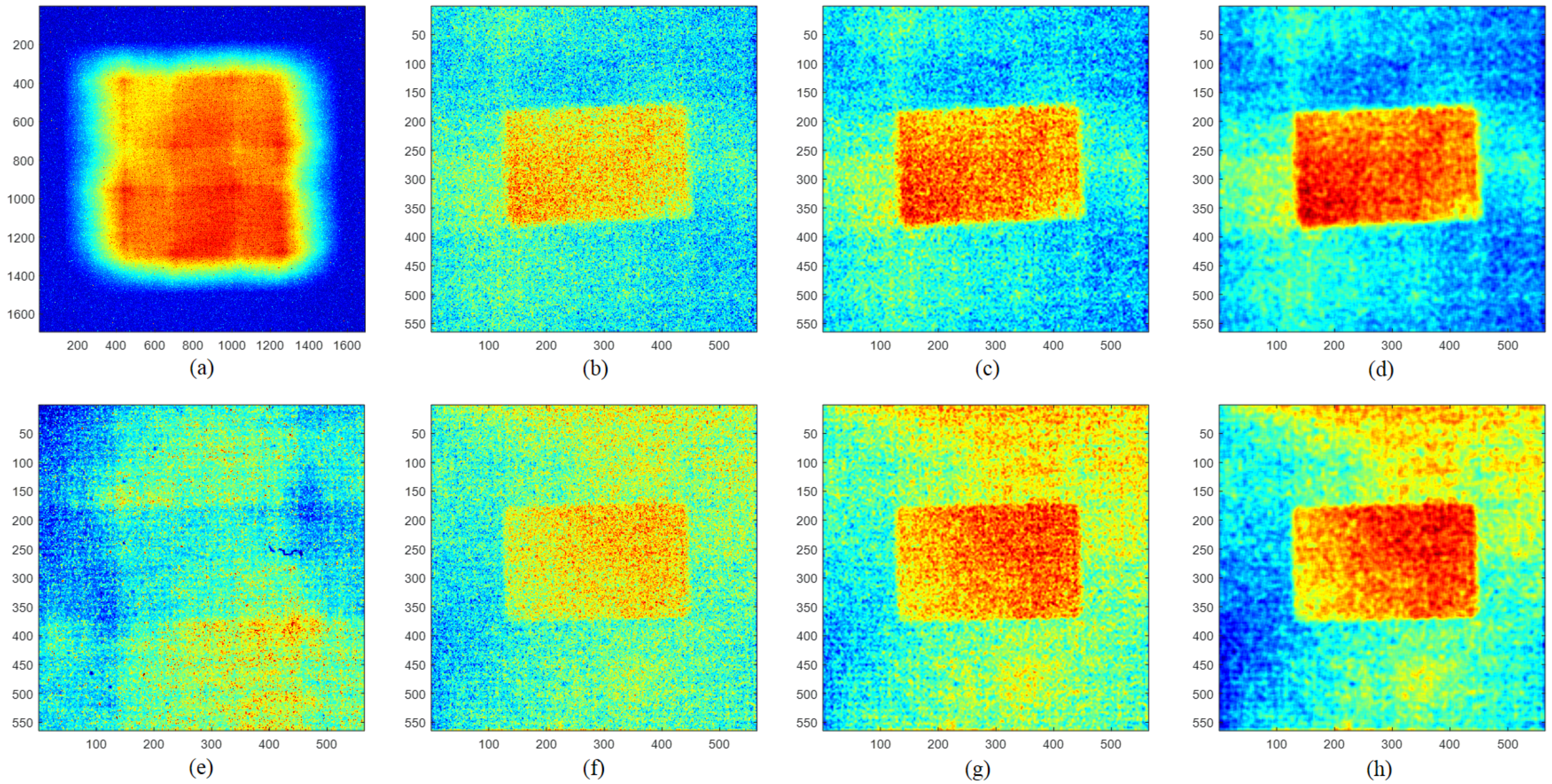

(a) (b) (c) (d)

(e) (f) (g) (h)

Figure 5.25 (a) The complete image of a rectangular opening, taken with the 200 µm mask and scintillator system at magnification of 4, and the reconstructed image with complete correlation method when (b) κ=1, (c) κ=4, and (b) κ=8. (e) The center portion of the image that can be used alone for reconstruction, and the reconstructed image with basic correlation method when (f) κ=1, (g) κ=4, and (h) κ=8.

In order to evaluate the effects of the magnification factor and the value of κ on reconstruction quantitatively, resolution and SNR were measured in the reconstructed images of the rectangular opening. The resolution was obtained as the width between 10% and 90% values of the ESF at one of the edges. The SNR was obtained as the ratio of the contrast between the open and the closed area over the standard deviation of the pixel values in the open area.

Table 5.3 shows the resolution and SNR measured from reconstructed results shown in Figure 5.23, with the magnification factor of 2 and the κ values of 1, 2 and 4. It can be seen that the resolution of the basic correlation image is much better than the one of the complete correlation image. But the complete correlation image provides higher SNR than the basic correlation image. As the κ value increases, the resolution of the reconstruction image gets larger (poorer sharpness) and the SNR gets higher (smoother image), which agree with the observations of the images. It should be noted that comparing to the complete correlation image, the resolution of the basic correlation image is much closer to the expected values calculated by Equation (3.36).

Table 5.3 The resolution and SNR measured from reconstructed results in Figure 5.23 (b)-(d) and (f)-(h). (the effect of κ value)

Reconstruction	Values for analysis	The value of κ		
		1	2	4
Expected resolution		185 µm	192 µm	238 µm
Complete correlation	resolution	280 ± 36 µm	283 ± 28 µm	313 ± 17 µm
	SNR	6.02	7.41	10.01
Basic correlation	resolution	205 ± 31 µm	227 ± 24 µm	248 ± 24 µm
	SNR	3.29	3.85	5.52

Table 5.4 shows the resolution and SNR measured from reconstructed results shown in Figure 5.23 (h), Figure 5.24 (g) and Figure 5.25 (g), respectively. These images were reconstructed from measurements at different magnification factors. And they were all obtained from the results using basic correlation with κ value of 4. The measured resolutions are slightly larger than the expected values calculated by Equation (3.36). By comparison, the resolution is enhanced as the magnification factor increases, while the SNR gets smaller with larger magnification factor.

Table 5.4 The resolution and SNR measured from basic correlation results Figure 5.23 (h), Figure 5.24 (g) and Figure 5.25 (g). (the effect of magnification factor)

Magnification factor	Expected resolution	Measured resolution	SNR
2	238 µm	248 ± 24 µm	5.52
3	196 µm	205 ± 15 µm	5.14
4	185 µm	192 ± 15 µm	4.05

5.5.3 Measurements with 100 µm Mask

The 100 µm mask was used with the scintillator system at the optimal settings. The pixel size was set to be 60 µm, which was the smallest value that can be achieved with the current Lens and the camera box. The size that is available for imaging is 12.29 cm×12.29 cm, since the CCD are composed with a 2048×2048 array of pixels. A cyclic arrangement must be used in this setup due to the limited size of the detector. The mask pattern is a 178×178 mosaicked MURA. The magnification factor can be set from 2.2 to 4, an increment of 0.6, limited by the available beam length.

With a magnification factor m, the mask pinhole projection on the image plane has a diameter of 100(m-1) µm, covering 1.67(m-1)×1.67(m-1) pixels. The mask grid projection on the image plane covers 3.33(m-1)×3.33(m-1) pixels. For the correlation reconstruction, the value of κ can be any integer between 1 and 3.33(m-1). The expected system resolution can be calculated based on Equation (3.36). Table 5.5 lists the calculations when the value of κ equals to 1, 4, and 8 at different magnification factors. When κ value equals to 4, the resolution shows an obvious improvement with the available magnification factors and approaches the size of mask pinhole at magnification 4. Therefore, the κ value was set to be 4 to reconstruct the images taken with this mask.

Table 5.5 The expected resolution in the reconstructed images with the use of 100 µm mask

Mag (m)	κ = 1				κ = 4				κ = 8			
	①	②	③	System res.	①	②	③	System res.	①	②	③	System res.
2.2	55	111	0	124 µm	55	111	82	149 µm	--	--	--	--
2.8	64	88	0	109 µm	64	88	64	126 µm	64	88	150	185 µm
3.4	71	72	0	101 µm	71	72	53	114 µm	71	72	124	160 µm
4	75	61	0	97 µm	75	61	45	107 µm	75	61	105	143 µm

Note: ①②③ have the same definitions as the ones in Table 5.2;

Based on the results in Section 2.4.2, the resolution of conventional system was measured to be 245 ± 6 µm;

All the calculated results are given in the unit μm.

The object used in the measurement was the 8 mm × 5 mm rectangular opening on 200 µm-thick gadolinium foil, the same one shown in Figure 5.21 (b). The measurements were taken at four different magnification factors: 2.2, 2.8, 3.4 and 4. The exposure times were 900 seconds, 1920 seconds, 3300 seconds and 5700 seconds, respectively.

5.5.3.1 Reconstruction with complete, basic and combined correlation methods

The recorded image needs to be pre-conditioned prior to reconstruction. At each magnification, two images were taken at the same location with the same detector settings. One was a coded image of the object, and the other one was a flat image without the removable part of the extension tube. The mean values and the standard deviations were then taken for both images. All the pixel values more than three standard deviations away from the mean were replaced by the cut-off value. Both images were then de-noised by a 4×4 median filter. The division of the coded image and the flat image was finally used as the input image for reconstruction.

Complete Correlation and Basic Correlation

Figure 5.26 shows the recorded images and the reconstructed results at magnification factor of 2.2. Figure 5.26 (a) is the complete image for reconstruction. It had a size of 6.41 cm×6.41 cm, equivalent to 1068×1068 pixels. Figure 5.26 (b) is the corresponding results obtained by complete correlation. Figure 5.26 (c) is the 356×356 pixels in the center of the complete image, which can be used alone for the reconstruction with the basic correlation method and Figure 5.26 (d) is the corresponding reconstructed image.

Quantitative analysis has been performed on the two reconstructed images. The results are listed in Table 5.6. The expected resolution was calculated using Equation (3.36). The measured resolution was the width of ESF. The details of measurements are shown from Figure 5.27 to Figure 5.29.

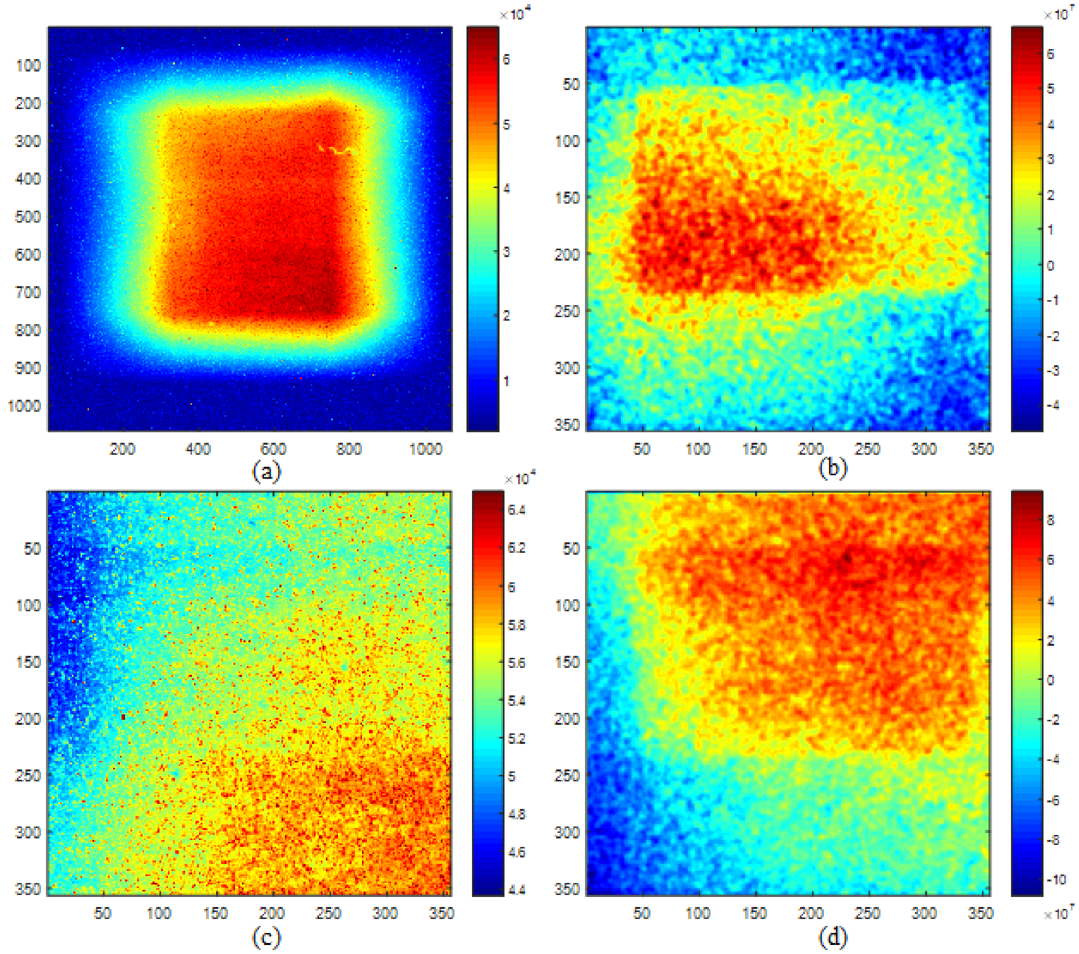

(a) (b) (c) (d)

Figure 5.26 (a) The complete image of a rectangular opening, taken with the 100 µm mask and scintillator system at magnification of 2.2. (b) The reconstructed image with complete correlation method. (c) The center portion of the image that can be used alone for reconstruction. (d) The reconstructed image with basic correlation method.

Table 5.6 The resolution and SNR measured from reconstructed results at magnification factor of 2.2.

Reconstruction	Expected resolution	Measured resolution	Contrast	SNR
Complete correlation	148.6 µm	167.5 ± 11.5 µm	1.54×10^{7}	2.32
Basic correlation		157.0 ± 11.8 µm	4.31×10^{6}	3.24

First of all, an area including 1 mm-long edge was selected on the reconstructed image, as shown within the white dashed lines in Figure 5.27 (a). ESF was calculated as the mean value of each column across the edge in the selected area. It is shown as the black dots in Figure 5.27 (b). Since the edge was still clearly defined, its starting point and ending point, as circled in the plot, were used as the 0% and 100% values for the edge. The 10% and 90% values were then determined and the distance rising from 10% to 90% was measured as the resolution.

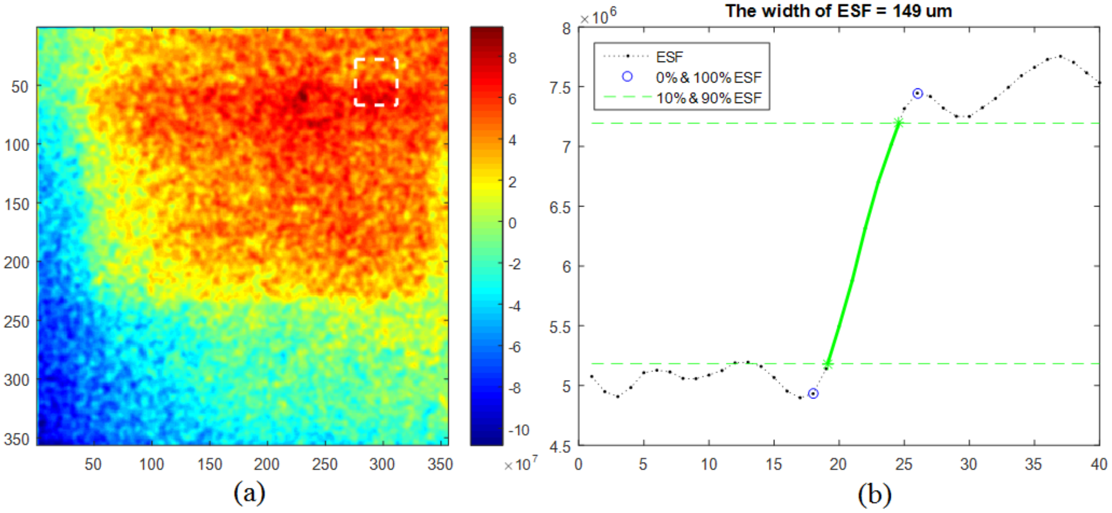

Figure 5.27 (a) An area (inside of the dashed lines) of the basic correlation result at magnification 2.2 was selected to be analyzed. (b) The ESF obtained in the selected area and the width of the ESF as resolution.

This procedure was then repeated in four other sections along the edge and the obtained ESF's are shown in Figure 5.28. Figure 5.29 plots the widths of all the five ESF's rising from 10% to 90%. The mean and the standard deviation of these values were 157.0 μm and 11.8 μm, which were reported as the measured resolution and the uncertainty.

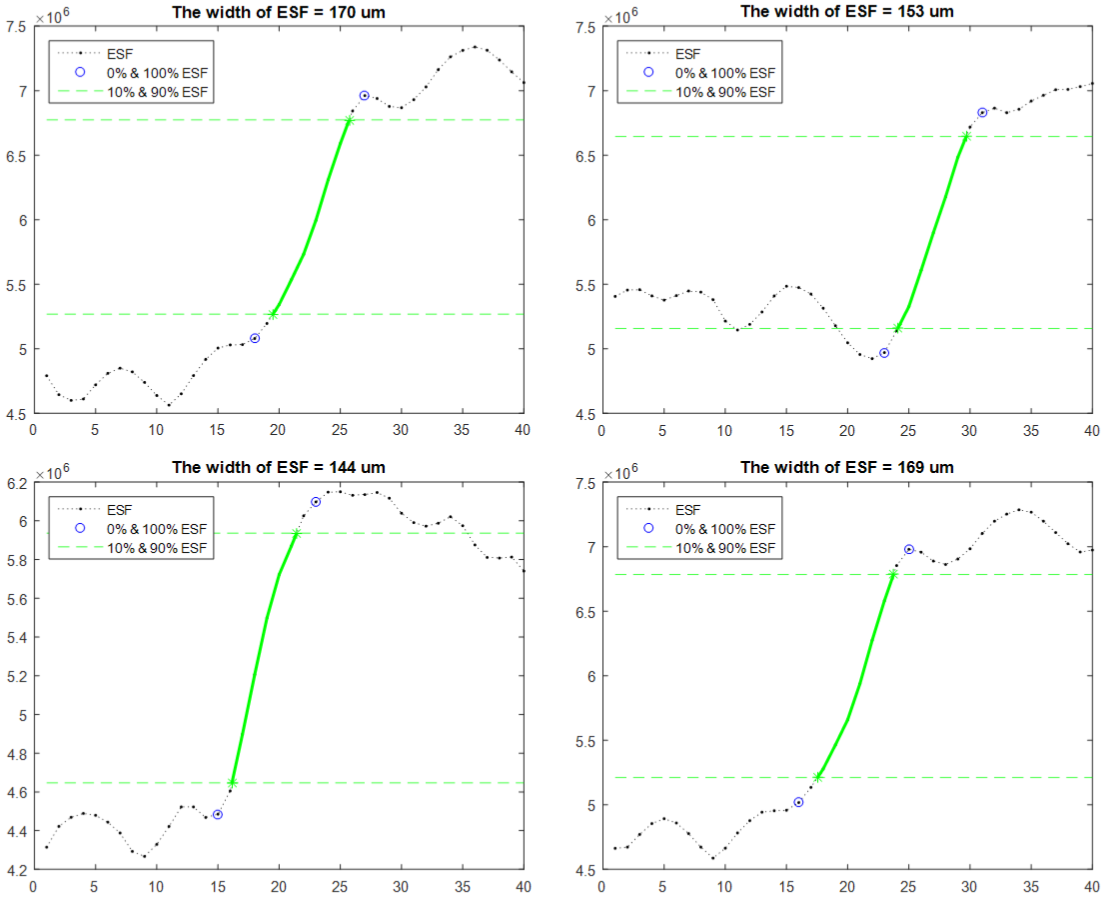

Figure 5.28 The resolution measured in other four sections of the edge in Figure 5.27 (a).

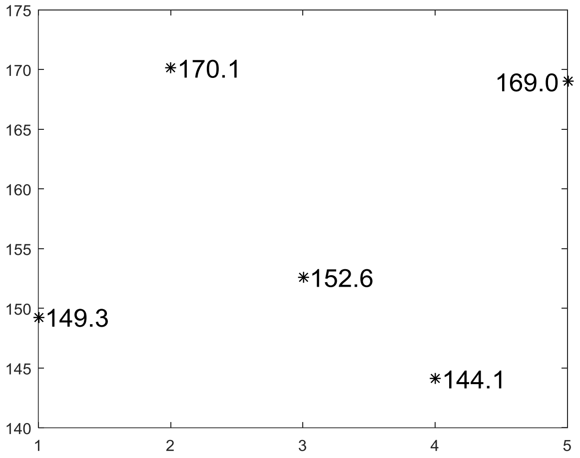

Figure 5.29 The 10% to 90% width of five ESF’s shown in Figure 5.28 (b) and Figure 5.28

Figure 5.30 shows resolution measurement on the reconstructed image using the complete correlation method. Figure 5.30 (a) – (e) are five ESF's obtained in different sections of the edges. Figure 5.30 (f) plots the width of each ESF rising from 10% to 90%. The resolution and uncertainty, which were the mean and the standard deviation of these values, was 167.5 ± 11.5 μm.

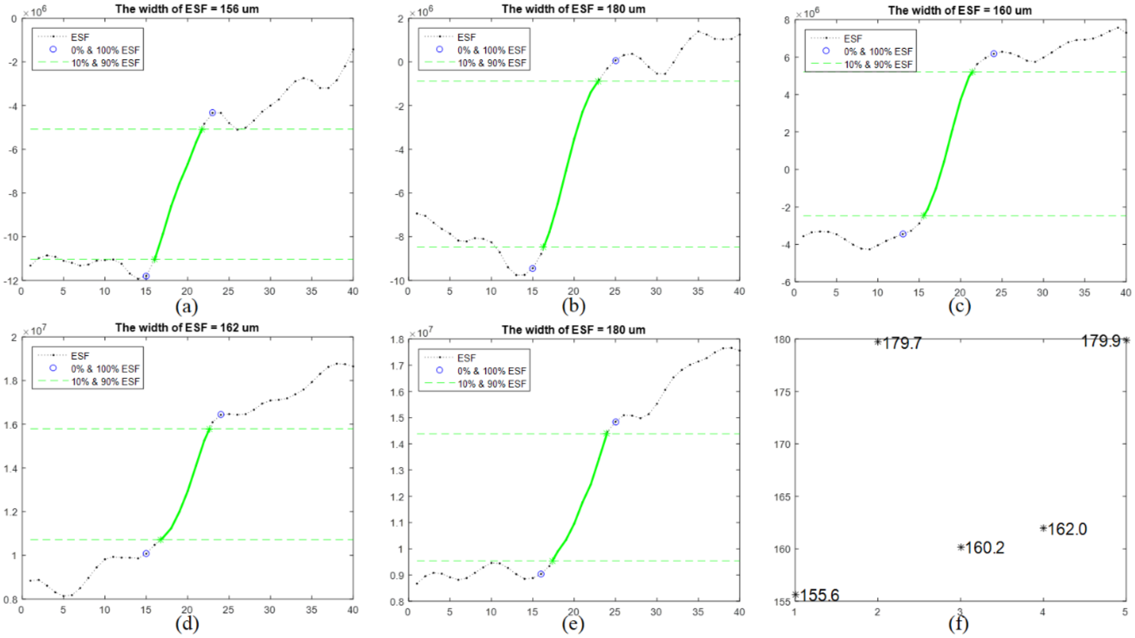

(a) (b) (c)

(d) (e) (f)

Figure 5.30 (a) – (e) Five ESF's obtained in different sections of the edges on the complete correlation result at magnification 2.2. (f) The 10% to 90% width of the ESF's.

The contrast was the difference between the means of pixel values in the open area and the opaque area of the object. The SNR was the contrast divided by the standard deviation of the pixel values in the open area. In order to exclude the influence of the edges on the results, two areas were selected as shown in Figure 5.31. The area inside of Box I was used to represent the rectangular opening; the area outside of Box II was used to represent the gadolinium foil.

Figure 5.31 (a) and (b) are corresponding to the complete correlation result and the basic correlation result, respectively. The positions of the boxes are the same in the two figures.

The resolution of the basic correlation result was close to the expected value, while the one of the complete correlation result was slightly larger. The degradation could be due to several reasons. First, it can be introduced by the difference between the real mask and the design. The complete correlation utilizes signals from more mask pinholes than the basic correlation does, thus the degradation is larger. Second, it could be due to the non-uniformity in the recorded image. From the flat image in Figure 5.18, it is known the camera response is higher in the center portion than the borders. The image used with complete correlation is nine times as large as the one used with basic correlation. The non-uniformity made more impact on the quality of the complete correlation result.

The contrast of the complete correlation result is 3.6 times as high as the basic correlation result. This is because the complete image includes three times more object

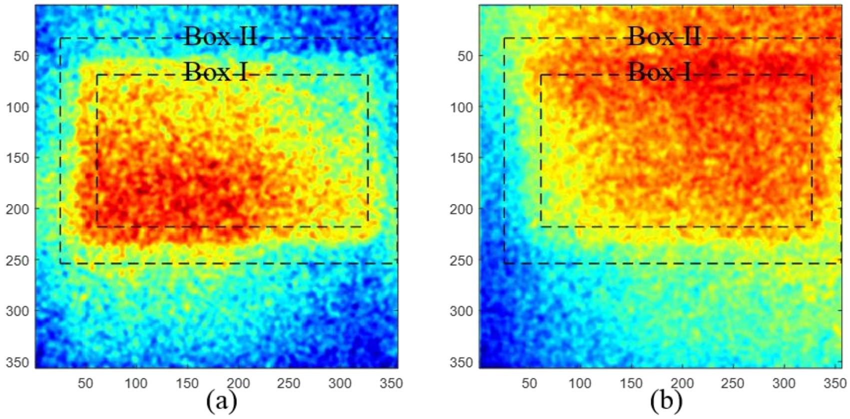

(a) (b)

Figure 5.31 The area inside of Box I and the area outside of Box II were considered as signal and background, on (a) the complete correlation result and (b) the basic correlation result at magnification factor of 2.2.

projections than the center portion used with basic correlation.

However, the SNR of the complete correlation result was smaller than the basic correlation result, indicating that the variance of the former reconstructed image was much larger than the one of the latter. As discussed in resolution analysis, it was due to the non-uniformity of the input images for reconstruction.

Combined Correlation

Since the image used in the basic correlation is the exact center of the image used in the complete result and the decoding arrays are the same, the object locates in the same position and the distributions of artifacts due to non-uniformity are almost complementary on the two reconstructed images. The artifacts can be noticeable reduced in the weighted sum of two images. To balance the contrasts, the basic correlation result is given weight three to four times as high as the weight of the complete correlation result. The summation is referred as the result of combined correlation.

Figure 5.32 (a) is the result of combined correlation at magnification of 2.2. The ratio of the weight for complete correlation result to the weight for basic correlation result was set to be 1 to 3.4. Figure 5.32 (b) shows the boundaries of the signal area and the background area for SNR calculation. With the weight ratio of 1:3.4, the SNR was maximized to be 6.2. The resolution was also measured on this image. Figure 5.33 shows the five ESF's obtained along the edge and the width of each ESF rising from 10% to 90%. The resolution of the combined correlation result was measured to be 153.2 ± 4.7 µm.

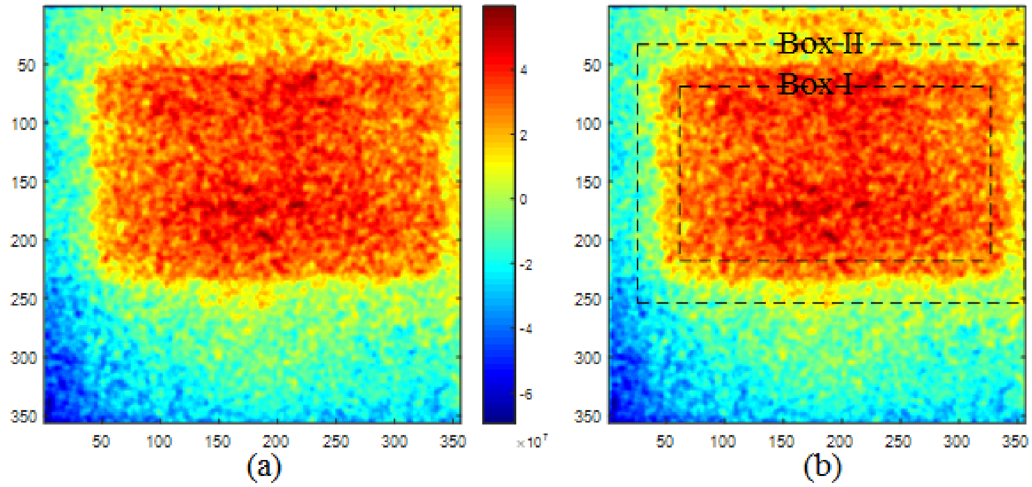

Figure 5.32 (a) The results of the combined correlation at magnification factor of 2.2. (b) The open area (inside of Box I) and the background area (outside of Box II) selected for SNR calculation.

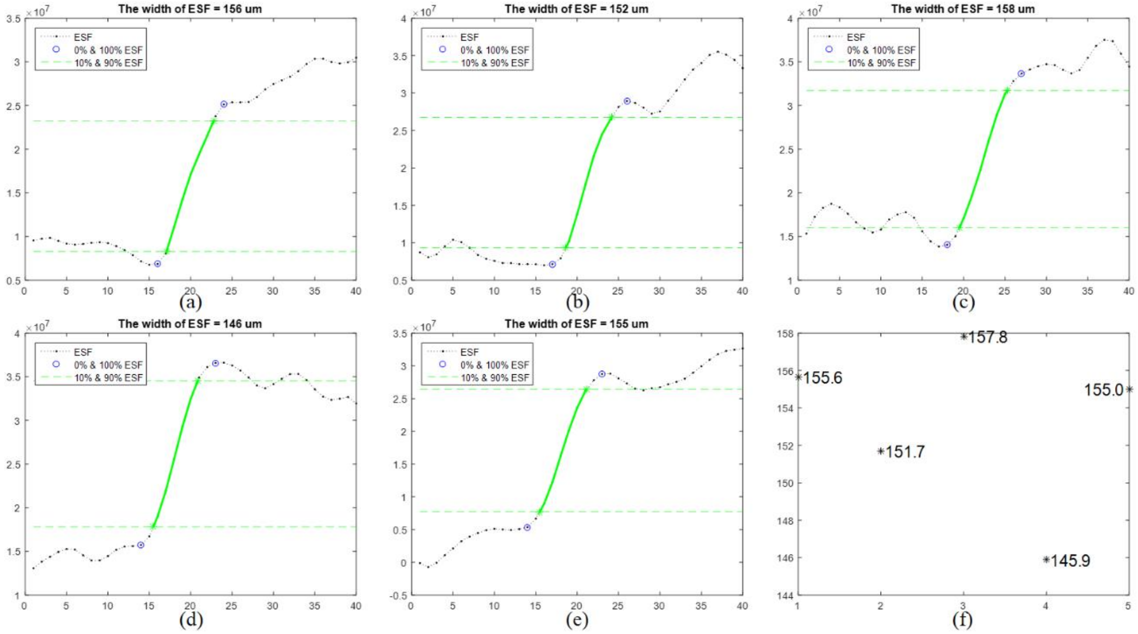

Figure 5.33 (a) – (e) Five ESF's obtained in different sections of the edges on the combined correlation result at magnification 2.2. (f) The 10% to 90% width of the ESF's.

Compared to the measured values listed in Table 5.6, the combined correlation produced an image with similar resolution as basic correlation, but with SNR much higher than the other two correlation methods.

5.5.3.2 Reconstruction at different magnification factor

The experiments have also been conducted at magnification of 2.8, 3.4 and 4.0. The recorded images and the reconstructed results are shown in this section. The resolution and SNR were measured at each magnification factor.

Magnification factor of 2.8

Figure 5.34 shows the recorded images and the reconstructed results at magnification factor of 2.8. Figure 5.34 (a) is the complete image for reconstruction. It had a size of 9.61 cm×9.61 cm, equivalent to 1602×1602 pixels. Figure 5.34 (b) is the corresponding results obtained by complete correlation method. Figure 5.34 (c) is the 534×534 pixels in the center of the complete image, which can be used alone for the reconstruction with basic correlation method and Figure 5.34 (d) is the corresponding reconstructed image. Figure 5.34 (e) is the combined correlation result, which was the weighted sum of the complete correlation result and the basic correlation result. The ratio of two weights was 1 to 4.

The SNRs were calculated with the signal area and the background area with the boundaries defined as in Figure 5.35. The SNR of the reconstructed images with complete correlation, basic correlation and combined correlation were 1.90, 1.95 and 3.11.

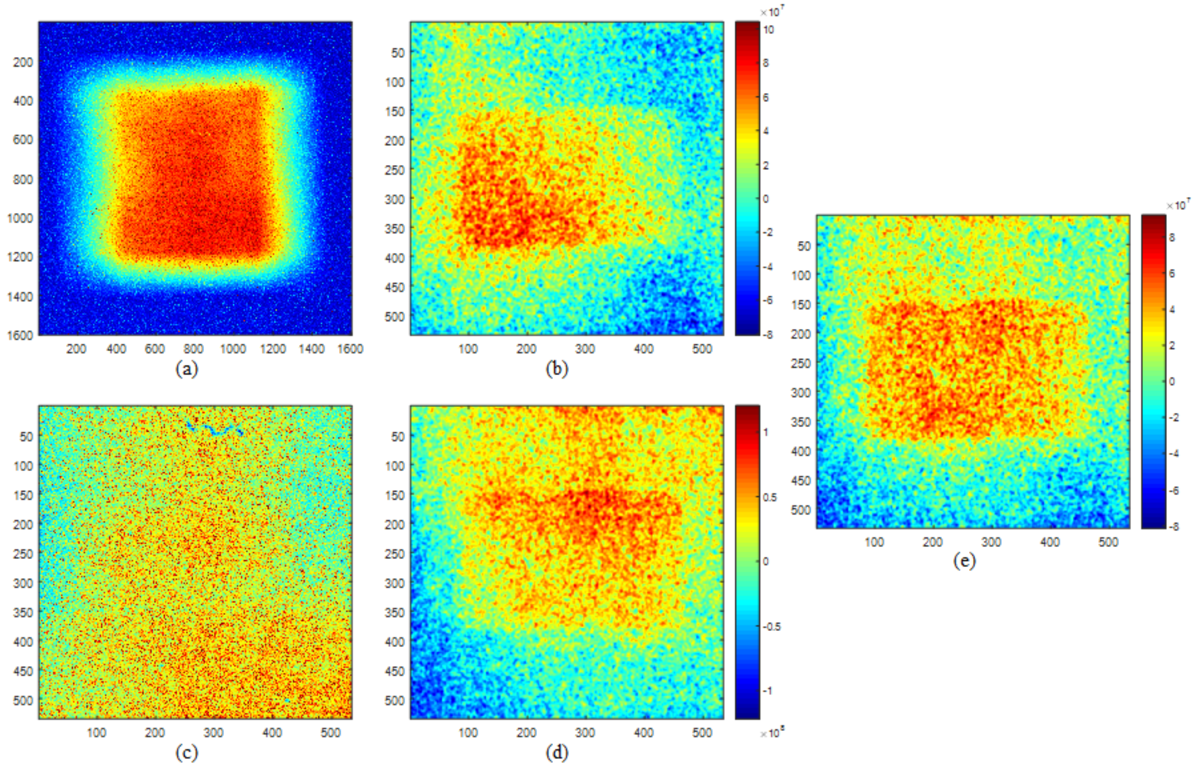

Figure 5.34 (a) The complete image of a rectangular opening, taken with the 100 µm mask and scintillator system at magnification of 2.8. (b) The result of complete correlation. (c) The center portion of the image that can be used alone for the reconstruction. (d) The result of basic correlation. (d) The result of combined correlation.

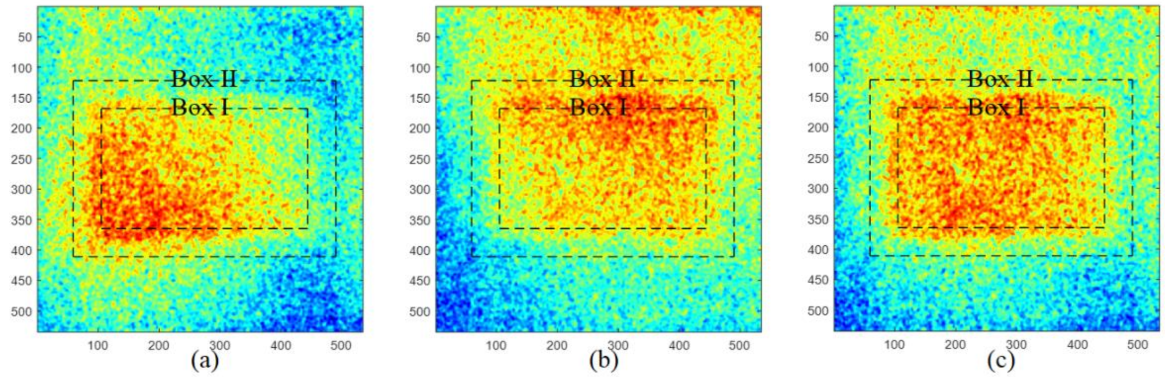

Figure 5.35 The open area (inside of Box I) and the background area (outside of Box II) selected for SNR calculation on the reconstructed images at magnification of 2.8 with (a) complete correlation, (b) basic correlation and (c) combined correlation.

Figure 5.36, Figure 5.37 and Figure 5.38 shows the resolution measurement of the reconstructed images using complete correlation, basic correlation and combined correlation. Figure (a) – (e) are five ESF's obtained in different sections of the edges. Figure (f) plots the width of each ESF rising from 10% to 90%. The resolution of the complete correlation result was 138.2 ± 21.6 µm. The resolution of the basic correlation result was 127.7 ± 16.4 µm. The resolution of the combined correlation result was 124.7 ± 11.3 µm.

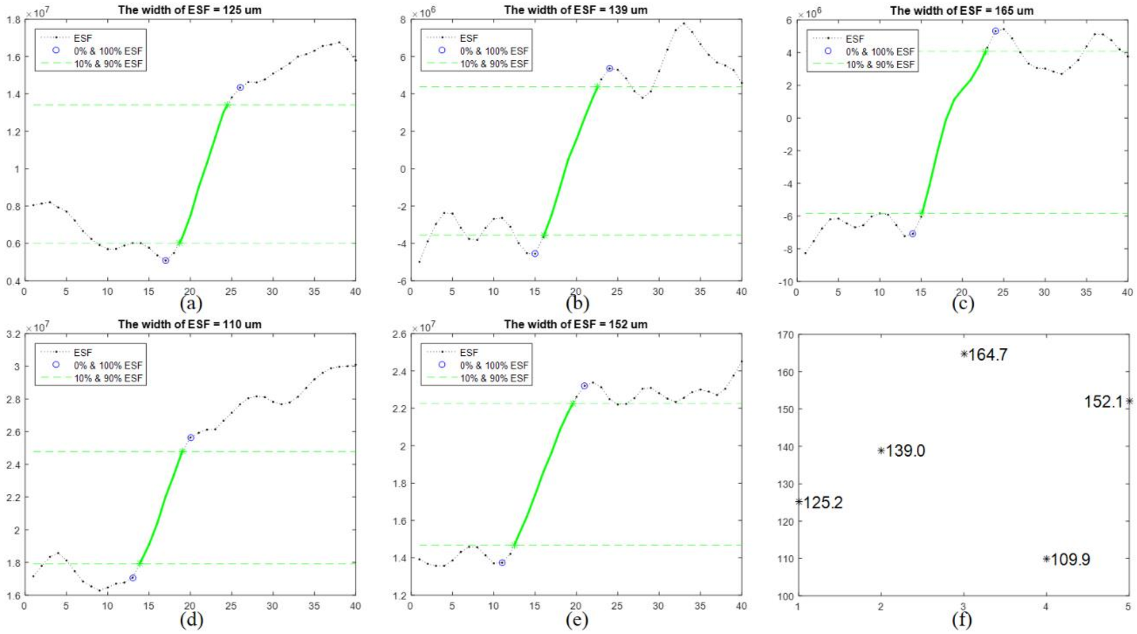

Figure 5.36 (a) – (e) Five ESF's obtained in different sections of the edges on the complete correlation result at magnification 2.8. (f) The 10% to 90% width of the ESF's.

Magnification factor of 3.4

Figure 5.39 shows the recorded images and the reconstructed results at magnification factor of 3.4. Based on the size of the rectangular opening (0.8 cm×0.5 cm) and the size of the mask (3.56 cm×3.56 cm), the size of the image was calculated to be 11.26 cm×10.24 cm,

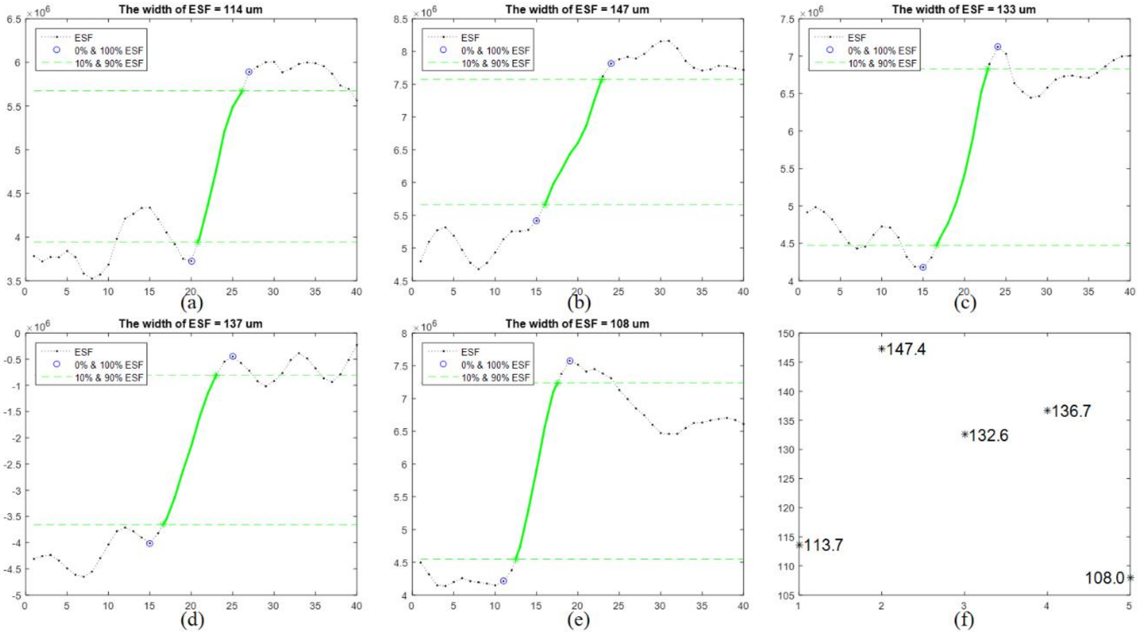

Figure 5.37 (a) – (e) Five ESF's obtained in different sections of the edges on the basic correlation result at magnification 2.8. (f) The 10% to 90% width of the ESF's.

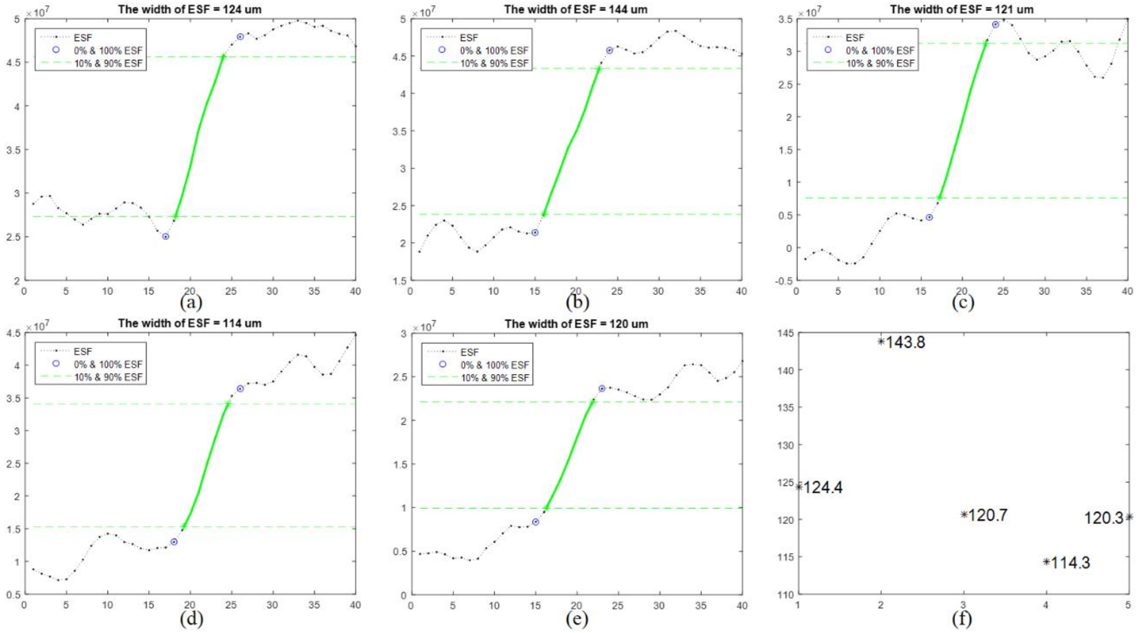

Figure 5.38 (a) – (e) Five ESF's obtained in different sections of the edges on the combined correlation result at magnification 2.8. (f) The 10% to 90% width of the ESF's.

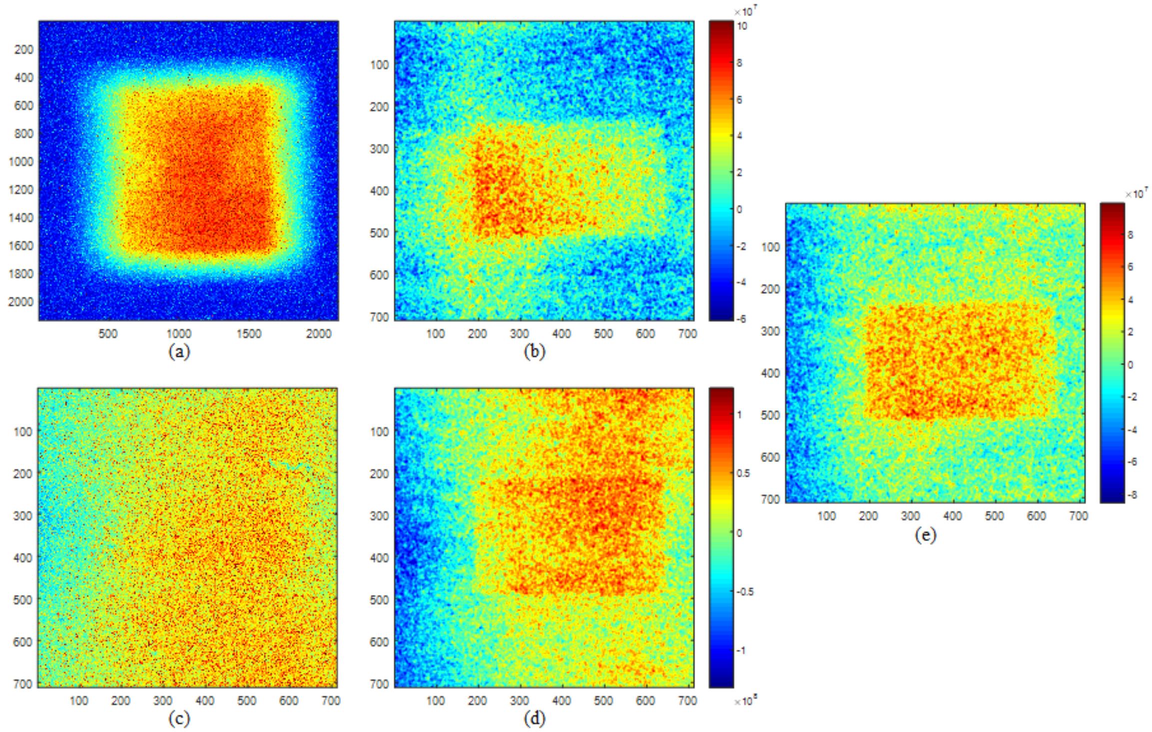
(a) (b) (c) (d) (e)

Figure 5.39 (a) The complete image of a rectangular opening, taken with the 100 µm mask and scintillator system at magnification of 3.4. (b) The result of complete correlation. (c) The center portion of the image that can be used alone for the reconstruction. (d) The result of basic correlation. (e) The result of combined correlation.

according to Equation (3.38). It was smaller than 12.29 cm×12.29 cm, which is the area that can be captured by 2048×2048 pixels of the CCD. However, the size of the image to be used with complete correlation was 12.82 cm×12.82 cm, equivalent to 2136×2136 pixels, which is larger than 2048×2048 CCD pixels. Since the missed pixels were due to noise, it was reasonable to fill them with the measured noise. The recorded image was mosaicked as illustrated in Figure 3.15 and then 2136×2136 pixels in the center was selected as the complete image. It is shown in Figure 5.39 (a) is the complete image for reconstruction. Figure 5.39 (b) is the corresponding results obtained by complete correlation method. Figure 5.39 (c) is the 712×712 pixels in the center of the complete image, which can be used alone for the reconstruction with basic correlation method and Figure 5.39 (d) is the corresponding reconstructed image. Figure 5.39 (e) is the combined correlation result, which was the weighted sum of the complete correlation result and the basic correlation result. The ratio of two weights was 1 to 3.3.

Figure 5.40 shows the boundaries of the two areas for SNR calculation. The area inside of Box I was used to represent the rectangular opening of the object. The area outside of Box II was used to represent the gadolinium foil of the object. The contrast was the difference between the means of pixel values in two areas. The SNR was the contrast divided by the standard deviation of the pixel values in the open area. The SNR of the reconstructed images with complete correlation, basic correlation and combined correlation were 2.19, 2.11 and 3.34, respectively.

Figure 5.41, Figure 5.42 and Figure 5.43 shows the resolution measurement of the reconstructed images using complete correlation, basic correlation and combined correlation. Figure (a) – (e) are five ESF's obtained in different sections of the edges. Figure (f) plots the

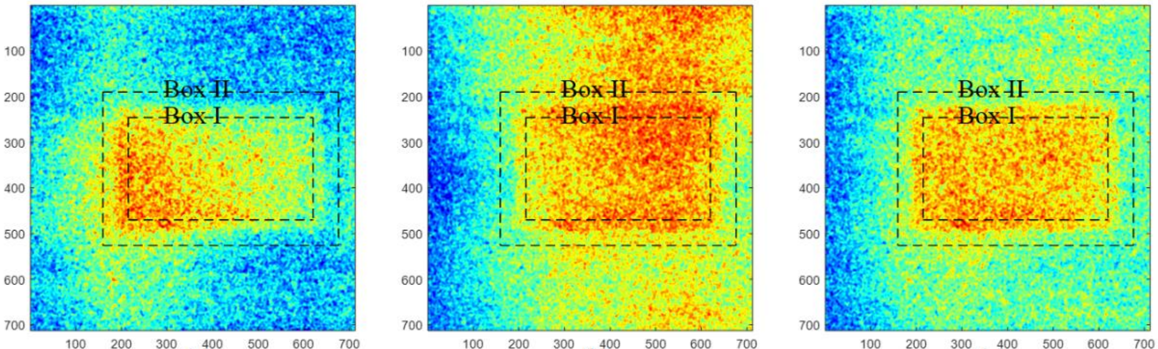

(a) (b) (c)

Figure 5.40 The open area (inside of Box I) and the background area (outside of Box II) selected for SNR calculation on the reconstructed images at magnification of 3.4 with (a) complete correlation, (b) basic correlation and (c) combined correlation.

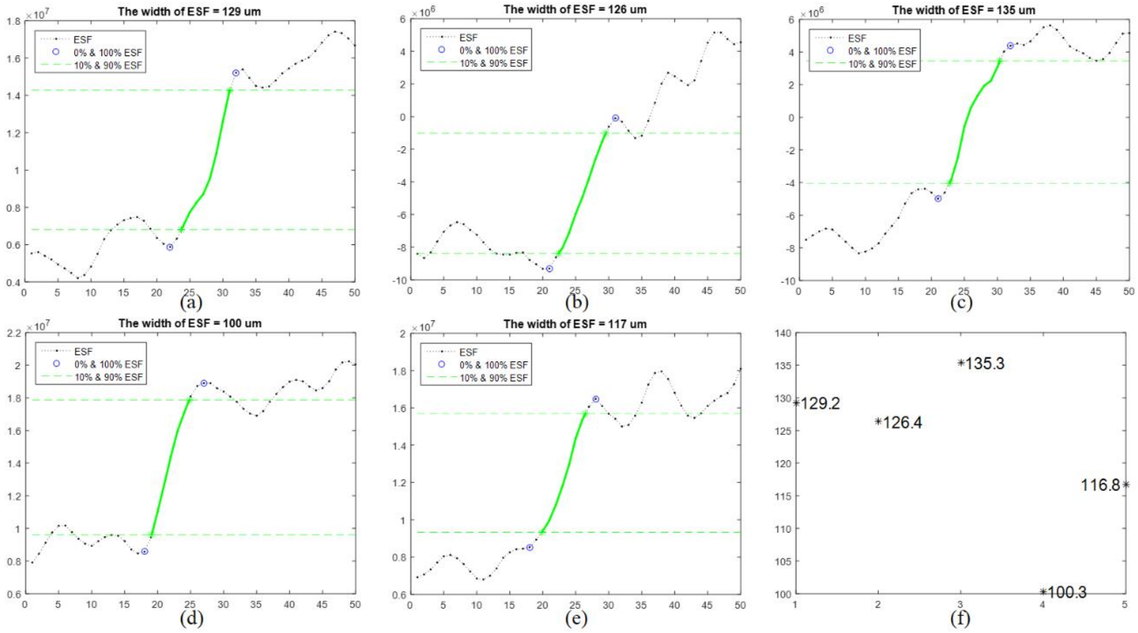

Figure 5.41 (a) – (e) Five ESF's obtained in different sections of the edges on the complete correlation result at magnification 3.4. (f) The 10% to 90% width of the ESF's.

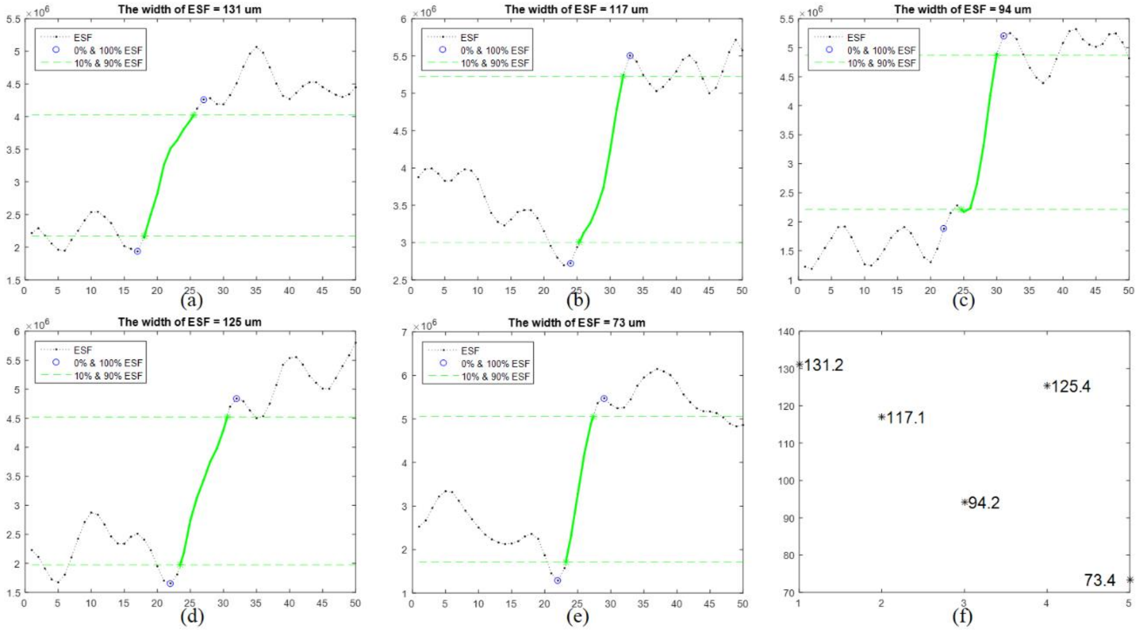

Figure 5.42 (a) – (e) Five ESF's obtained in different sections of the edges on the basic correlation result at magnification 3.4. (f) The 10% to 90% width of the ESF's.

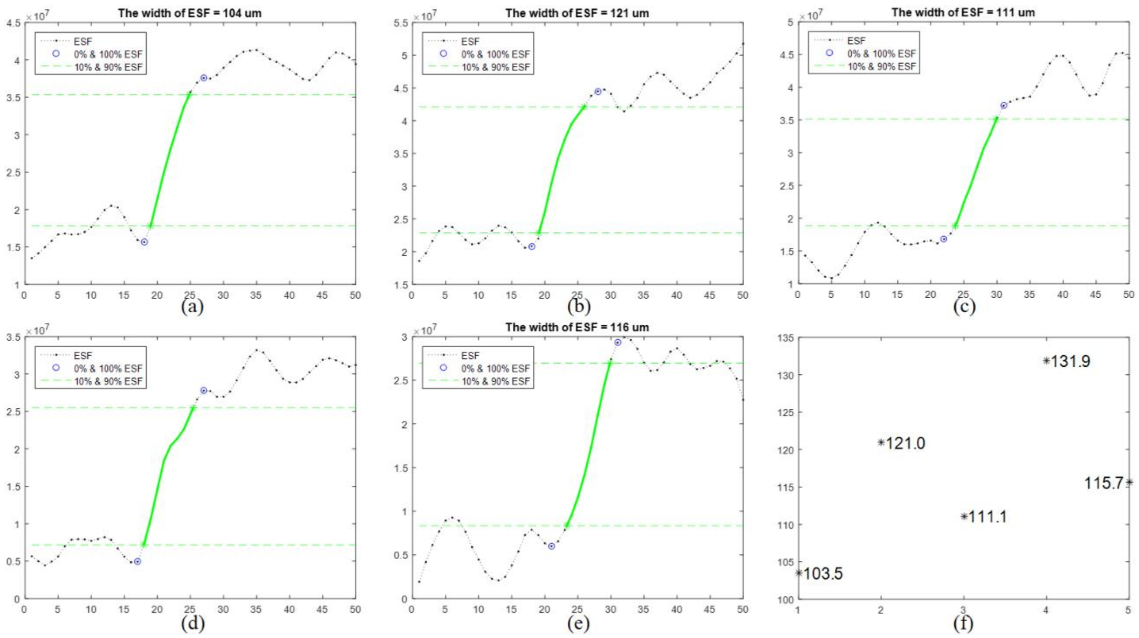

Figure 5.43 (a) – (e) Five ESF's obtained in different sections of the edges on the combined correlation result at magnification 3.4. (f) The 10% to 90% width of the ESF's.

width of each ESF rising from 10% to 90%. The resolution of the complete correlation result was 121.6 ± 13.7 µm. The resolution of the basic correlation result was 108.3 ± 24.0 µm. The resolution of the combined correlation result was 116.6 ± 10.7 µm.

Magnification factor of 4

Figure 5.44 shows the recorded images and the reconstructed results at magnification factor of 4. The size of the image at magnification factor of 4 was expected to be 13.88 cm×12.68 cm, which was larger than the area that can be captured by the CCD. Unlike the situation at magnification factor of 3.4, the recorded image, as shown in Figure 5.44 (a), did not contain all the signals related to the entire mask. Thus padding the borders of the image cannot be applied in this case. Only basic correlation can be used for reconstruction. Figure

5.44 (a) shows the recorded image with 2048×2048 pixels. Figure 5.44 (b) shows the 890×890 pixels of pre-conditioned image that can be used for the reconstruction with basic correlation method and Figure 5.44 (c) is the corresponding reconstructed image. The SNR of the reconstructed image were calculated to be 1.25, with the open area and the background area with the boundaries defined as in Figure 5.44 (d).

Figure 5.45 shows the resolution measurement of the reconstructed image. Figure 5.45 (a) – (e) are five ESF's obtained in different sections of the edges. Figure 5.45 (f) plots the

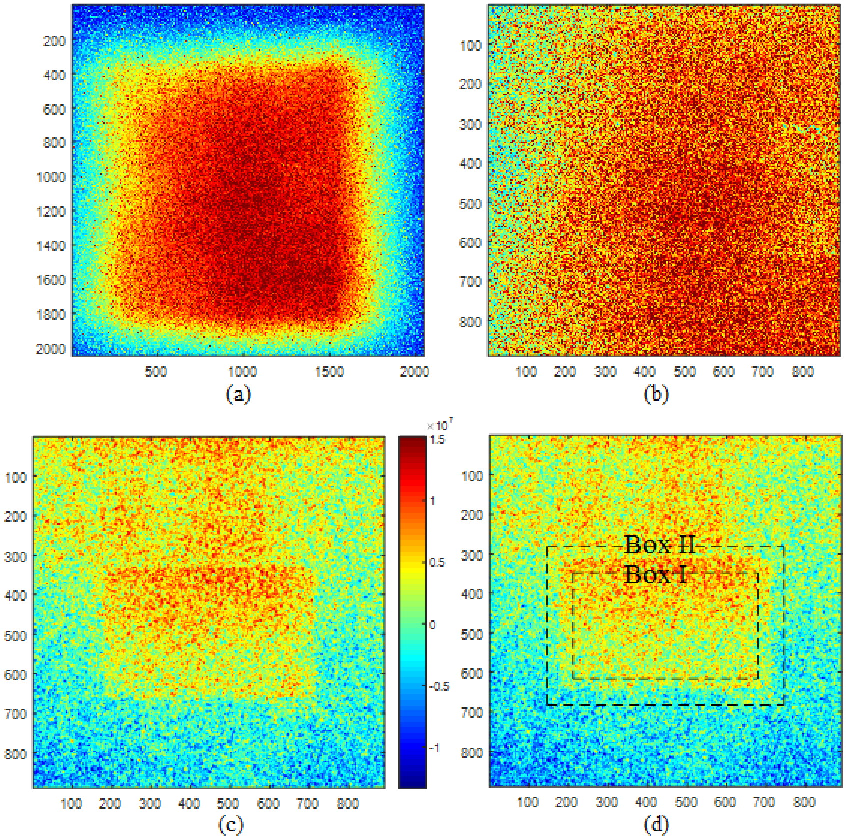

(a) (b)

(c) (d)

Figure 5.44 (a) The recorded image of a rectangular opening, taken with the 100 μm mask and scintillator system at magnification of 4. (b) The center portion of the image that can be used alone for the reconstruction. (c) The result of basic correlation. (d) The open area (inside of Box I) and the background area (outside of Box II) selected for SNR calculation on the reconstructed image.

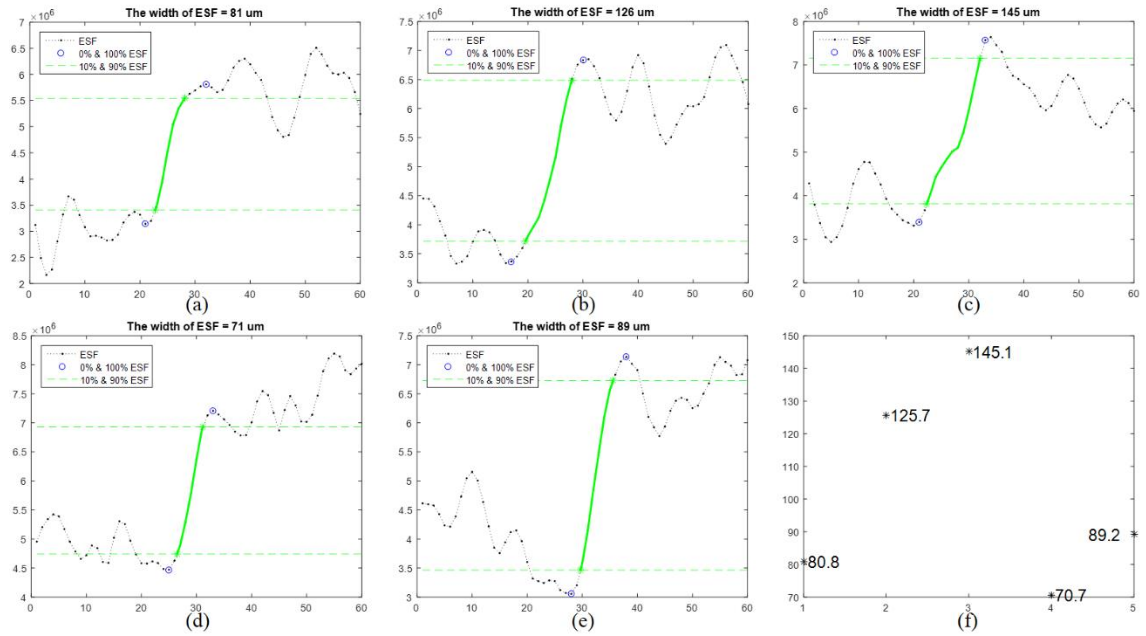

Figure 5.45 (a) – (e) Five ESF's obtained in different sections of the edges on the basic correlation result at magnification 4. (f) The 10% to 90% width of the ESF's.

width of each ESF rising from 10% to 90%. The resolution of the basic correlation result was 102.3 ± 31.7 μm.

Table 5.7 sums up the quantitative analysis results of the reconstructed images with three correlation methods at different magnification factors. The value of κ was set to be 4 in all the cases. The expected values were calculated by Equation (3.16).

Table 5.7 The resolution and SNR measured from results with three correlation methods at different magnifications

m	Expected resolution	Complete correlation		Basic correlation		Combined correlation	
		Resolution	SNR	Resolution	SNR	Resolution	SNR
2.2	148.6 μm	167.5±11.5 μm	2.32	157.0±11.8 μm	3.24	153.2±4.7 μm	6.15
2.8	126.2 μm	138.2±21.6 μm	1.90	127.7±16.4 μm	1.95	124.7±11.3 μm	3.11
3.4	113.9 μm	121.6±13.7 μm	2.19	108.3±24.0 μm	2.11	116.6±10.7 μm	3.34
4.0	106.8 μm			102.3±31.7 μm	1.25		1.25

The resolution approached to the size of the pinholes on the mask with the magnification factor increasing. The uncertainties were related to the SNR values. The resolution measurements were more stable (smaller uncertainty) on the images with larger SNR's. The reconstructed images obtained with complete correlation usually had larger resolution, while basic correlation and combined correlation produced reconstructed results with resolutions close to the expected values calculated using the mathematical model of the REMANI system.

The SNR depends on many aspects, such as the magnification factor, the exposure time, and the non-uniformity of the recorded image. Therefore, it is hard to conclude the effects of magnification on the SNR's of the reconstructed image. However, the effects of non-uniformity due to the detector response and neutron field on the reconstructed images can be largely reduced with the use of combined correlation. The combined correlation produced images with higher SNR than the other two correlation methods.

5.6 Other Reconstruction Methods

Besides the correlation method, the maximum likelihood solution and the least square solution can also be used as the reconstruction methods for the REMANI system. In this section, the quality of the reconstructed images obtained with different methods have been analyzed.

For the maximum likelihood estimations (MLE), Richard-Lucy algorithm as shown in Equation (3.28) was used. The flat images de-noised by a median filter was used as the weight of each pixel values. For the least square estimations (LSE), Tikhonov Regularization as shown in Equation (3.30) was used. The Tikhonov matrix was chosen to be Identity matrix. The conjugate gradient iterative technique (Mishra, 2010) has been implemented to solve the least square problems. Both methods involve iterative calculations, but the rate of convergence is different. The algorithm was run in a step of 10 iterations until an optimal solution was reached.

5.6.1 Measurements with 200 µm Mask

The first example is the image of the 12 pinholes as shown in Figure 5.22 (a), which was taken with the 200 µm mask at magnification of 2. Figure 5.46 shows the MLE reconstructed solutions with a step of 50 iterations. Figure 5.47 shows the LSE reconstructed solutions with a step of 20 iterations. It can be seen that the artifacts reduced with more iterations. The MLE solution was stable after about 150 iterations. The LSE solution was stable after about 60 iterations.

Two iterative reconstruction methods were also applied to the image shown in Figure 5.23 (a), which was the image of the rectangular opening taken with the 200 µm mask at magnification of 2. Figure 5.48 shows the MLE reconstructed images with a step of 50 iterations. Figure 5.49 shows the LSE reconstructed images with a step of 20 iterations.

The SNR in the reconstructed image decreased with the number of iterations for both methods. In MLE, iterations were used to approach a solution that maximized probability of producing the recorded image based on the forward model and Poisson noise. The MLE solution might not be convergent. Resolution would first improve with more runs, but after certain iterations, the SNR was so small that signals were not sufficient to define the edge and

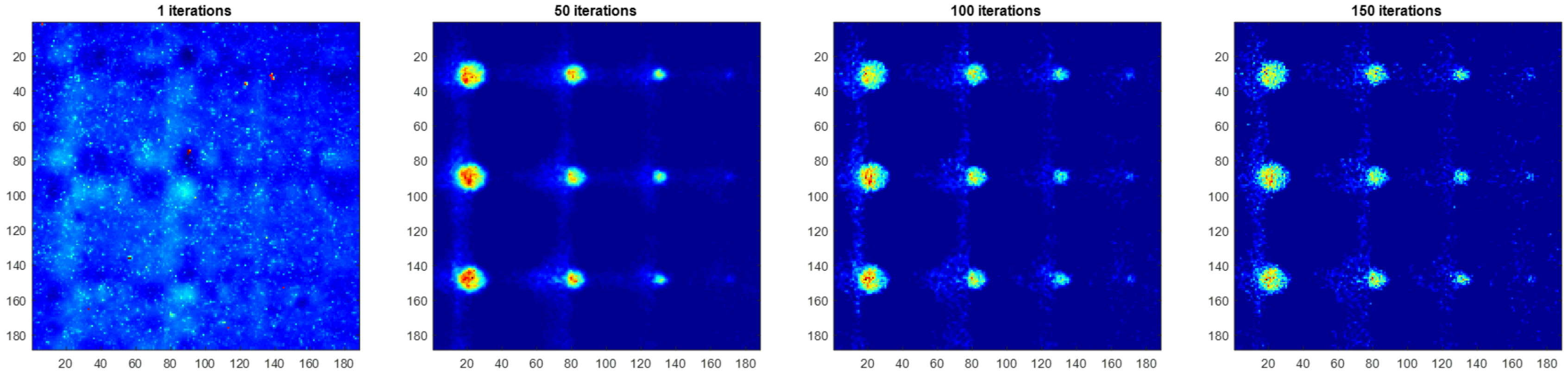

(a) (b) (c) (d)

Figure 5.46 The MLE solutions to reconstruct Figure 5.22 (a), with 1 iteration, 50 iterations, 100 iterations and 150 iterations

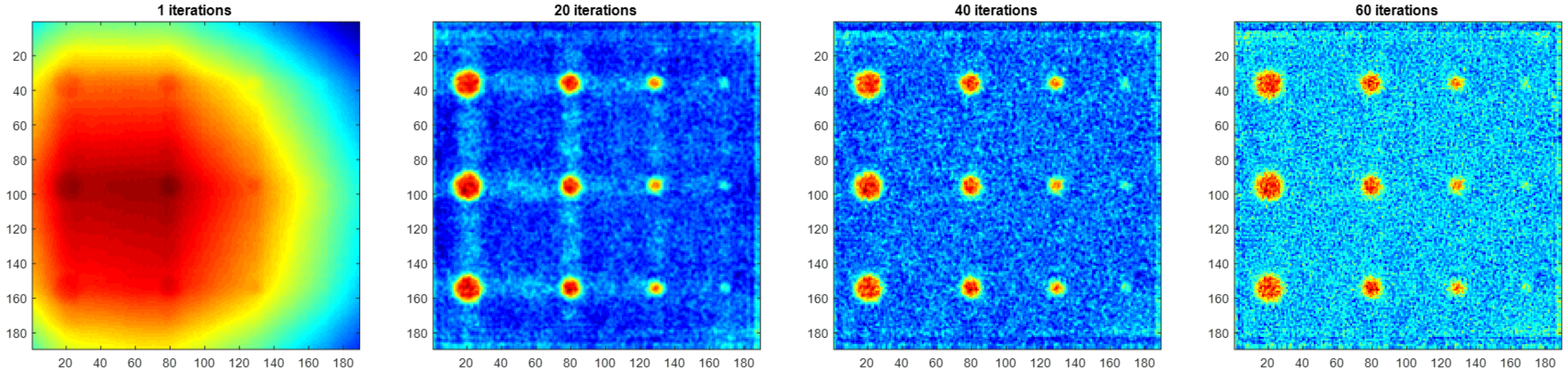

(a) (b) (c) (d)

Figure 5.47 The LSE solutions to reconstruct Figure 5.22 (a), with 1 iteration, 20 iterations, 40 iterations and 60 iterations

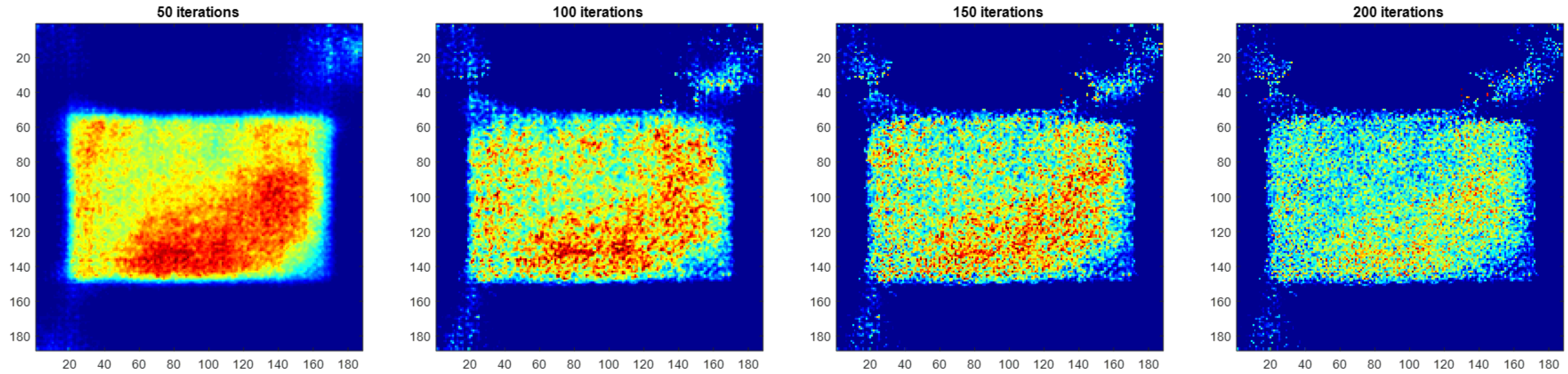

Figure 5.48 The MLE solutions to reconstruct Figure 5.23 (a), with 50 iterations, 100 iterations, 150 iterations and 200 iterations.

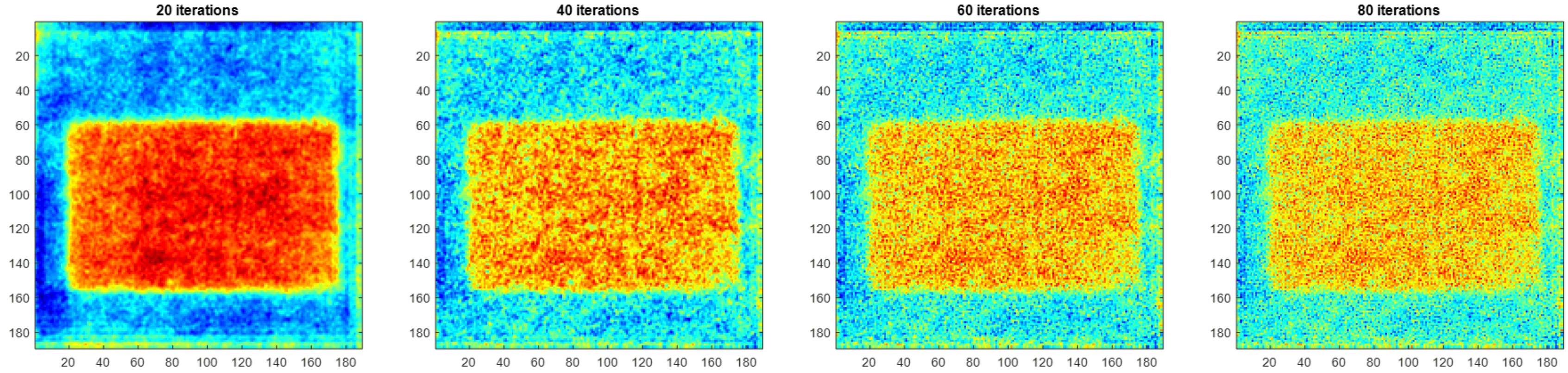

Figure 5.49 The LSE solutions to reconstruct Figure 5.23 (a), with 20 iterations, 40 iterations, 60 iterations and 80 iterations.

resolution started to degrade. In LSE, iterations were used in applying conjugate gradient method, with which the approximation can be monotonically improved to the exact solution. Resolution of LSE solution would stay at the optimum value after certain number of iterations.

The resolution and SNR were measured on these reconstructed images and the results are listed in Table 5.8. The resolution was predicted to be 185 µm with perfect reconstruction. As a comparison, the measurements of the reconstructed images using the correlation method are also presented. With MLE method, the best reconstruction was achieved at 150 iterations. The resolution was 226 µm, and the SNR was 4.3. With LSE method, the best reconstruction was achieved at 80 iterations. The resolution was 206 µm, and the SNR was also 4.3.

Table 5.8 The resolution and SNR measured from the reconstructed results of Figure 5.23 (a), using different reconstruction methods

MLE reconstruction				
	50 iterations	100 iterations	150 iterations	200 iterations
SNR	11.8	5.0	4.3	4.2
ESF Resolution	286 µm	229 µm	226 µm	248 µm
LSE reconstruction				
	20 iterations	40 iterations	60 iterations	80 iterations
SNR	15.0	5.8	5.0	4.5
ESF Resolution	315 µm	220 µm	210 µm	206 µm
Correlation reconstruction				
	κ = 1 (complete)	κ = 4 (complete)	κ = 1 (basic)	κ = 4 (basic)
SNR	6.0	10.0	3.3	5.5
ESF Resolution	280 µm	313 µm	205 µm	248 µm

The MLE and the LSE reconstructions were applied to the images taken at different magnification factors. Figure 5.23(a), Figure 5.24 (a) and Figure 5.25 (a) were taken with the same rectangular opening as the object and the same 200 µm mask. The images were first de-noised and then reconstructed with two iterative algorithms. The MLE (figure a) and LSE (figure b) reconstructed images were shown in Figure 5.50, Figure 5.51 and Figure 5.52. They are corresponding to the magnification factors of 2, 3 and 4, respectively. The number of iterations was optimized so that the result had the highest resolution and the largest SNR if more than one image had the same resolution.

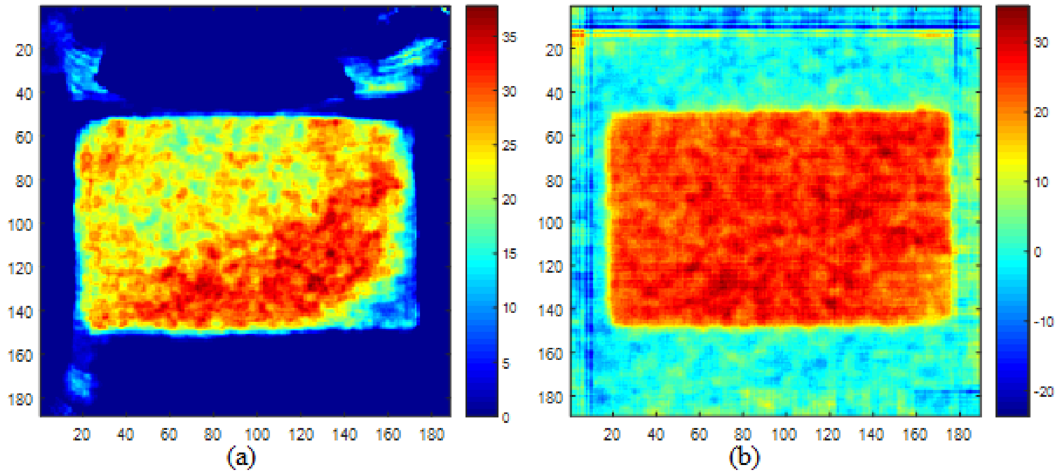

(a) (b)

Figure 5.50 The results to reconstruct the image in Figure 5.23(a), de-noised by median filter, using (a) the MLE algorithm with 150 iterations, (b) the LSE algorithm with 80 iterations.

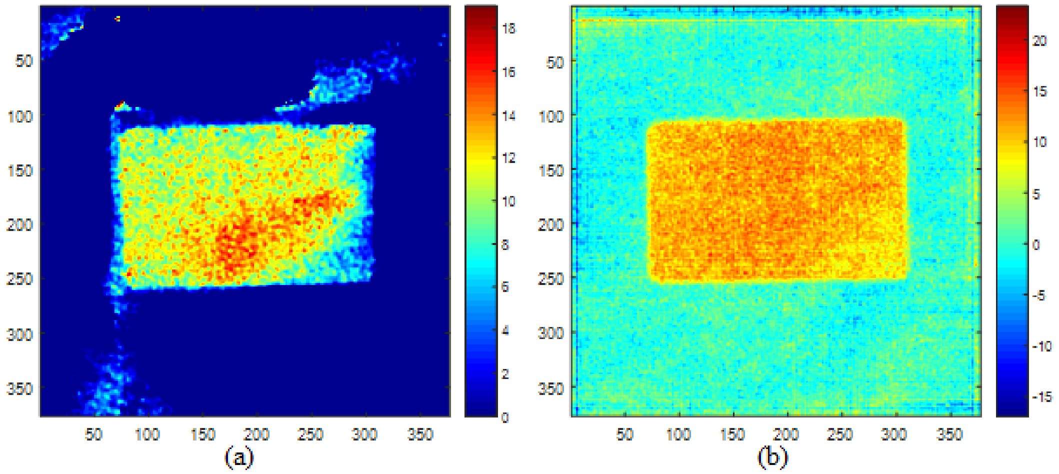

(a) (b)

Figure 5.51 The results to reconstruct the image in Figure 5.24 (a), de-noised by median filter, using (a) the MLE algorithm with 150 iterations, (b) the LSE algorithm with 100 iterations.

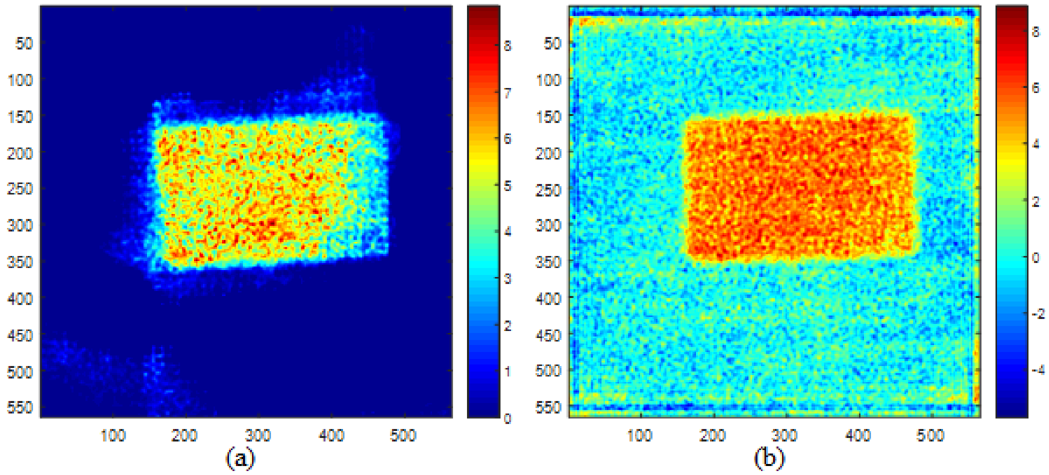

(a) (b)

Figure 5.52 The results to reconstruct the image in Figure 5.25 (a), de-noised by median filter, using (a) the MLE algorithm with 100 iterations, (b) the LSE algorithm with 40 iterations.

The resolution and the SNR of these images are listed in Table 5.9. Since the de-noise filter was a 4×4 median filter, the reconstructed results using basic correlation method with κ value of 4 were used as comparison. At magnification 2 and 3, the results of all the reconstruction methods had resolutions very close to the expected values. The LSE results had the largest SNR. However, at magnification factor of 4, the resolution of reconstructed images using the iterative methods were much larger than the one using correlation method.

Table 5.9 The resolution and SNR measured from the reconstructed results of images taken with 200 μm mask at different magnification factors, using different reconstruction methods

Mag	Expected resolution	Basic Correlation (κ = 4)		MLE		LSE	
		Resolution	SNR	Resolution	SNR	Resolution	SNR
2	238 μm	248 μm	5.5	239 μm	8.0	244 μm	10.6
3	196 μm	205 μm	5.1	228 μm	8.0	203 μm	8.7
4	185 μm	192 μm	4.1	360 μm	6.0	350 μm	6.6

5.6.2 Measurements with 100 µm Mask

The MLE and the LSE reconstructions were applied to the images taken with the 100 µm mask, which are shown in Figure 5.26 (a), Figure 5.34 (a) and Figure 5.39 (a). They were taken with the rectangular opening as the object, at magnification of 2.2, 2.8 and 3.4. The images were de-noised by a 4×4 median filter prior to reconstruction.

Figure 5.53, Figure 5.54 and Figure 5.55 present the corresponding reconstructed results using MLE method (figure a) and LSE method (figure b). Each reconstructed image was obtained with an optimized number of iterations so that the result had the highest resolution and the largest SNR if more than one image had the same resolution. The MLE solution was optimized with 100 or 150 iterations. The LSE solution was optimized with 60 or 80 iterations.

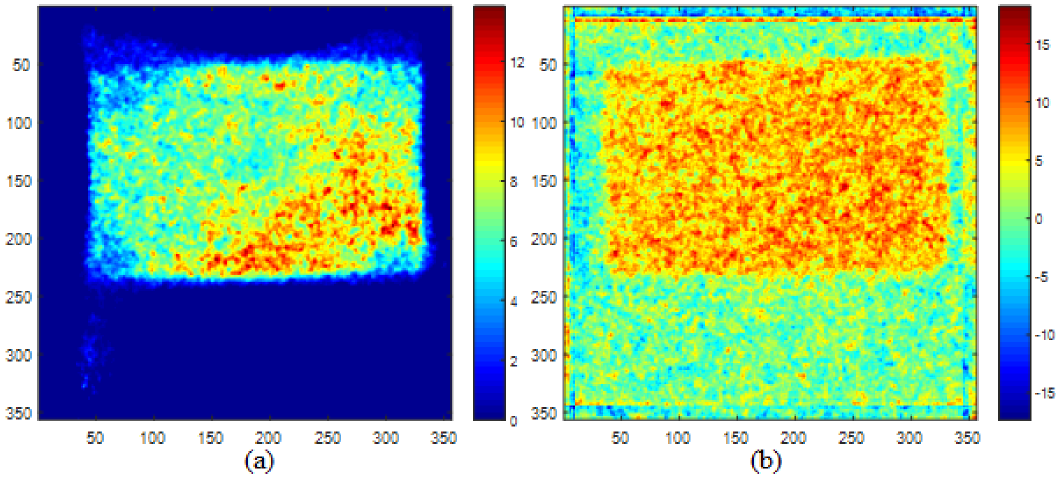

(a) (b)

Figure 5.53 The results to reconstruct the image in Figure 5.26(a), taken with the 100 µm mask at magnification of 2.2, using (a) the MLE algorithm with 100 iterations, (b) the LSE algorithm with 80 iterations.

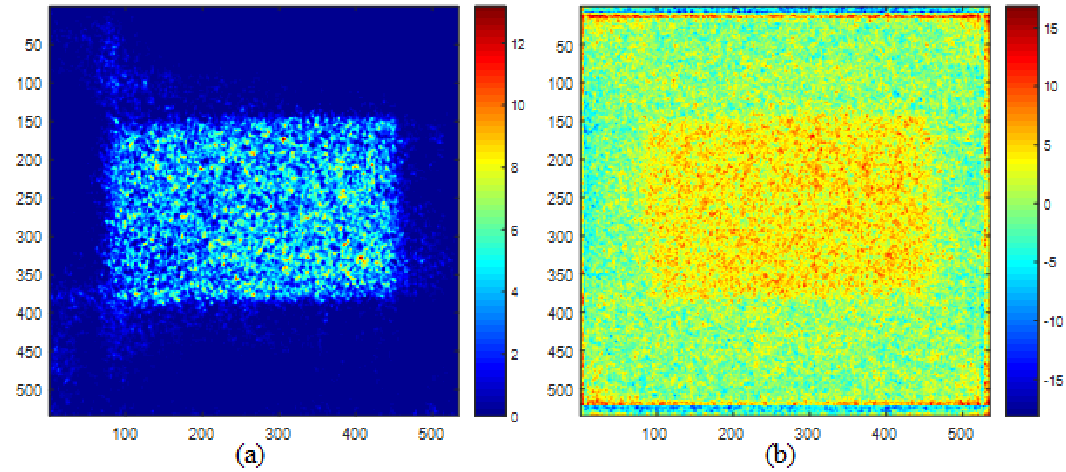

(a) (b)

Figure 5.54 The results to reconstruct the image in Figure 5.34(a), taken with the 100 µm mask at magnification of 2.8, using (a) the MLE algorithm with 150 iterations, (b) the LSE algorithm with 80 iterations.

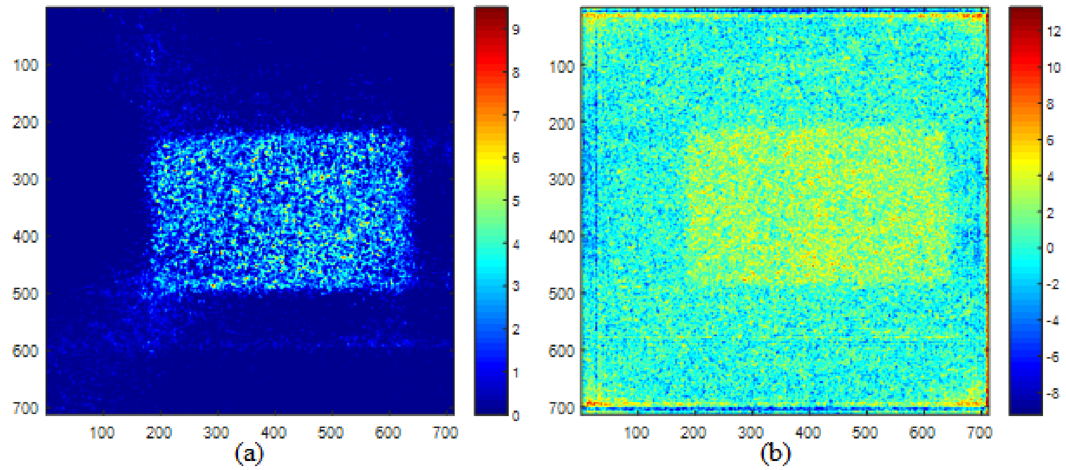

(a) (b)

Figure 5.55 The results to reconstruct the image in Figure 5.39 (a), taken with 100 µm mask at magnification of 3.4, using (a) the MLE algorithm with 150 iterations, (b) the LSE algorithm with 60 iterations.

The resolution and SNR were measured on these images. The results are listed in Table 5.10. The reconstructed results using combined correlation method with κ value of 4 were used as comparison.

Table 5.10 The resolution and SNR measured from the reconstructed results of images taken with 100 µm mask at different magnification factors, using different reconstruction methods

Mag	Expected resolution	Combine Correlation (κ = 4)		MLE		LSE	
		Resolution	SNR	Resolution	SNR	Resolution	SNR
2.2	149 µm	153 µm	6.1	212 µm	5.5	145 µm	3.5
2.8	126 µm	125 µm	3.1	202 µm	2.4	130 µm	2.2
3.4	114 µm	117 µm	3.3	204 µm	2.0	116 µm	1.9

The resolutions of reconstructed images using correlation method and LSE method were close to the expected value, which was better than resolution of MLE solution. In terms of the SNR values, combined correlation solution was better than MLE solution, which was better than LSE solution.

5.7 Discussion of Experimental Measurements

In sum, the experiments with the 200 µm mask and the 100 µm mask have successfully validated the model of the REMANI system. The results demonstrate the effects of the system parameters and reconstruction methods on the quality of reconstructed images.

1) Parameters in correlation method

For an image formed by a coded source with a mosaicked MURA pattern, correlation is the orthodox reconstruction method. There are two parameters impacting the quality of the reconstructed image: the value of κ to scale the decoding array and the size of the input image.

The κ value can be any integer number between 1 to the number of pixels on the image plane covered by the projection of single grid element on the mask. Table 5.3 presents the resolution and the SNR of images reconstructed from the same recorded image when κ was 1, 2 and 4. It can be seen that both the resolution and the SNR increase with the value of κ.

Based on the size of the input image, there are three ways to apply the correlation reconstruction. Complete correlation uses the image with side length of $1.5\left(m-1\right)s_M$, where s_M is a side length of the mask. Basic correlation uses the center portion of the image with a side length that is one third of the complete image. The result of combined correlation is a weighted sum of the complete correlation result and the basic correlation result. Table 5.7 compares the resolution and the SNR of reconstructed images obtained with three methods. It can be found that the resolutions of basic correlation solutions are close to the values calculated using Equation (3.36), which are smaller than the ones of complete correlation solutions. By properly assigning the weight, combined correlation can largely reduce the artifacts and increase the SNR values in the reconstructed images, while keep the resolutions close to the expected values.

2) System parameters and reconstructed image quality

There are two system parameters of significant importance in achieving resolution enhancement in the REMANI system: the size of the pinhole in the mask and the magnification factor. Table 5.4 compares the reconstructed images at different magnification factors taken with the 200 μm mask, and Table 5.7 compares the reconstructed images at different magnification factors taken with the 100 μm mask.

As expected in Equation (3.36), the resolution becomes smaller at higher magnification factor, and finally approaches the size of the mask pinhole. The resolution was measured to be 192 ± 15 µm with the 200 µm mask at magnification factor of 4, and 117 ± 11 µm with the 100 µm mask at magnification factor of 3.4. At magnification factor of 4, the resolution was measured as 102±32 µm. The large uncertainty was due to the low SNR, which is also an essential property in evaluating image quality. The SNR values would have a tendency to decrease with the magnification factor increasing, but it depends on many factors. With the same κ value and the same correlation method, the percentage of the signals that can be effectively used in the reconstructed images gets smaller at higher magnification, thus the SNR becomes less.

The reconstructed images with the 100 µm mask were noisier and have smaller SNR values than the ones with the 200 µm mask, if the same correlation method was used for reconstruction. For example, Figure 5.25 and (g) Figure 5.44 (c) are results of basic correlation at magnification factor of 4 with two masks. The SNR's were 4.05 and 1.25. This could be due to several reasons. First, the open fraction of the 100 µm mask is smaller than the 200 µm mask. Second, at the same magnifications, the 100 µm mask measurements use images with larger area for reconstruction. Third, the camera settings were different with the use of two masks. The response was more uniform in the 200 µm-mask measurements.

3) Different reconstruction methods

Other than correlation method, maximum likelihood estimation (MLE) and least square estimation (LSE) have also been used and evaluated as reconstruction methods. The reconstructed results were compared. The quantitative analyses are summarized in three tables.

Table 5.8 shows the reconstructed images with different numbers of iterations. SNR values in the reconstructed images decrease with the number of iterations for both methods. Resolutions of MLE solutions first improve with more runs, but will degrade after certain iterations due to low SNR. Resolutions of LSE solutions get smaller with numbers of iterations increasing and stay at the optimum value after certain iterations.

Table 5.9 and Table 5.10 compares the reconstruction methods in the 200 µm-mask measurements and 100 µm-mask measurements. If the signal is sufficient in the recorded image, the resolutions of the reconstructed images using correlation method and LSE method agree well with the values predicted by Equation (3.36). If a median filter is applied prior to reconstruction to de-noise the image, the LSE results are equivalent to the correlation results with the κ value set to be the size of the median filter. At higher magnification factors, LSE solutions may not converge and lose the sharpness. Usually, MLE would fail before LSE. It produces reconstructed image with relatively low resolutions.

In our case, for the 200 µm mask, LSE method has the best performance at magnification factor 2 and 3, but fails at magnification factor of 4. For the 100 µm mask, results using combined correlation have better than other reconstruction methods.

Chapter 6

Conclusion and Future Work

6.1 Conclusion

Design and implementation of a REMANI system has been investigated at the PULSTAR reactor. The studies include theoretical understanding, Monte Carlo simulations and practical performance. The performance of the PULSTAR's thermal neutron imaging facility in conventional radiography has been analyzed as a baseline for the design of REMANI system. Resolution and Noise performance has been quantified.

A mathematical model for a REMANI system have been developed and compared to MCNP simulations. It was found that the achieved resolution can be significantly improved over the limit set by the inherent resolution of the detector. The resolution is largely dependent on the size of the hole of the mask and magnification factor. REMANI system has been designed for use with film, imaging plate and real-time scintillator based systems, respectively.

Three coded masks have been fabricated and used with the different types of detection systems. The effect of enhancing resolution using a REMANI approach was successfully demonstrated with the scintillator system and a multi-pinhole mask. The mask was coded by a 178×178 modified uniform redundant array. The diameter of pinhole is 100 µm and the grid size is 200 µm. By analyzing the spread of the reconstructed image of a sharp gadolinium edge, the system resolution was shown to be improved from 245 ± 6 µm under the conventional imaging setup to 117 ± 11 µm at a magnification factor of 3.4, reconstructed by the correlation method.

The maximum likelihood estimation (MLE) and the least square estimation (LSE) have also been investigated as reconstruction methods, and were compared with the correlation method. It is found that the correlation method has the most stable performances among the three, while the LSE demonstrated high SNR and small artifacts at low magnifications. The resolution of the reconstructed images agreed well with the values predicted by the mathematical model.

The present work successfully demonstrates the validity of the model and the feasibility of practical implementation of the REMANI system. The spatial resolution of a neutron imaging system can overcome the limitation of the detection system. In order to use the REMANI system to image real objects, the neutron beam needs to be upgraded. First, a more intense neutron source and longer wavelength neutrons will shorten the exposure time, so high magnifications can be used in practical applications. Second, a cleaner thermal neutron beam will reduce the image noise introduced by the gamma and fast neutron components. Thus the contrast, which are due to the difference of neutron attenuation characteristics in the real object, will not be overwhelmed and can be shown clearly in the neutron images.

6.2 Future work

6.2.1 Update of Scintillator System

It is possible to further improve the resolution of the scintillator system with the use of REMANI system and investment in updating hardware. First of all, a major factor of the resolution degradation in the conventional system is the lens aberration. A high quality lens system can reduce the resolution in a conventional setup as low as 130 μm. Secondly, the REMANI system can be set up and the mask with 50 μm-diameter pinholes can be fabricated.

The resolution is expected to achieve 50 µm at the magnification factor of 4. The design of the 50 µm mask shown in Figure 6.1 is ready to be used. It contains 65,520 holes with a diameter of 50 µm, distributed on a grid size of 100 µm. The open fraction is 8.04%, the noise performance of this new mask will be in between the 100-µm mask and 200-µm mask.

The possibility of performing the tomographic measurements in the REMANI setup can also be investigated. The resolution of the 3D images in a tomographic system was limited by the resolution of the radiographic projections. Using the REMANI system with the currently available tomographic system can help in achieving high resolution neutron tomography in the facility. Two steps of reconstruction are required. One is used to resolve the multiplexed images from the multiple pinholes of the mask, and the other one is to retrieve 3D information of the objects. Two main challenges will be noise amplifications in reconstruction process and long exposure time in data acquisition process.

6.2.2 The use of Anti-mask

One of the shortcomings of the correlation methods is that the results are very sensitive to the system noise. This can be reduced with the use of an anti-mask.

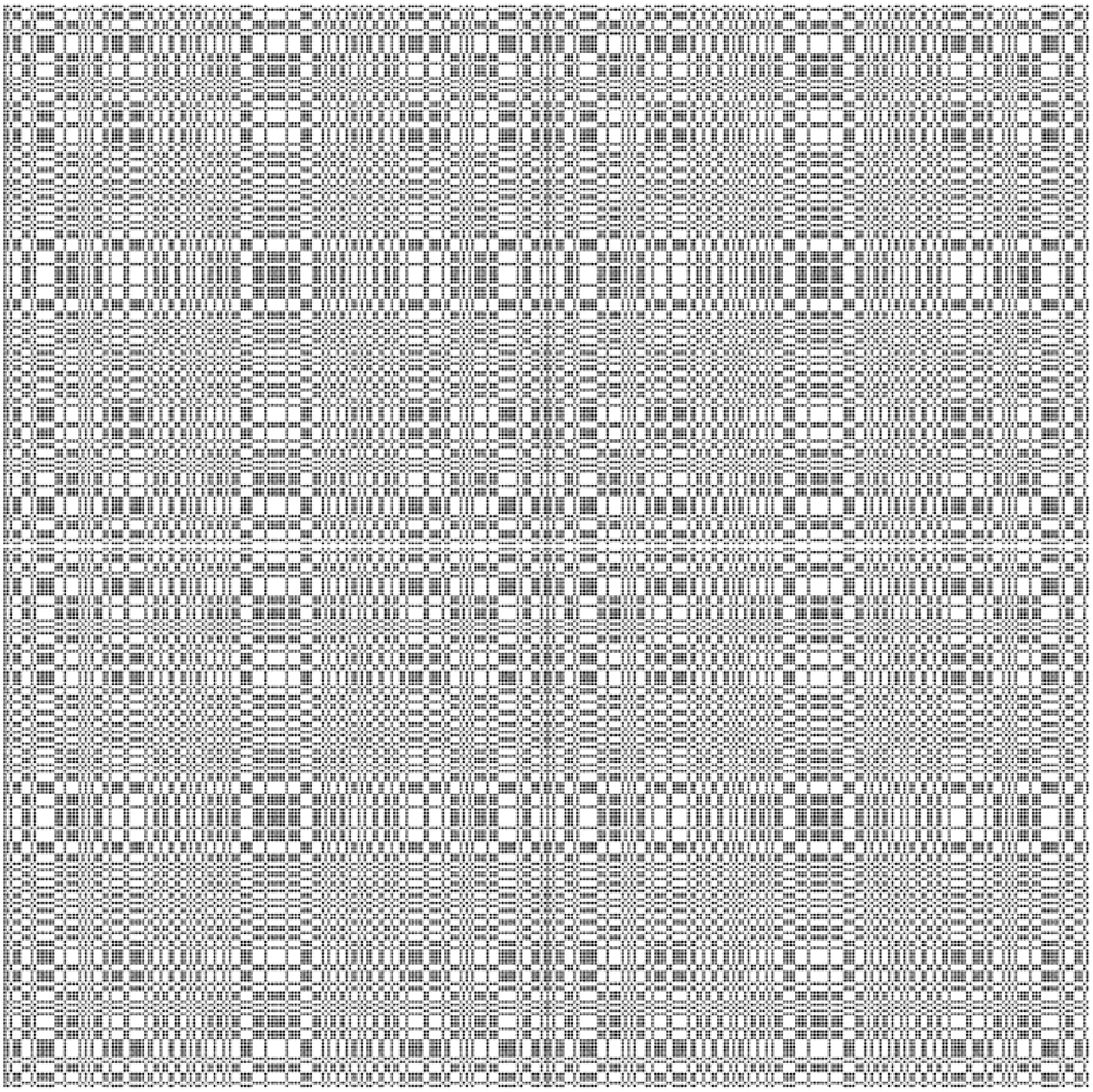

Figure 6.1 The design of a 50-μm mask

An anti- mask is generated from an array that is opposite to the mask array. Denote the arrays for the mask and the anti-mask by A^+ and A^-. When A^+ is 1, A^- is 0 and vice versa. The recorded images taken with both masks are given by

$$P^{+} = O * A^{+} + N$$
$$P^{-} = O * A^{-} + N \tag{6.1}$$

The decoding array G^+ and G^- are also opposite. The reconstructed images can be obtained by

$$\hat{O}^{+} = P^{+} \times G^{+} = O * (A^{+} \times G^{+}) + N \times G^{+}$$
$$\hat{O}^{-} = P^{-} \times G^{-} = O * (A^{-} \times G^{-}) + N \times G^{-} \tag{6.2}$$

The final reconstructed result is the summation of the two, in which the additive noise term can be cancelled out.

$$\hat{O} = \frac{\hat{O}^{+} + \hat{O}^{-}}{2} = \frac{O}{2} * \left(A^{+} \times G^{+} + A^{-} \times G^{-}\right) \tag{6.3}$$

The challenge to apply this method is to place the two masks at the same locations when taking the two images. A special collimator as shown in Figure 6.2 has been designed for this purpose. The new collimator has a length of 120 cm. The object plate can be attached directly to the exit of the collimator.

The front side is a mask positioning system to hold a pair of mask and anti-mask. It has already been fabricated and Figure 6.3 shows its picture. The pair of mask and anti-mask are mounted on a rack that can be moved horizontally by a bevel gear. A hole is drilled through

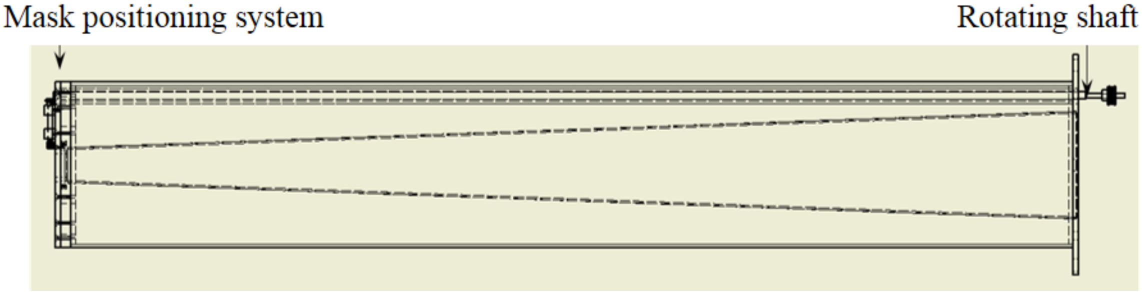

Figure 6.2 The design of a new collimator to use a pair of mask and anti-mask

Figure 6.3 The design of a new collimator to use a pair of mask and anti-mask

the collimator and the beam shielding and an inserted shaft can rotate and turn the bevel gear and adjust the location of the rack. Therefore, the aperture can conveniently switch among the two masks and the conventional open aperture. When the mask or the anti-mask is used, the shaft will be tensioned by a motor to the edges. Measurements show that by pushing the rack to the extreme locations, the mask returns to the same position with a precision of 12 μm.

REFERENCES

Ables, J. G. (1968, December). Fourier transform photography: a new method for X-ray astronomy. In Proceedings of the Astronomical Society of Australia (Vol. 1, p. 172).

Accorsi, R. (2001a). Design of a near-field coded aperture cameras for high-resolution medical and industrial gamma-ray imaging (Doctoral dissertation). Massachusetts Institute of Technology.

Accorsi, R., Gasparini, F., & Lanza, R. C. (2001b). A coded aperture for high-resolution nuclear medicine planar imaging with a conventional Anger camera: experimental results. Nuclear Science, IEEE Transactions on, 48(6), 2411-2417.

Aitken, G. J. M., Corteggiani, J. P., & Gay, J. (1981). Partially redundant apertures for infrared stellar imaging. JOSA, 71(6), 759-763.

Barrett, H. H. (1972). Fresnel zone plate imaging in nuclear medicine. Journal of nuclear medicine, 13(6), 382-385.

Barrett, H. H., & Swindell, W. (1981). Radiological imaging: the theory of image formation, detection and processing 1981.

Barton, J. P. (1967). Divergent Beam Collimator For Neutron Radiography. CEN, Grenoble, France.

Baumert, L. D. (1969). Difference sets. SIAM Journal on Applied Mathematics, 17(4), 826-833.

Berger, H. (1966). Characteristics of a thermal neutron television imaging system. Materials Evaluation (US) Formerly Nondestr. Test., 4.

Berger, H. (1971). Neutron radiography. Annual Review of Nuclear Science, 21(1), 335-364.

Berger, H. (1976). Practical applications of neutron radiography and gaging: a symposium Gaithersburg, Md. 10-11 Feb. 1975 (Vol. 586). ASTM International. Chicago.

Boedeker, K. L., Cooper, V. N., & McNitt-Gray, M. F. (2007). Application of the noise power spectrum in modern diagnostic MDCT: part I. Measurement of noise power spectra and noise equivalent quanta. Physics in medicine and biology, 52(14), 4027.

Boreman, G. (2001). Modulation transfer function in optical and electro-optical systems. Bellingham, Wash., USA: SPIE Press.

Cannon, T. M., & Fenimore, E. E. (1980). Coded aperture imaging: many holes make light work. Optical Engineering, 19(3), 193283-193283.

Caroli, E., Stephen, J. B., Di Cocco, G., Natalucci, L., & Spizzichino, A. (1987). Coded aperture imaging in X-and gamma-ray astronomy. Space Science Reviews, 45(3-4), 349-403.

Ceglio, N. M., Attwood, D. T., & George, E. V. (1977). Zone-plate coded imaging of laser-produced plasmas. Journal of Applied Physics, 48(4), 1566-1569.

Chalovich, T. R., Bennett, L. G. I., Lewis, W. J., & Brenizer, J. S. (2004). Development of neutron radioscopy for the inspection of CF188 flight control surfaces. Applied radiation and isotopes, 61(4), 693-700.

Dainty, J. C., & Shaw, R. (1974). Image science. Principles, analysis and evaluation of photographic-type imaging processes. London: Academic Press, 1974.

Dicke, R. H. (1968). Scatter-hole cameras for x-rays and gamma rays. The Astrophysical Journal, 153, L101.

Domanus, J. C. Practical neutron radiography. Kluwer Academic Publishers, 1992.

Estermann, M., & Dubois, J. (2005). Investigation of the properties of amorphous silicon flat-panel detectors suitable for real-time neutron imaging. IEEE transactions on nuclear science, 52(1), 356-359.

Fenimore, E. E., & Cannon, T. M. (1978). Coded aperture imaging with uniformly redundant arrays. Applied optics, 17(3), 337-347.

Fenimore, E. E. (1980). Coded aperture imaging: the modulation transfer function for uniformly redundant arrays. Applied optics, 19(14), 2465-2471.

Fleming, J. S., & Goddard, B. A. (1984). An evaluation of techniques for stationary coded aperture three-dimensional imaging in nuclear medicine. Nuclear Instruments and Methods in Physics Research, 221(1), 242-246.

Fraser, G. W., & Pearson, J. F. (1990). The direct detection of thermal neutrons by imaging microchannel-plate detectors. Nuclear Instruments and Methods in Physics Research Section A: Accelerators, Spectrometers, Detectors and Associated Equipment, 293(3), 569-574.

Frei, G., Lehmann, E. H., Mannes, D., & Boillat, P. (2009). The neutron micro-tomography setup at PSI and its use for research purposes and engineering applications. Nuclear Instruments and Methods in Physics Research Section A: Accelerators, Spectrometers, Detectors and Associated Equipment, 605(1), 111-114.

Gaskill, J. D. (1978). Linear systems, Fourier transforms, and optics.

Gabor, D. (1949). Microscopy by reconstructed wave-fronts. Proceedings of the Royal Society of London. Series A. Mathematical and Physical Sciences, 197(1051), 454-487.

Golay, M. J. (1971). Point arrays having compact, nonredundant autocorrelations. JOSA, 61(2), 272-273.

Golomb, S. W., & Taylor, H. (1984). Constructions and properties of Costas arrays. Proceedings of the IEEE, 72(9), 1143-1163.

Gottesman, S. R., & Fenimore, E. E. (1989). New family of binary arrays for coded aperture imaging. Applied optics, 28(20), 4344-4352.

Gourlay, A. R., & Stephen, J. B. (1983). Geometric coded aperture masks. Applied optics, 22(24), 4042-4047.

Gunson, J., & Polychronopulos, B. (1976). Optimum design of a coded mask x-ray telescope for rocket applications. Monthly Notices of the Royal Astronomical Society, 177(3), 485-497.

Harms, A. A., & Wyman, D. R. (1986). Mathematics and physics of neutron radiography. Springer Science & Business Media.

Harms, A., & Zeilinger, A. (1977). A new formulation of total unsharpness in radiography. Physics in Medicine and Biology, 70-80.

Hasegawa, B. H. (1990). The physics of medical x-ray imaging.

Hawari, A. I., et al. "Ab initio generation of thermal neutron scattering cross sections." Proc. Int. Conf. PHYSOR. 2004.

Heusdens, R., Engelen, S., Buist, P. J., Noroozi, A., Sundaramoorthy, P. P., Verhoeven, C. J. M., ... & Gill, E. K. A. (2012, December). Match filtering approach for signal acquisition in radio-pulsar navigation. In Proceedings of the 63rd International Astronautical Congress IAC 2012, Naples, Italy, 1-5 Oct. 2012. IAF International Astronautical Federation.

Hussey, D. S., Jacobson, D. L., Arif, M., Owejan, J. P., Gagliardo, J. J., & Trabold, T. A. (2007). Neutron images of the through-plane water distribution of an operating PEM fuel cell. Journal of Power Sources, 172(1), 225-228.

Hussey, D. S., Brocker, C., Cook, J. C., Jacobson, D. L., Gentile, T. R., Chen, W. C., & Arif, M. (2015). A New Cold Neutron Imaging Instrument at NIST. Physics Procedia, 69, 48-54.

IEC 62220-1. (2003). Medical electrical equipment: Characteristics of digital X-ray imaging devices – Part 1: Part 1: Determination of the detective quantum efficiency. International Electrotechnical Commission, Geneva, Switzerland.

Kallmann, H., & Kuhnm, E. (1940). U.S. Patent No. 2,186,757. Washington, DC: U.S. Patent and Trademark Office.

Kallmann, H. (1948). Neutron radiography. Research; a journal of science and its applications, 1(6), 254-260.

Karasawa, Y., Niimura, N., Tanaka, I., Miyahara, J., Takahashi, K., Saito, H., & Matsubayashi, M. (1995). An imaging plate neutron detector. Physica B: Condensed Matter, 213, 978-981.

Kardjilov, N., Manke, I., Strobl, M., Hilger, A., Treimer, W., Meissner, M., ... & Banhart, J. (2008). Three-dimensional imaging of magnetic fields with polarized neutrons. Nature Physics, 4(5), 399-403.

Kardjilov, N., Dawson, M., Hilger, A., Manke, I., Strobl, M., Penumadu, D., ... & Banhart, J. (2011). A highly adaptive detector system for high resolution neutron imaging. Nuclear Instruments and Methods in Physics Research Section A: Accelerators, Spectrometers, Detectors and Associated Equipment, 651(1), 95-99.

Kobayashi, H., & Satoh, M. (1999). Basic performance of a neutron sensitive photostimulated luminescence device for neutron radiography. Nuclear Instruments and Methods in Physics Research Section A: Accelerators, Spectrometers, Detectors and Associated Equipment, 424(1), 1-8.

Kockelmann, W., Chapon, L. C., Engels, R., Schelten, J., Neelmeijer, C., Walcha, H. M., & Gorini, G. (2006). Neutrons in cultural heritage research. Journal of Neutron Research, 14(1), 37-42.

Kopilovich, L. E. (1988). Construction of nonredundant masks over square grids using difference sets. Optics communications, 68(1), 7-10.

Lehmann, E. H., Frei, G., Kühne, G., & Boillat, P. (2007). The micro-setup for neutron imaging: A major step forward to improve the spatial resolution. Nuclear Instruments and Methods in Physics Research Section A: Accelerators, Spectrometers, Detectors and Associated Equipment, 576(2), 389-396.

Lehmann, E. H., Frei, G., Vontobel, P., Josic, L., Kardjilov, N., Hilger, A., ... & Steuwer, A. (2009). The energy-selective option in neutron imaging. Nuclear Instruments and Methods in Physics Research Section A: Accelerators, Spectrometers, Detectors and Associated Equipment, 603(3), 429-438.

Lehmann, E. (2014). NR IMAGES Advances in Neutron Radiology for Nondestructive Testing. Materials Evaluation, 72, 436-436.

Liu, D., Hussey, D., Gubarev, M. V., Ramsey, B. D., Jacobson, D., Arif, M., ... & Khaykovich, B. (2013). Demonstration of achromatic cold-neutron microscope utilizing axisymmetric focusing mirrors. Applied Physics Letters, 102(18), 183508.

Lucy, L. B. (1974). An iterative technique for the rectification of observed distributions. The astronomical journal, 79, 745.

Luo, X., & Penumadu, D. (2007). Visualization of the Muliphase Flow in the Lost Foam Casting Process by Neutron Radiography and Image Processing. Materials Science and Technology - Association for Iron and Steel Technology, 1, 347.

Mertz, L., & Young, N. O. (1961). Fresnel transformations of images. Proc. Int Conf. Opt. Inst., London, 305.

Mishra, K. K. (2010). Phase Contrast Neutron Imaging Using Single and Multiple Pinhole Apertures (Doctoral dissertation). North Carolina State University.

Mishra, K. K., & Hawari, A. I. (2011). Phase contrast neutron imaging at the PULSTAR reactor. Nuclear Instruments and Methods in Physics Research Section A: Accelerators, Spectrometers, Detectors and Associated Equipment, 652(1), 615-619.

Moghaddam, K. K., Taheri, T., & Ayubian, M. (2008). Bone structure investigation using X-ray and neutron radiography techniques. Applied Radiation and Isotopes, 66(1), 39-43.

Nagarkar, V. V., Tipnis, S. V., Gaysinskiy, V., Klugerman, Y., Squillante, M. R., & Entine, G. (2001). Structured LiI scintillator for thermal neutron imaging. Nuclear Science, IEEE Transactions on, 48(6), 2330-2334.

Neutron Imaging Facilities Survey. (2014). Jointly Prepared and Conducted by the ISNR and IAEA. Retrieved from https://www.isnr.de/images/facilities/2014-07-11_survey.pdf

Nishikawa, Robert M. (1999). The Fundamentals of MTF, Wiener Spectra, and DQE. The 41st Annual Meeting of the AAPM. Retrieved from https://www.aapm.org/meetings/99am/pdf/2798-87374.pdf

Oakley, J. (Ed.). (2003). Digital imaging: a primer for radiographers, radiologists and health care professionals. Cambridge University Press.

Padgett, R., & Kotre, C. J. (2005). Development and application of programs to measure modulation transfer function, noise power spectrum and detective quantum efficiency. Radiation protection dosimetry, 117(1-3), 283-287.

Proctor, R. J., Skinner, G. K., & Willmore, A. P. (1979). The design of optimum coded mask X-ray telescopes. Monthly Notices of the Royal Astronomical Society, 187(3), 633-643.

Richardson, W. H. (1972). Bayesian-based iterative method of image restoration. JOSA, 62(1), 55-59.

Samei, E., Flynn, M. J., & Reimann, D. A. (1998). A method for measuring the presampled MTF of digital radiographic systems using an edge test device. Medical physics, 25(1), 102-113.

Scanco Medical, General FAQ: Micro CT scanners, image analysis software, micro tomography scan services. Retrieved from http://www.scanco.ch/en/support/faq-general.html.

Schwarz, D., Vontobel, P., Lehmann, E. H., Meyer, C. A., & Bongartz, G. (2005). Neutron tomography of internal structures of vertebrate remains: a comparison with X-ray computed tomography. Palaeontologia Electronica, 8(2), 30A.

Siegmund, O. H., Vallerga, J. V., Tremsin, A. S., & Feller, W. B. (2009). High spatial and temporal resolution neutron imaging with microchannel plate detectors. Nuclear Science, IEEE Transactions on, 56(3), 1203-1209.

Singleton, R. M., Ransom, P. L., & Mittra, R. (1976). Digital imaging of gamma-ray sources with depth information. Biomedical Engineering, IEEE Transactions on, (3), 239-246.

Shestakova, I., Ovechkina, E., Gaysinskiy, V., Antal, J. J., Bobek, L., & Nagarkar, V. (2007). A high spatial resolution sensor for thermal neutron Imaging. Nuclear Science, IEEE Transactions on, 54(5), 1797-1800.

Subcommittee E07.05. (2014). ASTM E545-14 Standard method for determining image quality in direct thermal Neutron radiographic Examination. ASTM International

Subcommittee E07.05. (2008). ASTM E748-02 Standard Practices for Thermal Neutron Radiography of Materials. ASTM International.

Subcommittee E07.05. (2013). ASTM E803-91 Standard Test Method for Determining the L/D Ratio of Neutron Radiography Beams. ASTM International.

Subcommittee E07.05. (2010). ASTM E1496-05 Standard Test Method for Neutron Radiographic Dimensional Measurements. ASTM International.

Subcommittee E10.05. (2015). ASTM E261-15 Standard Practice for Determining Neutron Fluence, Fluence Rate, and Spectra by Radioactivation Techniques. ASTM International.

Subcommittee E10.05. (2013). ASTM E262-13 Standard Test Method for Determining Thermal Neutron Reaction Rates and Thermal Neutron Fluence Rates by Radioactivation Techniques. ASTM International.

Swank, R. K. (1973). Calculation of modulation transfer functions of x-ray fluorescent screens. Applied optics, 12(8), 1865-1870.

Takahashi, K., Tazaki, S., Miyahara, J., Karasawa, Y., & Niimura, N. (1996). Imaging performance of imaging plate neutron detectors. Nuclear Instruments and Methods in Physics Research Section A: Accelerators, Spectrometers, Detectors and Associated Equipment, 377(1), 119-122.

Thewlis, J. (1956). Neutron radiography. British Journal of Applied Physics, 7(10), 345.

Thompson-CSF. Boulogne, France. Data sheet on the TX 1432 tube.

Trtik, P., Hovind, J., Grünzweig, C., Bollhalder, A., Thominet, V., David, C., ... & Lehmann, E. H. (2015). Improving the spatial resolution of neutron imaging at Paul Scherrer Institut–The Neutron Microscope Project. Physics Procedia, 69, 169-176.

Van Eijk, C. W. E., Bessiere, A., & Dorenbos, P. (2004). Inorganic thermal-neutron scintillators. Nuclear Instruments and Methods in Physics Research Section A: Accelerators, Spectrometers, Detectors and Associated Equipment, 529(1), 260-267.

Wang, Y., Yagola, A., & Yang, C. (Eds.). (2012). Computational methods for applied inverse problems. Hawthorne, NJ: Walter de Gruyter & Co.

Williams, S. H., Hilger, A., Kardjilov, N., Manke, I., Strobl, M., Douissard, P. A., ... & Banhart, J. (2012). Detection system for microimaging with neutrons. Journal of Instrumentation, 7(02), P02014.

X-5 Monte Carlo Team (2003). MCNP-a general Monte Carlo N-particle transport code, version 5. Los Alamos National Laboratory, Los Alamos, NM. Report LA-UR-03-1987.

Xiao, Z., Mishra, K. K., Hawari, A. I., Bilheux, H. Z., Bingham, P. R., & Tobin Jr, K. W. (2009, October). Investigation of coded source neutron imaging at the North Carolina State University PULSTAR reactor. In Nuclear Science Symposium Conference Record (NSS/MIC), 2009 IEEE (pp. 1289-1294). IEEE.

Xiao, Z., Mishra, K. K., Hawari, A. I., Bingham, P. R., Bilheux, H. Z., & Tobin, K. W. (2010). Coded source neutron imaging at the PULSTAR reactor. Nuclear Instruments and Methods in Physics Research Section A: Accelerators, Spectrometers, Detectors and Associated Equipment, 652(1), 606-609.

Xiao, Z., & Hawari, A. I. (2011). Design considerations of a coded source neutron imaging system at the PULSTAR reactor. In Nuclear Science Symposium and Medical Imaging Conference (NSS/MIC), 2011 IEEE (pp. 450-454). IEEE.

Yehuda-Zada, Y., Orion, I., Dongwon, L., Hen, O., Beck, A., Kadmon, Y., ... & Osovizky, A. (2014). Monte Carlo Simulation for Optimizing 6LiF: ZnS (Ag) based Neutron Detector Configuration.

Yen, W. M., & Yamamoto, H. (Eds.). (2006). Phosphor handbook. CRC press.

Ziegler, J. F., Ziegler, M. D., & Biersack, J. P. (2008). SRIM–The stopping and range of ions in matter. Ion Implantation Press. Available at: http://www.srim.org/

APPENDIX

Appendix A

A.1 Derivation of Equation (3.5)

Equation (3.4) in section 3.1 is

$$T(x,y) = \iint\limits_{Aperture} A(\eta,\xi)\frac{\cos^3\theta}{4\pi\left(L+b\right)^2}O(u,v)d\eta d\xi$$

where (η,ξ), (u,v) and (x,y) follow the relationship $x = mu-\left(m-1\right)\eta, y = mv-\left(m-1\right)\xi$.

Since $\cos^3\theta$ is approximately equal to one at any point *(x,y)* on the image plane, the term $\frac{\cos^3\theta}{4\pi\left(L+b\right)^2}$ is a constant and can be neglected. Substitute $\eta = \frac{mu-x}{m-1}, \xi = \frac{mv-y}{m-1}$,

$$\begin{aligned} T(x,y) &= \iint\limits_{Aperture} A(\eta,\xi)O(u,v)d\eta d\xi \\ &= \iint\limits_{Aperture} A\left(\frac{mu-x}{m-1},\frac{mv-y}{m-1}\right)O\left(u,v\right)d\frac{mu-x}{m-1}d\frac{mv-y}{m-1} \\ &= \left(\frac{m}{m-1}\right)^2 \iint\limits_{Aperture} A\left(\frac{mu-x}{m-1},\frac{mv-y}{m-1}\right)O\left(u,v\right)dudv \end{aligned}$$

To further simplify the integrand, we define two new variables *x'*, *y'* as $x' = mu$ and $y' = mv$, and re-write the above equations as

$$T(x,y) = \left(\frac{1}{m-1}\right)^2 \iint\limits_{Aperture} A\left(\frac{x'-x}{m-1},\frac{y'-y}{m-1}\right)O\left(\frac{x'}{m},\frac{y'}{m}\right)dx'dy'$$

Substituting function *A* with *A'* defined as $A'(x',y') = A\left(\frac{-x'}{m-1}, \frac{-y'}{m-1}\right)$ and substituting function *O* with *O'* defined $O'(x',y') = O\left(\frac{x'}{m}, \frac{y'}{m}\right)$, we can obtain

$$\begin{aligned} T(x,y) &= \left(\frac{1}{m-1}\right)^2 \iint\limits_{Aperture} A\left(-\frac{x-x'}{m-1}, -\frac{y-y'}{m-1}\right) O\left(\frac{x'}{m}, \frac{y'}{m}\right) dx'dy' \\ &= \left(\frac{1}{m-1}\right)^2 \iint\limits_{Aperture} A'(x-x', y-y') O'(x',y') dx'dy' \\ &= \left(\frac{1}{m-1}\right)^2 (A' * O')(x,y) \end{aligned}$$

A.2 Derivation of Equation (3.8)

Based on Equation (3.5) and $O'(x',y') = O\left(\frac{x'}{m}, \frac{y'}{m}\right)$,

$$\begin{aligned} T_\delta(x,y) &= \left(\frac{1}{m-1}\right)^2 \iint A'(x-x', y-y') O'(x',y') dx'dy' \\ &= \left(\frac{1}{m-1}\right)^2 \iint A'(x-x', y-y') O\left(\frac{x'}{m}, \frac{y'}{m}\right) dx'dy' \end{aligned}$$

Substitute $x' = mu$, $y' = mv$ and $O(u,v) = \delta(u-u_\delta, v-v_\delta)$,

$$\begin{aligned} T_\delta(x,y) &= \left(\frac{m}{m-1}\right)^2 \iint A'(x-mu, y-mv) O(u,v) dudv \\ &= \left(\frac{m}{m-1}\right)^2 \iint A'(x-mu, y-mv) \delta(u-u_\delta, v-v_\delta) dudv \end{aligned}$$

Define a function $A_m\left(x,y\right)=A\left(\frac{-mx}{m-1},\frac{-my}{m-1}\right)=A'\left(mx,my\right)$. Therefore,

$$
\begin{aligned}
T_\delta(x,y) &= \left(\frac{m}{m-1}\right)^2 \iint A\left(-\frac{x-mu}{m-1},-\frac{y-mv}{m-1}\right)\delta\left(u-u_\delta,v-v_\delta\right)dudv \\
&= \left(\frac{m}{m-1}\right)^2 \iint A_m\left(\frac{x-mu}{m},\frac{y-mv}{m}\right)\delta\left(u-u_\delta,v-v_\delta\right)dudv \\
&= \left(\frac{m}{m-1}\right)^2 \iint A_m\left(\frac{x}{m}-u,\frac{y}{m}-v\right)\delta\left(u-u_\delta,v-v_\delta\right)dudv \\
&= \left(\frac{m}{m-1}\right)^2 A_m\left(\frac{x}{m}-u_\delta,\frac{y}{m}-v_\delta\right) \\
&= \left(\frac{m}{m-1}\right)^2 A\left(-\frac{x-mu_\delta}{m-1},-\frac{y-mv_\delta}{m-1}\right)
\end{aligned}
$$

A.3 Derivation of Equation (3.22)

A digital image obtained with a multi-pinhole aperture can be given in a form of integration as shown in Equation (3.20). Equation (3.22) can be derived based on Equation (3.20) and (3.21), taking advantage of the properties of δ functions.

With the definition of $I_{\text{single}}\left(x,y\right)=\left(\frac{1}{m-1}\right)^2\left(O'*A_1'*h_d\right)(x,y)$, Equation (3.19) can be re-written as,

$$
\begin{aligned}
P_{\text{multi}}\left(i,j\right) &= \int_{(i-0.5)\Delta s}^{(i+0.5)\Delta s}\int_{(j-0.5)\Delta s}^{(j+0.5)\Delta s}\left[\left(\frac{1}{m-1}\right)^2\left(A_\delta'*A_1'*O'*h_d\right)(x,y)\right]dxdy \\
&= \int_{(i-0.5)\Delta s}^{(i+0.5)\Delta s}\int_{(j-0.5)\Delta s}^{(j+0.5)\Delta s}\left[\left(A_\delta'*I_{\text{single}}\right)(x,y)\right]dxdy
\end{aligned}
$$

Function $A_\delta'(x',y')$ is a selection of δ functions,

$$A_\delta'(x',y') = \sum_p \delta\left(x' - x_p', y' - y_p'\right)$$

where $\left(x_p', y_p'\right)$ are coordinates of the p^{th} hole on the mask, scaling by a factor of *-(m-1)*.

$$\begin{aligned}
P_{\text{multi}}(i,j) &= \int_{(i-0.5)\Delta s}^{(i+0.5)\Delta s} \int_{(j-0.5)\Delta s}^{(j+0.5)\Delta s} \left[\iint_{x',y'} I_{\text{single}}(x',y') A_\delta'(x-x', y-y') dx'dy' \right] dxdy \\
&= \int_{(i-0.5)\Delta s}^{(i+0.5)\Delta s} \int_{(j-0.5)\Delta s}^{(j+0.5)\Delta s} \left[\iint_{x',y'} I_{\text{single}}(x',y') \sum_p \delta\left(x-x'-x_p', y-y'-y_p'\right) dx'dy' \right] dxdy \\
&= \sum_p \left\{ \int_{(i-0.5)\Delta s}^{(i+0.5)\Delta s} \int_{(j-0.5)\Delta s}^{(j+0.5)\Delta s} \left[\iint_{x',y'} I_{\text{single}}(x',y') \delta\left(x-x'-x_p', y-y'-y_p'\right) dx'dy' \right] dxdy \right\} \\
&= \sum_p \left\{ \int_{(i-0.5)\Delta s}^{(i+0.5)\Delta s} \int_{(j-0.5)\Delta s}^{(j+0.5)\Delta s} I_{\text{single}}\left(x-x_p', y-y_p'\right) dxdy \right\}
\end{aligned}$$

Discrete functions $A_s'(i,j)$ and $P_{\text{single}}(i,j)$ is obtained by sampling continuous functions $A_\delta'(x,y)$ and $I_{\text{single}}(x,y)$ with an interval of *Δs*.

$$A_s'(i,j) = \sum_p \delta\left(i - i_p', j - j_p'\right), \text{ where } i_p' = \frac{x_p'}{\Delta s}, j_p' = \frac{x_p'}{\Delta s}$$

$$P_{\text{single}}(i,j) = \int_{(i-0.5)\Delta s}^{(i+0.5)\Delta s} \int_{(j-0.5)\Delta s}^{(j+0.5)\Delta s} I_{\text{single}}(x,y) dxdy$$

Since $A_\delta'(x,y)$ is a collection of Diract delta functions, $A_s'(i,j)$ is a collection of Kronecker δ functions. To be noted, in order to make i_p' and j_p' to be integer numbers, it is required the rectilinear distance between the mask holes to be an integral multiple of the pixel size.

$$\begin{aligned}\left(A_s{}'*P_{\text{single}}\right)(i,j) &= \sum_{i'}\sum_{j'} A_s{}'(i',j')\,P_{\text{single}}(i-i',j-j') \\ &= \sum_{i'}\sum_{j'}\left[\sum_p \delta\left(i'-i_p{}',j'-j_p{}'\right)\right]P_{\text{single}}(i-i',j-j') \\ &= \sum_p\left[\sum_{i'}\sum_{j'}\delta\left(i'-i_p{}',j'-j_p{}'\right)P_{\text{single}}(i-i',j-j')\right] \\ &= \sum_p P_{\text{single}}\left(i-i_p{}',j-j_p{}'\right)\end{aligned}$$

We can equate two functions

$$\sum_p\left\{\int_{(i-0.5)\Delta s}^{(i+0.5)\Delta s}\int_{(j-0.5)\Delta s}^{(j+0.5)\Delta s} I_{\text{single}}\left(x-x_p{}',y-y_p{}'\right)dxdy\right\} = \sum_p P_{\text{single}}\left(i-i_p{}',j-j_p{}'\right)$$

Therefore, $P_{\text{multi}}(i,j)=\left(A_s{}'*P_{\text{single}}\right)(i,j)$.